Synthesis, Structure and Properties of Photofunctional Oxide Materials

by

Bethany Rae McBride

A thesis submitted for the degree of Doctor of Philosophy

of

The Australian National University

February, 2019

© Copyright by Bethany Rae McBride 2019

All Rights Reserved

Declaration

Except where specifically acknowledged in the text, this thesis constitutes original work conducted by the candidate.

- Bethany Rae McBride

Acknowledgements

Advisors

I'd like to give thanks to my supervisor, Professor Yun Liu for taking me on as a student and helping me develop skills for my future. To Associate Professor Terry Frankcombe for providing advice when needed. To Professor Ray Withers, whose endless friendliness and expertise in crystallography were invaluable. To Dr. Lasse Norén who taught me an immense amount about synthesis and diffraction that I would be lost without and is firmly to blame for an ongoing coffee addiction.

I would also like to thank the academics Professor Garry McIntyre, Dr. Mark Ellison, Professor John White AO, Professor Inger Mewburn, and Professor Gottfried Otting for their sage advice and exposure to invaluable opportunities.

Collaborators

There are many people I would like to thank and acknowledge for their assistance with the experiments presented in this thesis.

To my research colleagues in Professor Liu's Group both past and present. Dr. Teng Lu, Haoxin Mai, Dr. Wen Dong, Dr. Jian Wang, Dr. Wanbiao Hu, Dr. Jianli Wang and Kenny Lau provided assistance over the years with experiments including electrical characterisations and Atomic Force Microscopy. Dr. Qingbo Sun, Claire Tjokrowidjaja, and Jonathon Lieschke collaborated on a number of synthetic experiments which formed part of Chapters 3, 5 and 6, and I am very grateful for their help. I also extend my immense gratitude to postdoctoral fellows Dr. Naren Narayanan (for help with magnetic data collection) and Dr. David Cortie (for help with DFT calculations).

I would like to extend further thanks to other ANU based staff who collaborated on projects including Dr. Hua Chen and Dr. Jeff Chen at the Centre for Advanced Microscopy for their assistance with microscope operation. The Research School of Chemistry (RSC) researchers Dr. Nick Cox and Julien Langley also provided technical and theoretical assistance with ESR.

There were numerous collaborators external to ANU whom contributed expertise and access to equipment which I would like acknowledge. To Dr. Wayne Hutchison, Professor Sean Cadogan, and Dr. Nancy Elewa from UNSW Canberra for access to magnetic measurement equipment and Mössbauer spectroscopy. To Professor Wensheng Shi and Shaoyang Zhang for assistance in measuring absorbance and photocatalytic properties of samples at the

Chinese Institute of Chemistry and Physics. To Dr. Adam Berlie and Dr. Helen Playford for their measurements and assistance with interpretation of data from magnetization, neutron and muon experiments at the ISIS Muon and Neutron Source in the UK. To Dr. Dehong Yu and Dr. Max Avdeev for support and assistance with neutron measurements at the Australian Centre for Neutron Scattering. To Dr. Bill Gong and Outi Mustonen at UNSW Sydney for their expertise in and measurement of XPS on various samples.

Support Network

I would like to thank many people for helping me get so far.

To the RSC administrative and technical staff for supporting my research. To my fellow students at ANU (including students taught over the last 5 years) that have provided a network that I would be lost without and who helped me grow as a person and a communicator. To ANU Research Training Skills and PARSA for provision of Thesis Boot Camp and Shut Up and Write respectively which really got this thesis done. Specific thanks to Victoria Firth-Smith who is a fantastic human being and a real champion of the students.

To my friends who made this thesis happen thanks to their unwavering support. To Sarah for always letting me to talk to her about everything and providing endless warmth, to Emma whose humour and outrageous strength motivate me constantly, to Reyner who has never failed to be there with advice and go along with my ridiculous ideas, and to all three for always believing I was capable when I didn't.

I thank my amazing family for providing unconditional love and reassurance that they are proud no matter what happens. To my brother for facilitating regular chill out sessions. To my grandparents who are always happy to see me no matter what. To my extended family for helping me find places to stay and providing much needed company. Finally, to my parents for calmly fielding stressed out queries, sending me pictures of pets at precisely the right moment and never doubting me.

Financers

I was supported by The Australian Government Research Training Program Scholarship throughout my candidature and received Scholarships from the Research School of Chemistry, ANU. I was also sponsored to attend an overseas school by ANSTO and AINSE.

Abstract

Photofunctional materials convert light into other forms of energy and are key to a number of emerging technologies such as solar cells, light sensors and photocatalysts. Crystalline metal oxides are cheap, robust and tuneable options for such applications.

In this thesis, five oxide materials are thus identified and systematically studied as viable photofunctional candidates: Cr modified perovskite $BiFeO_3$ (BFCO); Ti^{4+} and M^{2+} modified $BiFeO_3$ perovskites (M = Fe, Ni, Mg, Zn and Cu, labelled as BF*F*TO, BFNTO, BFMTO, BFZnTO and BFCuTO respectively); Aurivillius $Bi_{(m+1)}Fe_{(m-3)}Ti_{(3)}O_{(3m+3)}$ where m = 4 – 6; (V,N) modified anatase TiO_2 (VTON) and V modified rutile TiO_2 (VTO).

BFCO was synthesized in bulk for the first time with a quartz crucible at near ambient pressure. Systematic X-ray, neutron and electron diffraction studies reveal that it has a chemically disordered *R*3*c* structure. This leads to exhibition of antiferromagnetism (AFM) above room temperature, measured with magnetometry and muon spin resonance spectroscopy. The material is also ferroelectric as observed with piezoresponse force microscopy, making it multiferroic, in addition to also having a narrow band gap (~ 1.5 eV) and ability to generate photocurrent.

BFNTO and BFMTO were synthesized at ambient pressure with solid-state reaction and metal organic decomposition (MOD) methods respectively. Their light absorption, photo-excited electronic and ferroelectric properties were investigated for the first time. The magnetic properties of each are complex, with BFMTO paramagnetic to 3 K contrary to previous reports, and BFNTO possibly ordered below ~ 200 K (and thus potentially multiferroic). The dilution of paramagnetic centres and likely random chemical ordering (from Mössbauer spectroscopy) explain this result.

Aurivillius phases were also synthesized using an MOD method at ambient pressure, avoiding magnetic impurities that have plagued other studies. Their structures were refined from X-ray diffraction and Mössbauer data, appearing to be chemically disordered. Like the perovskite systems, random ordering and dilution lead to paramagnetism at room temperature, but an ordered state with AFM-like interactions may exist below 100 K in m = 5, 6. Striped ferroelectric domains in the bulk samples were imaged for the first time in m = 4, 6. Combined with visible light absorption, this leads to a clear photocurrent generation, with m = 6 being very promising for photofunctional application.

VTON anatase nanoparticles were produced using a solvothermal method new to the literature. Up to 3.5 at. % V could be introduced to make a phase pure product. However, the V exists as V^{4+} and V^{3+} and the V^{3+} increases with increasing N incorporation. In conjunction

with electron spin resonance studies, it appears V^{4+} is incorporated substitutionally and a V^{3+}-N association exists in a likely non-substitutional environment. The reduced V appears to form a gap state within the band structure and is likely the origin of low catalytic performance in degrading Rhodamine B under visible light.

VTO rutile was synthesized in the solid-state under an N_2 atmosphere to increase V levels to ~ 50 at. % (VTO50). This method incorporates V in multiple valance states (V^{5+} and V^{4+} from X-ray photoelectron spectroscopy). The optical band gap is narrowed from the 3 eV of TiO_2 to below visible in VTO50. Semiconductor behaviour with an unusual two-mechanism charge transport was observed with impedance spectroscopy for the first time. This dual valence state also seems to preclude the metal-insulator behaviour noted in other works.

Across each study, there are links between the synthesis methods, structure type, element choice, chemical ordering, valence states, and the physical properties of these photofunctional materials. This holistic understanding of linked factors contributes to gauging crystalline oxide materials for future energy transformation technologies.

Contents

Glossary

Materials and Chemicals

Acronym	Nominal Formula/Name	Intended Structure Type
BFO	$BiFeO_3$	Perovskite
BTO	$Bi_4Ti_3O_{12}$	Aurivillius
BFCO	$BiFe_{0.5}Cr_{0.5}O_3$	Perovskite
BF*F*TO	$BiFe^{3+}_{0.25}Fe^{2+}_{0.375}Ti_{0.375}O_3$	Perovskite
BFMTO	$BiFe_{0.25}Mg_{0.375}Ti_{0.375}O_3$	Perovskite
BFNTO	$BiFe_{0.25}Ni_{0.375}Ti_{0.375}O_3$	Perovskite
BFZnTO	$BiFe_{0.25}Zn_{0.375}Ti_{0.375}O_3$	Perovskite
BFCuTO	$BiFe_{0.25}Cu_{0.375}Ti_{0.375}O_3$	Perovskite
BFTO-513	$Bi_5FeTi_3O_{15}$	Aurivillius
BFTO-623	$Bi_6Fe_2Ti_3O_{18}$	Aurivillius
BFTO-733	$Bi_7Fe_3Ti_3O_{21}$	Aurivillius
VTO1	$V_{0.01}Ti_{0.99}O_2$	Rutile
VTO2	$V_{0.02}Ti_{0.98}O_2$	Rutile
VTO5	$V_{0.05}Ti_{0.95}O_2$	Rutile
VTO10	$V_{0.10}Ti_{0.90}O_2$	Rutile
VTO20	$V_{0.20}Ti_{0.80}O_2$	Rutile
VTO50	$V_{0.50}Ti_{0.50}O_2$	Rutile
VTO70	$V_{0.70}Ti_{0.30}O_2$	Rutile
VTON	$V_{0.05}Ti_{0.95}O_{2-x}N_x$	Anatase
ITO	In_2O_3•SnO_2 (indium tin oxide)	N/A
MB	$C_{16}H_{18}ClN_3S$ (Methylene Blue)	N/A
RhB	$C_{28}H_{31}ClN_2O_3$ (Rhodamine B)	N/A
EG	$(CH_2OH)_2$ (ethylene glycol)	N/A

Note: additional lettering and numbering in text differentiates synthesis methods

Techniques and Equipment

Acronym	Full Name
XRPD	X-ray Powder Diffraction
NPD	Neutron Powder Diffraction
TEM	Transmission Electron Microscopy
ED	Electron Diffraction
SEM	Scanning Electron Microscopy
BSE	Back Scattered Electron Imaging
SE	Secondary Electron Imaging
EDXS	Energy Dispersive X-ray Spectroscopy
WDXS	Wavelength Dispersive X-ray Spectroscopy
PFM	Piezoresponse Force Microscopy
μSR	Muon Spin Resonance
ESR	Electron Spin Resonance
XPS	X-ray Photoelectron Spectroscopy
UV-Vis	Ultra Violet to Visible Spectrophotometry / Diffuse Reflectance Spectroscopy
MOD	Metal Organic Decomposition
LCR meter	Inductance, Capacitance, Resistance meter

Frequently Used Symbols for Physical Properties and their Units (by subject)

Symbol	Meaning	Units
	Magnetometry	
χ (M/H)	Mass Magnetic Susceptibility	$m^3\,kg^{-1}$
θ_w	Weiss Temperature	K
μ_{eff}	Effective Moment (Curie-Weiss)	μ_B (Bohr Magneton)
m	Average Cluster Moment (Langevin)	μ_B
M	Mass Magnetization	$A\,m^2\,kg^{-1}$
S	Spin Angular Momentum	$kg\,m^2\,s^{-1}$
L	Orbital Angular Momentum	$kg\,m^2\,s^{-1}$
J	Total Angular Momentum	$kg\,m^2\,s^{-1}$
H	Magnetic Field Intensity	Oe or A/M
B	Magnetic Field Strength	T, or mT (millitesla)
T_N	Neel Temperature	K
T_c	Curie Temperature	K
	Muon Spin Resonance Spectroscopy	
λ	Relaxation	μs^{-1}
A	Asymmetry	%
	Mössbauer Spectroscopy	
QS	Quadrupole Splitting	$mm\,s^{-1}$
IS	Isomer Shift	$mm\,s^{-1}$
HWHM	Half Width Half Maximum	$mm\,s^{-1}$
I	Total Nuclear Spin Number	-
	Electron Spin Resonance Spectroscopy	
g	Scalar g-factor	-
g	***g***-tensor (with perpendicular and parallel terms)	-
A	Hyperfine Tensor (with perpendicular and parallel terms)	MHz
S	Total Electron Spin Number	-

Electrical and Optical Measurements		
X	Reactance	Ω
R	Resistance	Ω
Z	Impedance	Ω
C	Capacitance	F
L	Inductance	H (Henry)
f	Frequency	Hz
ρ	Resistivity	Ω.m
A	Electrode Area	m^2
l	Sample Thickness	m
hv	Photon Energy	eV
E_g	Band Gap Energy	eV
Abs.	Absorbance	-
F(R)	Kubelka-Munk Function	-
V	Voltage	V
Crystallography		
θ	Diffraction Angle of Incidence	◦ (degree)
λ	Radiation Wavelength	Å (ångström)
a, b, c	Lattice Vectors	Å
α, β, γ	Lattice Angles	◦
h, k, l	Miller Indices	-
d	Spacing Between (hkl) Planes	Å
D	Crystallite size from Scherrer equation	nm
[uvw]	Direction in Real Space	-
<uvw>	Family of Directions in Real Space	-
(hkl)	Plane in Real Space	-
[hkl]*	Reflection in Reciprocal Space	-
<hkl>*	Family of Reflections in Reciprocal Space	-
Subscript 'R'	Rhombohedral Setting	-
Subscript 'H'	Hexagonal Setting	-
Subscript 'P'	Primitive Setting	-
U_{iso}	Isotropic Atomic Displacement/Thermal Parameters	$Å^{-2}$
R_{wp}	Weighted Profile Residual	-
BVS	Bond Valence Sum	v.u. (valence units)
GII	Global Instability Index	v.u.

Other Descriptive Abbreviations

Abbreviation	*Meaning*
'm'	Number of perovskite layers in Aurivillius structures
*R*3	Rhombohedral space group #146
*Fmm*2	F-centred orthorhombic, space group #42
*B*2*cb*	B-centred orthorhombic, space group #41
$A2_1am$	A-centred orthorhombic, space group #36
$P4_2/mnm$	Primitive tetragonal, space group #136
$I4_1/amd$	Body-centred tetragonal, space group #141
*P*1	Triclinic, space group #1
*P*3	Rhombohedral, space group #143
*R*3*c*	Rhombohedral, space group #161
FM	Ferromagnetic
AFM	Antiferromagnetic
PV	Photovoltaic
FC	Field Cooled
ZFC	Zero Field Cooled
M-H	Field Intensity Dependent Magnetization Measurements
M-T	Temperature Dependent Magnetization Measurements
DC	Direct Current
AC	Alternating Current
RT	Room temp, 22°C in our labs
A-site	12- coordinate cation site in the perovskite structure
B-site	Octahedral 6- coordinate cation site in the perovskite structure
O-phase	B-site ordered, double perovskite
D-phase	B-site disordered, perovskite
Mössbauer	^{57}Fe Mössbauer
VB	Valence Band (highest occupied electronic bands)
CB	Conduction Band (lowest unoccupied electronic bands)
1s	Electrons in orbital with quantum numbers n = 2, l = 0
$2p_{3/2}$	Electrons in orbital with quantum numbers n = 2, l = 1, j = 3/2
3d	Electrons in orbital with quantum numbers n = 3, l = 2
$4f_{7/2}$	Electrons in orbital with quantum numbers n = 4, l = 3, j = 7/2
Kα	Relaxation of electron from 2p to 1s shell (emitting an X-ray)
A_B^C where: A,B = atom, Va, or I and C = ˙ or ′	Kröger-Vink defect notation A = species, B = lattice site and C = charge difference Va = vacancy, I = interstitial, ˙ = one positive charge , ′ = one negative charge

Publications by the Author

Related to the work presented in this thesis:

McBride, B. R., Lieschke, J., Berlie, A., Cortie, D. L., Playford, H. Y., Lu, T., Narayanan, N., Withers, R. L., Yu, D., & Liu, Y. Study of the B-site ion behaviour in the multiferroic perovskite bismuth iron chromium oxide. *Journal of Applied Physics* **123**, 154104 (2018).

Sun, Q., McBride, B. R. & Liu, Y. (N3-, M5+) Co-Doping Strategies for the Development of TiO2-Based Visible Light Catalysts. *Research and Reviews in Electrochemistry* **8**, 106 (2017).

Unrelated to the work presented in this thesis, but published during candidature:

Cortie, D. L., McBride, B. R., Narayanan, N., de Souza, N. R., Avdeev, M., Mole, R. A., McIntyre, G. J., Kearley, G. J., Withers, R., Yu, D, & Liu, Y. *et al.* Time-Disordered Crystal Structure of AlPO4-5. *The Journal of Physical Chemistry C* **121**, 18762-18770 (2017).

Lu, T., Studer, A. J., Norén, L., Hu, W., Yu, D, McBride, B., Feng Y, Withers, R. L., Chen, H., Xu, Zhuo & Liu, Y. et al. Electric-field-induced AFE-FE transitions and associated strain/preferred orientation in antiferroelectric PLZST. *Scientific Reports* **6**, 23659 (2016).

Chapter 1 Introduction

We live in an environment where there is a need for adoption of renewable energy technologies. Sunlight is an excellent source of renewable power and the solar irradiance of Earth far exceeds our power needs[1]. With the right technologies, and most importantly the right materials, we can transform sunlight (or any available light source) into another useful form of energy (i.e. by using a *'photofunction'*). Solar cells, light sensors, and photocatalysts all hinge on the usage of photofunctional materials.

When looking for materials to be used in such applications, we want to choose something cost effective, highly photofunctional, tuneable and optionally capable of other electronic functions. Oxide materials can be all of these things[2-8], but widespread implementation depends on research into appropriate combinations of crystal structures and composition that can foster the necessary physical properties.

The aim of this work is to understand the characteristics of specific candidate photofunctional oxide materials and thereby contribute to the development of future energy transformation technologies. This is necessarily achieved through the sub-aims of: identifying candidate cost-effective photofunctional oxide materials, developing low-complexity syntheses for them, studying their underlying structural and chemical features, and measuring their physical properties. This thesis shows that synthesized Cr- and Ti^{4+}/M^{2+}- modified *perovskite* bismuth ferrites, *Aurivillius* bismuth ferrite titanates, (V,N)- modified *anatase* titanium dioxide and V-modified *rutile* titanium dioxide possess photofunctional traits, and that their structural and chemical features are linked to their physical properties.

The purpose of Chapter 1 is to provide descriptive information about chemical and physical concepts key to this thesis and justify the selection of specific oxide materials through a review of the available literature.

1.1 General Concepts

1.1.1 Photofunctionality

In this thesis 'photofunctionality' is described as an ability to convert light into another form of energy to be used in a practical function. The principal requirement of a photofunctional material is an ability to absorb light of the desired wavelength, which excites an electron across the materials band gap (E_g), and results in an electron-hole pair (e^-, h^+). For visible light photofunctions, semiconducting materials with band gaps 1.5 – 3 eV wide are desirable.

In crystalline solids, the band gap of a material refers to the forbidden energy gap between the highest occupied electronic bands (the valence band, 'VB') and lowest unoccupied ones (the conduction band, 'CB'). An electronic band structure for a crystalline material is typically expressed in terms of the energy of specific electron bands with respect to their wave vectors, ***k***. The energy dispersion of these bands through ***k*** reflects how individual orbitals overlap through space. A band gap might be direct (where the CB minimum and VB maximum exist at the same ***k*** (**Figure 1.1 (a)**), or indirect (CB minimum and VB maximum occur at different ***k*** and a phonon is needed to mediate the transition (**Figure 1.1 (b)**). The crystal structure and the symmetry and energy of the orbitals for each individual element dictate the achievable band gap[9].

Through the process of chemical substitution/doping it is possible to change the fundamental band gap of an oxide. A change in the bonding might extend the valence or conduction bands resulting in an effective narrowing of the band gap, or new states may occur which sit within the gap of the host. This is illustrated in **Figure 1.1 (c)**, where density of states reflects the number of possible states that exist at a certain energy, averaged over all directions. Gap states can be detrimental to photofunctionality if excited charges become trapped there.

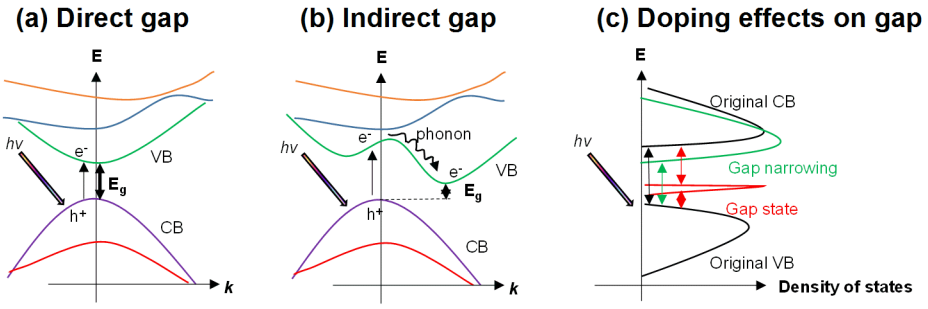

Figure 1.1. *Pictorial representation of band structures with a direct band gap* ***(a)*** *and an indirect band gap* ***(b)****. In* ***(c)*** *a pictorial representation is shown of the density of states in a semiconductor when the band gap is narrowed (green) or a gap state is formed (red) through chemical modification.*

Of interest in this thesis is to have materials with a narrow bandgap across which charges can be excited with light, and have them long-lived rather than recombine and led to re-emission of light or heat. Long-lived photoexcited charges can then be made available for transport elsewhere for electrical or chemical utilization. In semiconducting materials, bending of the electronic band structures at the interfaces between materials, electrodes and/or solvents can be used to separate and direct photoexcited charges.

The 'p-n' junction of two semiconducting materials with different band structures (one with extra acceptor bands, 'p-type' and one with donor bands, 'n-type'), is a key part of conventional solar

cells. This results in a depletion region between the materials, and an electric field is established (**Figure 1.2 (a)**)[10]. When light is shined on the system, it exhibits a voltage (this is the 'photovoltaic' or 'PV' effect). Similarly, the different energies between the surface of a material and that of a solution will also result in band bending, through establishment of a depletion region. Doping in such materials might be employed to help tailor the thickness and polarity of this layer[11] (**Figure 1.2 (b)**). Band bending in photocatalysis affects delivery of charge to the catalyst surface and the redox potential of the charges on arrival.

Other factors can also be manipulated to achieve better photofunctionality. For example, indirect band gap materials typically have less recombination than direct band gap materials[12]. Reducing the distance charges must travel to the surface or contacts by using small particles or thin films too can be advantageous. Ferroelectric materials with an internal field can also be used to separate charge (see next section).

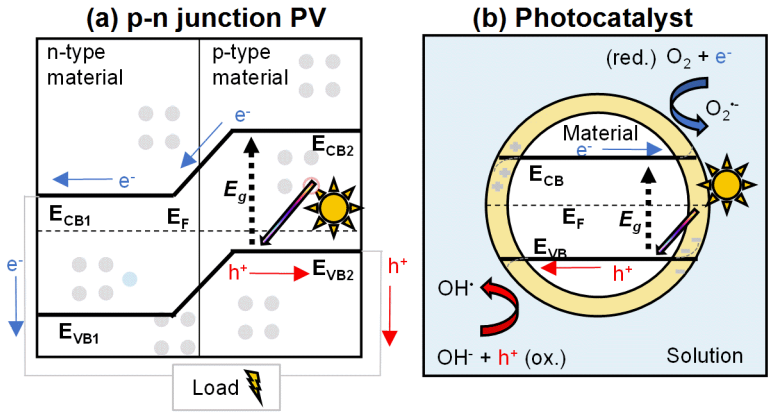

Figure 1.2. *Basic schematic of* ***(a)*** *the classic PV effect mediated through a p-n junction, and* ***(b)*** *the operation of a photocatalyst, suggesting how a space charge layer (yellow) might lead to band bending depending on the surface charges (grey) and affect typical redox reactions in solution.* E_{CB}*,* E_{VB}*,* E_F *and* E_g *refer to the energies of the conduction band, valence band, fermi level and band gap respectively.*

It is clear that establishing photofunctionality hinges particularly upon the crystal structure and elemental composition, and this has guided the selection of metal oxides for exploration in this thesis. Consideration of the other physical properties in such materials is also key to understanding their utility in energy transformation technology.

1.1.2 Ferroelectricity

Materials with ferroelectric properties can possess a permanent internal electric field, which is very promising for charge separation in photofunctional applications. Ferroelectric materials are spontaneously polarisable, switchable with an applied electric field, and when the field is withdrawn, non-zero polarisation can exist[13].

Polarisation is the density of permanent or induced electrical dipoles (***p***) per unit volume**.** Electrical dipoles in a material are established through displacement (***d***) of charge (*q*)**:**

$$\boldsymbol{p} = q.\boldsymbol{d} \qquad \textbf{(1.1)}$$

The magnitude of the dipole response will be affected by the charge of the ion and its neighbours and the flexibility of the structure to large displacements. When a structure permits long range coupling of dipoles parallel to one another, and are not 'cancelled' through symmetry, net polarisation of the sample occurs.

When a strong electric field (***E***) is applied, the polarisation response is inherently non-linear with diminishing returns at higher electric field strengths (**Figure 1.3 (a)** below). Ferroelectric materials by definition are also piezoelectric, meaning the strain of the material also changes non-linearly with applied field (**Figure 1.3 (b)**). The non-linear responses arise from the alignment of domains within the sample to applied field.

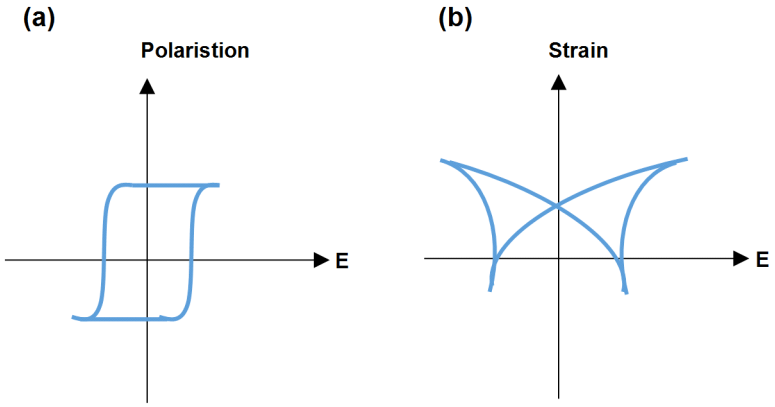

Figure 1.3. *Typical* ***(a)*** *polarisation and* ***(b)*** *strain switching spectra under applied field for a ferroelectric material.*

Ferroelectric domains are large blocks (many unit cells) within a crystal which have net polarization oriented in the same direction. Depending on the symmetry of the crystal system, polarisation might be allowed to develop along many crystallographically related directions. This can result in many domains within the natural state of the crystal that are all oriented differently. A domain wall occurs when neighbouring regions of the crystal are polarised in different crystallographic orientations, as shown in **Figure 1.4**.

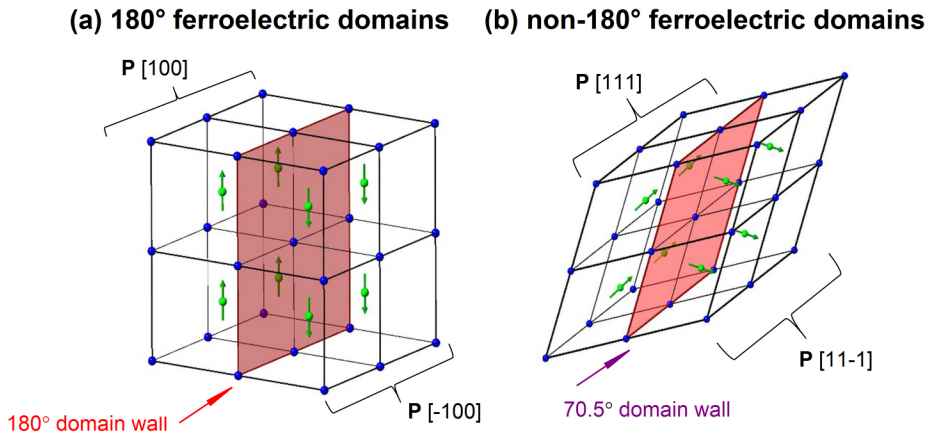

Figure 1.4. *Graphical representation of ferroelectric domains. Green arrows represent the net dipole direction per unit cell. In* ***(a)*** *the case where the alignment of domains changes by 180° across a domain wall is shown and* ***(b)*** *shows an example case where the alignment change is 70.5° due to different symmetry restrictions.*

Ferroelectric materials can have widespread applications as a consequence of such properties. The piezoelectric effect exhibited by ferroelectric materials such a $PbZr_xTi_{1-x}O_3$ (PZT)[14] make them exceedingly useful as sensors and actuators. The ability to reverse the domain direction through application of an electric field ('domain writing') in ferroelectric materials such as PZT also makes them attractive for the ongoing development of non-volatile Random Access Memory (RAM) devices[15].

Recently, impressive light absorbing organometallic molecular framework materials such as $CH_3NH_3PbI_3$ have become attractive for use in solar cells, and the ferroelectric capability of these crystals appears to be a key component to their high photovoltaic efficiencies[16]. Using domain writing to configure polar junctions could be applied to other highly absorbing ferroelectric materials to guide photoexcited charges (**Figure 1.5**). Such systems would exhibit a 'ferroelectric', 'bulk' or 'anomalous' photovoltaic response[17], and could in theory produce above band gap voltages. This thesis considers inorganic ferroelectric materials in its quest to identify photofunctional oxides. When modified with transition metals to simultaneously possess a narrowed band gap, other types of dipoles can also arise.

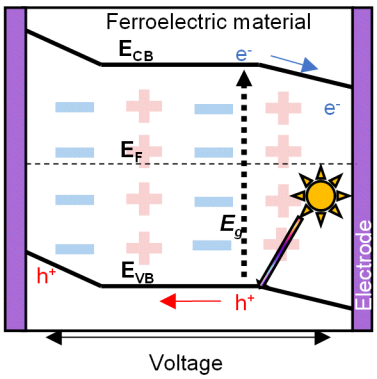

Figure 1.5. *The ferroelectric PV effect where the internal permanent polarisation (+/-) directs the transport of photo-generated e^- and h^+ after excitation across the bandgap (E_g) to generate a voltage.*

1.1.3 Magnetism

Magnetic properties in materials arise from magnetic dipole moments. Each magnetic ion in a crystal structure has a total magnetic moment ($\boldsymbol{\mu_J}$) that arises from the unpaired electrons moving around the nucleus with orbital (***L***) and spin (***S***) angular momentum:

$$\boldsymbol{\mu_{total}} = \boldsymbol{\mu_L} + \boldsymbol{\mu_s} = -\mu_B g \boldsymbol{J} \qquad \textbf{(1.2)}$$

where ***J*** is the total angular momentum, dictated by coupling of ***S*** and ***L*** according to Hund's rules, *g* is the Landé *g*-factor and μ_B is the Bohr magneton[18].

Neighbouring magnetic moments, of the same or different sizes, in a crystal can interact with one another. They might for example align parallel (ferromagnetic, 'FM'), antiparallel (antiferromagnetic, 'AFM', or ferrimagnetic) or not at all (paramagnetic) with respect to one another (**Figure 1.6**). How they align is governed by their 'exchange interaction'.

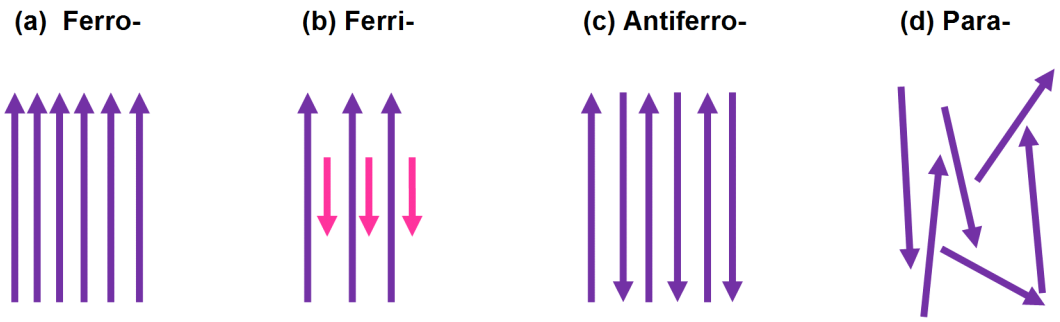

Figure 1.6. *Examples of magnetic moment alignment in crystals where **(a)** and **(b)** can lead to a net moment if extended long range throughout a crystal, and where **(c)** and **(d)** result in cancellation. Note: in ferrimagnets, moments with different magnitudes are aligned antiparallel.*

The crystal structure, elements, temperature, pressure and applied magnetic field all influence the exchange interaction. In transition metal oxides, such as those under consideration in this thesis, the exchange interaction is mediated through oxygen atoms between paramagnetic transition metals. This is called 'superexchange' and the paramagnetic d-electrons 'hop' virtually through the oxygen 2p orbital. Goodenough[19], Kanamori[20] and Anderson[21] independently postulated simple rules ('GKA rules') to predict the relative spin orientation from the orbital occupation of the involved elements and their overlap: (a) exchange between half-filled or empty orbitals through a 180° bond is strong and antiferromagnetic, (b) the 180° exchange between a half-filled and an empty orbital is weak and ferromagnetic and (c) the 90° exchange between half-filled or empty orbitals is weak and ferromagnetic. This is illustrated in **Figure 1.7** below.

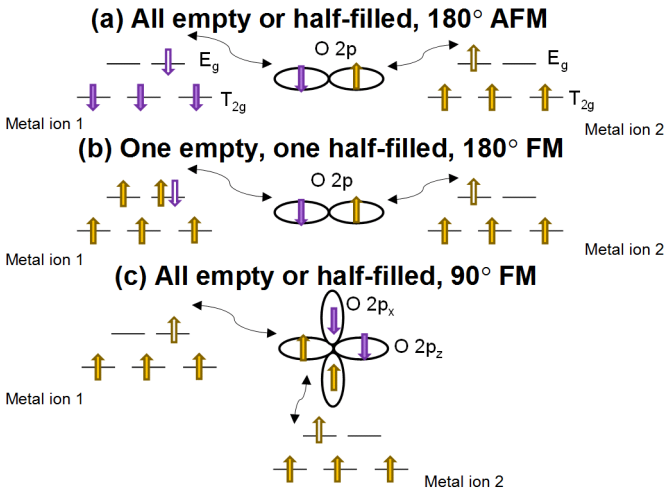

Figure 1.7. *In* ***(a)*** *180° antiferromagnetic exchange,* ***(b)*** *180° ferromagnetic exchange and* ***(c)*** *90° ferromagnetic exchange between the d-electrons of two, oxygen-bridged, octahedrally coordinated transition metals are illustrated. Information from refs. [22] and [23].*

Over three dimensions in a regularly repeating crystalline structure, these interactions can lead to long range magnetic structures. Moments could be aligned collinearly, or non-collinearly though space, leading to a variety of complex magnetic structures, all depending on the symmetry and competing exchange interactions with the crystal. These configurations will determine how the dipole moments will align with an external magnetic field.

Magnetization (***M***) is the density of the permanent or induced magnetic dipoles per unit volume. The relationship between magnetisation and applied magnetic field and temperature can give insight into the type of exchange interactions present. For example, ferromagnetic and ferrimagnetic structures can exhibit spontaneous magnetization, switchable with a field, and non-zero magnetization when the field is withdrawn[24].

Similar to ferroelectric materials, magnetic materials (such as CrO_2) can be 'written' to hold a magnetic logic state[24], and so find broad applications in magnetic memory and information processing. Miniaturization of magnetic materials also continues to draw attention for their potential use in medicine. Superparamagnetic iron oxide nanoparticles for example, find applications in medical imaging and targeted drug delivery as they can be non-invasively manipulated *in-situ* using magnetic fields[25].

In this thesis, many oxide materials with octahedral coordination and near 180° metal-oxygen-metal bonds are studied. By modifying them with paramagnetic elements, there is potential for creating long range magnetic ordering and spontaneous magnetization in addition to altering the photofunctional properties. This expands the possible applications of such materials considerably and should also be characterised.

1.1.4 Multiferroicity

In both ferroelectric and ferro/ferrimagnetic materials, dipoles can be aligned with an external field, and when that field is withdrawn, alignment remains. Potentially even more exciting is the case in which a material can be both ferroelectric and ferro/ferrimagnetic at the same time. Such materials are called multiferroics (and also includes ferroelasticity, which is not discussed in detail in this thesis). This behaviour can be coupled, with a change in either one of the electric or magnetic properties resulting in a change in the other. They can also coexist independently of one another (Type I multiferroics)[26].

This functionality gives multiferroic materials extensive applications. The ability to control a magnetic state with an applied electric field would possibly permit lower power consumption in a logic writing process. This effect could also be used to enable voltage tuning of radio/microwave frequency devices, as seen in some iron alloy/lead perovskite composites[27], and advance telecommunications technologies. Excitingly, multiferroics could also in theory possess memory storage capability with more than 2 bits, as demonstrated in part with $La_{0.1}Bi_{0.9}MnO_3$[28]. If a 1 and 0 logic state could be encoded using polarisation, and a 1 and 0 with magnetism, the number of effective combinations increases to 4. Only very specific structures could support this functionality, and in oxide systems, cations that are d^0 are generally needed to foster the ferroelectricity while paramagnetic ions are necessary to foster magnetism[29].

Based on the discussion above in the General Concepts Section, key oxide materials are identified as potential photofunctional materials to be explored in this thesis (below). These are strongly correlated materials with octahedrally coordinated metal oxide motifs that simultaneously exhibit a range of physical properties. Studying the influence of properties on one another and how these are connected to the structure and element choice will permit a

holistic understanding of their functionality and so contribute to their implementation in energy transformation technology. The following sections present an analysis of the literature, to highlight why these materials are considered good candidates and the specific gaps in understanding that this thesis will address.

1.2 Narrow Band Gap, Multiferroic Perovskite Bismuth Ferrite Based Materials

1.2.1 Why Perovskite Bismuth Ferrite?

The first structural and elemental framework explored in this thesis is that of $BiFeO_3$ (BFO). BFO is a flagship multifunctional material among oxides. The elements Bi and Fe in conjunction with its structure led it to possess a number of highly useful functions at the same time, including photofunctionality, though there is room for improvement.

BFO possesses a distorted *perovskite* structure with the general formula ABO_3. The perovskite structure can happily accommodate almost 90% of the periodic table of elements[30], making it a good host material to target for further property modification. In the perovskite structure, larger cations can fit into the '*A*' site, which are typically 12-coordinate with oxygen. Smaller cations can be placed in the '*B*' site, which are 6-coordinate octahedra linked to one another via the corner sharing of oxygen atoms. In BFO, bismuth (Bi^{3+} cation) is located in the *A*-site and iron (Fe^{3+}) in the *B*-site. At room temperature, the structure adopts a rhombohedral space group *R*3*c*[31] with all octahedra tilted with respect to accommodate the size differences of the ions[8] in an ***a*⁻*a*⁻*a*⁻** fashion according to Glazer notation[32]. This tilting can be clearly seen when compared with the cubic perovskite $SrTiO_3$[33] (**Figure 1.8 (a), (b)**).

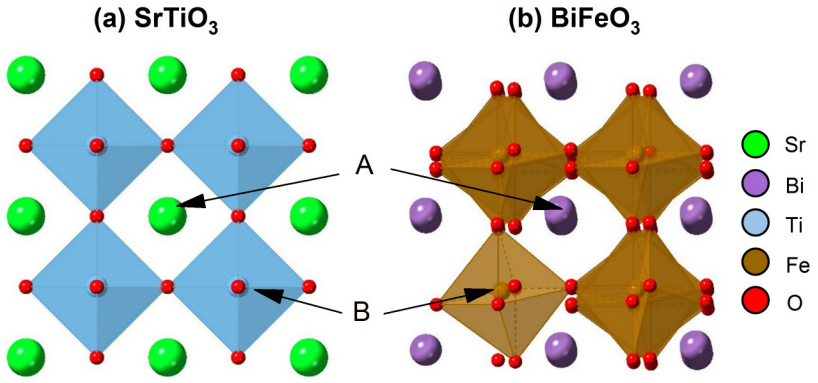

Figure 1.8. *Examples of materials with the perovskite structure. In* ***(a)****, an undistorted, cubic perovskite cell for* $SrTiO_3$ *is shown and* ***(b)*** *shows the BFO structure with clear tilting of the octahedra and off-centre location of Bi. The* A *and* B*-sites of each are indicated.*

A practical consequence of this arrangement is that the structure is non-centrosymmetric at room temperature. The inclusion of Bi^{3+} ions (d^0) allows large dipoles to develop, sustaining ferroelectricity up to T_c ~ 830 °C[34, 35] ('Curie' temperature), after which the structure becomes centrosymmetric and paraelectric[36]. The bismuth stereoactive lone pair drives dipole alignment along the crystallographic $<111>_R/<001>_H$ directions (**Figure 1.9**, equivalent hexagonal unit cell [subscript H] is shown). The magnitude of remnant polarisation at room temperature can be as high as ~ 100 μC/cm^2 from prediction but only seemingly attainable in single crystals[36] due to issues with high leakage currents[36-38]. This is an issue for practical implementation in electronics, but the fact this material is lead-free makes it an attractive starting point for non-toxic ferroelectrics.

Having iron in the structure (Fe^{3+} (d^5) has 5 unpaired electrons per ion) also gives it significant potential to develop magnetic properties. Experimentally, magnetic properties of BFO are quite complex. At room temperature, BFO is said to exhibit a close-to 'G-type' antiferromagnetic structure[36] (moments are aligned antiparallel between neighbouring Fe, **Figure 1.9**) with a ~ T_N = 370 °C ('Néel' temperature) arising from magnetic superexchange. However, this arrangement is not perfectly antiparallel, with the moments thought to be slightly canted in a cycloidal fashion along $<110>_H$ [38, 39] with a repeat length of approximately ~70 nm[40] (**Figure 1.9**), leading to a slight net magnetization.

The magnetically ordered state and ferroelectric state can be linked in BFO[41], and has been shown to exhibit a strong magnetoelectric effect by using strain or high fields[42] to disrupt the spin cycloid. Fundamentally, this combination of elements is ideal as a starting point in generating type I multiferroism[43]. However to apply bulk BFO to memory storage for example, modifications to increase the net magnetization would be necessary[15].

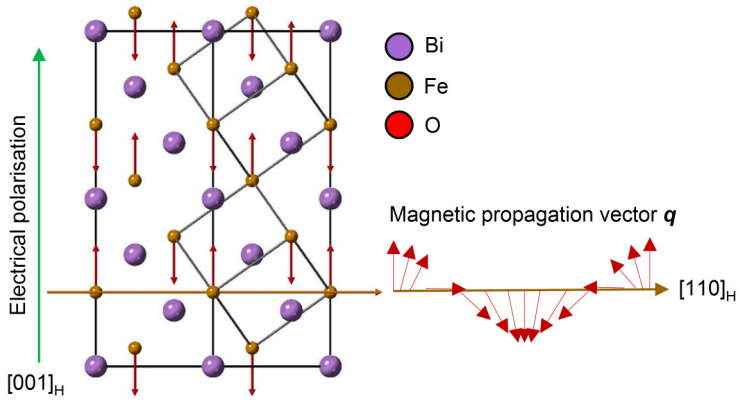

Figure 1.9. *Magnetic and polar ordering in a hexagonal unit cell of BFO. AFM alignment of magnetic spins that alternate along* **c**, *$[001]_H$, are indicated, with G-type magnetic cell indicated in black. The canting of moments into a cycloid along vector* **q** = *$<110>_H$ over the repeat ~ 70 nm is also illustrated. The direction of ferroelectric polarisation along one $<001>_H$ type direction driven by off-centre motion of Bi along this axis is shown.*

The d-electrons responsible for magnetism also play a large role in dictating the ability of this material to absorb visible light. Simulations of the electronic band structure describe it as a direct band gap material, with the valence band being composed of states associated with oxygen 2p orbitals, and some contribution from Bi 6p, while the conduction band is mainly influenced by the empty 3d orbitals of the iron[44-46]. The band gap of BFO has been reported to be 2 – 3 eV depending on the synthesis process[3, 36].

The narrow band gap in conjunction with the internal field from the ferroelectricity could potentially permit a photovoltage[47]. Experimentally, photovoltaic-like properties have been observed in BFO [48, 49], though there is conjecture concerning whether this is truly from the bulk photovoltaic effect arising from separation of charges within a domain, or if this is conduction between grains or domain walls[4]. Nonetheless, it is an important result. In addition, the material is seen to be active as a catalyst, showing the ability to degrade some organic pollutants on visible light exposure[3, 50-52]. One part of the difficulty in obtaining stronger responses may lie with its fabrication.

The synthesis of BFO is notoriously difficult. The energy landscape of phase formation leads to competition between three stable phases[53] the amounts of which are sensitive to the diffusion process[54] and impurities[55]. Many methods have been investigated[56] but it appears that it is extremely challenging to minimize the formation of these phases in bulk form without short syntheses and fast cooling, leading to low macroscopic sample quality. The sample processing unsurprisingly has an impact on the properties, particularly the ferroelectric response[57].

Therefore, issues with the synthesis of BFO and its often low ferroelectric, magnetic and photofunctional responses hinder its application. This thesis addresses these issues by selecting elements to substitute into the *B*-site, such as Cr and Ti^{4+}/M^{2+}, which are expected to improve characteristics of BFO and result in photofunctional oxides. These ideas are detailed in the next two sections.

1.2.2 Cr-modified Bismuth Ferrite

As outlined above, BFO has shortcomings when it comes to the strength of its magnetic properties, and while it shows some photovoltaic character, it is not particularly efficient. One specific modification of BFO that targets both of these properties is the addition of chromium (Cr^{3+}).

A substitution of 50% of the iron in BFO with chromium, is predicted to produce a more useful material[43, 58]. It is possible that by introducing two types of ions into the perovskite *B*-site, spontaneous chemical order may result. An alternation of these two ions throughout the

structure could lead to a 'double perovskite' with rhombohedral *R*3 symmetry ('O-phase' BFCO) and tilted octahedra (as in unmodified BFO) thus leading to a potential internal field for effective charge separation in addition to a modified band structure.

It is apparent in the literature that Cr^{3+} incorporation has an effect on the band structure, and retaining the non-centrosymmetric structure type permits photovoltaic character in studies on thin films[59, 60]. These films have been shown to exhibit experimental band gaps of ~ 1.5 eV which is ideal for solar applications. Indeed, in a landmark study, a very impressive 8.1% power conversion efficiency was observed in a multilayer device[59]. Evidence for ferroelectric control of photovoltaic character in thin films has also recently been reported[61]. However, a more general study of connected phenomena has not been conducted on samples in the bulk form.

Adding Cr^{3+} with its differing number of d-electrons (3 unpaired electrons vs. the 5 unpaired electrons of Fe^{3+}) not only influences the photofunctional response, but also its magnetic properties and may have greater potential than the host BFO. Iron and chromium are capable of magnetic interaction through the oxygen ions, but because their electron configurations are different, even when they are antiferromagnetically coupled a net magnetic moment can arise. The predicted impact is a net magnetization of 160 emu/cm^3 (~ 18 Am^2/kg) and a spontaneous polarization of 79.6 μC/cm^2 [43, 58].

Experimentally however, the range of multiferroic properties attainable for BFCO vary widely, with magnetizations of ~ 5 – 150 emu/cm^3 and remnant polarisations from ~ 0.445 – 53 μC/cm^2 observed[62-65]. This range of values appears to reflect not only the form of the material (film, powder or bulk), but problems attaining chemical ordering of Fe and Cr, which is intrinsically linked to the maximum magnetization of the material and perhaps also to its photofunctionality.

There is considerable disagreement in the literature about whether BFCO can form in the double perovskite arrangement with Fe and Cr ions regularly ordered (**Figure 1.10 (a)**). Mostly ordered structures[60] for BFCO are often reported in thin films. In bulk and powder studies it appears more likely that the elements are not ordered at all[65], instead resulting in the *R*3*c* space group ('D-phase' BFCO) (**Figure 1.10 (b)**). Full ordering might be attainable by artificial layering[66] but other superstructure options are also possible[63]. Overall, it is hard to say what the true structure of BFCO might be without a more comprehensive diffraction study. Using X-ray diffraction alone, which is the typically reported method, to determine the degree of ordering in BFCO is not necessarily conclusive.

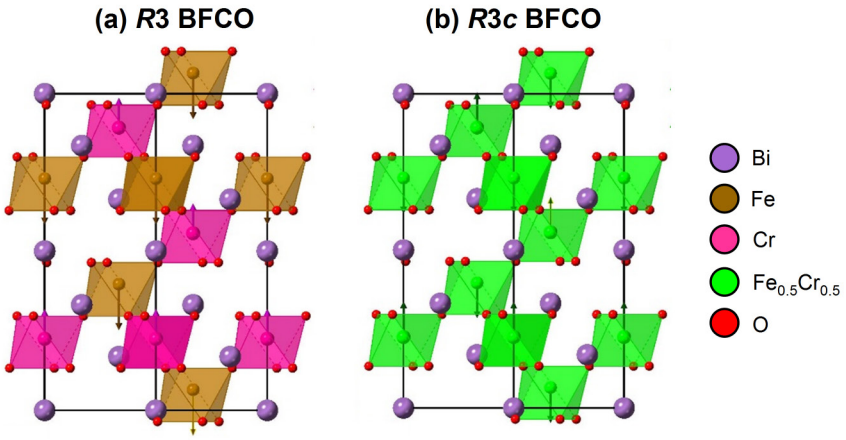

Figure 1.10. *In* ***(a),*** *the double perovskite BFCO is shown, having full chemical ordering of Fe and Cr and* ***(b)*** *depicts fully disordered BFCO. Antiparallel moment aligned is also illustrated.*

Poor scattering contrast in common diffraction methods can be problematic for determining placements of Fe and Cr ions (e.g. X-ray form factors 'f_1' at ~ 8 keV for Bi = 79.9 , Cr = 24.7, Fe = 23.8 *e*/atom[67], therefore Bi dominates and Fe and Cr are hard to distinguish). Analytic techniques such as neutron diffraction pose a solution to this problem (scattering lengths '*b*' for Bi = 8.53, Cr = 3.64, Fe = 9.45 fm[68], leading to better scattering contrast), but large samples are required for adequate diffracted intensity.

One of the main hindrances to the study of the structure before now has been the ability to synthesize it in suitable amounts for such studies. While thin films have been produced many times[62, 64, 69-71], production of powders or bulk samples are uncommon. Typically, high pressure has been reported as necessary to produce this material in powder form in the rhombohedral perovskite structure[63, 65], which is problematic due to the low amounts of product that can be made at any one time. To date, ambient pressure syntheses of bulk samples have led only to multiphase products[72, 73].

This work overcomes the problematic bulk synthesis of BFCO, to permit determination of chemical ordering, as presented in **Chapter 3**. It confirms photofunctionality in this candidate oxide through measurement, and also links multiferroic properties to the chemical ordering. This provides a foundation for understanding the underlying physics in perovskite structured multifunctional materials.

1.2.3 Ti^{4+} and M^{2+} Modified Perovskite Bismuth Ferrite

The synthesis of BFO is notoriously difficult and Cr introduction, while potentially helpful for magnetic properties, does not necessarily overcome this issue. A combination of elements that can be introduced into BFO to make it more cleanly synthesizable and enhance the physical

properties is highly sought after. The goal would be to preserve the non-centrosymmetric rhombohedral structure of BFO to retain an internal field, while substantially modifying the elemental content of the *B*-site in order to narrow the band gap and permit ambient pressure synthesis. This section focuses on substituting Fe^{3+} in the *B*-site as depicted in **Figure 1.11** with Ti^{4+}, Fe^{2+}, Mg^{2+}, Ni^{2+}, Cu^{2+} and Zn^{2+} to make the target compounds in **Table 1.1**. The target compositions are chosen with reference to known literature phases[74], and for their closeness in Goldschmidt tolerance factor to that of BFO. These are evaluated with **Equation 1.3** and results are also given in **Table 1.1**, suggesting a distorted perovskite structure like in BFO could be formed (t = 0.71-0.9) with these choices.

$$t = \frac{r_A + r_0}{\sqrt{2}(r_B + r_0)} \qquad \textbf{(1.3)}$$

Table 1.1. *Target compounds for Chapter 4 and their calculated Goldschmidt tolerances.*
Figure 1.11. *Basic perovskite arrangement showing A, B and O locations and relevant radii to the Goldschmidt equation.*

Nominal target compounds	*Tolerance (t)**
$BiFeO_3$ (BFO)	0.889
$BiFe_{0.25}Fe^{2+}_{0.375}Ti_{0.375}O_3$ (BF*F*TO)	0.873
$BiFe_{0.25}Mg_{0.375}Ti_{0.375}O_3$ (BFMTO)	0.883
$BiFe_{0.25}Ni_{0.375}Ti_{0.375}O_3$ (BFNTO)	0.888
$BiFe_{0.25}Cu_{0.375}Ti_{0.375}O_3$ (BFCuTO)	0.881
$BiFe_{0.25}Zn_{0.375}Ti_{0.375}O_3$ (BFZnTO)	0.880

*data from ref. [75]

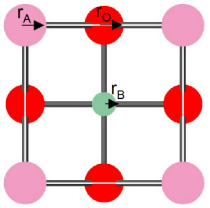

Titanium is the core addition in each of these combinations. With a fairly stable octahedral coordination and valence state, it may assist in stabilizing the synthesis of BFO based materials. In addition, Ti^{4+} would act as a 'donor' transition metal within BFO, both manipulating the energy level of the conduction band and helping improve the ferroelectric properties. During synthesis, BFO develops a natural population of oxygen vacancies and Fe^{2+} (d^6) [57], leading to a high leakage current which affects ferroelectric performance. By adding up to 10 at. % Ti^{4+}, such vacancies can be reduced[76-81]. This combination of Ti^{4+} and Fe^{2+} in small amounts is also noted to alter the absorption characteristics[76-81]. It is foreseeable that Ti^{4+} could be introduced into BFO with other acceptor M^{2+} species as well, manipulating the band gap and properties in different ways.

Other paramagnetic ions such as Ni^{2+} (d^8) and Cu^{2+} (d^9) could also be paired with Ti^{4+}. On its own, Ni^{2+} doping of BFO up to 10% leads to products with visible light absorption and photoluminescence capability, and a larger leakage current[76, 82-84]. The incorporation of Cu^{2+} appears to increase conductivity when incorporated into BFO alone in small amounts (~ 3% – 5%), and may give it more general semiconductor properties than photoexcited

ones[80]. Diamagnetic elements Mg^{2+} (d^0) and Zn^{2+} (d^{10}) may also make a stable pairing with Ti^{4+}. In small amounts, Mg^{2+} doping results in a p-type visible-light semiconducting material[85, 86]. Zinc may also reduce the band gap in small amounts (though at the expense of impurity formation at 5 – 10%)[87].

Importantly, one of the targets, $BiFe_{0.25}Mg_{0.375}Ti_{0.375}O_3$ (BFMTO), is a known phase and shows photoresponsive behaviours[88, 89] with a <2 eV band gap and the ability to photocatalytically degrade methyl blue. If such a significant modification from BFO retains photofunctional activity, the suggested combinations of elements at the same concentrations may also show interesting results. In addition to the band structure effect, these combinations of elements will also have an effect on the polarisation, conductivity and long range magnetism.

Doping of up to 10 at. % Ti in BFO with some Fe^{2+} have been reported to permit magnetism and ferrelectricity[76-81]. There is a theoretical report that suggests ferromagnetism could also coexist at Ti^{4+} levels as high as 50 at. %[90], though it is not experimentally verified, and all iron is Fe^{2+}. The BF*F*TO target composition has not been synthesized before. The effect of low levels of paramagnetic Ni^{2+} doping in BFO by contrast leads to increased magnetization, but at the expense of a larger leakage current and ferroelectric aging[76, 82, 83, 91]. While the BFNTO phase is known to be synthesizable, ferroelectricity and magnetism are yet to be confirmed, with semiconductor character being the only known property[74]. It may be a leaky ferroelectric and antiferromagnetic, as in the $BiNi_{0.5}Ti_{0.5}O_3$ (BNTO) metastable distorted perovskite phase[92-94]. The introduction of Cu^{2+} (~ 3 – 5 at. %) in BFO seems to result in a moderate increase in conductivity, a moderate increase in magnetization (though is virtually linear with respect to field), and a decrease in spontaneous polarisation[80, 95]. The BFCuTO phase is unreported, but when pairing copper with titanium, as in the dielectric perovskite related phase $Bi_{2/3}Cu_3Ti_4O_{12}$[96], polar properties may be improved.

Diamagnetic pairings are expected to produce different responses through dilution of magnetic Fe^{3+}. Magnetism can be mediated through oxygen vacancies induced by Mg^{2+} [85, 86, 97]. The target phase BFMTO has also been shown to be synthesizable and exhibit ferroelectricity though only one report exists on the magnetic behaviour[88], and it is not clear if it is 'ferromagnetic' or something else. The Zn^{2+} and Ti^{4+} combination can also result in reduced leakage current in BFO when added at small levels[98], fostering ferroelectric character. Higher levels of incorporation into BFO may be possible by solid state means[99] and in films[100] but the effect on the polarisation and magnetism at very high levels remains unclear as the target phase BFZnTO is unreported.

Thus, many of these elemental combinations are candidates for multiferroic behaviour, but in order to confirm this, they must be synthesizable. No experimental data exists regarding the

targeted materials BF*F*TO, BFZnTO or BFCuTO in terms of synthesis or properties. It is suspected that part of the reason for this is the complex energy landscapes for synthesis of a pseudo-quaternary system leading to stable side phases, and metastable perovskite phases. Therefore, exploratory synthetic study is needed before any further work on properties can be undertaken.

The targeted materials BFMTO and BFNTO are known to be synthesizable. For these compounds, there is a likelihood of being able to obtain further information on their properties to supplement the literature. Reports of BFMTO draw attention to the somewhat complicated local symmetry environment[101-103] of the bismuth leading to some cancellation of emergent ferroelectric properties (but possessing an average *R*3*c* structure[74]). There is also much more to elucidate about BFNTO itself, as despite being reported to be a stable perovskite with an average rhombohedral structure (*R*3*c*), there appears to be only one report on properties and synthesis[74].

Despite the combination of elements in these systems potentially affording multiferroic and photofunctional character, these candidates are not well investigated. This thesis addresses what is synthesizable, and characterises missing properties in **Chapter 4**, thus expanding the known library of photofunctional oxides. It also gives further insight into how structure and local chemistry dictate property evolution in perovskite based photofunctional materials.

1.3 Narrow Band Gap, Multiferroic, Aurivillius Bismuth Titanate Based Materials

1.3.1 Why Aurivillius Bismuth Titanate?

The basic perovskite framework with corner-linked octahedra is a highly useful structural motif for engineering functional oxide materials and also appears in other structure types such as the *Aurivillius* phases. The Aurivillius phases[104-106] have a general formula $(Bi_2O_2)(A_{m-1}B_mO_{3m+1})$, which describes blocks of perovskite layers (number of layers = m) sandwiched between a layer of bismuth oxide. Large atoms occupy the 12-coordinate *A*-sites in the perovskite blocks, while smaller atoms fill the octahedral *B*-sites.

The number of layers (m) can be as low as 1 and at the upper limit can be m = ∞ with the full perovskite structure as the end member of the series (**Figure 1.12**). This structure type is tolerant to a large range of *A* elements including lanthanides (e.g. La^{3+}), alkali metals (e.g. Na^{+}) and alkali earth metals (e.g. Sr^{2+}) and the *B* elements are typically transition metals with a large range of valence states (e.g. Fe^{3+}, Ti^{4+}, Nb^{5+}, Mo^{6+}). So long as charge balance is retained, there are many possible combinations of elements in both sites and the number of layers, as depicted in **Figure 1.12** with Bi_2WO_6[107], $Bi_2SrTa_2O_9$[108] and $Bi_4Ti_3O_{12}$[109].

These structures are considered to be tetragonal above their Curie temperatures (T_c), and possess non-centrosymmetric orthorhombic (or monoclinic) crystal structures at lower temperatures, where they exhibit ferroelectricity[110]. A range of properties including spontaneous polarisation[111], magnetism[112], oxide-ion conduction[113] and photofunctionality[2, 3] can be established with the right combinations of elements and layering.

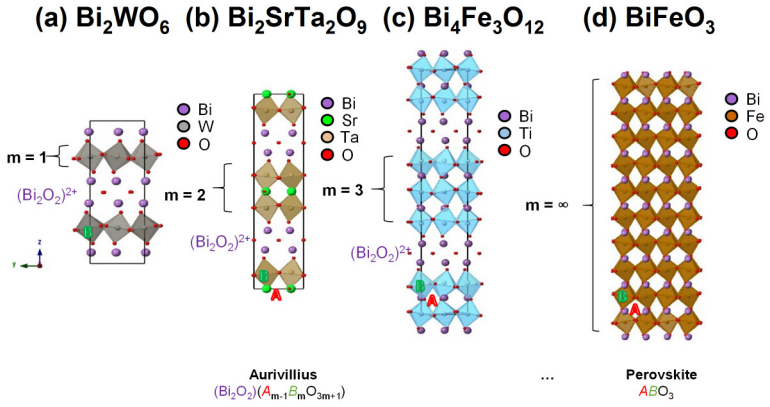

Figure 1.12. *Aurivillius structures depicting different elemental combinations and layering trends. In* ***(a)*** *Bi_2WO_6 is depicted with a single perovskite layer m = 1,* ***(b)*** *shows two-layered $Bi_2SrTa_2O_9$* ***(c)*** *shows three-layered $Bi_4Ti_3O_{12}$ and* ***(d)*** *depicts an end member perovskite ($BiFeO_3$) which can be considered as having infinite layers.*

The compound $Bi_4Ti_3O_{12}$ (BTO) is a ferroelectric Aurivillius material with spontaneous polarisation along two axes (50 μC/cm^2 along ***a*** and 4 μC/cm^2 along ***c***)[111]. It has been of interest to the materials science community for many years due to potential applications in non-volatile memory storage as a consequence of its highly variable domain formation[114]. The structure of BTO is quite unusual, showing significant octahedral tilting, dropping its symmetry to monoclinic[109].

The synthesis of BTO is relatively straightforward in comparison to BFO[115] and it is tolerant to elemental substitution at the '*A*' type Bi sites and the '*B*' type Ti sites. Many combinations of '*A*' site doping have been tested, with the goal of making it an upconverter[116], and to make fatigue-free ferroelectric films (with La^{3+})[117].

The material BTO is a semiconductor with an apparent indirect band gap, but at ~ 2.9 eV[118], it is only accessible to UV light. Despite this, its charge transport properties are good, and it finds use as a UV detector[119] and shows photovoltaic character[120]. If this strong ferroelectric and charge transport character could be retained while the band gap is narrowed, it would be a highly promising visible light photofunctional material. The valence band of BTO is mostly comprised of O 2p and Bi 6s states, with the conduction band being mostly Ti 3d and Bi 6p[121]. Thus, narrowing the band gap of BTO may be possible by replacing titanium with iron to alter the conduction band. This is effectively the reverse case of Ti-modified BFO in the previous section. In this scenario, the Aurivillius layered structure is retained, but the band gap is narrowed for visible light utility, and allows for the possibility of multiferroism via magnetic interactions.

This thesis explores the Aurivillius structure type to contrast with discussion on the perovskite structure in previous sections and so gain a new perspective on factors affecting functionality. The below section highlights how modifying Aurivillius BTO systematically with iron is suspected to lead to photofunctionality, and what is presently missing from the literature understanding of this system.

1.3.2 Aurivillius Bismuth Ferrite Titanates

Many bismuth ferrite titanate Aurivillius compounds with the general formula $Bi_{m+1}Fe_{m-3}Ti_3O_{3m+3}$ have been identified throughout the literature with 'm' ranging from 4 to as many as 9[122-124], including non-integer 'm' values[125]. The number of reports of the 4-layered compound ($Bi_5FeTi_3O_{15}$) compared with other members, shows that there is great interest in this material, and strongly suggests that this is the most energetically favoured of the layered compounds during synthesis.

The bismuth ferrite titanate Aurivillius phases have orthorhombic, non-centrosymmetric crystal structures. The perovskite blocks contain iron and titanium in the octahedral sites and between these blocks is a layer of $Bi_2O_2^{2+}$. In this thesis focus is placed on the 4, 5 and 6 layered variants in which the ratio of Fe:Ti is 1:3 ($Bi_5FeTi_3O_{15}$, 'BFTO-513'), 2:3 ($Bi_6Fe_2Ti_3O_{18}$, 'BFTO-623') and 3:3 ($Bi_7Fe_3Ti_3O_{21}$, 'BFTO-733') respectively. The 4-layered compound BFTO-513 has a comparable level of Ti in octahedral sites to BFMTO and BFNTO and the 6-layered compound BFTO-733 has a comparable level of Fe to BFCO, all mentioned in the preceding sections.

By adding paramagnetic iron systematically in this way, it is expected that changes to the conduction band will result in an effective narrowing from the UV accessible gap of BTO. This is predicted computationally for $Bi_5FeTi_3O_{15}$[126]. Experimentally, on an individual basis $Bi_5FeTi_3O_{15}$ is reported to have band gaps from ~ 2 – 3.5 eV[127-133] depending on the synthesis, as well as demonstrated photocatalytic[127, 128, 133] and photovoltaic activity[132]. Photofunctionality is not assessed for $Bi_6Fe_2Ti_3O_{18}$ but it has an estimated band gap of 3.75 eV[134]. $Bi_7Fe_3Ti_3O_{21}$ is suggested to have a band gap of 2.22 eV (narrower than $Bi_5FeTi_3O_{15}$[135]) and photofunctional properties[136]. A direct comparison between the three different materials has not been done before, and may give an understanding of the systematic effect of increasing iron.

By adding in paramagnetic iron to these non-centrosymmetric crystal structures, there is potential for magnetic ordering in addition to photofunctionality. Past systematic studies suggest that as more layers are added, a magnetic transition appears below room temperature (RT)[137-139], but its origin is debated. Considering each individually, in $Bi_5FeTi_3O_{15}$, some reports suggest there may be no long-range magnetic ordering[126, 140], while others suggest superparamagnetism arising from short range AFM interactions[131, 141], or 'weak ferromagnetism' due to isolated Fe among non-magnetic Ti/Bi layers[129, 130, 142-144] or from canted AFM[145]. In $Bi_6Fe_2Ti_3O_{18}$, the magnetic properties appear to be more transient between paramagnetism and antiferromagnetism[134, 146], with a number of suggestions of magnetic transitions reminiscent of long range order[147] and short range ferromagnetic effects[148]. This is not clear, nor definitively linked to the structural compositional ordering. In $Bi_7Fe_3Ti_3O_{21}$, the magnetism is less clear cut, with a number of references suggesting a true antiferromagnetic to paramagnetic transition exists below room temperature[122, 149, 150], another suggesting an intermediate ordered state[136, 151, 152], and yet another, strongly ferromagnetic behaviour[153]. Complications from impurities may be in part responsible for the contrasting reports for $Bi_7Fe_3Ti_3O_{21}$. However, overall these inconsistent trends might be better understood through systematic study and structural interpretation.

In addition to potential magnetic ordering, comparative studies on films show $Bi_5FeTi_3O_{15}$, $Bi_6Fe_2Ti_3O_{18}$ and $Bi_7Fe_3Ti_3O_{21}$ can exhibit ferroelectricity[139, 154, 155], though the magnitude and

the T_C decreases as more iron is added[138, 156]. The systematic response in bulk samples however is not known. In bulk $Bi_5FeTi_3O_{15}$ specifically, the magnitude of the remanent polarisation ranges from ~ 3 – 7 μC/cm^2 [141, 143, 144, 157] and the Tc is quoted to be near ~ 750 °C[143, 157-161]. Polarisation properties do not appear to have been reported for bulk $Bi_6Fe_2Ti_3O_{18}$, and are weak for bulk $Bi_7Fe_3Ti_3O_{21}$[151]. Studying polarisation in bulk samples would give new insight on the effect of changing composition and structure on this property.

Despite the inconsistent trends, strong evidence for magnetic and ferroelectric ordering exists for these materials. In fact, $Bi_5FeTi_3O_{15}$ has been noted on several occasions to show appreciable magneto-electric coupling[140, 141, 145, 162, 163] . Thus, these phases comprise another system with the potential to be multiferroic in addition to photofunctional. However, it is difficult to understand how these properties arise and change without understanding the structure more deeply, which in turn requires better synthetic methods.

There is a general lack of reported crystal structures for these phases which include consideration of octahedral tilting which impacts ferroelectricity, and iron/titanium ordering which will affect the extent of possible magnetic interactions. In $Bi_5FeTi_3O_{15}$, the structure is considered to be orthorhombic with space group $A2_1am$[160, 164, 165], though often refined in $F2mm$ which does not consider tilting modes[159]. Most reports suggest that Fe and Ti are distributed in a disordered fashion[127, 159, 164], but theory and some Mössbauer results imply a preference for inner octahedral sites[124, 126]. In $Bi_6Fe_2Ti_3O_{18}$, which has an odd number of perovskite layers, authors mainly suggest a $B2cb$ space group evolves from tilting[134, 146, 166] but there is no structural data available from refinement. Instead refinement is done with the parent space group $F2mm$ which again does not account for tilting[167]. In terms of elemental distribution, there are reports that suggest a preference for Fe in the inner perovskite sites again[167, 168] but studies are few in general. In $B_7Fe_3Ti_3O_{21}$, an $A2_1am$ tilted structure is suspected, much like its fellow even numbered compound $Bi_5FeTi_3O_{15}$. The only structural data is again in the space group $F2mm$[169]. Chemical ordering is not noted in this compound, and is suggested in general to decrease as more layers are added, with two unique sites of equal occupancy often seen with Mössbauer[124]. Investigating the structure and chemical ordering may be key to understanding the unusual properties trends, but the lack of published structures may indicate issues with synthesis.

It appears these individual compounds can be quite close in energy, and synthesizing a compound without a proportion of a lower layered structure and/or stacking faults appears difficult[138, 170]. Purity is also much more difficult to obtain as layers (and iron) are added[156, 169, 171-173]. The iron-rich end member of the Aurivillius series is BFO, which as has been mentioned so far, suffers from its own phase control issues. It is therefore not surprising that the synthesis

of BFTO becomes more difficult as layers are added. The most stable of the compounds seems to be the 4 layered $Bi_5FeTi_3O_{15}$ which has a number of reportable synthetic methods including solid state, molten salt, hydrothermal, sol gel and variations thereof, leading to grains with 'plate like' morphology[127, 174, 175] in a single sintering step. The compound $Bi_6Fe_2Ti_3O_{18}$ on the other hand, is less frequently reported, and some bulk syntheses appear to be multiphase[176], suggested to arise from the compounds lower stability in comparison with $Bi_5FeTi_3O_{15}$. Reports of $Bi_7Fe_3Ti_3O_{21}$ are even less frequent, and issues synthesizing the compound in the solid state are apparent, with as many as four phases detected in products[151, 177]. Some better success is noted with films[150, 152, 153], but determining the phase from XRD in this case is difficult. Addressing the synthesis issues is key to establishing better understanding about both the structure and the functionality in these materials, uncomplicated by impurity phases.

In **Chapter 5** of this thesis, synthesis methods are developed to permit study of the three BFTO materials in bulk in previously unattained levels of purity. The magnetic, electrical and photofunctional properties are systematically observed and the local and average structure is analysed to add clarity to the literature trends.

1.4 Narrow Band Gap, Photocatalytic Titanium Dioxide Based Materials

1.4.1 Why Titanium Dioxide Polymorphs?

Titanium oxides are another group of materials that could be utilized in cost effective energy conversion technologies due to their physical properties, the good natural abundance of titanium, and the range of synthesizable crystal structures. Titanium dioxide (TiO_2, where titanium is in the valence state Ti^{4+}) can be grown in several 'polymorphs', differentiated by different corner and edge sharing of octahedra and relative amounts of free space. Common polymorphs include *rutile* (tetragonal, $P4_2/mnm$[178] crystal structure) where each octahedron shares edges with two others and *anatase* (tetragonal, $I4_1/amd$[179]) where octahedra share four edges (**Figure 1.13**). All are centrosymmetric structures, meaning they cannot be ferroelectric as the perovskites and Aurivillius phases sometimes can.

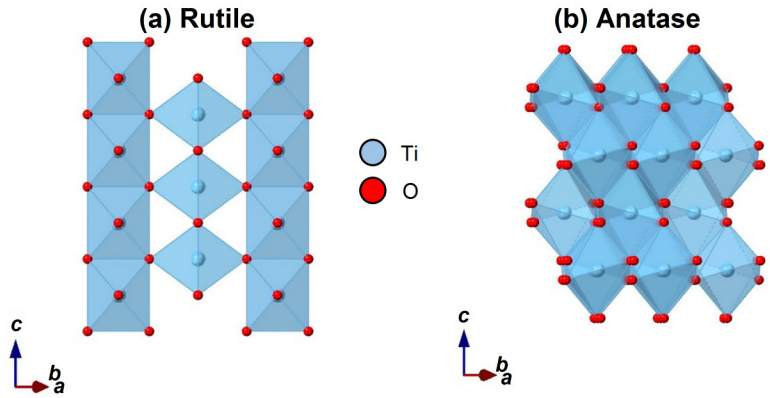

Figure 1.13. *The TiO_2 polmorphs* ***(a)*** *rutile and* ***(b)*** *anatase are shown. Polyhedra can share two edges in rutile and four in anatase.*

The polymorph that forms during synthesis is highly dependent on the temperature, applied pressure, pH and particle size due to their influence on bond formation and growth[180]. Notably, anatase is somewhat more stable at small particles sizes below 11 nm, and beyond 35 nm, rutile is the most favoured. In the intermediate range, a third polymorph '*brookite*' can also form[181]. This means that when synthesizing nanocatalysts, controlling the particle size is important to dictating which polymorph is made. Each polymorph leads to different band structures.

Rutile has a narrower, direct band gap of 3.0 eV and anatase has a wider indirect band gap of 3.2 eV[182-184]. Both gaps are too wide for efficient visible light usage, but with some UV, properties such as photocatalysis (of organic species[7], water [185], and microbes[186]), photo-induced superhydrophilicity[7], and semiconductivity in dye sensitized solar cells[6, 7] have been reported. The latter is also related to a natural population of defects that give them n-type semiconductor behaviour[187-189].

Of the polymorphs, anatase has been noted to perform best in photocatalysis and in dye sensitized solar cells, and this is attributed to its indirect bandgap leading to a reduced recombination rate[12], its ability to be synthesized in a small size, and its different chemical potential[190]. Rutile is often used when thermal stability is key, such as in memristive switching devices[191] but is perhaps better known for its excellent dielectric properties, fine-tuned through doping[192, 193].

Improving both photocatalytic and semiconductive ability may be achievable with doping to narrow the band gap. Vanadium is one promising element with which to modify both TiO_2 polymorphs due to its comparable ion size and flexible valence states. Vanadium forms a number of stable oxides including: V_2O_3, a metallic paramagnet at RT with complex low temperature behaviour[194]; VO_2, a narrow bandgap semiconductor with a metallic transition

above RT[195] and structural similarity to rutile TiO_2[196]; and V_2O_5, a photocatalytic[197] semiconductor[198] at room temperature. The electronic character of different valences of vanadium is expected to alter the photofunctional and electrical properties in both polymorphs of TiO_2.

This thesis explores how the anatase and rutile polymorphs of TiO_2 can be modified principally with vanadium to alter their photofunctionality. Consideration of these new structure types expands the known library of photofunctional materials and introduces a new perspective about how the chemistry of elements affects properties. The following sections highlight why these modifications are promising, and what is currently unknown about the resulting materials.

1.4.2 Vanadium and Nitrogen Modified Anatase

The anatase polymorph of TiO_2 has the most potential for engineering into a functional photocatalyst. Anatase is relatively easy to synthesize nanoform[180], and is robust to a wide range of environmental conditions, making it a favoured candidate for waste water clean-up[199] and other environmental applications[186]. The anatase polymorph also has an indirect band gap which can help for photoexcited charge longevity, but is wide at ~ 3.2 eV[200], allowing absorption of only the ultraviolet portion of the solar spectrum, and is therefore limited as a photocatalyst. In order to generate better photofunctionality, the band gap needs to be narrowed, but this must be done with caution, as detrimental defects acting as recombination centres will quickly impede its ability to do useful work. As anatase is centrosymmetric, charge transport is mostly controlled through the size of the particles and band bending at the material surface.

It is possible to narrow the anatase bandgap by chemical modification[201]. The anatase structure is tolerant to cation substitution, which can improve visible light absorption, but the overall effect on catalytic performance can be mixed due to suboptimal distribution of dopants causing recombination[202]. It is also possible to modify the anions in the structure, leading to improvements in the catalytic properties[203], but they can be comparatively difficult to control and incorporate (<2 at. % doping typically reported for nitrogen)[204].

In order to engineer photofunctional properties, it can be of interest to target specific defects using dopants. By introducing a pair of them at once to charge and/or size compensate one another, properties may be improved. Pairings of nitrogen anions (N^{3-}) with an M^{5+} transition metals have been broadly investigated[205] and recently Nb^{5+}-N^{3-} co-doped TiO_2 anatase has been shown to exhibit exceptional photocatalytic activity[206]. The origin of this effect is ascribed to directly bonded Nb^{5+}-N^{3-} defect pairs which facilitate a shallow acceptor level above the VB, effectively improving visible light absorbance.

There are a series of computational studies available which indicate that the V^{5+}-N^{3-} co-doping combination could also show significant visible light utility by adding a vanadium donor level close to the bottom of the conduction band in addition to the nitrogen induced valance band extension, when the dopants are directly bonded[207-213]. From these studies, one might predict the photocatalytic activity to be impressive like the aforementioned Nb^{5+}/N^{3-} scenario, however this is not definitively the case in practice.

There are some reports of experimentally realised (V,N) co-doped TiO_2 nanostructures[214-220] but the relationship between reactants and products, the behaviour of the dopants inside the product and their connection with the observed properties is unclear. Catalytic degradation of target molecules can range from full degradation of the target in 60 minutes[214] to only 20% degraded in 5 hours[216]. All of these studies report the presence of reduced vanadium in either the V^{4+} or V^{3+} states, despite using a range of raw materials and techniques. The vanadium location in these co-doping experiments is also often not discussed, despite many V single-doped studies showing the possibility for isolated, aggregated, substitutional, interstitial and surface vanadium coordination environments[221-227]. This system has theoretical potential for photofunctionality, but is clearly complex with much experimental variability.

By using a solvothermal synthetic method that has been previously shown to produce M^{5+}-N^{3-} defect clusters in the analogous (Nb,N)-TiO_2 system[206] it may be possible to produce the predicted V^{5+}-N^{3-} cluster. The influence of purposefully introducing other valence states could also be examined to help understand the experimental results in the literature. In this thesis, a synthesis for V and N doped nano-anatase is presented in **Chapter 6**. Materials are synthesized and the valence state and destination of dopants within the synthesized nanomaterials is explored. Another photofunctional material class is thus identified, and the impact of common themes like synthesis method, structure and chemistry on this functionality is noted.

1.4.3 Vanadium Modified Rutile

The rutile phase of TiO_2 is considered to have a direct band gap of 3.0 eV. The band gap and conductivity of rutile can be altered through chemical modification, though this does not tend to result in good photocatalysis like anatase, but rather in useful semiconductive properties. For example, Ta^{5+} introduction (<1 at. %) can change the current-voltage character of rutile TiO_2[228] and increase the conductivity but the photofunctionality decreases on increasing substitution[229, 230]. The Nb^{5+} ion is similarly noted to produce a decrease in photocatalytic activity with increasing concentration of dopant[231] while conductive defects increase[232]. The changes occur due to the generation of defects compensating for their stable M^{5+} valence states. This also affects solubility and limits their ability to form homogeneous samples[233, 234].

An interesting, contrasting example is the introduction of V^{5+}, which is known to be multivalent and has broader possibilities for defect formation and solubility.

Early studies showed V_2O_5 supported on/impregnated in TiO_2 [235-246] in low quantities did have some useful catalytic functionality toward breakdown of organic compounds like o-xylene[247]. However, it was routinely found that vanadium could penetrate the TiO_2 support under elevated temperature conditions and make a substituted rutile '$V_xTi_{1-x}O_2$' phase and at least one of the resulting valence states was V^{4+}. This contrasts to the Ta and Nb examples, and implies that irrespective of the valance of vanadium in the starting material, vanadium can be reduced even under standard synthesis conditions.

Throughout the literature, the limits to which vanadium is incorporated and which valence states it ends up in vary widely. Studies that synthesize $V_xTi_{1-x}O_2$ from V_2O_5 in air appear to note solubility to only x = 0.1 (10 at. %) before a separate V_2O_5 phase re-forms[248-253]. Starting with raw materials in other valence states or using reducing gases have also been shown to be successful at low levels[252, 254-256], but introduction from 10% to a limit of ~ 80 at. % vanadium can only apparently be introduced prior to a structure change by starting with VO_2 and operating in a vacuum environment[249, 257-261].

The reason for a valence decrease during rutile incorporation in the absence of a reducing atmosphere is unclear and may be due to the temperatures used or a fundamental need for vanadium to adopt V^{4+} (or a lower valence state) to fit into the rutile structure and generate other defects. There is suggestion that the rutile structure limits V^{5+} to the surface with only reduced states in the deeper substitutional sites[237, 262]. Additionally, the proportion of bulk V^{4+} that results in rutile $V_xTi_{1-x}O_2$ made from a V_2O_5 source is also noted to increase[263] perhaps as the surface sites become saturated. However an argument can also be made that the V^{4+} level remains constant until a second phase appears, perhaps reflecting the reducing power of the atmosphere[264].

Most theoretical studies show that introduction of vanadium frequently results in a V^{4+} state, shown through calculation of magnetic moments[265-271]. This forms a defect level below the conduction band of TiO_2. In some studies this is seen as a band gap narrowing to form a semiconductor[265, 267, 268, 272, 273] while others suggest semi-metallic[265, 266] or metallic[266] behaviour as a result of a fermi level shift to sit mid-band, due to vacancies or due to the calculation method. It remains unclear if this change is also a function of vanadium doping level. Other valence states have been tested but are not conclusively eliminated as possible states in V-modified TiO_2 rutile[268, 271, 274-276] especially if they coexist with oxygen vacancies[268]. The depth of defect states within the TiO_2 bandgap arising from these other valence combinations is similarly unclear, with some suggestion of V^{5+} levels very close to the conduction band and

others very deep in the gap[268, 271, 275]. It has been suggested semi-empirically however that surface vanadium species are more likely to exhibit V^{5+} states while the deeper sites are V^{4+} [277], an observation that is somewhat mirrored by experiment.

Vanadium is shown to increase the visible light absorption of rutile TiO_2, extend photocurrent generation to longer wavelengths and produce gap states in optical experiments[253, 263, 278-284]. It is suggested that the band gap of rutile can be dropped from ~ 3 eV to 1.7 eV at 10 at. % doping[278], though it is not clear at what concentration the band gap is reduced to an infrared range. Several valence states are attributed to band gap alteration including V^{3+} [279, 284] V^{5+} [263, 278-280] and Ti^{3+} [253, 283, 285] instead of or in addition to V^{4+}. It is desirable to track how visible light absorption changes with respect to valence state over a large doping range to understand its influence on the electronic structure and associated properties like conductivity and magnetism.

Changes in conductivity and magnetism with respect to vanadium often show anomalies[258, 261, 286, 287]. A particularly interesting case exists when the incorporation of ~ 40 – 70 % of V^{4+} into TiO_2 results in spinodal phase decomposition[261]. Discontinuities in magnetic and conductivity measurements are observed related to metal-insulator transitions of some VO_2-like lamellae in the samples. It is not known whether introducing vanadium in different valance states would also show such unusual behaviour.

Questions then exist about what methods could be used to maximize vanadium solubility so valence state evolution can be tracked. Further, understanding what is then happening in terms of defects and how this affects semiconductive and magnetic properties is valuable to understanding how modified rutiles function. These materials could exhibit unusual and useful physical properties if more than one valence state of vanadium was found to coexist. Methods to synthesize heavily vanadium modified rutile TiO_2 are presented in **Chapter 7**. Spectroscopic characterisations help make sense of inconsistent literature trends. This follows on from the anatase study to show how similar chemical modifications on different structure types affect functionality.

1.5 Thesis Scope and Overview

In this thesis, focus is placed on Cr and Ti^{4+}/M^{2+} modified perovskite $BiFeO_3$, Aurivillius $Bi_{m+1}Fe_{m-3}Ti_3O_{3m+3}$ and V/N modified TiO_2 polymorphs. In addition to showing potential photofunctionality, these oxide materials are also novel, elusive to synthesize or exhibit inconsistent properties.

The synthetic methods utilized to make these candidate materials have been purposefully chosen to require low processing for high purity, in line with a desire to develop cost-effective candidate materials. For this reason, low-complexity methods such as traditional solid state processing were used. The potential of materials made by low complexity methods can thus be demonstrated, and the adaption of the oxides into functional devices becomes an opportunity for future study.

A structural and compositional evaluation of these candidates is a key component of this thesis, as they directly impact the exhibited physical properties. Where possible and not limited by specific sample characteristics, structure and composition across multiple length scales is explored including local structure (defects, clustering of elements, short range magnetic interactions, ferroelectric domains), average structure (chemical and magnetic periodicity and symmetry effects) and morphology (grain growth, phase purity) through diffraction, spectroscopy and microscopy.

In addition to the structure, the physical properties of these materials have been measured to understand any possible interplay between the structure and useful functions. These include photo-induced changes in DC current and voltage, surface potential, optical absorption, and photocatalysis (for a photofunctional assessment) and AC impedance, piezoresponse, and magnetization (for electrical and electronic properties assessment).

Within these limits, literature questions can be answered about the characteristics of the candidate photofunctional materials. This thesis shows how factors including the synthesis method, structure, chemical composition, and photofunctional, electrical and electronic properties in five classes of materials are linked. This holistic understanding contributes to the future of energy transformation technology.

In **Chapter 2** the methods used in this thesis are presented, providing general principals and specific measurement details. In **Chapter 3**, an investigation of the candidate material perovskite $BiFe_{0.5}Cr_{0.5}O_3$ (BFCO) is presented including development of a novel near-ambient pressure synthesis method and determination of chemical ordering through diffraction. This gives valuable insight into the impact of chemical ordering on properties, particularly magnetism, in perovskites. This is extended in **Chapter 4**, where several new titanium-containing $BiFeO_3$-related perovskites are investigated for the first time. Viable materials are synthesized and characterised, highlighting the sensitivity of the perovskite structure type to other elemental combinations and providing novel insights on achievable magnetic, electrical and photofunctional properties. **Chapter 5** includes a systematic study of $Bi_{m+1}Fe_{m-3}Ti_3O_{3m+3}$ (m = 4, 5 or 6) Aurivillius phases, introducing the impact of a new structure type on achievable photofunctionality. This chapter presents innovative metal organic decomposition synthesis

methods that allowed high purity synthesis and subsequent clarification of trends in structure, chemical ordering and properties as ‘m’ is increased. Promising photofunctional compositions are also identified. **Chapter 6** builds on local structure ideas to understand photofunctionality in nanosized vanadium and nitrogen modified anatase titanium dioxide. This chapter uses solvothermal synthesis methods to create theoretically predicted samples and analyse the actual dopant location and valence distributions with spectroscopy, giving insight to rational design of photocatalysts. This is extended in **Chapter 7**, to vanadium modified rutile titanium dioxide. Syntheses methods are developed to systematically alter vanadium concentration in rutile and study the emergent valence states and their connection to electronic functional properties. This work further adds to the understanding of interlinked electronic, photofunctional and structural phenomena. **Chapter 8** is the final chapter and presents the overall conclusions of this thesis, highlighting discoveries made about each materials system, how they contribute to a holistic understanding of the characteristics of photofunctional oxides and what is yet to come.

Chapter 2 Methods

In the previous chapter, five groups of materials were identified as candidate photofunctional materials. There were however several questions raised from the available literature on each. The first is that they all appear to be difficult to synthesize in high purity in the bulk state without using complex methods and forcing conditions. Secondly, the true nature of the crystal structure, including chemical ordering and the presence of defects, is unclear in several of the candidates. Thirdly, the photofunctionality of some of these materials is unconfirmed. Lastly, the ancillary properties of these candidates, including magnetism, ferroelectricity and semiconductivity, show unclear trends with respect to chemical composition.

The hypothesis for this study is that the candidate materials are indeed photofunctional and their syntheses, structures and physical properties are intrinsically linked and critical to their overall functionality. This chapter outlines the methods that will be applied to the materials of interest in order to answer the questions raised and test the hypothesis.

2.1 Synthetic Methods

A major undertaking in this study was developing synthetic methods that could produce large amounts of a material in a high purity that were appropriate for further study. Descriptions of the optimization of each method are given in further detail in the chapters corresponding to each specific material.

2.1.1 Solid State Synthesis

The basic solid state synthesis method was applied to iterations of materials presented in Chapters 3, 4, 5 and 7. This method was used for its relative simplicity, enabling bulk synthesis of functional ceramics. This method refers to reacting (sintering) solid raw materials at elevated temperature after milling and pressing them together, in order to form a homogenous product with a single crystal structure.

2.1.1.1 Raw Materials

The raw materials were commercially sourced (**Table 2.1**). Prior to use the raw materials were placed and stored in an oven at 150 °C to remove moisture. Materials were weighed in stoichiometric amounts to make batches with masses in the range of 15 – 20 g in total.

Table 2.1. *Reagent details for solid state syntheses.*

Reagents/Solvents	*Brand*	*Purity (%)*	*Chapters*
Bi_2O_3	Alfa Aesar	99	3, 4, 5
Fe_2O_3	Sigma-Aldrich	≥99	3, 4, 5
Cr_2O_3	Koch-Light	99.999	3
TiO_2	Sigma-Aldrich	≥99	4, 5, 7
MgO	Hudson	99.999	4
$Mg(CH_3COO)_2.4H_2O$	Analar	≥98	4
$3MgCO_3.Mg(OH)_2.3H_2O$	M&B	≥97	4
NiO	Alfa Aesar	99	4
$Ni(CH_3COO)_2.4H_2O$	Unilab	98	4
CuO	Univar	≥99.9	4
ZnO	Univar	99.5	4
V_2O_5	Research Organic Chemicals	99.8	7
C_2H_5OH (ethanol)	Merck	≥99.9	3, 4, 5
C_3H_6O (acetone)	Merck	≥99.8	7
Fe*	Puratronic	Grade II	5

*powder for production of FeO, after mixing with Sigma-Aldrich Fe_2O_3 and sealing inside a quartz tube for heat treatment.

2.1.1.2 Milling and Pressing

Milling and mixing of the reagents was conducted via either hand or ball milling (specified within relevant chapters). Hand milling involved adding the raw materials to an agate mortar and pestle, covering with ~ 50 mL of suitable solvent for containment (ethanol for all but Chapter 7 in which acetone was used) and grinding. The grinding process was continued until the solvent evaporated three times, then the mixture was allowed to fully dry in air before further processing.

Ball milling was conducted by adding the materials to Teflon canisters filled with yttrium-stabilized zirconia balls of sizes 1 to 12 mm and around 100 mL of suitable solvent. The sealed canisters were rotated in a planetary ball mill at 20 Hz for at least 16 hours. The milled mixture was then sieved through a mesh sieve into a shallow glass dish to remove the balls, and then allowed to evaporate in air until totally dry (~ 12 hours for ethanol). The dried mixtures were then briefly milled by hand using a mortar and pestle to prepare for pressing.

In some samples the dried, milled powder was further processed, including sieving for the VTO50 (60 – 120 μm grade) and BFNTO samples (~ 300 μm), where the smallest grains were retained for this pressing, and PVA solution was added to other samples (noted in text). When suitably prepared, milled powders were loaded into the cavity of a 12 mm stainless steel die, and a weight of ~ 5 tonnes (unless otherwise noted in text) was applied to the ram using a hydraulic press to result in a pressure of ~ 60 MPa, and pellets ~ 3 mm thick.

2.1.1.3 Sintering

The resulting pellets were placed directly onto/into alumina crucibles with lids in Chapters 3 to 5. In Chapter 3 samples were also placed into quartz crucibles constructed using glass blowing techniques. Samples were placed into alumina foil crucibles/boats in Chapter 7. The samples were reacted (sintered) in furnaces, while inside/on their specified vessels (**Figure 2.1**).

A KSL 1200X muffle furnace was used for Chapter 3 and parts of Chapter 4, 5, 6, and 7. This furnace had a gas supply option to 'blanket' the chamber in N_2 gas. A Daihan Scientific Ceber muffle furnace (max. 1200 °C) was also used in Chapter 5, which had a temperature offset of 40 °C in comparison to the KSL furnace, and the quoted operation temperatures in text are adjusted as such. High temperature iterations in Chapter 7 were conducted using a KSL1700X muffle furnace, with blanketing gas supply option. Also in Chapter 7, a Labec horizontal tube furnace was used to achieve a low oxygen atmosphere. These samples were placed on platinum inside a quartz tube, where nitrogen was passed through and vented into a fume hood (**Figure 2.1 (b)** below).

Heating rates were typically set to 5 °C/minute unless otherwise specified in the body of the text. Natural cooling of samples referred to leaving the sample in the closed furnace chamber until it was at room temperature. Quenching of samples from high temperature was done by extracting the vessel with tongs at high temperature and placing on a heat proof mat in open air to cool. Specific detail on temperatures and dwell times used in the sintering steps are given in the body of each chapter.

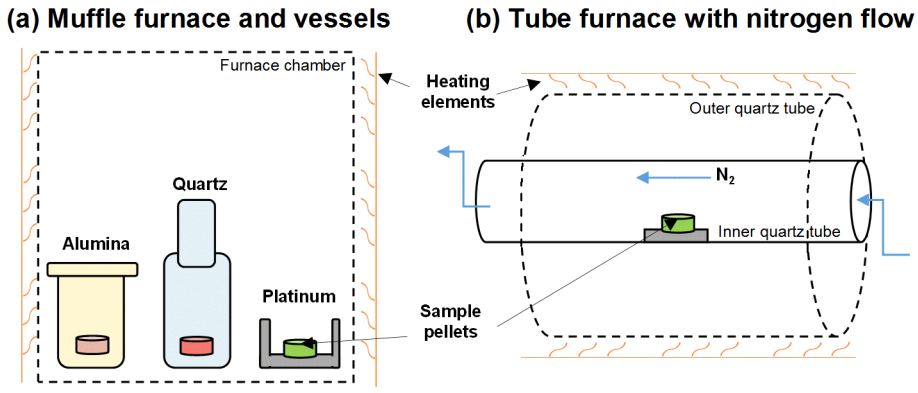

Figure 2.1. *Schematic illustration of* ***(a)*** *the muffle furnace and* ***(b)*** *the tube furnace setups for sample sintering.*

2.1.2 Metal Organic Decomposition

The metal organic decomposition (MOD) method was used in Chapters 3, 4 and 5. This involves starting with metal organic and nitrate precursors which are decomposed to oxides in

a ‘calcining’ step. This ‘precursor’ is then pressed and sintered in place of the milled oxide solid state synthesis method addressed above. The MOD method was used to promote homogenous mixing of metal ions and preclude some types of impurity formation that the solid state method suffered from.

2.1.2.1 Raw Materials

The raw materials (**Table 2.2**) were weighed in stoichiometric quantities for a targeted 4 g of oxide product. These were added to a beaker. Approximately 40 mL of solvent (ethylene glycol, ‘MOD-EG’ or reverse osmosis water, ‘MOD-H_2O’) was added and magnetically stirred. Liquid reagents were delivered by syringe where necessary.

Table 2.2. *Reagent details for metal organic decomposition syntheses.*

Reagents/Solvents	*Brand*	*Purity (%)*	*Chapters*
$Bi(NO_3)_3.5H_2O$	Sigma-Aldrich	≥98	3, 4, 5
$Fe(NO_3)_3.9H_2O$	Sigma-Aldrich	≥98	3, 4, 5
$Ti(OC_4H_9)_4$	Aldrich	97	3, 4, 5
$Cr(NO_3)_3.\ 9H_2O$	HW	~98	3
$Mg(NO_3)_2.6H_2O$	Merck	≥99	4
$Ni(NO_3)_2.6H_2O$	Alfa Aesar	98	4
$C_2H_4(OH)_2$ (ethylene glycol)	Fluka AG	≥99.5	3, 4, 5

2.1.2.2 Volume Reduction and Calcination

Chromium containing MOD-EG solutions in Chapter 3 began as a dark green/black colour, while magnesium and nickel solutions were orange and green respectively in Chapter 4. Bismuth iron and titanium only solutions in Chapter 5 were yellow to red depending on the iron content, and when using the MOD-H_2O approach, contained white particulate with yellow supernatant.

These mixtures were then transferred into shallow glass dishes and the ethylene glycol (or water) was evaporated slowly into a fume hood at 100 – 200 °C using a hotplate. This was conducted with continual stirring for approximately 3 hours until the volume was reduced to ~ 10 mL. During this volume reduction, typically MOD-EG solutions would darken in colour, then lighten back to a pale yellow or pale green (**Figure 2.2 (a) – (c)** illustrates this process for preparation of BFTO-623 in Chapter 5). If the solution is over reduced, a precipitation may occur resulting in an opaque paste.

The resulting cooled viscous solutions were removed from heat and transferred to an alumina crucible (**Figure 2.2 (d)**) and cooled to room temperature. These were then placed in a secondary containment crucible and into a Kilnwest furnace that vents into a fume cupboard for calcination (note: only 10 mL could be calcined at one time using this method). The

solutions were heated to 600 °C at 5 °/min then held for two hours as the solvent and metal organic/nitrate species decomposed. These were then cooled naturally to room temperature. The final dried products resembled a porous mass, often orange in colour (**Figure 2.2 (e)**), which was ground with a mortar and pestle for pressing as outlined in the previous section.

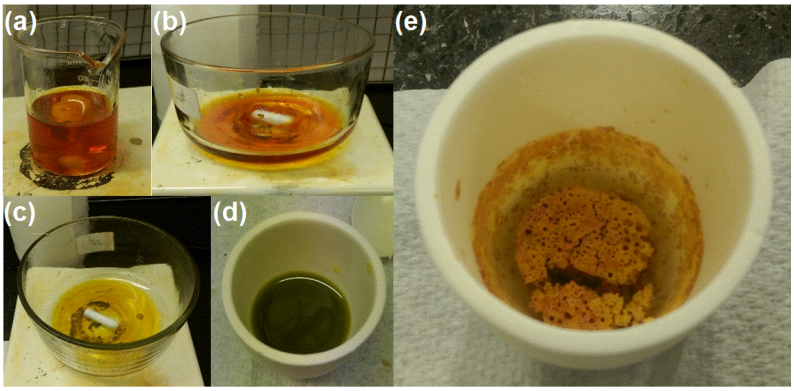

Figure 2.2. *Example MOD-EG process for BFTO-623 in Chapter 5. A dissolved bismuth nitrate, iron nitrate, titanium butoxide and ethylene glycol solution at room temperature is shown in* ***(a)****,* ***(b)*** *shows the solution after transfer to a shallow dish and commencement of heating,* ***(c)*** *depicts the solution lightening after 3 hours when near minimum volume,* ***(d)*** *shows the solution cooling in a crucible and* ***(e)*** *shows the decomposed product after calcining at 600 °C.*

2.1.3 Solvothermal Synthesis

The solvothermal method was used in to produce samples presented in Chapter 6. This method involved performing reactions under pressure to crystallize the desired phase from solution. This method was used for its ability to produce nanostructured materials.

2.1.3.1 Raw Materials

To generate solutions for the solvothermal reaction, first titanium tetrachloride was delivered to 240 mL of ethanol via a syringe. The vanadium source was then added (in a fixed V:Ti ratio ~ 0.05:1 between trials) and the solution magnetically stirred for an hour until the solution became transparent green (vandyl acetylacetonate), or yellow (vanadium oxychloride). The nitric acid was then added (in a different amount per individual trial ranging from 4 – 16 mL) with due care and stirred for a further 30 minutes, during which the solutions turned ‘neon’ green or yellow. These solutions were then split equally among four autoclaves, filling to 60% capacity. Details of reactants are outlined in **Table 2.3**.

Table 2.3. *Reagent details for solvothermal syntheses.*

Reagents/ Solvent	*Brand*	*Purity (%)*	*Chapter*
$TiCl_4$	Sigma-Aldrich	99.9	6
$VOCl_3$	Sigma-Aldrich	99	6
$VO(C_5H_7O_2)_2$	Fluka AG	≥96	6
$C_2H_5O_5$ (ethanol)	Merck	≥99.8	6
HNO_3 (nitric acid)	Univar	70	6

2.1.3.2 Reaction and Processing

The Teflon lined autoclaves were tightly sealed, then transferred to a low temperature oven in a specially designed lab for high pressure experiments. The vessels were heated for 17 hours at 200 °C. After reaction the vessels were removed from the oven and cooled to room temperature before being carefully opened. The reaction mixture was decanted into plastic containers with screw seal lids for use in a Sigma 3-30KS centrifuge. The products were centrifuged for 20 minutes, decanted, and then washed with H_2O. They were then centrifuged and washed a further two times before decanting and placing the whole tube in an oven to dry at 100 °C. After 24 hours of drying, the powders were collected into containers for use in the experiments outlined in Chapter 6.

Throughout each of the synthetic approaches addressed in this section, the phase purity and crystal structure of the synthesized samples had to be monitored. The next section outlines the diffraction and microscopy methods used and how in-depth characterisations of their crystalline natures were performed.

2.2 Structure Characterisation

2.2.1 Diffraction and Refinement

In this thesis, powder diffraction was predominately used to identify phases present in polycrystalline samples, and also determine the crystal structures of individual phases. The unique symmetry and elemental characteristics of each phase leads to a fingerprint pattern of reflections that can be identified in a mixture. The weight ratio of phases within the mixture also scales with the intensity of the Bragg peaks observed, and so some information on purity can also be obtained.

For phases in which the underlying crystal structure producing the diffraction pattern is not well known, the Rietveld method[288] can be used to extract crystallographic information. This method addresses powder specific structure solution problems such as overlapping peaks, and

crystallite shape effects. It uses least squares refinement to fit the measured pattern Y_{i0} at each point '*i*' due to the 'h^{th}' reflection, with a simulated pattern Y_{ic}:

$$Y_{ic} = I_0 \sum (k_h F_h^2 m_h L_h P(\Delta_h) + I_b) \quad \textbf{(2.1)}$$

where I_0 is the incident intensity, k_h is the phase scale factor, F_h^2 is the structure factor for the reflection *h*, m_h is the multiplicity of that reflection, L_h encompasses correction factors such as preferred orientation, $P(\Delta_h)$ is the function for peak shape and I_b is the background intensity. Simplified equation adapted from [289].

The fit of the models is evaluated in this thesis using the metric 'weighted profile residual' (R_{wp}) which includes a statistical weight w_i,[290] and is defined below:

$$R_{wp} = \sqrt{\left[\frac{\sum w_i (Y_{i0} - Y_{ic})^2}{\sum w_i (Y_{i0})^2}\right]} \quad \textbf{(2.2)}$$

Several different radiation sources are used in this thesis to achieve different resolution and contrast in the diffraction data. These radiation sources and their experimental parameters are detailed below.

2.2.2 X-ray Powder Diffraction

The X-ray Powder Diffraction (XRPD) method involves using X-rays as a radiation source to determine structural information on powdered polycrystalline samples. X-rays are relatively easy to generate, and this is an accessible lab-based technique to monitor the purity of materials as they are synthesized and conduct structure refinement.

In this thesis, XRPD data were collected using a PANalytical Empyrean X-ray Powder Diffractometer with a Cu Kα1/α2 radiation source (λ = 1.5406 and 1.5444 Å). Powdered samples were loaded on silicon zero-background plates with a small amount of ethanol and dried. Data were collected over an appropriate angular range and scan rate for resolution in the pattern (typically 5 – 90° 2θ for an hour). Basic phase matching was conducted with HighScore Plus[291]. Refinement was conducted with Jana2006[292] using pseudo-Voigt peak shapes, and model data were sourced from the International Crystal Structure Database[293]. Further specific detail about refined parameters is given within the relevant chapters.

In Chapter 6, crystallite size (*D,* nm) is estimated from the diffraction data through the Scherrer[294] equation:

$$D = \frac{K\lambda}{\beta\cos\theta} \quad \textbf{(2.3)}$$

where *K* is the shape factor (taken = 0.9 in this investigation), *λ* is the radiation wavelength, *β* is the line broadening at full width half maximum (FWHM) fitted via Jana2006, and *θ* is the Bragg angle for the relevant peak.

While XRPD is used extensively in this thesis, it is important to note that as X-rays scatter from the electrons of atoms, scattering strength scales linearly with atomic number. This can lead to issues refining crystal structure that contain light elements, or neighbouring elements on the periodic table. Some elements will also fluoresce X-rays if they are of similar atomic weight to the element used as the X-ray source, resulting in a high background (and low signal to noise ratio). For this reason (where possible) X-ray diffraction was complemented with other diffraction techniques.

2.2.3 Neutron Powder Diffraction

Unlike X-rays, neutrons scatter from the nuclei of atoms through the strong nuclear force. This interaction varies non-monotonically with increasing atomic number and is sensitive to an element's isotope. Electron magnetic moments can also scatter neutrons, as neutrons possess a spin. In this thesis, the neutron powder diffraction technique is used to obtain contrast between elements of a similar atomic mass and information on magnetic structure.

In Chapter 3 specifically, data from neutron diffraction experiments are presented. The high resolution powder diffractometer 'Echidna'[295] at the Australian Centre for Neutron Scattering was used to collect room temperature powder diffraction patterns. A monochromatic neutron beam of wavelength of 1.622 Å was used and the data were fitted using Jana2006. These samples were then measured on a different high intensity, medium resolution diffractometer called 'Polaris'[296] at the ISIS Muon and Neutron Source (Rutherford-Appleton labs, United Kingdom). With this instrument, room temperature and 500 K data were obtained *in situ* using a double-skinned resistive element furnace from a sample sealed in a 1.5 mm glass capillary. A polychromatic neutron beam produced from a spallation source was used, and the data were processed and refined using Mantid[297] and GSAS[298, 299] respectively.

2.2.4 Electron Diffraction

An electron beam can also be used as a radiation source for diffraction studies. A convenient way to obtain information is by using Transmission Electron Microscopy (TEM). With this method an electron beam can be passed through very small (ideally) individual crystallites and an intensity pattern can be collected on the other side.

In electron diffraction, the electrons scatter off the electrostatic Coulomb potential. This interaction is very strong and as a consequence, multiple diffraction events can occur before the electrons leave the sample. For this reason, unlike with neutrons and X-rays, refinement of the intensity is not meaningful. However, due to the strong interaction weak reflections and non-Bragg intensity features can be seen in Electron Diffraction Patterns (EDPs). In this thesis, electron diffraction is used to supplement diffraction information from the aforementioned methods.

EDPs presented in Chapters 3, and 4 and were collected using a 200 kV JEOL2100F FEGTEM Transmission Electron Microscope at the Centre for Advanced Microscopy, ANU. Patterns were collected from samples ground in n-butanol and dropped onto a holey carbon film on a copper grid. This gave a well dispersed array of crystallites that could be individually isolated for analysis.

2.2.5 Structure Validation from Simulation

2.2.5.1 Bond Valence Sum

In order to validate crystal structures determined through Rietveld refinement, one can calculate the bond valence sum of ions in the structure. The sum (V) of bond valences (v_i) from each bond around an atom should add to its formal valence state per Pauling's principles for electrostatic valence[300]. The bond valence of each bond to atom i is calculated as:

$$v_i = \exp\left(\frac{R_0 - R_i}{b}\right) \quad \textbf{(2.4)}$$

where R_0 is the ideal bond length (calculated such that the atom i will have an exact valence), R_i is the experimentally determined bond length and b is an empirical constant (typically 0.37 Å[301]). This comparison to empirical data allows one to judge if a refinement is reasonable based on data from other structures with the same elements and valence states.

Large deviations are expected to make the structure 'unstable', and an overall parameter called the 'global instability index' (GII) can be calculated:

$$GII = \sqrt{\frac{\sum_{i=1}^{N} d_i^2}{N}} \quad \textbf{(2.5)}$$

where d_i is the deviation between the bond valence sum and the formal valence state of atom i, and N is all atoms in the structure. The GII of the structure has been correlated before with the total energy calculated by density functional theory[302].

After refinement of a crystal structure, a '.cif' file was generated and input into the web program 'SoftBV'[301, 303] for evaluation of each ion's bond valence sums and the overall GII. Deviations lower ('underbonding') and higher ('overbonding') than the ideal valence were considered points within the structure for further refinement and/or local structure investigation.

2.2.5.2 Density Functional Theory

Evaluation of the total energy of condensed matter systems can be performed using computational quantum mechanical means. In this thesis density functional theory (DFT) is used to calculate low energy crystal structures and magnetic configurations. This method uses the idea that the system's total energy can be determined in terms of functionals of the electron density in the system[304]. The DFT method is limited by the use of an exchange-correlation approximation when calculating total energy. Given metal oxide systems such as the ones under investigation are strongly correlated, the choice of approximation will influence the results, but these calculations are a convenient method for predicting the properties of large periodic systems nonetheless.

In this thesis the code package WIEN2k[305] was used to perform the DFT calculations associated with Chapter 3. The GGA+U[306] approach was used, with the PBE-GGA exchange correlation functional and the on-sight repulsion U and on-sight exchange J from the literature[58]. Radial muffin tin sizes of Bi (2.3 a.u.), Fe (1.94 a.u.), Cr (1.94 a.u.), and O (1.67 a.u.) were used to simulate the atomic potentials. A grid of 64 $\boldsymbol{k}$ points was applied, and the product of the muffin tin size and maximum $\boldsymbol{k}$ vector was set to 8 to optimize computational time. The starting geometry was a single unit cell of BFCO (though converted to $P1$ space group for magnetic spin analysis) which had 6 iron/chromium sites, and forces were converged at <1 mRy/Bohr to attain a relaxed geometry. Both a double perovskite unit cell and a unit cell with a single antisite defect were calculated and compared for total energy and magnetic moment distribution. Initial alignments of the magnetic moments were set to be antiparallel (to form an antiferromagnetic structure).

While diffraction and simulation give information about the crystalline nature of the phases within produced samples, more information on the chemical nature and morphology can be obtained by other means. The following section details spectroscopy and microscopy techniques to further characterise the synthesized materials.

2.3 Composition and Morphology Characterisation

2.3.1 Scanning Electron Microscopy

Scanning Electron Microscopy (SEM) uses an electron beam to obtain morphological and chemical information from sample surfaces. Electrons from the beam can be bounced off the surfaces (backscattered electrons, 'BSE'), or cause more electrons (secondary electrons, 'SE') and other types of radiation (e.g. X-rays) to be emitted by the surfaces. These can be detected and analysed to reconstruct useful micrographs and spectra.

Ability to backscatter electrons increases with increasing atomic number. Contrast between phases that have different elemental compositions can be seen in BSE micrographs. This is used in this thesis to supplement X-ray diffraction phase analysis. Micrographs constructed from SE information on the other hand give good morphological resolution, and are used in this thesis to study the shape of particles and grains within materials. X-rays that are emitted from the sample after exposure to the electron beam can be collected and quantified to pinpoint the identity and quantity of specific elements. In Energy Dispersive X-ray Spectroscopy (EDXS), a spectrum of X-rays is collected and analysed for detection of broad number of elements. The Wavelength Dispersive X-ray Spectroscopy (WDXS) method focuses on quantifying specific X-ray wavelengths to more accurately determine quantities of specific elements. This is slow, but especially useful if the elements of interest have overlapping spectral peaks[307].

From morphological analysis of nanoparticles in Chapter 6, the particles were spread in a thin layer directly onto carbon tape on a sample stub. For BSE and EDXS analysis, the samples were polished through sequentially finer sandpapers (from 240 grit commercial grade sandpaper, to 1 μm diamond lapping & polishing film) by hand until the surface was smooth, with washing and sonicating between. The samples were then directly mounted onto a sample stub using carbon tape. Manual polishing was used instead of thermal or chemical etching in order to circumvent issues with preferential leeching of bismuth and vanadium (higher volatility and solubility than other component elements). For WDXS, samples were set in hard resin then polished sequentially though 1200, 2400 and 4000 grit sandpapers, before finally polishing with 6, 3, then 1 μm diamond paste, all using an Allied MetPrep3 grinding/polishing system. All samples were coated in carbon prior to analysis.

Data presented in Chapters 3 - 7 were collected at the Centre for Advanced Microscopy, ANU. An Hitachi 4300 SE FESEM in conjunction with an Oxford Instruments INCA X-MAX EDXS Analysis system and backscattered electron detector were used for Chapters 3 – 6 for elemental analysis and general imaging. The EDXS data were obtained at a voltage of 15 kV. A Zeiss Ultrapluss was used in Chapter 6 in which a higher resolution was required for particle imaging. The secondary electron imaging mode was utilized at a lower voltage (1.5 kV). In Chapter 7, a JEOL JXA-8530F Plus Electron Probe Microanalyzer was used to obtain WDXS data and thus better resolution of overlapping Ti and V characteristic X-ray peaks. A voltage of 15 kV was used on this instrument.

2.3.2 X-ray Photoelectron Spectroscopy

X-ray photoelectron spectroscopy is in some ways the reverse of EDXS mentioned above. This method hinges on shining an X-ray source (E_{hv}) on a sample surface and detecting the energies of electrons which are ejected (E_{KE}), then calculating their 'binding energy' (E_{BE}) from the known spectrometer work function ($\phi_{spectrometer}$) per:

$$E_{BE} = E_{hv} - E_{KE} - \phi_{spectrometer} \quad \textbf{(2.6)}$$

The peaks in binding energy in the XPS spectra are specific to element types, orbitals, and valence states. The structure of the valence band can also be analysed with this method and some information about the relationship of the valence band (and any gap states) to the fermi level can be determined. This technique is limited to information from the surface to a depth of 1-10 nm in the sample[308].

Samples for XPS analysis were in pellet or powder form, with pellets being polished in hexane before measurement. The data were collected using a Thermo Scientific ESCALAB250Xi spectrometer with an Al Kα X-ray source at UNSW Sydney. The spectra were then fit using the Thermo Scientific 'Avantage' program to the reference C 1s = 284.8 eV in order to establish relative proportions of valence states and atomic percentages of each detected element.

This method is used in this thesis to get an idea about how elemental incorporation influences defect formation and the band structure. While extremely useful, it should be noted that information gathered comes only from the sample surface. Other techniques are used to supplement this information.

2.3.3 Mössbauer Spectroscopy

Another spectroscopic technique which provides useful chemical information is ^{57}Fe Mössbauer spectroscopy. This technique is used in this thesis to confirm the iron valence, see if the samples are magnetic and examine if iron occupies different sites within the crystal. This method works by exposing the sample to gamma radiation produced by a ^{57}CoRh source. The

wavelength of the radiation is altered by linear accelerator, which moves the source through a range of velocities. This creates a Doppler Effect, the outcome of which is that the sample is scanned through a range of closely related wavelengths. Iron nuclei in the sample which are of the same isotope (^{57}Fe) will absorb gamma rays when a resonance condition is reached[309]. This can occur at different velocities depending on the environment of the iron in the sample.

The ^{57}Fe nucleus has a ground spin state of I = 1/2 and an excited state of I = 3/2. These energy levels experience Quadrupole Splitting (QS), leading to a doublet being observed in paramagnetic systems. The magnitude of the energy difference between the split excited states of the nuclei is influenced by the electric field gradient, in turn dictated by parameters such as the coordination number, type of ligands and crystallographic site. Magnetic Hyperfine Splitting can occur when the iron nucleus is surrounded by a magnetic field, such that a sextet of possible transitions at different energies can be seen for magnetic samples. The shift of all peaks with respect to the normal velocity of the source, is referred to as the Isomer Shift (IS). These shifts arise from effective s-electron density around the nucleus. The Fe^{2+} has a larger shift than Fe^{3+} due to screening by d-electrons[307].

^{57}Fe Mössbauer spectra were collected at room temperature using a standard constant-acceleration spectrometer in a transmission geometry using a ^{57}CoRh source (UNSW Canberra). Samples were powdered and mixed with boron nitride (BN) for a final concentration 13 – 16 mg/cm^2 of the compound under test on the sample holder. An α-Fe foil standard was also measured for calibration. Spectra were fitting using IMSG2011 [310] to extract the isomer shift, quadrupole shift, Half Width Half Maximum (HWHM) and in the case of more than one species being present, their relative proportions, for each material.

Together with the diffraction methods, these microscopic and spectroscopic studies provide a picture of the nature of the structure and bonding in each of the materials. Techniques used to measure the properties of whole samples are detailed below.

2.4 Magnetic Property Characterisation

The valence states of the elements inside materials can reflect electronic properties of the whole. Of particular interest throughout this thesis are the magnetic properties of materials, as Fe^{3+}, Cr^{3+}, Ni^{2+} and V^{4+} in materials from Chapters 3 - 7 possess unpaired electrons.

2.4.1 Magnetization Measurements

In an external magnetic field, a magnetic material may respond and become magnetized. The material's mass magnetization can be seen as the density of induced magnetic moments per unit mass. The proportionality factor between the external magnetic field ***H*** and the response magnetization ***M*** is called the magnetic susceptibility χ.

$$\boldsymbol{M} = \chi \boldsymbol{H} \tag{2.7}$$

Different magnetic systems result in different behaviours for χ due to the interactions between other magnetic ions within the material. Magnetically ordered systems typically have non-linear ***M-H*** responses, and χ is a tensor. Temperature also affects χ, and critical temperatures where thermal energy can overcome exchange interactions and the material reverts to paramagnetism (T_C for ferromagnets and T_N for antiferromagnets) can be seen. Some simple examples are depicted in **Figure 2.3** below.

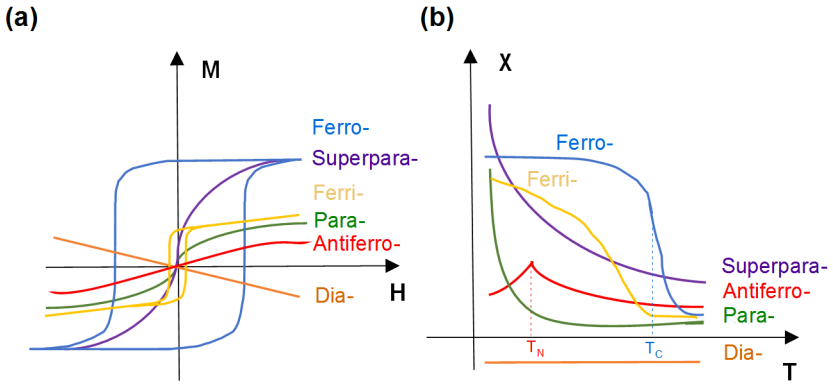

Figure 2.3. *Part* ***(a)*** *shows typical* **M-H** *responses for materials with different magnetic interactions ('dia-' = 'diamagnetic' etc.) and* ***(b)*** *illustrates the temperature dependence of χ for different magnetic interactions. This illustration is based on information from [*[311]*],[*[312]*] and [*[24]*].*

In this thesis, the ***M***-T and ***M-H*** data are collected to get information about the type of ordering present and any transition points within the sample. Then 1/χ is fitted with the Curie-Weiss model within the paramagnetic temperature ranges to obtain some information about the size of moments and the nature of the exchange interaction, and the ***M-H*** data are fitted with the Langevin function to see if any clustered behaviour is occurring.

2.4.1.1 M-T Modelling: Curie-Weiss

The susceptibility χ is temperature dependent, as shown in **Figure 2.3** above. At weak fields, paramagnetism can be modelled using the Curie-Weiss law[313]. According to this law, the magnetic susceptibility determined from the mass magnetization plot can be expressed as:

$$\chi = \frac{xN_A\mu_0\mu_{eff}^2}{3k_BM_mT} = \frac{C}{T-\theta_w} \quad \textbf{(2.8)}$$

where x is the molar fraction of the magnetic species in the material, N_A is Avogadro's number, μ_0 is the permeability of free space, k_B is the Boltzmann constant, M_m is the molar mass of the material, C is the Curie constant and θ_w is the Weiss constant. This means, by plotting 1/χ vs. temperature and applying a linear fit to the paramagnetic part of the curve, the slope is the Curie constant C and the intercept is the Weiss constant θ_w. Weiss constants of $-\theta_w$ K and $+\theta_w$ K are typical for materials with some antiferromagnetic and ferromagnetic interactions respectively.

Rearranging and applying the fitted slope C, an estimate of the effective magnetic moment (μ_{eff}), in bohr magnetons (μ_B), can be obtained via:

$$\mu_{eff} = \sqrt{\frac{3k_B \times C \times M_m}{x \times N_A \times \mu_0 \times \mu_B^2}} \quad \textbf{(2.9)}$$

This determination of effective moments from fitting allows comparison to expected values for different magnetic ions, as μ_{eff} is also equal to:

$$\mu_{eff} = \mu_B g\sqrt{\boldsymbol{J}(\boldsymbol{J}+1)} \quad \textbf{(2.10)}$$

where g is the Landé g-factor and $\boldsymbol{J}$ is the total angular momentum.

A special case arises for the ions with partially filled d-levels such as in Fe^{3+}. They are prone to a quenching of orbital angular momentum $\boldsymbol{L}$[314] and the μ_{eff} instead becomes:

$$\mu_{eff} = \mu_B g\sqrt{\boldsymbol{S}(\boldsymbol{S}+1)} \quad \textbf{(2.11)}$$

where $\boldsymbol{S}$ is the spin angular momentum. This is often referred to as the 'spin-only' moment.

2.4.1.2. M-H fitting: Langevin

At low temperature and high field, paramagnetic behaviour can be modelled using the classical depiction of magnetization[312]:

$$\boldsymbol{M} = M_0 \cdot L(\beta) \quad \textbf{(2.12)}$$

Where $M_0 = Ng\mu_B\boldsymbol{J}$, N is the number of atoms, and $L(\beta)$ is the Langevin function:

$$L(\beta) = tanh^{-1} - \frac{1}{\beta} \quad \textbf{(2.13)}$$

Fitting for β will gives the cluster moment '*m'* (not equal to effective moment above).

$$\beta = \frac{\mu_0 \cdot m \cdot \boldsymbol{H}}{k_B \cdot T} \quad \textbf{(2.14)}$$

Therefore the Langevin function does not describe the behaviour of individual independent atoms/ions but the behaviour of some kind of macroscopic spin in a magnetic field[315]. Such macroscopic spins occur in systems with ferromagnetic or ferrimagnetic clusters in a nonmagnetic matrix or in magnetic nanoparticles which can be aligned in an external magnetic field.

2.4.1.3 Experimental Methods

The SQUID ***M-H*** and ***M***-T magnetization measurements in Chapter 3 were conducted with a Quantum Design Magnetic Property Measurement System (MPMS) at the ISIS Neutron and Muon Source, UK. Low temperature field-cooled (FC) and zero field-cooled (ZFC) ***M***-T data were collected from 2 – 324 K. The ***M-H*** data were collected at 10, 80, 150, 200 and 300 K in a field with intensity up to 70 kOe. The high temperature ***M***-T from this Chapter was conducted with a Quantum Design MPMS with oven option (Durham University, UK), and FC data was collected from 300 – 535 K in a field of 175 Oe.

In Chapter 4, the BFNTO DC ***M-H*** data were measured using a Quantum Design Physical Properties Measurement System (PPMS) at UNSW Canberra, Australia to a field of 90 kOe and temperatures 2, 10, 100, 200 and 300 K.

The remaining ***M-H*** measurements in Chapter 4, 5 and 7 were conducted using the Vibrating Sample Magnetometer (VSM) mode of a Quantum Design PPMS at the Australian Centre for Neutron Scattering (Lucas Heights Australia) at 3 K. The FC and ZFC ***M***-T data were collected at various fields over a temperature range of 3 – 300 K, and 5 – 373 K for VTO50 in Chapter 7 specifically.

While these are the most basic methods of measuring magnetic responses in a material, information can often be difficult to extract if there are any magnetic impurities present. For this reason, other complementary techniques can be employed.

2.4.2 Heat Capacity

Heat capacity reflects the energy required to change the temperature of a material. When a material is magnetically ordered, the spontaneous magnetization of the material increases the heat capacity according to the equation below[316]:

$$C_m = -\frac{1}{2}\mu_0 N_W \frac{d\boldsymbol{M}^2}{dT} \quad \textbf{(2.15)}$$

where C_m is the specific heat increase from magnetization, μ_0 is the permeability of free space, N_w is the molecular field constant (which is related to χ above), $\boldsymbol{M}$ is magnetization and T is temperature. Magnetization varies significantly near a magnetic phase transition, and results in a discontinuity in the heat capacity.

Heat capacity data are presented in Chapter 4 for sample BFNTO. A Quantum Design PPMS (UNSW Canberra) was used to record data over the temperature range 2 – 200 K on a 9.3 mg solid pellet sample. The specific heat is determined from the difference between a reference addenda with a small amount of Apiezon N grease and the total heat capacity of the sample also attached with grease. In this thesis, this method is used to help pinpoint critical transition temperatures.

2.4.3 Electron Spin Resonance Spectroscopy

In this thesis, Electron Spin Resonance Spectroscopy (ESR) is used to obtain information about the interactions between magnetic moments in these materials and their surroundings. A magnetic dipole can interact with a magnetic field ($\boldsymbol{B}$). In the simplest case, a single isolated unpaired electron (possessing a magnetic moment) can occupy two energy levels split by the applied external field (electron Zeeman splitting) with an energy difference of:

$$\Delta E = hv = g\mu_B \boldsymbol{B} \quad \textbf{(2.16)}$$

A transition between such split energy levels can be promoted by application of a light source (hv) satisfying the energy requirement (e.g. microwaves for $\boldsymbol{B}$ fields ~ 1 T). When the light source is fixed, and the resonance field is known, the value of g can be calculated. The value of g is dependent on the exact local environment the electron finds itself in and as such, is dependent on how the chemical system is aligned relative to the applied magnetic field. This can be accounted for by replacing the scaler g-value with a $\boldsymbol{g}$-tensor, where the different components of the $\boldsymbol{g}$-tensor describe the different chemical environments the electron finds itself in. An electron's local environment is impacted by field effects induced by the external $\boldsymbol{B}$

field and internal factors mostly independent of $\boldsymbol{B}$[317]. For example, in materials with symmetry restrictions, moments within the structure will align anisotropically with the applied field. This occurs in materials such as those with axially distorted octahedra, where there are two unique components to the $\boldsymbol{g}$ tensor ($g_x = g_y$, the 'perpendicular' components and g_{zz}, *the* 'parallel' component).

The local effects include the electron and nuclear Zeeman interactions (already mentioned), nuclear quadrupole interactions, the electron-nuclear hyperfine interactions and the fine structure or zero-field interactions. The nuclear based interactions are typically too weak for ESR to resolve, but other interactions are large and can lead to more than two states for the moment to occupy and transition between. The total electron spin 'S' and nuclear spin 'I' of the ions under study will dictate the possible interactions and resulting energy levels. In this thesis Fe^{3+} (S = 5/2, I = 0) and V^{4+} (S = 1/2, I = 7/2) are examined predominately. In the V^{4+}, this combination of electron and nuclear spins can result in the hyperfine coupling interaction. This interaction, just like the Zeeman interaction, is dependent on how the system is aligned in the magnetic field as such is described by a tensor ($\boldsymbol{A}$). Eight ESR transitions can arise from the I = 7/2 and S = 1/2 interaction.

The zero field splitting interaction comes about only in systems that have multiple unpaired electrons. For example Fe^{3+}, a 5 electron (S = 5/2) spin system with 6 magnetic sublevels, has its levels perturbed due to dipole-dipole interactions between the unpaired d-electrons of the metal ion. Half integer spin systems like Fe^{3+} always give rise to an ESR signal as these will always have a degeneracy at zero-field, whereas integer spin systems (even number of electrons) often do not give rise to an ESR signal. Electron-electron coupling is another important zero-field interaction which involves coupling between electron moments on separate atoms. These interactions can also be very large, much larger than the electron Zeeman interaction, such that the system can be described in terms of an effective or total spin. For example, a ferromagnetic material with interacting S = 1/2 ions (single unpaired electrons on each ion) may be described as an S = 1 system when the electron-electron coupling is large. Similarly, an antiferromagnetic system with the same ions can be described as an S = 0 antiferromagnet (with no readily observed signal). Any observed peaks are often broad due to these electron-electron interactions[307].

Thus, there can be many observable transitions in ESR spectra with different values of $\boldsymbol{g}$ that give information about the symmetry of the paramagnetic ions and their neighbouring interactions. In Chapters 4 and 7, powdered samples were measured using a Bruker E500 ESR spectrometer. X-band ESR spectra were obtained at room temperature, 20 K and 50 K using an Oxford ESR helium cryostat. Solid ESR samples used in Chapter 4 were magnetically

diluted with ESR silent KCl and placed into quartz ESR tubes such that the material under test comprised 3 – 4 wt. % of the total volume in the test cavity. Samples used in Chapter 6 were undiluted. The resulting data were simulated and fitted (where possible) using the 'Easy Spin' [318] Matlab toolbox.

2.4.4 Muon Spin Resonance Spectroscopy

Where ESR is good at probing environments of isolated paramagnetic centres, it is sometimes less fruitful in probing information about systems in which there is significant electron-electron interaction. Information about the internal magnetic field of a sample and its dynamic behaviour can be probed with muon spin resonance spectroscopy (μSR).

The μSR method utilizes positive muons (μ^+) which decay into positrons (e^+) over time. A magnetic sample can be placed in a spin polarised muon beam where muons implant by pairing up with an electron (in semiconductors). The direction of the muon spin will precess at the Lamor frequency if not influenced by a magnetic field. When the muon decays into a positron, this particle will be ejected from the sample preferentially along the direction the muon spin was pointing. By monitoring positrons hitting detector banks placed around the sample and the asymmetry between them over time, the precession can be monitored. If the muon is affected by an internal magnetic field, this asymmetry will change according to the strength and disorder of this field[319]. The muon probes are statistically more likely to experience the field of the main phase, thus the technique is less influenced by magnetic impurities. By fitting the data and extracting time dependent parameters, information about the main magnetic phase can be gathered that is complementary to magnetization studies.

The Argus Muon spectrometer at the RIKENRAL Muon Facility (ISIS Muon and Neutron Source, UK) was used for the μSR measurements presented in Chapter 3 of this thesis. The sample was contained in a 1 cm^2 silver foil packet for measurement in fly-past mode. The sample was cooled with a cold-finger helium flow cryostat over the temperature range 100 – 400 K. Double pulses separated by 324 ns such that the FWHM is 70 ns were used for data collection. Full asymmetry of a blank scan was 22%. The data fitting equations providing further details are in the body of Chapter 3.

Together, this suite of techniques can provide useful and complementary assessments of magnetic properties of the materials under test. A range of other methods are required in order to assess other functional properties of the materials.

2.5 Electrical and Optical Property Characterisation

2.5.1 Atomic Force Microscopy Techniques

2.5.1.1 Piezoresponse Force Microscopy

The Piezoresponse Force Microscopy (PFM) technique can give information about polarisation within samples at a local scale. In this method a small modulated voltage (V_{tip}) is applied to cantilever as it scans the surface:

$$V_{tip} = V_{DC} + V_{AC}cos(\omega t) \quad \textbf{(2.17)}$$

which contains DC and AC components, and t is time and ω is angular frequency.
If the material is piezoelectric, the surface deforms slightly as a response to the DC and AC parts of the applied voltage and the cantilever displaces (d_{PFM}) according to:

$$d_{PFM} = d_{DC} + Dcos(\omega t + \varphi) \quad \textbf{(2.18)}$$

where D is the amplitude and φ is the phase difference, containing information about the magnitude of the piezoelectric constant and the direction of polarization in the sample[320]. A laser tracks this deflection and the position, comparing the drive signal and the actual deflected signal to determine the material's piezoresponse. This has arbitrary units, and is calculated from:

$$piezoresponse = Dcos\left(\frac{\pi.\varphi}{180}\right) \quad \textbf{(2.19)}$$

In this thesis, ferroelectric materials are studied, which by definition are also piezoelectric, making this a powerful technique. Oppositely aligned ferroelectric domains within a sample will possess the same piezoelectric constant. In such cases, an applied voltage will induce the same amplitude of distortion to each domain, but exhibit a different phase response (**Figure 2.4** below). Non-180 degree domains, and domains with an in-plane component can also be imaged with PFM.

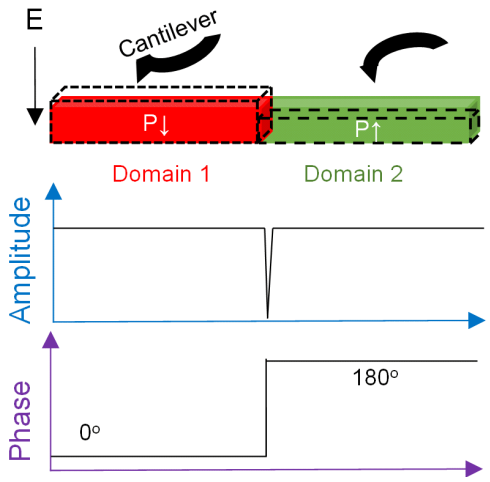

Figure 2.4. *Pictorial illustration of the PFM technique. For domains polarised parallel (red) or antiparallel (green) to the applied field (***E***), a 180° phase difference (purple), and equal amplitudes (blue) are measured.*

Using PFM, the amplitude, phase and piezoresponse switching behaviours in response to an applied electric field can also be observed from point to point[321]. The measured responses for ferroelectrics typically mimic the bulk polarisation and strain responses mentioned in the introduction and can be a good indicator of the type of polar ordering in the sample, without needing a dense sample. Large voltages can also be applied over a small area to manually switch whole domains in a desired pattern.

In this thesis, PFM is used to gain insights about the nature of ferroelectric domains and switching behaviours of the materials under study. Bulk measurements are not presented in this thesis as samples were typically not dense enough to endure exposure to large electric fields over the whole sample (further noted within each relevant chapter). PFM measurements from Chapters 3 – 6 were made using an Asylum 'Cypher' Atomic Force Microscopy (AFM) system. Conductive AC240TM silicon probes were used on well-polished samples with a contact force of ~ 100 nN. Dual AC Resonance Tracking mode was used to image pristine and written domains. Switching spectra were also collected. Specific area sizes and applied voltages are explained in the relevant chapters.

2.5.1.2 Kelvin Probe Force Microscopy

Kelvin Probe Force Microscopy (KPFM) can be used to measure surface potential of a sample. With this technique, the probe forms an electric field with the surface. When the probe is driven at a fixed height across the sample, a change in potential difference between the probe and the surface will cause the probe to vibrate. A small voltage can then be applied to nullify this detected force. This is known as the contact potential, which can be mapped over the sample surface[322].

If one scans the surface of the sample slowly, and changes the ambient conditions through application of a light source, resulting changes in the surface potential from photoexcitation are detectable *in situ*. A pictorial representation is given in **Figure 2.5**. Such a change might reflect, for example, promotion of electrons from the valence to conduction band, thus changing the potential difference between the sample and probe. This gives some information about how strong a photoexcitation might be in these samples, but is limited to the laser light source compatible with the equipment.

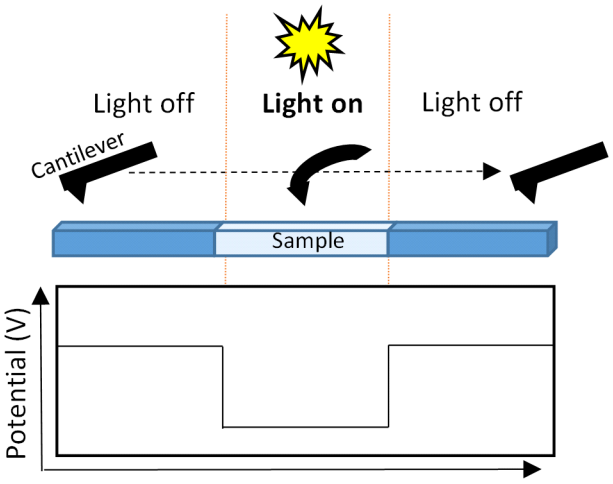

Figure 2.5. *Pictorial representation of a typical* in situ *measurement of the light dependent surface potential response. As the cantilever traces the surface, the light is switched on partway, leading to a change in the potential measured.*

Surface potential was monitored in Chapters 3 - 6 through KPFM, also using an Asylum 'Cypher' Atomic Force Microscopy system. While in dual-pass mode, and a tip elevation of ~ 50 nm, a 458 nm laser was switched on and off to illuminate the sample via optical fibre. This allowed surface potential changes due to light exposure to be measured *in situ*.

2.5.2 Photoelectronic Measurements

In order to determine if the materials explored in this thesis could produce a bulk photocurrent and photovoltaic response, the change in the DC current as an electric field was applied in dark and light conditions was monitored. A photovoltaic material will show a non-zero current at zero applied voltage when the light is on[10]. A sample without a significant field will show a more linear response (ohmic type behaviour), while curvature and asymmetry would imply the existence of some type of internal field or dynamic resistive character. A change in slope between light and dark would indicate a photo-induced change in resistance.

Prior to measurement, the samples were polished and cleaned. Circular gold electrodes were applied by sputtering at 30 mA for 3 minutes through a mask. Gold electrodes worked best for

the high resistivity samples and the low resistivity BFCO samples were instead coated in transparent ITO. This was done using pulsed laser deposition (excimer laser, power 1.5 J/cm^2, 5 Hz pulse) to ablate the target and coat circular electrodes over 30 minutes on the sample substrate at 500 °C also though a mask.

Measurements were made across the surface electrodes using the FE probe head unit of an aixACCT TF2000 Analyzer. The data were collected using the aixACCT hysteresis software, which involves application of voltage in a stepped triangular waveform and extracts DC current information from the voltage dependent resistive parts of ferroelectric samples. The maximum applied voltage in any test was 10 V and the step interval depended on the sample (0.05 – 0.5 V). The 'white' light conditions were imposed using a Nikon HB-10104AF 100 W mercury lamp. The median currents from the looped measurement in dark and light conditions were then compared. Any offset from zero in the dark conditions was taken as error and applied to the measurements made in light conditions.

2.5.3 Impedance Spectroscopy

In order to further study the electrical behaviour of samples in this thesis, impedance spectroscopy was used. By applying an AC field at different frequencies across the samples, dynamic electrical features of the materials can be investigated. The way a material 'impedes' current flow when an AC voltage is applied is given by the complex expression:

$$\boldsymbol{Z} = R + jX \tag{2.20}$$

Where $\boldsymbol{Z}$ is impedance, R is resistance, X is reactance, and j is the imaginary unit. Samples can be considered as electrical circuits with components connected in series or parallel that have individual $\boldsymbol{Z}$ values (e.g. a crystal grain and a grain boundary). Each component may contain different proportions of resistance and reactance. For example, perfect inductors and capacitors might have the following reactance expressions as their only contribution to $\boldsymbol{Z}$:

$$X_L = 2\pi f L \tag{2.21}$$

$$X_C = \frac{1}{2\pi f C} \tag{2.22}$$

where L is inductance, C is capacitance and f is frequency.

A Nyquist plot is a common way to present impedance data[323] and typical results from samples with different components are shown below in **Figure 2.6**:

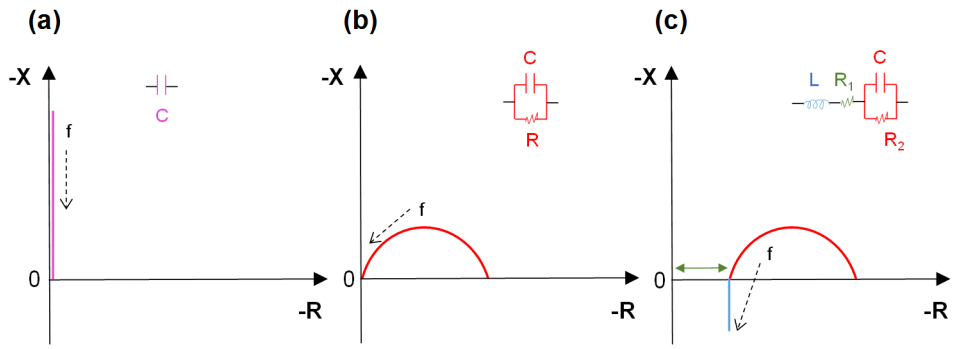

Figure 2.6. *Typical Nyquist plot for various kinds of equivalent circuits that might occur in a material. In (a) the response of an ideal capacitor is shown, (b) shows a capacitor and resistor in parallel and (c) shows an inductor and resistor in series with a capacitor and second resistor in parallel. The direction of increasing frequency is noted by 'f' and an arrow.*

These plots are qualitatively analysed in this thesis to obtain information on capacitive, inductive and conductive/resistive mechanisms within the sample as a consequence of composition, valence, and temperature changes. The real resistivities (ρ) obtained at certain frequencies are also quantitatively compared to determine semiconductor trends. This is done by taking the measured 'R' and applying the sample dimensions electrode area (A) and thickness (l) as follows:

$$\rho = \frac{R \cdot A}{l} \qquad \textbf{(2.23)}$$

Samples for measurement were coated in gold for 3 minutes at 30 – 40 mA using sputtering. Room temperature impedance spectra were obtained using an Agilent E4980A Inductance-Capacitance-Resistance (LCR) meter with an Agilent 16034E test fixture. Spectra were collected from 20 Hz to 2 MHz under ambient temperature and light conditions. For temperature controlled measurements, samples were fixed into the sample holder with GE Varnish then placed in a CTI Cryogenics Cryodyne refrigerator unit and the sample chamber was evacuated to 1 x 10^{-5} mbar for cooling. Temperature was controlled with a Lakeshore 335 temperature controller between 10 K and 450 K. Impedance measurements were at a range of frequencies between 20 Hz and 2 MHz every 15 seconds via an Agilent E4980A LCR meter and Tonghui TH26011B test fixture wired to the sample stage during the cooling and heating cycles.

2.5.4 UV-Vis Diffuse Reflectance Spectrophotometry

In this thesis, diffuse reflectance spectrophotometry was used to determine how the synthesized materials absorbed light. Polycrystalline samples typically reflect in a diffuse manner, rather than a specular one, and this can be measured with the appropriate equipment. The proportion of light that is reflected by the material can be related to how it absorbs via the Kubelka-Munk function (*F(R)*)[324].

$$F(R) = \frac{(1 - R_\infty)^2}{2R_\infty} = \frac{k}{s} \quad \textbf{(2.24)}$$

where *k* is absorption coefficient, *s* is scattering coefficient, R_∞ is diffuse reflectance. This can then be processed into a Tauc plot[325] with the axes:

$$(F(R) \cdot hv)^{1/n} \qquad vs. \qquad hv \quad \textbf{(2.25)}$$

where *n* = 2 for indirect transitions, *n* = 1/2 for direct transitions and *hv* is the photon energy. This gives valuable information about potential band gaps in the samples. A drastic drop off in the Tauc relation at an energy value that corresponds to the band gap should be expected. This method can be used to help identify photofunctional materials and which wavelengths of light they may be able to absorb best. There are drawbacks however, in that the particle size and packing can affect measurements from sample to sample, and so this method is used only to get a general estimate of the band gap.

Measurements were made using a Cary 5G UV-Vis spectrophotometer with Diffuse Reflectance Accessory (DRA) in Chapters 3, 6 and 7. Powdered samples were pressed on white filter paper for placement against the measurement window. The paper spectrum was removed from the background. Measurements were made in *F(R)* mode where possible, and otherwise in absorption mode, over the visible light range. A Cary 7000 with a newer DRA was used in Chapters 4 and 5 (Chinese Academy of Sciences Technical Institute of Chemistry and Physics).

2.5.5 Photocatalysis

One of the key photofunctions of interest to this thesis is photocatalysis. The photocatalytic behaviour of the nanoparticles was tested in a 20 mg/L Rhodamine B (RhB) solution. The photocatalysts were added to water to make a 1 g/L mixture. The dye concentration after catalyst addition was first measured with the light off. Then the sample was irradiated with a visible 500 W Xe lamp (cut off at 380 nm). The RhB dye is pink and loses its colour on breakdown, allowing monitoring of the catalyst's effectiveness through the light absorption of the solution over time. The concentration of RhB was determined at regular 20 minute intervals by taking aliquots of the solution and subjecting them to UV-Vis spectrophotometry. The

intensity of the 552 nm absorption band was used in a calculation of concentration decrease over a period of 2 hours. Experiments were conducted at the Chinese Academy of Sciences Technical Institute of Chemistry and Physics.

2.6 Summary

This chapter gives background information, justification and specific experimental detail about methods used in this thesis to synthesise, determine structure, and measure properties of a suite of materials. These techniques were selected to provide information on each aspect of the material and bring them together for a unified understanding of their functionality. The following five chapters detail the findings from these experiments.

Chapter 3 Cr-modified Perovskite-type Bismuth Ferrite Materials

In this first content chapter, the material bismuth iron chromium oxide (BFCO) is explored. BFCO is a modification of the host oxide BFO. By adding chromium, the magnetic and photofunctional characteristics are predicted in the literature to improve considerably. As outlined in the introduction, this material has shown considerable promise as a photovoltaic material in thin film investigations, hence its selection as a worthy candidate for further investigation in this thesis.

However, a number of questions remain unanswered in the literature on BFCO including the nature of the underlying chemical ordering of iron and chromium within the perovskite structure and the implications this has for the physical properties, most notably the magnetism. In addition, the synthesis of this material has not previously been achieved in the bulk, precluding this kind of thorough investigation until now.

By developing a new synthesis, investigating the structure thoroughly, and measuring its physical properties, these questions can be answered. The following sections detail a newly developed synthetic procedure to generate large quantities of bulk BFCO with appreciable purity at near-ambient pressure. It then focuses in on a systematic study of the underlying structure of the material, in particular the determination of this Fe/Cr chemical ordering using X-ray, electron and neutron probes, which is supported by theoretical simulation and helps answer long standing questions about the origin of the properties. A verification of the physical properties of the bulk BFCO materials is then performed, including experimental magnetization studies, local electrical properties measurement and observation of responses to UV-Vis irradiation.

3.1 Synthesis

3.1.1 Near-Ambient Pressure Method Development

One of the main hindrances to ongoing study of BFCO is being able to synthesize it in bulk. The conventional solid state method is typically used to produce large volumes of bulk ceramics. However, this method can often be fraught with difficulty when trying to prepare $BiFeO_3$ based materials.

As is noted by many authors, parasitic phase formation in the Bi_2O_3-Fe_2O_3 phase system in nearly unavoidable[54], especially in the presence of impurities (including Si and Al, common in

reaction vessels)[55] and when introducing a third oxide such as Cr_2O_3[53]. Ways to reduce the prevalence of the extra phases include high purity reactants (not useful if scaling up is your goal), very fast heating and cooling to circumvent the kinetic challenges of phase formation[56], using closed vessels to reduce Bi_2O_3 evaporation and the application of pressure[53]. It would appear from the reports to date that pressure is very important in establishing any quantity of perovskite structured material in the product[63, 65] and no phase formation appears possible at ambient pressure[72, 73]. An important first step of this investigation was to determine if such high pressures were strictly necessary and if a near ambient pressure approach (enabled with some inexpensive lab equipment) could be utilized instead.

Quartz quick-fit glassware with 24/29 or 34/35 size ground joints, the kind typically found in chemistry laboratories, can be fashioned into a crucible using glassblowing techniques (**Figure 3.1 (a)**). The seal on the vessel is loose and easy to handle, but at higher temperatures becomes well sealed and an above-ambient pressure is generated. A similar effect can be produced by vacuum sealing samples inside quartz ampules using glassblowing if necessary, though this is not a reusable method. By placing prepared oxide pellets directly into such a quartz vessel and sintering for short reaction times (30 – 60 minutes), followed by a quench, a phase which can be indexed to a rhombohedral perovskite structure can be identified using XRPD (**Figure 3.1 (a)**).

It is notable that if an alumina crucible is used instead, which does not tightly seal, no perovskite phase can be formed instead producing separate bismuth oxide and transition metal oxide phases (**Figure 3.1 (b)**). Packing the sample with extra powder to help control bismuth evaporation also had no effect, which indicates that the lack of perovskite phase formation in the Bi_2O_3-Fe_2O_3-Cr_2O_3 system is related to the vessel pressure.

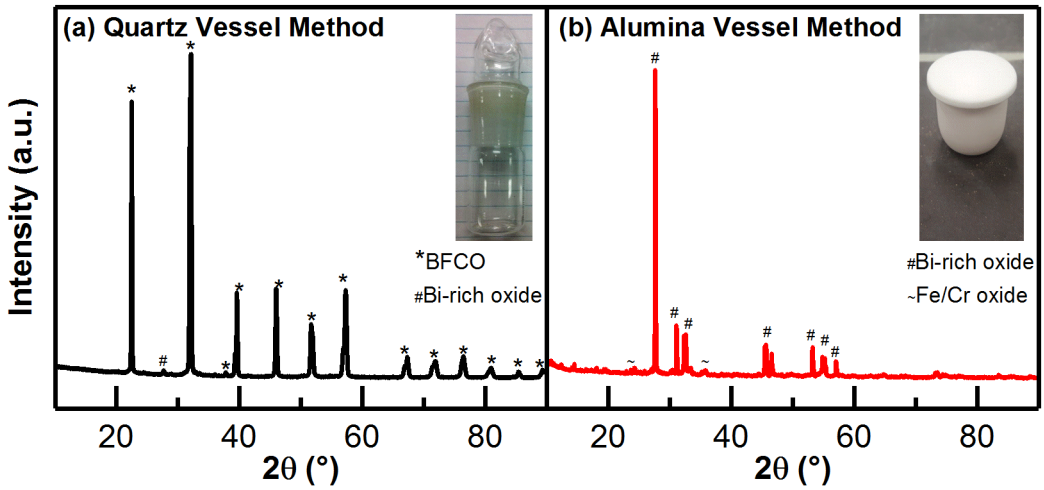

Figure 3.1. *In **(a)**, a quick-fit quartz glass crucible and an XRPD pattern of a sample produced inside at 860 °C for 1 hour (then quenching to air) is shown and **(b)** shows a standard alumina crucible and pattern associated with sintering a sample inside with excess un-pressed power at 860 °C for 30 mins (2 hour sinter also showed no improvement. Not shown).*

The use of quartz glass, which while very useful in affording the necessary pressure for synthesis, did also come with drawbacks that had to be overcome with optimization. XRPD patterns presented in **Figure 3.2 (a)** show the formation of highly reduced Bi metal (an impurity phase) in vessels which have been used many times. This was also obvious in BSE micrographs obtained with SEM (**Figure 3.2 (b)**). A composition summary of specific points in this micrograph determined by EDXS is given in T**able 3.1**. It would appear that the lack of airflow in the vessels may facilitate a reaction between the reactants and the quartz vessel over time, leading to reduction of bismuth and introduction of some silicon (and aluminium) content in the product. For these reasons, in order to produce the best quality samples, freshly made quartz vessels were used to produce samples for testing.

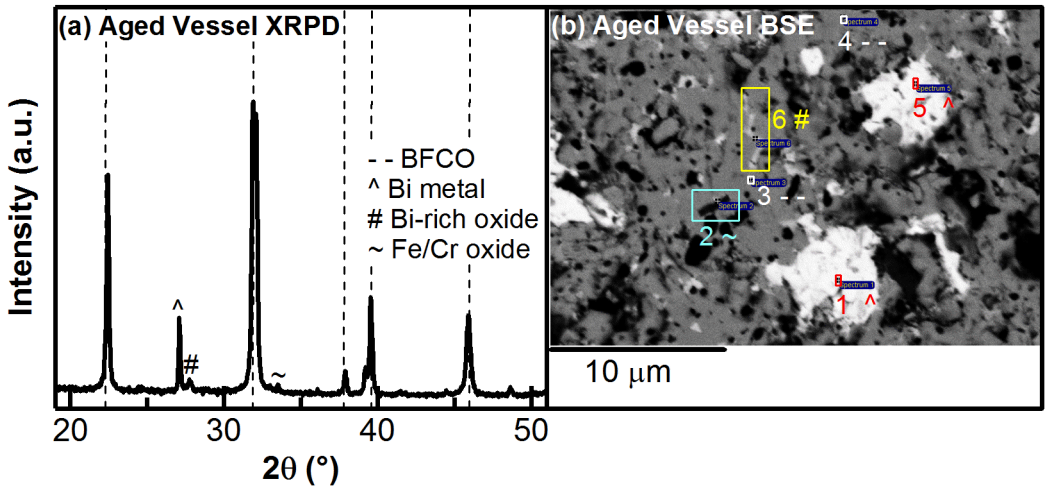

Figure 3.2. *In* ***(a),*** *an XRPD pattern of a BFCO sample made in aged quartz crucibles at elevated temperature (880 °C) is shown and in* ***(b)****, a backscattered electron micrograph of the same sample is presented. Large Bi metal regions can be observed (^) in addition to pale whites/grey (#), the main grey phase (--) and a dark phase (~).*

Table 3.1. *EDXS spectra obtained from points in* ***Figure 3.2 (b)*** *and a phase assignment.*

Point	*Al (wt. %)*	*Si*	*Cr*	*Fe*	*Bi*	*O*	*Total*	*Assignment*
1	0.11	0	0.27	0.49	105.21	12.51	118.58	Bi metal
2	0	0.18	13.49	17.78	48.5	19.64	99.6	Oxide of Cr and Fe
3	0	0.07	6.14	11.19	66.14	15.32	98.86	Fe-rich BFCO
4	0	0	6.61	10.2	66.23	15.04	98.08	Fe-rich BFCO
5	1.17	0	0.22	0.42	94.9	12.22	108.94	Bi metal
6	0.64	0.5	3.5	5.95	64.24	12.69	87.52	Bi-rich oxide phase

3.1.2 Optimization

While successful production of a perovskite BFCO phase obviously hinges on use of a fresh quartz crucible, improvement can also be made to the phase purity by optimizing synthesis conditions such as sintering temperature and time. XRPD was used to monitor the success of the synthesis optimization, with the angular range 20–50° 2θ being the most diagnostic range for confirming the presence of additional phases. Henceforth in this chapter only this angular range will be shown in XRPD plots, and a larger angular range example of a successful BFCO synthesis can be found in **Figure 3.1 (a).**

Figure 3.3 is a comparative plot of XRPD patterns demonstrating the effect of sintering temperature on the synthesis. Below 860 °C it can be seen that there is a prevalence of unreacted materials (e.g. Bi_2O_3 at ~ 27.2° 2θ and oxides of Fe and Cr at ~ 33.5° 2θ (**Figure 3.3 (a)**), as phase-matched with software[291]). This likely reflects the higher melting point of Cr_2O_3 in comparison to Fe_2O_3. Above the optimal 860 °C, the growth of parasitic

phases/decomposition of the perovskite product into bismuth rich phases begins to appear (Bi metal, cubic Bi_2O_3 type ('Bi-rich oxide') at ~ 27.0 – 27.8° 2θ, **Figure 3.3 (b)**).

The peaks labelled 'Bi-rich' oxide detected at lower temperatures match well to the tetragonal phase $Bi_{14}CrO_{24}$[326] indicating a valence change of a small population of the chromium. However, the weak peak seen in the 860 °C sample is not necessarily attributable to the same phase, as this location is coincident with peaks from other bismuth rich oxides, such as the $Bi_{25}FeO_{39}$ phase commonly seen in BFO syntheses[56], and Bi_2O_3 based sillenites with other transition metal dopants[327].

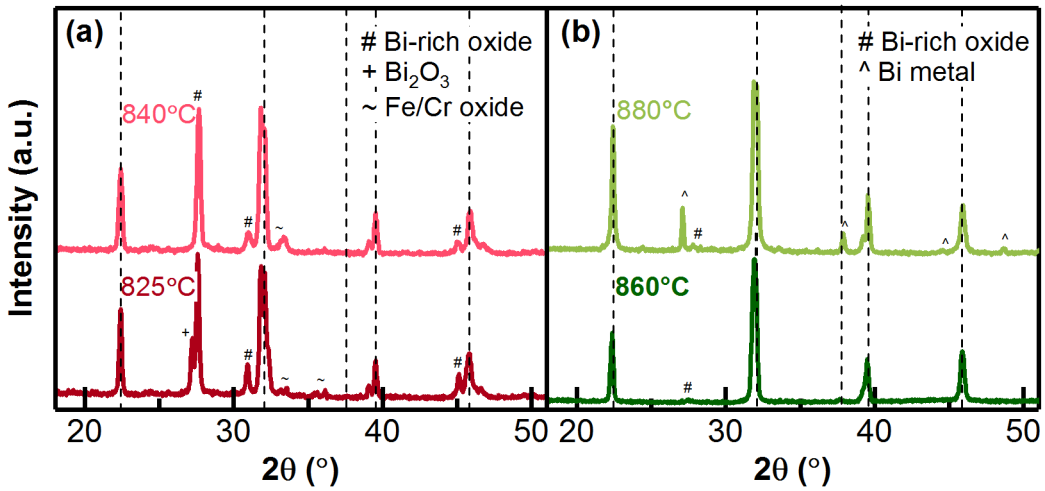

Figure 3.3. *In **(a)**, a low sintering temperature comparison is presented showing unreacted oxides and in **(b)** a higher sintering temperature comparison is presented, showing 860 °C to be optimal with no improvement at high temperatures. The expected peak locations for a rhombohedral BFCO phase are indicated with dashed lines.*

In an attempt to further improve not only the phase purity of the samples, but the sample quality, the preparation of the reaction powders was explored. Hand milling, ball milling and a preparation of a precursor powder by the metal organic decomposition (MOD) method were compared among other variables outlined in **Table 3.2**. Of the oxide methods, it was found that ball-milling produced the best samples (**Figure 3.4 (a)**), likely owing to the better distribution of reactant oxides. In that vein, it was though that the preparation of a precursor powder from Bi, Fe and Cr nitrates in ethylene glycol might be more fruitful. However, after the calcination of the mixture it was already evident that the low pressure parasitic phases had developed. Irrespective of the vessel used after this point, no perovskite phase could be formed (**Figure 3.4 (b)**) mimicking the results of the quartz crucible vs. alumina crucible tests in **Figure 3.1**. It is therefore very important for some pressure to be present during all application of heat to this system.

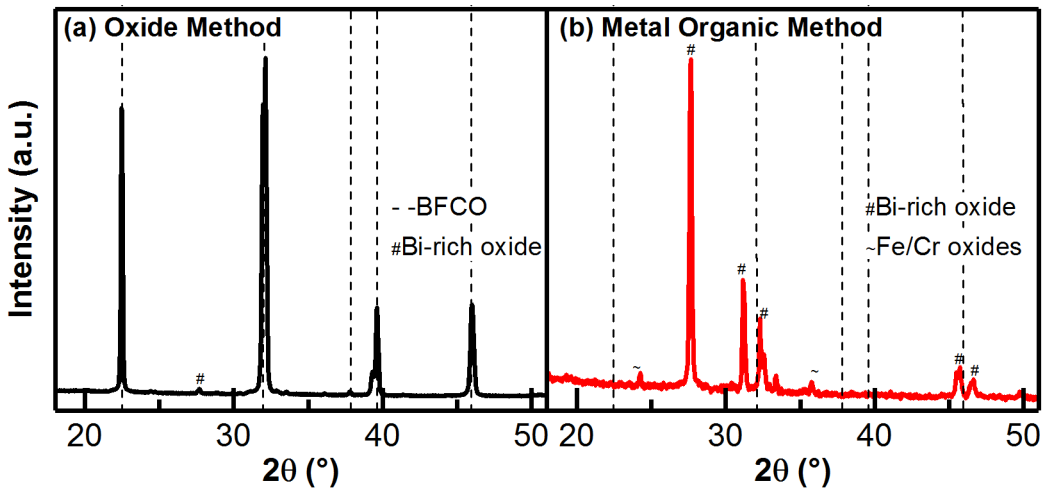

Figure 3.4. *In* ***(a)****, a typical XRPD pattern of a sample produced from a ball milled oxide mixture at 860 °C for 1 hour in a quartz crucible followed by a quenching to air is shown and* ***(b)*** *shows an XRPD pattern of a sample sintered by the sample procedure, but made from an MOD precursor first calcined at 600 °C at ambient pressure. The ambient pressure calcining appears to have caused impurity formation that cannot be eradicated during the quartz sintering step.*

Table 3.2. *Variables tested during synthetic optimization of BFCO and the optimum conditions.*

Conditions	*Variations tested*
Reactant mixture	Hand milled oxides, ball milled oxides (optimum), Bi-deficient hand milled oxide, and MOD prepared precursor.
Pre-sintering Steps	Pellets pressed to 5 tonnes (optimum), pellets pressed to >5 tonnes, pellets placed in alumina crucible, pellets placed in quartz crucible (optimum), and pellets placed in with additional powder in the vessel.
Main Sintering Temperature	825, 835, 840, 845, 850, 855, 860 (optimum), and 880 °C.
Main Sintering Time	30 mins (optimum), 1 hour (optimum), and 3 hours.
Post-Sintering Steps	Quench to cool (optimum) and natural cool.

Therefore, the optimal synthesis conditions for the production of bulk samples of BFCO with a dominant rhombohedral phase appears to be from ball milling of oxide reactants, and sintering the pressed pellets in quartz crucibles at 860 °C for approximately 60 minutes, then quenching the vessels to air. In addition to these conditions, best results are obtained from the use of fresh crucibles.

This is the first time in the literature that a major rhombohedral BFCO phase has been synthesized at near ambient pressure. These samples have a deep purple/black colouration and a grain size of ~ 2 μm. Purity levels of ~ 86% (~ 9 wt. % Bi metal and ~ 5 wt. % Cr_2O_3) as refined from neutron diffraction patterns (more in the next section) are easily attainable and

sufficient for further structural analysis and a bulk properties assessment. So far in this section, XRPD has been used for purity monitoring but the next section deals with in-depth structural analysis.

3.2 Structural Analysis and Simulation

Having achieved the production of a predominant rhombohedral phase using a near ambient method, attention could be turned to elucidating the nature of this rhombohedral phase and, importantly, if there could be any exhibition of chemical ordering in the product. A double perovskite structure with the typical formula $A_2B'B''O_6$ was predicted for BFCO by computational means by Spaldin et al[43, 58]. This structure would have the space group *R*3 and be characterised by alternating planes of Fe and Cr *B*-site octahedra along the $[111]_p$ pseudo-cubic direction (along ***c*** in the hexagonal setting of *R*3*c*) as shown in **Figure 3.5 (a)**. For the remainder of this thesis, this structure will be referred to this as the chemically ordered 'O-phase' of BFCO. However, there is also the possibility that the Fe and Cr ions do not order when they form the perovskite arrangement. In this case, the *B*-site is randomly occupied and they become equivalent in the average structure. This means now that (111) planes of ions are symmetrically related by a ***c***-glide operation due the site equivalency. The space group for the disordered variant necessarily becomes *R*3*c*. This structure is also comparatively shown in **Figure 3.5 (b)** and throughout this thesis will be referred to as 'D-phase' BFCO. The determination of which kind of ordering these synthesized samples exhibit is key to understand their properties.

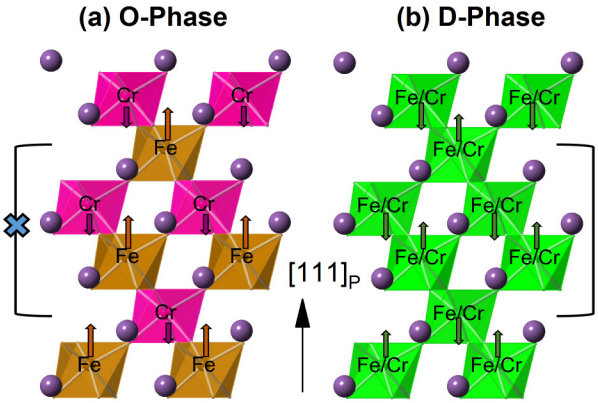

Figure 3.5. *In* ***(a),*** *an O-phase BFCO hexagonal unit cell is shown, illustrating the* **c***-glide breaking chemical ordering in the 'B'-site along the* $[111]_P$ *pseudo-cubic direction and* ***(b)*** *shows the D-phase BFCO structure with random chemical occupation that results in the exhibition of the* **c***-glide symmetry operation. Figure adapted from ref. [328] with permission.*

The principal way to distinguish between these two phases would be to observe the presence of diffraction peaks related to the ***c***-glide operation. In the rhombohedral setting these are reflections of the type $\langle hhl \rangle_R^*$ (equivalent to $\langle ½½½ \rangle_P^*$ commonly quoted in thin film investigations) which are present in O-phase BFCO, but absent in D-phase BFCO. While an apparently straightforward distinguishing feature, there are many hindrances to their observation in most diffraction-based techniques.

3.2.1 X-ray Diffraction Analysis

In X-ray diffraction, the scattering factors for Fe and Cr are very similar and much lower than the Bi scattering factor. Since the reflections of interest are primarily contributed to by intensity from the *B*-site ions, they are going to be very weak. In addition, the Cu X-ray source used in most lab-based X-ray powder diffractometers will promote fluorescence of the Fe and the increased background scattering levels may obscure the weak peak of interest. **Figure 3.6** shows an XRPD pattern of a typical BFCO sample. The peaks of interest in powder diffraction will overlap at a location of ~ 19.4° 2θ for typical Cu Kα radiation. The inset of **Figure 3.6** shows this region of interest plotted on a log scale to accentuate any peak that would exist. There is no obvious indication of a peak here. This gives the impression of having synthesized D-phase BFCO, however, as previously stated there are practical problems with the X-ray technique which do not allow a definitive assessment.

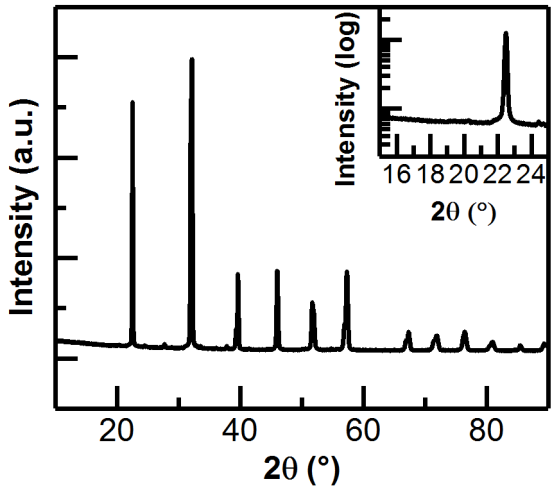

Figure 3.6. *An XRPD pattern of a typical BFCO sample exhibiting a rhombohedral structure.* ***Inset:*** *absence of anticipated chemical ordering peak noted at ~19.4°. Figure adapted from ref. [328] with permission.*

3.2.2 Electron Diffraction Analysis

Foreseeably, another method that could be used to observe the presence or absence of ordering would be a single crystal diffraction technique. Given the small grain size from the

synthetic method that was introduced in the previous subsection, the single crystal technique that can best deal with this is electron diffraction. Collecting electron diffraction patterns (EDPs) could be done using an electron microscope. However, yet again there are experimental challenges associated with data collection. Firstly, finding a grain in the sample with the appropriate orientation to collect a pattern from a zone axes that shows the relevant peaks of interest is statistically difficult. Secondly, due to the structural closeness of this sample to the cubic perovskite structure, the lattice parameters are incredibly similar. In this system, there are six symmetry related $<1\text{-}10>_R$ zone axes and only the three $<1\text{-}10>_R \equiv <\text{-}110>_P$ set of axes will show the reflection of interest, whereas the three $<001>_R \equiv <110>_P$ axes will not. Subscript 'R' indications the rhombohedral crystallographic setting, and 'P' is the primitive setting. **Figure 3.7** shows a typical EDP collected from the BFCO sample which can be indexed to either the $[1\text{-}10]_R$ (green) or $[001]_R$ (red) axes. The presence of reflections along the dotted lines would mean that if the green axis is the correct choice, the sample is potentially O-phase, and if red is the right choice, it could be a either O or D-phase. Additionally, if there is twinning in the sample, due to the strong interaction of electrons with the sample, it may also be possible to see reflections in these places. For these reasons, it cannot be concluded if there is or is not ordering in the sample based on the electron diffraction method either.

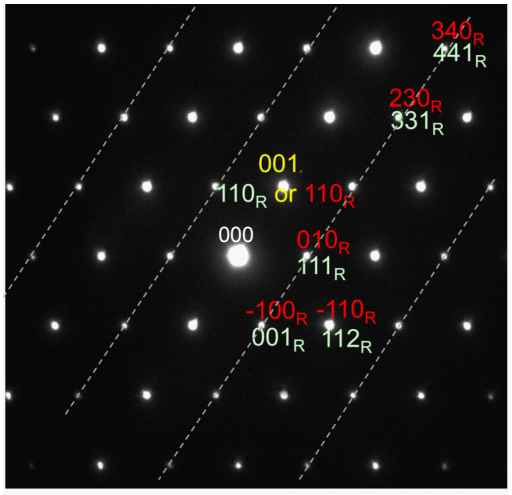

Figure 3.7. *An EDP obtained from a crystallite of BFCO. The zone axis can be assigned within error to both* $[1\text{-}10]_R$ *(leading to red indexation) or* $[001]_R$ *(light green). If the red indexation is true, then the presence of reflections on the dashed lines (*$<hhl>_R$** type) would suggest an* R3 *structure. If the light green indexation is true, some reflections along these lines are permitted for* R3c*. It is uncertain which the correct choice is, or if twinning in the sample is present. Figure adapted from ref. [*[328]*] with permission.*

3.2.3 Neutron Diffraction Analysis

3.2.3.1 Room Temperature Studies

A third diffraction technique that has a good chance of being able to observe the presence or absence of the reflections associated with chemical ordering, is neutron powder diffraction. The scattering lengths for Bi, Fe, Cr and O are now dissimilar enough that weak features associated with the ordering of the *B*-site can be distinguished without domination from the Bi signal or the background. Neutrons can interact with magnetic spins giving rise to magnetic scattering from electrons in addition to nuclear scattering. This method requires a large amount of sample which has not yet been achieved in other literature reports, but due to the new synthesis method detailed above, the nature of the chemical ordering and magnetic ordering (if any) in bulk BFCO samples can be determined.

Figure 3.8 shows a preliminary dataset collected at room temperature using the Echidna diffractometer at the Australian Centre for Neutron Scattering, showing several important features. Firstly, with the change in scattering factors an enhanced signal can now be seen from the impurity phases which were not immediately obvious in the XRPD data, and they are now positively identified as Cr_2O_3 and Bi metal. This does mean that the main phase of BFCO in this sample more than likely deviated from the nominal stoichiometry and is in fact iron rich. Secondly, and most importantly, a peak can be seen at *d* = ~ 4.6 Å which is where a peak corresponding to chemical ordering would be expected (and cannot be matched to other additional phases). However, this is also the same location one would expect to see a peak from G-type antiferromagnetic ordering which is reported for in the majority of BFO related compounds and is also predicted in the initial computational studies[43, 58].

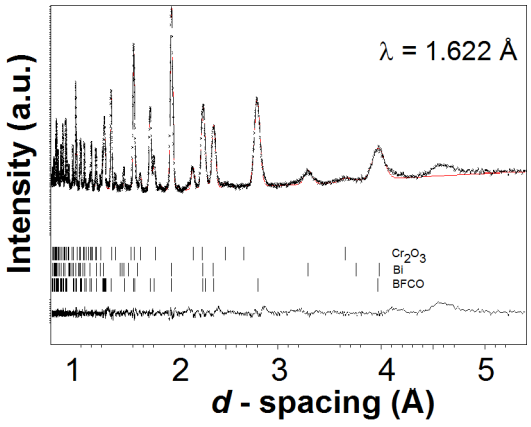

Figure 3.8. *A neutron powder diffraction pattern of BFCO collected with the 'Echidna' diffractometer. A basic profile fitting (no magnetism, via Jana2006) is shown in red, for phases BFCO (*R3c*, D-phase), Bi (*R-3m*) and Cr_2O_3 (*R-3c*). An extra peak is noted at d = ~ 4.6 Å.*

G-type magnetic ordering is described by $(111)_P$ planes of *B*-site ions which are ferromagnetically coupled within the plane (have spins pointing in the same directions) but antiferromagnetically coupled between planes (neighbouring planes along $[111]_p$ will have antiparallel spin alignment). A basic pictorial representation of this type of magnetic ordering for both the O-phase and D-phase variants is shown back in **Figure 3.5**. This means, scattering from the magnetic structure will also produce a diffraction peak of the type $<½\ ½\ ½>_P$* which describes the magnetic propagation vector. It is important to note that both the chemically ordered (O-phase) and chemically disordered (D-phase) unit cells can potentially exhibit antiferromagnetic coupling like this, but the net magnetization will have different values.

The existence of this extra peak in the neutron pattern gives three possible options here: (1) the structure is D-phase with antiferromagnetic ordering only, (2) the structure is O-phase with no magnetic ordering or (3) the structure is O-phase and also possesses antiferromagnetic ordering. This experiment was repeated by collecting further neutron diffraction data on the Polaris neutron spectrometer at the ISIS neutron and muon source in the UK. When the data were refined considering Model (1) the additional peak could be described as being contributed to be *B*-site ions with a moment of ~ 0.21 μB and an overall R_{wp} factor of 1.67%. This moment is below what that expect from the Hund's rule predictions, but is not outside the realm of possibility for a highly frustrated system. The refinement result using this model is shown in **Figure 3.9 (a)**. When applying Model (2) to the data, a fit with a comparable R factor, also 1.67% can be obtained (shown in **Figure 3.9 (b)**), which does not allow separation of these two options based on statistics. Refining both the chemical and magnetic ordering as is needed for Model (3) was not meaningful due to the resolution of the detector bank in this region, and attempts to try this resulted in an overestimation of the peak which does suggest that this model is unlikely. Given the comparable statistics for Model (1) and (2), a further experiment was required.

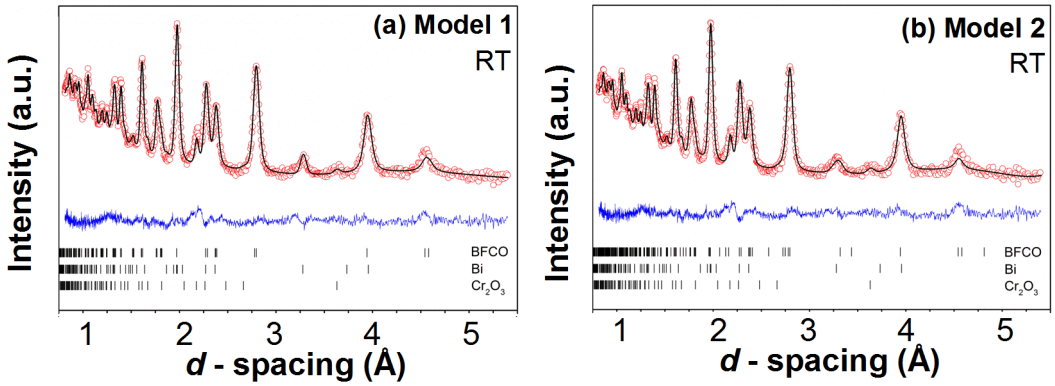

Figure 3.9. *In* ***(a)*** *a neutron powder diffraction pattern obtained from the Polaris instrument is shown (room temperature) refined in GSAS using Model 1 (chemically disordered, magnetically ordered) and* ***(b)*** *shows the same data refined with Model 2 (chemically ordered, no magnetism). The fit is in black, the raw data is red and the difference plot is blue. Figure adapted from ref. [328] with permission.*

3.2.3.2 High Temperature Study

Foreseeably if this low angle neutron diffraction peak is contributed to in any way by magnetic ordering, then heating the sample above its T_N, should remove that contribution. From magnetization experiments (to be presented later in **3.3.1.1**) it was suspected that the T_N temperature was around 400 K. Neutron diffraction data collected at 500 K presented in **Figure 3.10** show that the peak at *d* = ~ 4.6 Å has vanished, leaving no signal behind that could correspond to chemical ordering eliminating model (2) and (3) as options. This quite strongly suggests that the material has the D-phase structure and possesses antiferromagnetic order at room temperature.

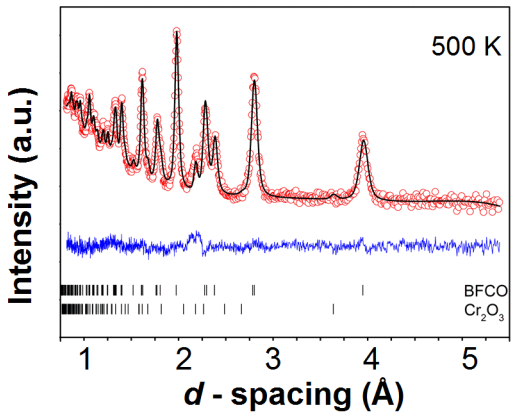

Figure 3.10. *Neutron powder diffraction data obtained from the Polaris instrument at 500 K, refined with chemical disorder and no magnetic ordering (having passed through T_N), R_{wp} = 1.74 %. An absence of underlying chemical ordering is indicated. Note: Bi peaks have disappeared, and having not recrystallized after the heating cycle. Figure adapted from ref. [328] with permission.*

3.2.4 Structural Simulations

3.2.4.1 Bond Valence Sum

To further validate the assignment of the D-phase structure to BFCO, semi-empirical and theoretical studies were undertaken. Beginning with validation of the crystal structure refinements, the resulting refined structures associated with **Figure 3.9 (a)** and **(b)** (presented earlier) were subjected to bond valence calculations and analysis using the Soft BV method[301, 303]. The results of the analysis are presented in **Table 3.3**, which demonstrate a lower overall GII for the disordered structure, and the bond valences of individual ions are consistent with their expected valences (Bi^{3+}, Fe^{3+}, Cr^{3+}, O^{2-}). As GII has been shown to scale with total energy calculated from DFT[302], it would appear the disordered structure is more plausible for this system than the ordered variant.

Table 3.3. *Results of bond valence sum calculations for the validation of BFCO refinements.*

	Bi (v.u.)	*Fe (v.u.)*	*Cr (v.u.)*	*O (v.u.)*	*GII (v.u.)*
D-phase	2.9087	2.9726	2.7180	1.9181	0.1346
O-phase	3.0197	2.9317	2.6818	1.8841	0.1445
	2.7834	3.0321	2.7709	1.9667	

3.2.4.2 Density Functional Theory

From a theoretical standpoint, difference in energy between a fully ordered and a partially disordered structure can also be calculated using DFT. In order to do this, two structural arrangements were evaluated for the relative energy difference and net magnetic moment (and alignment) per unit cell, using the GGA+PBE method[329], which was outlined in Chapter 2. The resulting calculated lattice parameters in comparison with the experimental study are shown in **Table 3.4**. Larger lattice parameters than the previous computational simulations are observed[43, 58], but are closer to the experimental values. It is acknowledged that the computational methods used in this work are different from this previous report, and deviation is not unexpected, though the energetic trend remains reliable.

The O-phase structure, relaxed from the experimental lattice constants in the hexagonal setting (therefore capturing 6 *B*-sites, shown in **Figure 3.11 (a)**), was found to have a stable G-type magnetic ordering with a net moment of 6 μB per unit cell. However, the DFT energy was 0.09 eV higher than a partially disordered structure, in which one 'anti-site' defect was introduced (shown in **Figure 3.11 (b)**). This partially chemically disordered structure, also exhibited G-type ordering but resulted in a reduction of the net moment to 2 μB per unit cell. This reduction in the net moment is the result of magnetic frustration. When iron and chromium are switched between their ordered planes, but conserve G-type ordering, one Fe-Cr pair is

seen to contribute 2.0 μB to the total moment per unit cell, but the next neighbouring Cr-Fe pair contributes -2.0 μB, thus cancelling and reducing the net moment. Just a single *B*-site defect is enough to reduce the moment by 1/3. This is an important observation to be verified in the following section. In addition, the individual moments of Fe and Cr are calculated at around 4 and 2 μB, below what might be expected for S = 5/2 and S = 3/2 ions based on a spin-only calculation. While this model is only exploring partial disorder owing to difficulties modelling such a result, it is believed to be a good indicator of a trend. Other researchers have performed Monte Carlo simulation on the analogous $BiFe_{0.5}Mn_{0.5}O_3$ system and found that tendency towards chemical disorder results in inhibition of ferrimagnetism and low net magnetization[330].

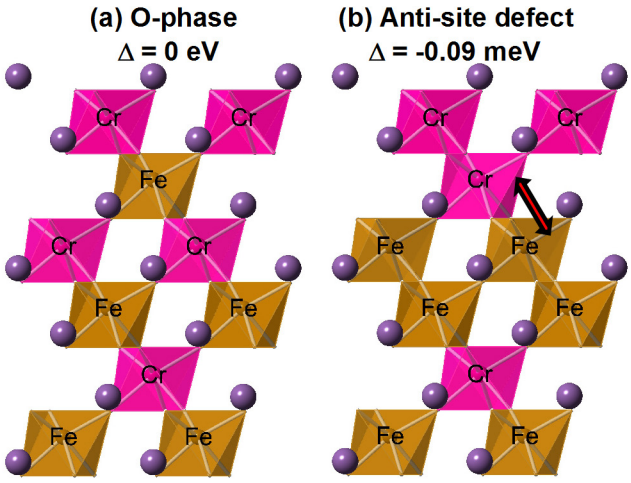

Figure 3.11. *In* ***(a)****, a hexagonal BFCO unit cell with full chemical ordering is shown and* ***(b)*** *shows a partially disordered BFCO cell with an anti-site defect. Figure adapted from ref. [328] with permission.*

The energetic results also reflect what was seen in the sample preparation, namely that the high entropy, disordered structure is more likely to be favoured under fast synthesis conditions. The only literature reports which claim to observe a high degree of chemical ordering do so by growing thin films[331-333], under very different conditions to the solid state method. These non-standard conditions may allow them to traverse a different energy landscape and achieve some ordering imposed by the sample geometry and controlled reactant delivery. It appears obtaining ordered solid state samples remains elusive.

Table 3.4. *Experimental and theoretical structural and magnetic parameters obtained for different* B*-site ordering configurations in BFCO. Table adapted from ref. [328] with permission.*

	Experiment	*DFT- Ordered*	*DFT - p-Disordered*
Relative Energy (eV)	--	0.0	- 0.09 eV
Cell Volume (Å^3)	367.62(3)	377.07	376.52
Lattice **a** (Å)	5.5574(2)	5.604	5.601
Lattice **c** (Å)	13.7444(5)	13.863	13.856
Emergent Symmetry	*R*3*c*	*R*3	*P*3
Net magnetic moment (μ_B) per unit cell	~0	6.00	2.00

Having experimental and theoretical evidence to support the presence of chemical disorder in this system, antiferromagnetic ordering is predicted below room temperature resulting in a near zero net sample magnetization. Magnetic experimental measurements were conducted to further verify this assertion and make an estimate about possible transition temperatures.

3.3 Physical Properties

3.3.1 Magnetic Properties

From the neutron experiments, the magnetic moment refined from individual *B*-site ions in the magnetic structure was 0.21 μB per *B*-site ion. Given this system contains the transition metals Fe^{3+} (S = 5/2, high spin) and Cr^{3+} (S = 3/2) with calculated moments of 4 and 2.5 μ_B respectively from the simulations, the refined moment is low. This may indicate appreciable magnetic frustration in this system. According to the Goodenough-Kanemori-Anderson rules for magnetic superexchange (see Chapter 1), the exchange interaction between pairs of Fe-O-Fe and Cr-O-Cr ions would be antiferromagnetic in nature, but Fe-O-Cr would be ferromagnetic. Given the *B*-site occupation has been determined to be random, all three types of interactions are possible and will be competing to result in frustration.

Despite the frustration, the average, long range magnetic structure appears to be antiferromagnetic. The bond angles measured from refinement are close to 155°, which likely allows Fe-O-Cr linkage to approximate more antiferromagnetic type interactions, explaining the observation of AFM magnetic peaks in the neutron data below 500 K. To further confirm this apparent antiferromagnetic behaviour, magnetization measurements can be made. Low magnetization from antiferromagnetic cancellation of spins, and complex temperature dependence due to competing exchange interactions might be expected in such measurements.

3.3.1.1 Magnetization

The results of field intensity dependent mass magnetization (***M***) measurements are presented in **Figure 3.12**, made on a powdered BFCO sample. At all temperatures a degree of hysteresis can be seen at low field. This is consistent with commonly reported spontaneous spin canting, which persists in many orthoferrites[334] and disordered doped BFO[335, 336]. There is also a non-linear response at all fields which does not saturate, typical of an antiferromagnetic system. Calculating the net moment from the magnetization at the highest field and 300 K, the result is 0.053 μB per formula unit. This is far lower than could be reasonably expected from O-phase BFCO, indicating again that this is a D-phase canted antiferromagnetic system.

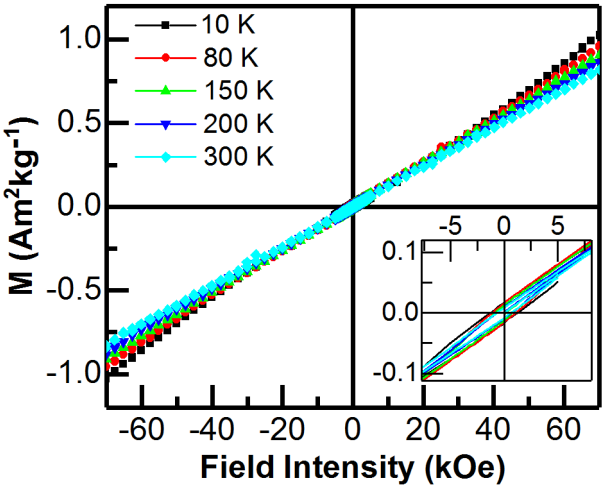

Figure 3.12. *Field dependent magnetization of BFCO at five different temperatures. A near linear, non-saturating response is observed with a small inner hysteresis (**inset**), suggesting antiferromagnetic ordering with a possible weak spin canting. Figure adapted from ref. [328] with permission.*

Figure 3.13 shows the temperature dependence of χ (***M/H***) for a powdered sample of BFCO under a field of 10 kOe. There is a notable difference in the FC and ZFC curves at low temperature which indicates there is a component of 'ferromagnetism' in this sample, contributing to a hysteretic effect, again likely attributable in part to spin canting. Though due to the fact that the BFCO is more than likely iron rich, this may also be related to an imbalance of ions not causing full cancellation of moments. The curves show quite a complex response at very low temperature and there is another notable broad feature at ~ 100 K. A number of related materials exhibit similar features which are attributed to spin reorientation transitions[337, 338] and in some cases spin state transitions[339].

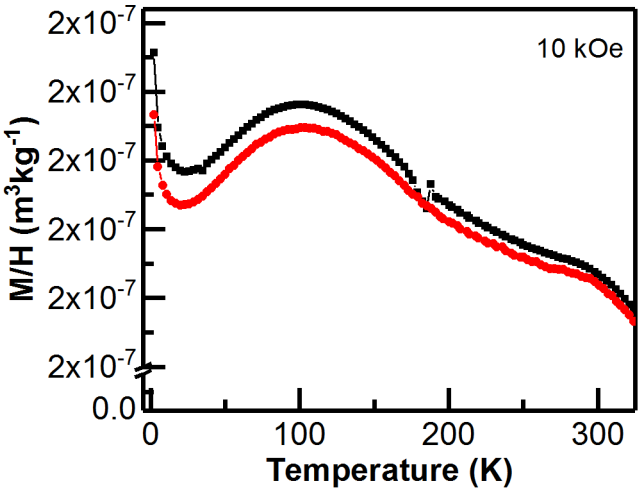

Figure 3.13. *Temperature dependence of χ for BFCO at 10 kOe, showing some ZFC/FC hysteresis at low temperatures, and convergence above room temperature indicating an approach to a critical transition. Low temperature features are complex. Figure adapted from ref. [328] with permission.*

At high temperatures the curves begin to converge indicating an approach to a transition temperature. **Figure 3.14** shows high temperature measurements made on the sample using an oven option. Due to the nature of the instrument, there is a limitation to the field applied but there does appears to be an inflection point near 400 K to indicate a transition of some kind. It should be acknowledged that the technique used to obtain this data is very sensitive to impurities and so is likely to be affected by the presence of the antiferromagnetic Cr_2O_3 impurity identified in the neutron experiment. This phase has a T_N of ~ 308 K meaning that inflexions above this temperature are likely attributable to the bulk BFCO material, but the magnitude may be affected by background from this phase. In order to make sure this study grasps the bulk behaviour of BFCO and not the impurities, the material was subjected to Muon Spin Resonance spectroscopy (μSR).

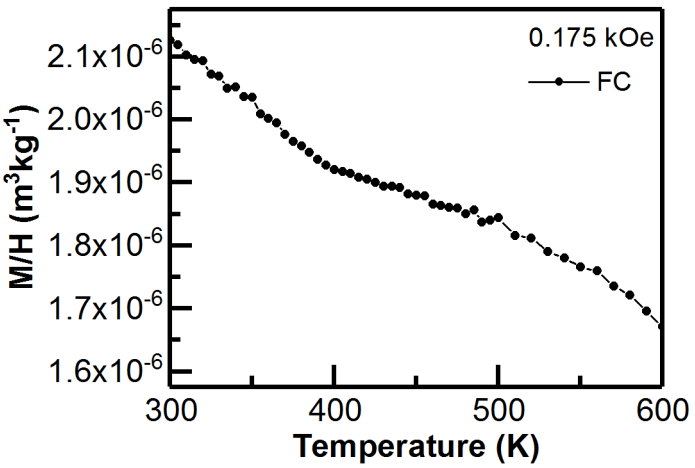

Figure 3.14. *Temperature dependent field-cooled magnetisation, measured in the high temperature range under a field of 175 Oe, showing an inflection near 400 K indicating transition behaviour. Figure adapted from ref. [328] with permission.*

3.3.1.2 Muon Spin Resonance Spectroscopy

The μSR technique can much better probe the behaviour of the majority component of the sample due to its low flux and local binding nature. Muons are spin polarised on implantation, become coupled to internal magnetic moments in the samples, de-phase and then decay over a period of nanoseconds. The speed and directionality of the decay is associated with the internal magnetic field in the sample. Therefore, by monitoring the asymmetry and relaxation rate of the muons passing through the sample with respect to temperature can give valuable information about the magnetic behaviour inside the main phase of the material.

Fitting the raw data with the following function can be done to obtain asymmetry and relaxation rate information:

$$G(t) = Ae^{-\lambda t} + A_0 \qquad \textbf{(3.1)}$$

where A is the asymmetry, A_0 is the baseline asymmetry (from instrumental setup, 11.7%) and λ is the relaxation rate.

In the raw asymmetry plot with respect to time (**(Figure 3.15 (a)**) a large 'missing fraction' is noted at low temperatures. Missing fractions occur when a strong internal magnetic field quickly dephases the muons outside of the measurable time scale. Further investigating this though fitting, very low asymmetry can be seen up until near 300 K where is starts to climb and is recovered after 375 K (**Figure 3.15 (b)**). This implies that the internal magnetic field is lost somewhere in this range, consistent with what was seen in the magnetization measurements. Additionally, the relaxation shows a peak at low temperature near 200 K **(Figure 3.15 (b)**) which indicates a fluctuating magnetic process within the sample that has a

comparable time scale to the muon probe. This may correspond to the 100 K feature in the magnetization, but is frequency dependent and shows a shift to high temperatures in response to the fast muon probe. In addition, the relaxing asymmetry at 100 K was observed to be almost 1/3 of that at 400 K. Given that a powdered sample will have a 1/3 + 1/3 + 1/3 directional average in the magnetization, this observation suggests an ordered magnetic phase in the sample below room temperature.

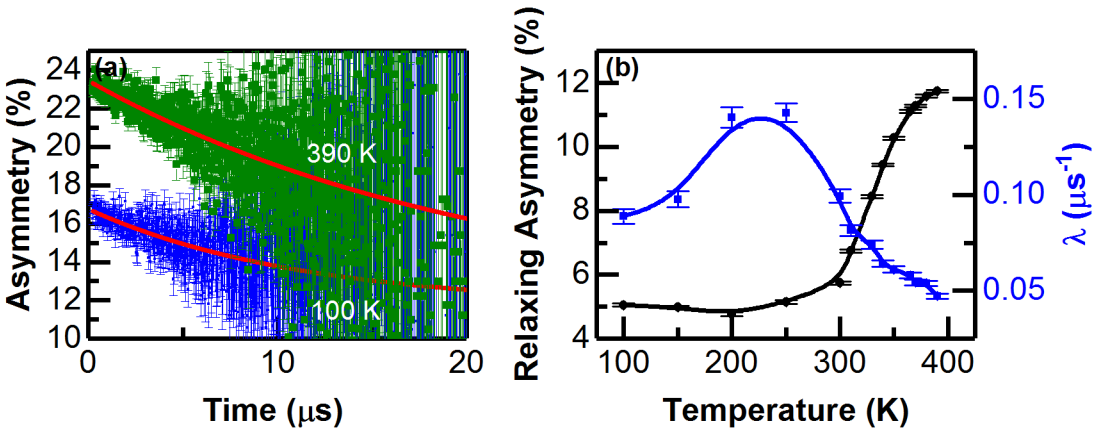

Figure 3.15. *In* ***(a)****, raw data showing an asymmetry difference between low and high temperatures is presented, and* ***(b)*** *shows fitted data with clear recovery of a missing fraction above room temperature (and an implied loss of magnetic ordering). A peak in relaxation rate at low temperature suggests a possible frequency dependent dynamic process. Figure adapted from ref. [328] with permission.*

Importantly, these measurements are consistent with the bulk phase being magnetically ordered at room temperature which is compatible with the earlier proposed antiferromagnetically ordered, chemically disordered model. The combined suite of magnetic measurements and neutron diffraction analyses support the assignment of D-phase BFCO with a T_N ~ 400 K when produced in the bulk. Whether or not multiferroism and photoresponsiveness was retained in bulk BFCO was also unclear from the literature, and so further characterisations were conducted and are presented in the following section.

3.3.2 Electrical Properties

It is of interest to see what other properties this chemically disordered system can exhibit at room temperature. Ferroelectric properties for example are of particular interest for exhibition of the bulk photovoltaic effect and multiferroism. In order to determine if a ferroelectric response might be fundamentally present, Piezoresponse Force Microscopy (PFM) was used. This was more informative than bulk ferroelectric measurements which were impacted by insufficient sample density. Looking at individual grains within BFCO (**Figure 3.16**), the presence of what appear to be 180° domains in the amplitude and phase images are detected

(**Figure 3.16 (b)** and **(c)**), which are not artefacts of the morphology (**Figure 3.16 (a)**). Additionally, switching spectra can be collected from BFCO which show a hysteretic phase change (**Figure 3.17 (a)**) and a 'butterfly' strain response (**Figure 3.17 (b)**) induced by an applied voltage. In combination with the calculated piezoresponse (**Figure 3.17 (c)**), this is typical of a ferroelectric material. It would appear that disordered BFCO simultaneously exhibits antiferromagnetic and ferroelectric type ordering at room temperature, and is therefore classified as a multiferroic.

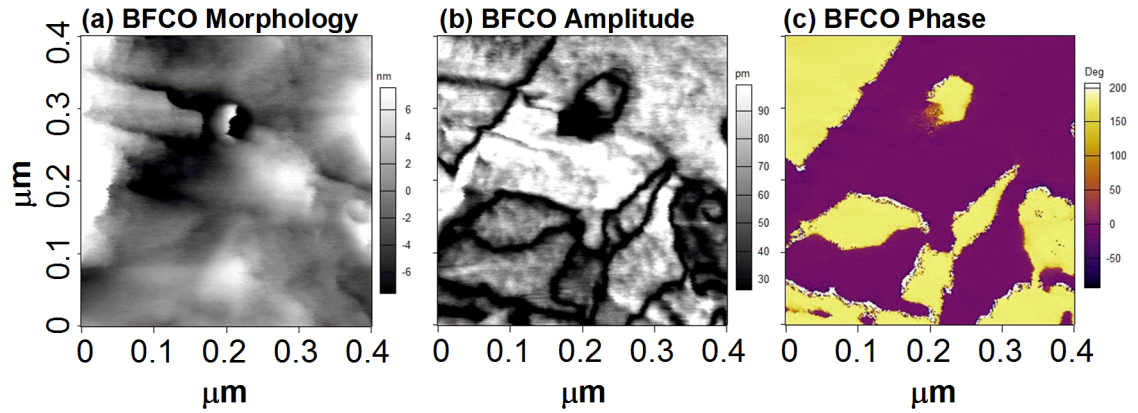

Figure 3.16. *Measurements made on polished BFCO samples using PFM. In* ***(a)****, morphology,* ***(b)*** *amplitude and* ***(c)*** *phase images are presented, obtained from same area. These show obvious domains unconnected with surface height variation. Figure adapted from ref. [*[328]*] with permission.*

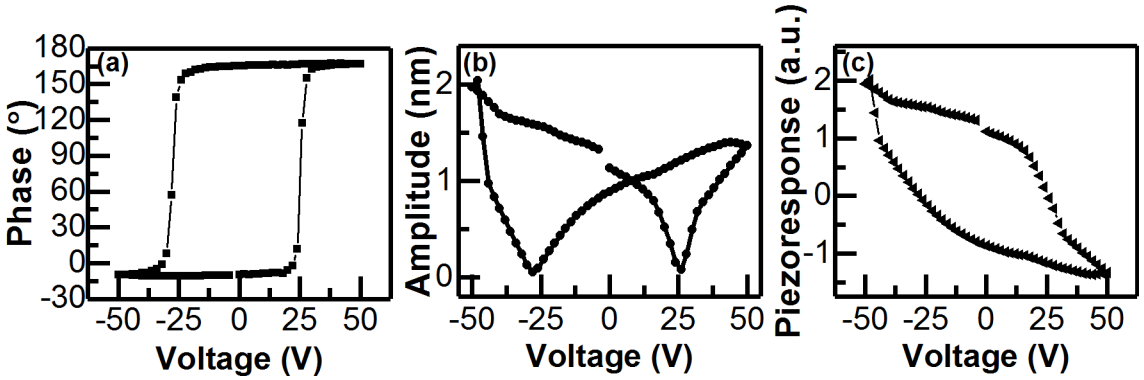

Figure 3.17. *Switching spectra obtained from BFCO using PFM. A phase change typical of a 180° ferroelectric domain is shown in* ***(a)****, a butterfly strain response can be seen in* ***(b)*** *and the calculated piezoresponse is presented in* ***(c)****, showing hysteresis. Figure adapted from ref. [*[328]*] with permission.*

3.3.3 Optical and Photofunctional Properties

An interesting observation made on thin film samples of BFCO in the literature was that they could exhibit the photovoltaic effect[59, 61], and with appreciable efficiency for such a thin layer

of oxide material. The functionality has been correlated with both the chemical ordering and presence of ferroelectricity. In BFCO made in this study, appreciable visible light absorption is observed (**Figure 3.18 (a)**) despite the apparent chemical disorder. By measuring diffuse reflection via UV-Vis-Spectrophotometry, the Kubelka-Munk function could be applied to the data, then produce a Tauc plot to estimate the band-gap of the material (**Figure 3.18 (b)**). While the fit is rough, two possible, separate transitions occur at ~1.5 eV, which is extremely promising for photofunctional applications.

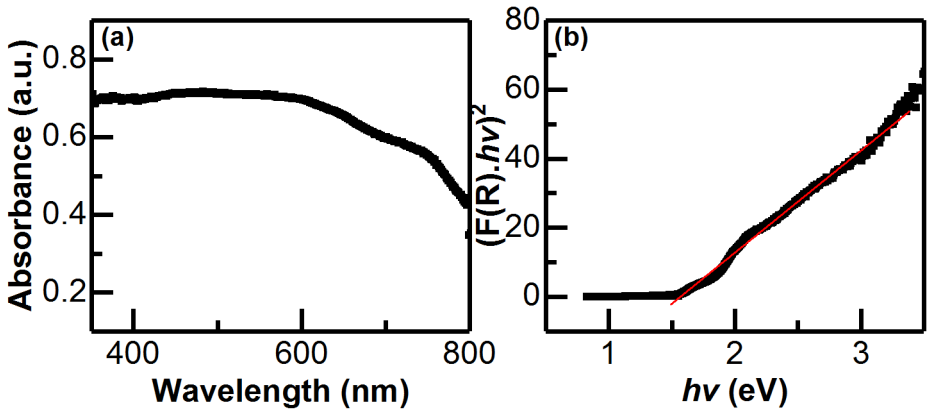

Figure 3.18. *In* ***(a)*** *the UV-Vis absorption of powdered BFCO is shown, suggesting broad visible light absorption and* ***(b)*** *shows a direct band gap Tauc plot which indicates possible photoexcited transitions in the range 1.5 – 2 eV.*

It was also possible to make further measurements which gave positive indications of a photofunctional response. Using Kelvin Probe Force Microscopy (KPFM), the surface potential change in the sample when exposed to a laser light source of 458 nm was mapped. There is a significant change in the surface potential on light exposure, indicating a net flow of photoexcited charges in the sample (**Figure 3.19**).

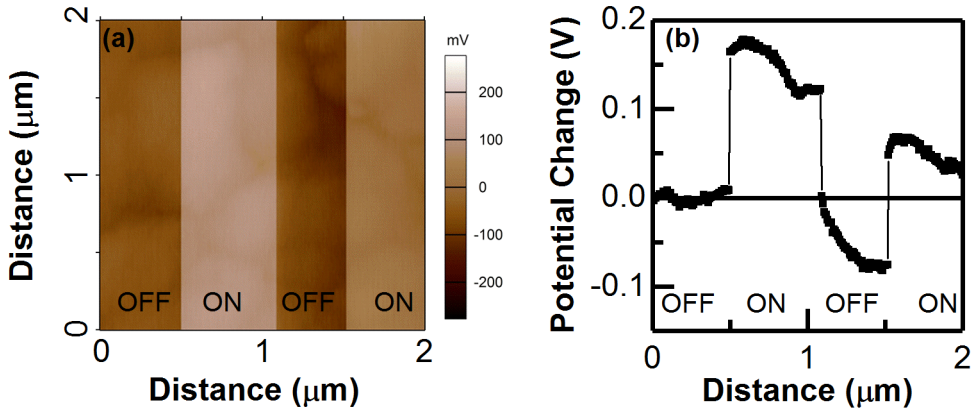

Figure 3.19. *In* ***(a)****, the surface potential variation map scanned across a 2 μm grid with 458 nm laser switched on and off is shown. The resulting plot of surface potential variation during light condition switching is shown in* ***(b)****.*

These samples were also coated with small 0.3 mm^2 ITO (indium tin oxide) electrodes with a 0.5 mm spacing on the surface and subjected to a +/- 10 V DC field. Current vs. voltage curves were obtained in darkness, and on exposure to a 100 W Mercury lamp across the surface electrodes. Clear non-linear behaviour is observed in darkness, though the behaviour becomes more linear on exposure to light (**Figure 3.20**). This is not unexpected based on the low-density polycrystalline nature, though the magnitude of current increase on light exposure is quite promising if the samples can be further optimized.

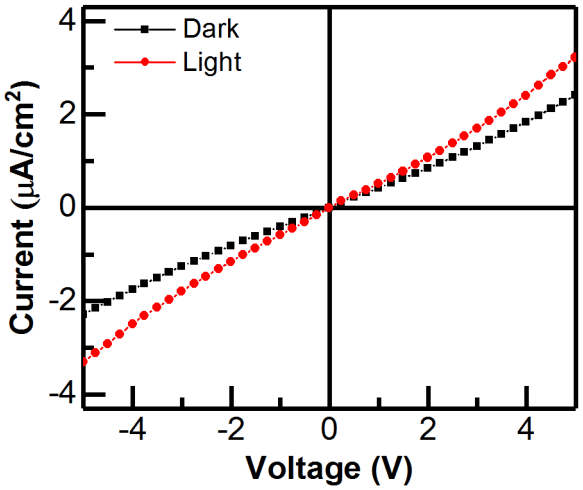

Figure 3.20. *Voltage dependent current between ITO surface electrodes on BFCO sample in the dark (black) and on exposure to mercury lamp (red) demonstrating non-linear curves and an obvious photoresponse.*

3.4 Summary of Chapter 3

By utilizing a carefully developed near-ambient pressure, solid state method, large amounts of BFCO were produced to an appreciable purity at low cost. This is the first time a synthesis of rhombohedral BFCO has been successful at such low pressure and resulted in the exhibition of a suite of magnetic, electrical and optical properties.

The structure was shown to correspond to a rhombohedrally distorted perovskite phase with random chemical ordering of Fe and Cr in the *B*-site demonstrated by neutron diffraction. This resulted in G-type antiferromagnetism up until above room temperature, confirmed with muon characterisation techniques. It was suggested that formation of a chemically ordered structure might be energetically disfavoured under these synthesis conditions.

Despite the disordered nature, the samples exhibited ferroelectric type properties observed with PFM, strong visible light absorption with a band gap of ~ 1.5 eV, and production of a

photocurrent. This means BFCO is not only photofunctional, but also multiferroic in this bulk newly synthesized form.

By addressing the gaps in the literature, it has been shown that the combination of elements and structure type in this material leads to a multifunctional material. Factors such as the synthesis method and structure control are identified as key factors though would affect its implementation. The exploration of how functionality is established in perovskite structured materials is continued in the next chapter.

Chapter 4 Ti^{4+} and M^{2+}-modified Bismuth Ferrite Perovskite-type Materials

In the previous chapter, one specific chemical modification of the host BFO structure was explored. There are however many foreseeable elemental combinations this structure could accommodate. By interchanging the elements in the perovskite *B*-site an extensive and tuneable suite of properties could be obtained in the bulk state. This chapter targets other combinations of elements with the ability to fit into BFO, to rationally design compounds with apparent photofunctionality and improved ancillary properties.

Specifically, this chapter deals with titanium containing chemical modifications, inspired by suggestions in the literature that introducing Ti^{4+} may stabilize the electrical properties and retain photofunctionality, as addressed in the introduction. This is done by partnering Ti^{4+} with a suitable M^{2+} species (Fe^{2+}, Zn^{2+}, Cu^{2+}, Mg^{2+} or Ni^{2+}) to balance the introduced charge and simultaneously target the magnetic and photofunctional properties. It is also hoped that such modifications will permit truly ambient pressure syntheses, further improving on Chapter 3. There is however little known in the literature about these combinations.

The main literature questions include which of the specific chemical modifications will lead to a perovskite phase (Mg^{2+}/Ti^{4+} and Ni^{2+}/Ti^{4+} are the only known ones so far), and of the possible combinations, how their ferroelectric, magnetic and photofunctional properties are changed in relation to their composition. Insights from Chapter 3 can be used to answer these questions, and build together a picture of functionality development in perovskite systems.

Synthesis options for various combinations of BFO *B*-site modification are explored in this chapter. The syntheses of viable materials are then refined, and their novel local chemical, structural and physical features are investigated through techniques such as Mössbauer spectroscopy, X-ray diffraction, magnetometry and piezoresponse force microscopy.

4.1 Synthesis

As outlined in the introduction, the target materials for synthesis in this chapter include:

- $BiFe^{3+}_{0.25}Fe^{2+}_{0.375}Ti_{0.375}O_3$ (BF*F*TO)
- $BiFe_{0.25}Zn_{0.375}Ti_{0.375}O_3$ (BFZnTO)
- $BiFe_{0.25}Cu_{0.375}Ti_{0.375}O_3$ (BFCuTO)
- $BiFe_{0.25}Mg_{0.375}Ti_{0.375}O_3$ (BFMTO)
- $BiFe_{0.25}Ni_{0.375}Ti_{0.375}O_3$ (BFNTO)

The following subsections outline synthetic pursuits to each target material.

4.1.1 Ti^{4+} and Fe^{2+}, Zn^{2+} or Cu^{2+} Incorporation

The first combination of elements tested was Ti^{4+} and Fe^{2+}. There was some suggestion that the perovskite $BiFe^{2+}_{0.5}Ti_{0.5}O_3$ might exist and exhibit multiferroism in a theoretical study[90]. This had not been experimentally verified in the literature, nor had other levels of titanium incorporation beyond 30 at. % of the total *B*-site cations. It was found in this study, that the BF*F*TO composition of interest did not form a single phase product. This sample was created from a mix of FeO and Fe_2O_3 sources and synthesized under ambient conditions and formed a mixture of Aurivillius phases and $Bi_2Fe_4O_9$ (as matched via phase matching software[291], **Figure 4.1 (a)**). It would appear the iron valence state is not stable under these synthesis conditions, and so was not further pursued in the context of this chapter.

The theoretically more stable divalent ions Zn^{2+} and Cu^{2+} were also tested for their ability to balance Ti^{4+} and be incorporated in a perovskite structure. However, BFZnTO and BFCuTO are also not known phases in the literature. Based on the ability of Zn and Cu to form perovskite related phases with titanium such as $BiZn_{0.5}Ti_{0.5}O_3$[340-342] and $Bi_{2/3}Cu_3Ti_4O_{12}$[96], they were considered stronger candidates than Fe^{2+}. Unfortunately, in early trials significant sample melting was noted at temperatures > 850 °C, and even using lower synthesis temperatures, neither the Zn or Cu samples resulted in the desired product (**Figure 4.1 (b)** and **(c)**). Both are clearly multiphase, with BFZnTO resulting in a prevalent Bi-rich $Bi_{38}ZnO_{58}$-type phase, an Aurivillius phase and a zinc oxide phase, while BFCuTO sees a Bi_2CuO_4 and Aurivillius mix forming.

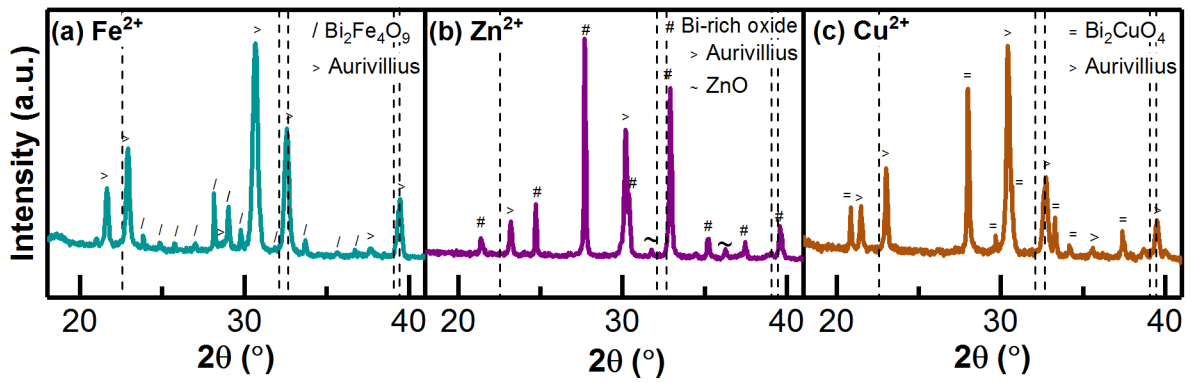

Figure 4.1. *XRPD comparison of the products of M^{2+} =* ***(a)*** *Fe^{2+},* ***(b****b Zn^{2+} and* ***(c)*** *Cu^{2+} trials to produce $BiFe_{0.25}M_{0.375}Ti_{0.375}O_3$. BFFTO was sintered at 900 °C for 90 minutes, and BFZnTO and BFCuTO at 750 °C for 90 minutes. Dotted lines indicate the main peaks for a $BiFeO_3$ rhombohedral phase, used as a reference.*

Looking at the phase relationships between the component oxides in the Cu and Zn systems, combinations of Bi_2O_3 and CuO lead to the phase Bi_2CuO_4[343] which forms readily and Bi_2O_3 and ZnO mixes can lead to $Bi_{38}ZnO_{58}$[344], which also readily forms. Importantly, these phases

form under ambient pressure conditions and at low temperature ($BiCu_2O_4$ liquidus at ~ 850 °C [343] and $Bi_{38}ZnO_{58}$ ~ 750 °C [344]), in competition with the target phase. These phases dominate the XRPD patterns and appear to be the biggest factor in not achieving a perovskite phase in the composition range investigated.

Within the scope of this study, BF*F*TO, BFCuTO and BFZnTO were not successfully synthesized. There may be other viable compositions, particularly for the Zn^{2+}/Ti^{4+} pairing[99, 100], and provides direction for future study. In this thesis however, focus was shifted to other potential M^{2+} species.

4.1.2 Ti^{4+} and Mg^{2+} Incorporation (BFMTO)

The transition metal ion Mg^{2+} has no d-electrons and is known to have a similar reactivity to Zn^{2+}, forming interesting and seldom reported compounds like semiconducting Bi_2MgO_4 with the trirutile structure[345, 346]. However, comparing the Bi_2O_3-Fe_2O_3-MgO-TiO_2 phase system to those containing ZnO or CuO, there is excellent solubility of Mg-Ti-Fe oxides[347, 348] and only the comparatively rare bismuth-based Bi_2MgO_4 phase. This likely explains why, unlike the previous combinations, the perovskite phase $BiFe_{0.25}Mg_{0.375}Ti_{0.375}O_3$ (BFMTO) is actually reported to form at ambient pressure in the literature[74, 88, 89, 102].

4.1.2.1 Solid State Synthesis Methods

The first attempts at using a solid state preparation and sintering method to produce BFMTO did produce some of the desired phase. It was clear though that phase formation was highly sensitive to sintering temperature and time, with very narrow windows for production before parasitic phases formed. This behaviour was monitored using XRPD. In this chapter, the angular range 27–40° 2θ was the most diagnostic for confirming the presence of additional phases in BFMTO samples and is presented in subsequent figures. A broader angular range XRPD that indicates successful synthesis can be found in **Figure 4.9 (a)**.

Figure 4.2 (a) illustrates the effect of temperature when sintering for 90 minutes, identifying 900 °C as the optimal temperature, and **Figure 4.2 (b)** shows how 12 hours is a good length of time to best improve perovskite to impurity ratios. These iterations were performed in alumina crucibles, meaning for BFMTO, ambient pressure is adequate to grow a perovskite phase. In these early iterations it was also found that high levels of additional phases were related to the choice of raw materials.

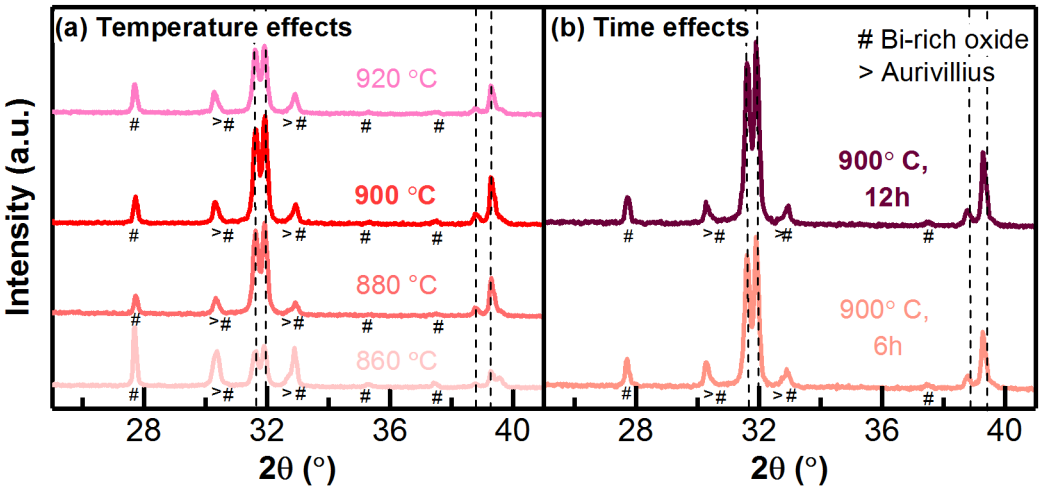

Figure 4.2. *In **(a)**, a comparison of sintering temperatures is shown, each with a 90 minute dwell, indicating 900 °C to be the most beneficial for perovskite formation and lower impurity levels. In **(b)**, a comparison of sintering times at 900 °C, shows some improvement for a longer sintering of 12 hours.*

4.1.2.2 Alternate Method Optimization

The production of BFMTO with MgO via the solid state method showed a number of impurities such as a cubic Bi-rich phase analogous in structure to $Bi_{25}FeO_{39}$ and the Aurivillius phase $Bi_5FeTi_3O_{15}$. The Bi-rich phase is reported to be a difficult to eradicate impurity in other syntheses[74, 88, 89]. Notably, quenching the samples after sintering did not improve the purity as was the case for BFCO in Chapter 3. In this study, the Aurivillius impurity was most often seen in more coarse mixtures using solid MgO or $MgCO_3$ sources (**Figure 4.3 (a)**) despite a broad range of tested synthesis conditions (**Table 4.1**). To circumvent this, methods to improve mixing were explored including the use of ethanol-soluble magnesium sources. Magnesium acetate mixed in with ethanol in the milling procedure did result in a proportional reduction the Aurivillius phase, but the Bi-rich oxide phase remained (**Figure 4.3 (b)**).

In order to also reduce the bismuth oxide phase, a new synthesis method was attempted. Nitrates of magnesium and iron and titanium butoxide were dissolved in ethylene glycol, then decomposed to form an oxide precursor (a 'metal organic decomposition method', MOD). The precursor was then sintered using the previously optimized time and temperature parameters. This resulted in just a small detectable amount of Aurivillius side phase via the XRPD method (**Figure 4.3 (b)**).

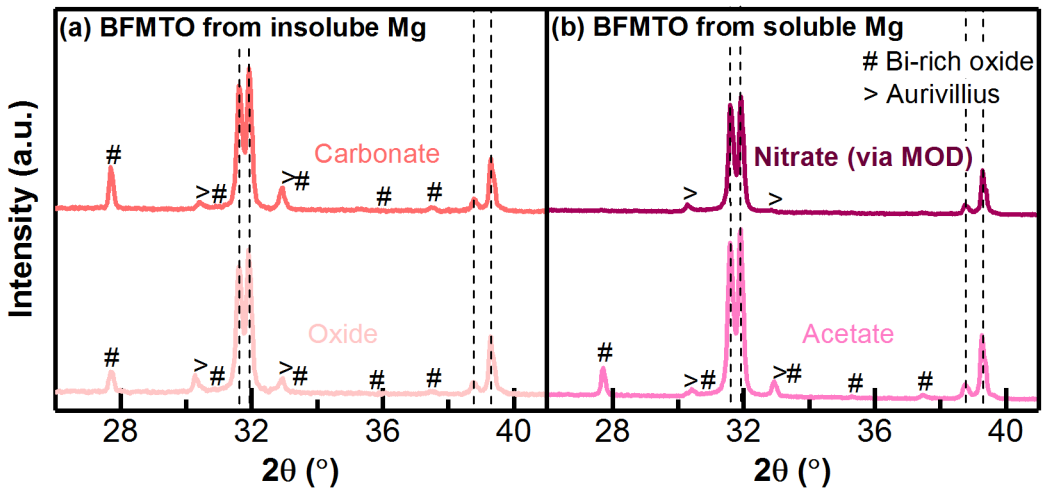

Figure 4.3. *In* ***(a)*** *a comparison of solid Mg sources used in solid state synthesis is shown. Both MgO and $MgCO_3$ variants (synthesized at 900 °C/12 hours, and 350 °C/4 h + 900 °C/12 h respectively) showed significant Aurivillius and cubic Bi-rich type impurities. In* ***(b)*** *the soluble acetate method (340 °C/4 h + 900 °C/12 h) is shown to decrease the cubic Bi-rich impurity, but metal organic decomposition (of nitrates in ethylene glycol, 600 °C/2 h + 900 °C/12 h) is better, also diminishing the Aurivillius impurities.*

Table 4.1. *Summary of investigated synthesis conditions for BFMTO. Optimum conditions are indicated.*

Conditions	*Variations tested*
Reactant mixture	Hand milled oxides, hand milled oxides with Bi-deficiency, hand mill oxides and magnesium acetate, hand mill oxides and magnesium carbonate, MOD prepared precursor (optimum).
Pre-sintering Steps	Calcine ≤ 400 °C/ 4 hours, calcine 600 °C/ 2 hours (opt.), sieving mixture to retain small particles, and pressing pellets at 5 tonnes (opt.).
Main Sintering Temperature	860, 880, 900 (opt.), and 920 °C.
Main Sintering Time	90 mins, 3 hours, 6 hours, and 12 hours (opt.).
Post-Sintering Steps	750 °C post annealing, grinding and re-sintering at main sintering temperature, quench cooling, and normal cooling (opt.).

Given that the phase purity appeared very high when produced via the MOD method, these samples were further investigated with microscopy. The morphology of the samples were porous, with smaller grains inside the pockets, likely a result of using an MOD precursor which may retain some volatile groups prior to sintering (**Figure 4.4 (a)**). As shown in the backscattered micrograph (**Figure 4.4 (b)**), grains of another phase can be see with a needle-like structure. This is typical of the phase $Bi_5FeTi_3O_{15}$ (see Chapter 5) and matches the XRPD peaks seen in **Figure 4.4 (b)** for this sample, though from the EDXS analysis it is found that it contains a proportion of magnesium (**Table 4.2**). This is an illustrative image and this phase

was found to be only minor impurity, with grains infrequently spotted. The main phase appears uniform in colour in the BSE micrograph (**Figure 4.4 (b)**) and the average composition of the main phase matches that expected for BFMTO albeit with a slight deficiency in Mg (**Table 4.2**). This is likely due to leaching into the alumina crucible which was sometimes observed during synthesis. The deficiency of *B*-site elements in general as analysed is most likely the consequence of an over representation of bismuth coming from the neighbouring side phase or influenced by the rough surface. However, the potential for *B*-site vacancies is to be considered in later analysis.

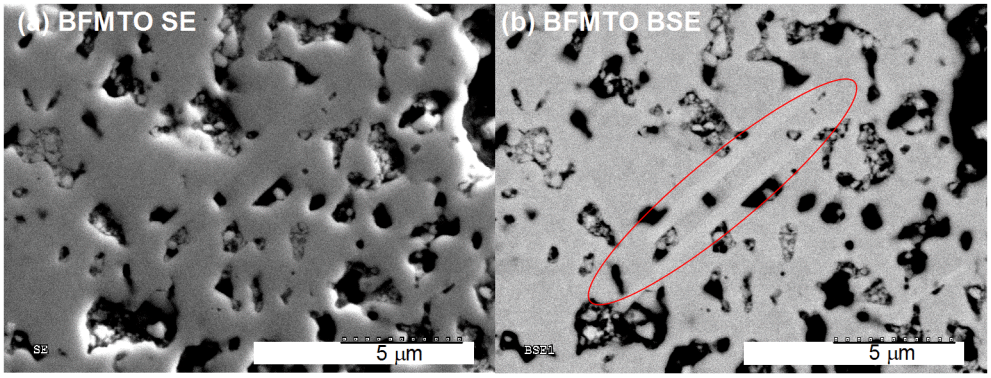

Figure 4.4. *In* ***(a)****, an SE micrograph of BFMTO shown. The morphology indicates larger regions of BFMTO and smaller grains in pores. In* ***(b)*** *a BSE micrograph indicates there is a needle-like impurity (red oval) in the sample, consistent with* $Bi_5FeTi_3O_{15}$*. No other impurities were observed.*

Table 4.2. *Elemental analysis of BFMTO using EDXS from micron-scale areas.*

*Area**	*Cation Fraction*				*Phase ID*
	Mg	*Ti*	*Fe*	*Bi*	
Grey	0.35	0.38	0.25	1**	BFMTO
Light Grey	0.41	2.93	0.65	4.85	Mg-doped $Bi_5FeTi_3O_{15}$

*Refering to colour scale in **Figure 4.4 (b).**
**Assuming ABO_3 formula with all *A* occupied by Bi

In summary, the optimized method for producing BFMTO involved producing a precursor from magnesium, iron and bismuth nitrate with titanium butoxide in ethylene glycol, decomposed at 600 °C for two hours. The resulting powder was ground and pressed into pellets for optimal sintering in alumina crucibles at 900 °C for 12 hours. Samples of BFMTO appear orange/pink in pellets and yellow in powder. This material forms a large part of the properties investigation in this chapter.

4.1.3 Ti^{4+} and Ni^{2+} Incorporation (BFNTO)

The final choice of M^{2+} investigated for incorporation was Ni^{2+}. Nickel can comfortably hold a 2+ valence state and has unpaired electrons, therefore potentially allowing a magnetically

ordered state as well as improved electrical properties. A stable perovskite phase of BFNTO is only known for the composition $BiFe_{0.25}Ni_{0.375}Ti_{0.375}O_3$[74]. It is interesting that this is the only clearly viable composition that results in a rhombohedral perovskite phase, as is also the case for BFMTO. Both the Bi_2O_3-Fe_2O_3-NiO-TiO_2 and Bi_2O_3-Fe_2O_3-MgO-TiO_2 systems contain many phases, and it is extraordinary that these elementally complex phases form at ambient pressure. In both systems though, there is a similar number of competing stable phases[345-354], and this specific composition is generally well balanced between each competing phase. This is different to the systems containing Zn and Cu mentioned earlier.

4.1.3.1 Solid State Method Optimization

The synthesis of BFNTO was initiated with the solid state method to confirm it could be made. Firstly, using a single step sintering of the raw pressed oxides in an alumina crucible at ambient pressure, it was found that the synthesis of this material was highly sensitive to sintering temperature and time, with a very narrow window within which phases could be formed and not result in the formation of alternate stable phases. This behaviour was monitored using XRPD. In this chapter, the angular range 28–40° 2θ was the most diagnostic for confirming the presence of additional phases in BFNTO samples and is presented in subsequent figures. A broader angular range XRPD that indicates successful synthesis can be found in **Figure 4.8 (a)**.

Figure 4.5 illustrates how a sintering of 960 °C for 12 hours was identified as the condition most conducive to a high proportion of perovskite BFNTO to impurities.

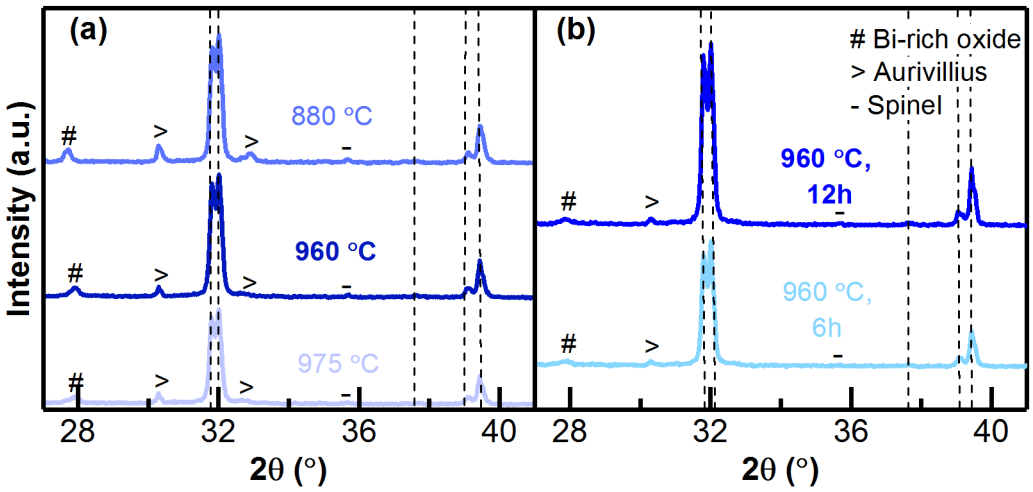

Figure 4.5. *In* ***(a)*** *conventional solid state oxide-based preparations of BFNTO at different temperatures are compared, showing good perovskite to impurity ratios at 960 °C (90 minutes sinterings) and in* ***(b)*** *sintering times are compared, showing a longer sintering of 12 hours helps conversion of additional phases to maximize BFNTO formation.*

Samples produced by this simple method were observed to crack after synthesis in the furnace. Efforts were made to control this effect by manipulating the processing procedure (adding PVA, adding extra re-grindings, slow cooling, using nickel acetate, changing the pressure of the press etc. **Table 4.3**), but the cracking problem remained. This may be arising from different thermal expansion of the phases present, or a phase transition of BFNTO on cooling. Thicker samples were generally used to minimize detrimental cracking. More important for the investigation was optimizing the purity of the BFNTO samples, and with the smallest amount of processing to improve on the available literature synthesis[74] .

Table 4.3. *Summary of synthetic conditions tested in optimization of BFNTO samples. Conditions used for optimum purity are indicated (also illustrated in* ***Figure 4.6*** *(below)).*

Conditions	*Variations tested*
Reactant mixture	Hand milled oxides, hand milled oxides and nickel acetate, ball milled oxides (optimum methods 1, 2 and 3), and MOD prepared precursor.
Pre-sintering Steps	Sieving mixture prior to pressing to retain small grains (opt. 1, 2 and 3), PVA binder added prior to pressing (opt. 2), pellets pressed at three tonnes pressure (opt. 1), pellets pressed at 5 tonnes pressure (opt. 2 and 3), pellets pressed thick (opt. 1, 2 and 3), pellets pre-calcined at ≤ 600 °C and pellets slowly heated to maximum sintering temperature (opt. 2).
Main Sintering Temperature	780, 800, 820, 850, 880, 900, 920, 960 (opt. 1, 2, 3), 975, and 1000 °C
Main Sintering Time	90 minutes, 2, 6, 12 (opt. 1, 2, 3), 24, and 72 hours.
Post-Sintering Steps	Quench cooling, natural cooling (opt. 1, 2, 3), and regrinding and re-sintering at main sintering temperature.

Throughout the optimization process, the purity was monitored by XRPD. The detected secondary phases were fitted to a spinel type structure (likely related to $NiFe_2O_4$), a tetragonal Bi-rich phase related to β-Bi_2O_3 (note: not the same Bi-rich oxide that appears sometimes in BFMTO) and the Aurivillius phase $Bi_5FeTi_3O_{15}$, as indicated in **Figure 4.5** above. Interestingly, methods involving multiple temperature steps or regrinding suggested in the literature to improve purity and quality[74] led to worse purity in this study. Using the MOD method that was successful for the BFMTO did not help reduce the additional phases. Quenching the samples after sintering also did not improve the purity. Instead it was found that best mixing was achieved when the raw materials were sieved (gauge ~ 300 μm) after initial mixing. Only the small, similarly sized particles were then pressed for reactions. This drastically reduced the Aurivillius phase leaving only small levels of the $NiFe_2O_4$ type phase, and Bi-rich oxide phase (**Figure 4.6**). Like BFMTO addressed above, and BFCO and BFO discussed in previous chapters, it was not possible to completely eradicate secondary phases from the final sample, and instead a manageable level was obtained via this sieving method.

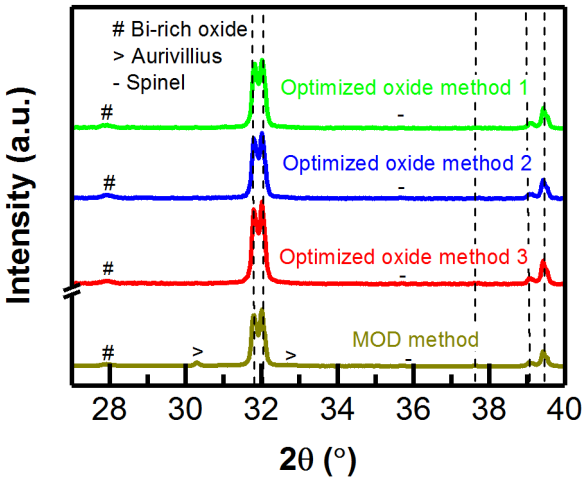

Figure 4.6. *XRPD patterns of samples sintered for 12 h at 960 °C with different processing. Small grain, oxide based raw materials followed with a single sintering step lead to the best results, showing similar purity despite changes to pressure, heating rate and binder addition as noted in* ***Table 4.3*** *above. For comparison, the MOD method sample is shown which clearly contains more impurities. Dashed lines represent peak positions for the desired BFNTO phase.*

The samples produced using the optimized solid state synthesis with sieving were further analysed with microscopy. SE and BSE micrographs of a high purity sample are shown in **Figure 4.7**, with corresponding elemental analysis in **Table 4.4**. There is a spinel type transition metal oxide phase that is apparent in the SEM by its distinctive shape and contrast in the BSE (dark region, circled in **Figure 4.7 (b)**). Solid solutions of transition metal spinels are known, and this appears to be a mixed element product from **Table 4.4**. Such 'islands' are sometimes seen in BFO syntheses with Bi-rich areas nearby due to a mismatch of diffusion in Bi and the transition metals[54] and impurity driven nucleation of parasite phases[55]. A Bi-rich phase shows up in light grey in **Figure 4.7 (b)** (also circled) and is interesting due to its high transition metal population as analysed by EDXS (**Table 4.4**), which is beyond that of $Bi_{25}FeO_{39}$ type sillenites most frequently reported in BFO type synthesis. However due it its small grain size, it may be influenced by the signal from the surrounding phases. Further evidence relating to this phase is presented in **Section 4.2.1** and while its presence is noted, time was not spent focussing on it in this thesis. The main grain phase is analysed by EDXS and the stoichiometry is close to expectation. There is a slight deficiency of iron detected in this sample, but is expected to be an artefact of the sample surface rather than an indication of vacancy in the *B*-site.

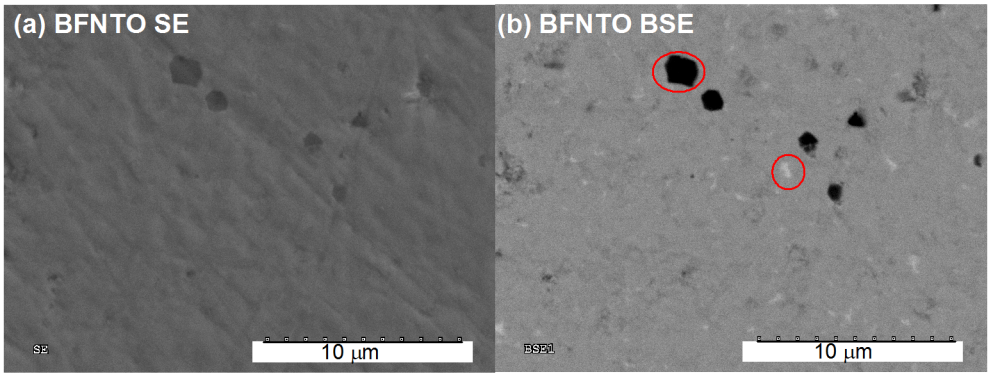

Figure 4.7. *In* ***(a)*** *an SE micrograph shows an area of BFNTO with obvious impurities. Depressions (not holes) are noted in the morphology. In* ***(b)*** *the BSE micrograph of the sample area shows the depressions to be another low molar weight phase, likely a transition metal spinel (circled). The pale white regions correspond to a Bi-rich phase (circled), and medium grey is the BFNTO bulk.*

Table 4.4. *Elemental analysis of BFNTO using EDXS, from micron-scale areas.*

*Area**	*Cation Fraction*				*Phase ID*
	Ti	*Fe*	*Ni*	*Bi*	
Grey	0.38	0.23	0.37	1**	BFNTO
White	0.23	0.12	0.16	1.45	Bi-rich oxide
Black	0.20	1.42	1.26	0.11	Spinel type oxide

* Refering to colour scale in **Figure 4.7 (b).**
**assuming ABO_3 formula with all *A* occupied by Bi

The optimized procedure used Bi_2O_3, NiO, Fe_2O_3 and TiO_2 in oxide form, milled in ethanol, then dried and sieved (gauge ~ 300 µm), with the smallest particles pressed at 5 tonnes for sintering at 960 °C for 12 hours. The small grain size of the raw material was important to reduce the production of the Aurivillius phase, perhaps by mediating a better distribution of nickel in the mixture and faster reaction rate from the small reactant particles. In pellet form, BFNTO samples appear dark grey, but when powdered, they are an orange colour.

4.1.4 Summary of Synthetic Achievements and Viable Materials

It is apparent that it is difficult to design a Ti^{4+}-M^{2+} pairing that gives rise to a perovskite structure under ambient conditions at the desired concentrations. Of the conditions tested, compounds containing Fe^{2+}, Cu^{2+} and Zn^{2+} could not be made and only the ambient pressure perovskites BFNTO and BFMTO formed. While both BFNTO and BFMTO have been reported before, the syntheses developed in this thesis have fewer steps for similar levels of purity.

For example, the MOD method designed for the synthesis of BFMTO cuts out the Bi-rich phase seen in other syntheses[74, 88, 89], and does so in just two high temperature steps (comparable to molten salt methods and better than solid state). In addition, this method produced very well

crystallized samples with big grains in comparison to the syntheses of BFNTO and BFCO from the previous chapter (as evidence by sharp diffraction peaks, and PFM images in **Section 4.3.2**). This technique is also key to the success of the subsequent Chapter 5. Samples of BFMTO made by this MOD method with ~ 97% purity (as estimated with XRPD) are analysed in subsequent sections.

The solid-state based BFNTO synthesis involving sieved raw materials led to manageable levels of impurities using only a single sintering in comparison with the multiple sinterings used in the previous report[74]. It is acknowledged though that in making the time/impurity trade-off for BFNTO, the apparent properties may be influenced. In particular, these samples contain a minor spinel phase, which is discussed in further detail in **Section 4.3.1.1**. Henceforth in this thesis, BFNTO samples measured and analysed are made by the optimized solid state procedure with purity ~ 96% (as determined by XRPD).

Therefore, two candidate photofunctional materials have been successfully synthesized in this Chapter. There is little known about either BFMTO or BFNTO, so the remainder of this chapter focuses on determining the chemical distribution of elements within their structures, and their arising physical properties for a novel evaluation of the origin of their multifunctionality.

4.2 Chemical and Structural Analysis of BFMTO and BFNTO

Both BFMTO and BFNTO are reported to have the same structure type as BFO, thus they in theory might also be multiferroic and photovoltaic. Time was spent trying to understand the nature of each compound's structure and elemental complexity to best explain the emergent functionality.

4.2.1 Average and Local Structure Analysis from Diffraction

X-ray powder diffraction patterns of both BFNTO and BFMTO samples were refined in order to match the synthesized phases to the reported structures. The fitted XRPD patterns and refined structures of BFNTO and BFMTO are presented in **Figure 4.8** and **4.9** respectively. Associated refinement details are also given in **Table 4.5** and **4.6** respectively, including bond valence (BV) sum calculations for each ion and the global instability index (GII). Approximate purity is refined using .cif files from the literature[74, 159, 355, 356] to model the extra phases.

Both compounds were found to refine reasonably well in the reported *R*3*c* space group which is also similar to BFO and BFCO in Chapter 3. The refinement of BFMTO did result in some deviations from the average structure model in the literature, indicating possible complexity of the local structure. This is further suggested in the bond valence validation of these

refinements. It is notable that the titanium ions in both structures are considerably underbonded (bond valence < 3.5). It has been mentioned by other others that from simulation, titanium is the most flexible in its bonding environment and its own off centre motion might be contributing to electrical responses in BFMTO[102]. The asymmetry of the bismuth site is also noted as a local structural effect. It appears the bismuth bond valence is better in BFNTO than BFMTO, mirroring previous refinements[74].

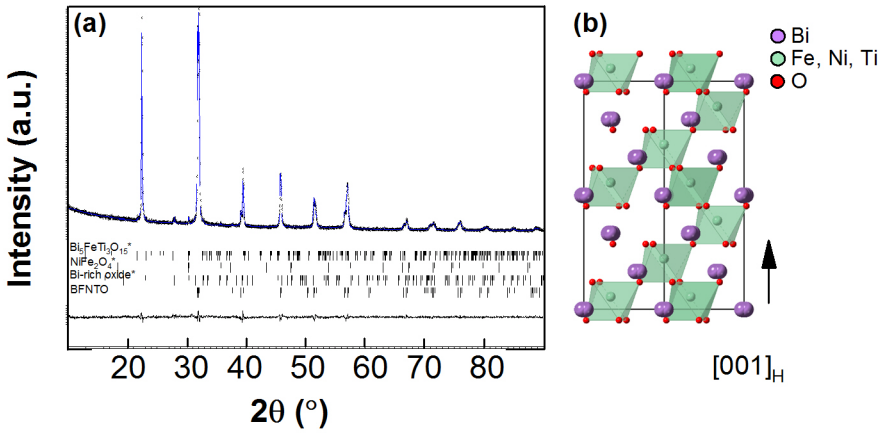

Figure 4.8. *In* ***(a)****, the Rietveld refinement of BFNTO using Jana2006 is shown (blue) including the extra phases* $Bi_5FeTi_3O_{15}$*,* $NiFe_2O_4$ *and* $Bi_{7.68}Ti_{0.32}O_{12.6}$ *('Bi-rich oxide'). *Chosen for best structural match, but noting that the EDXS results indicate some elemental variability in each. In* ***(b)****, a graphical representation of the refined crystal structure is shown.*

Table 4.5. *Crystallographic refinement details and bond valence assessment for BFNTO.*

BFNTO					
Lattice	***a*** = 5.5853, ***c*** = 13.8120, *β* = 120° (*R*3*c*)				
	Fractional Coordinates (x y z)			U_{iso} (Å^{-2})	BV (v.u.)
Bi	0	0.0258	0	0.0334	3.0247
Fe	0	0	0.2223	0.0204	2.9082
Ti	″	″	″	″	3.4594
M^{2+}	″	″	″	″	2.1678
O	0.4687	0.02985	0.9528	0.0462	1.9537
GII					0.1935
Fit	R_{wp} = 4.65%				

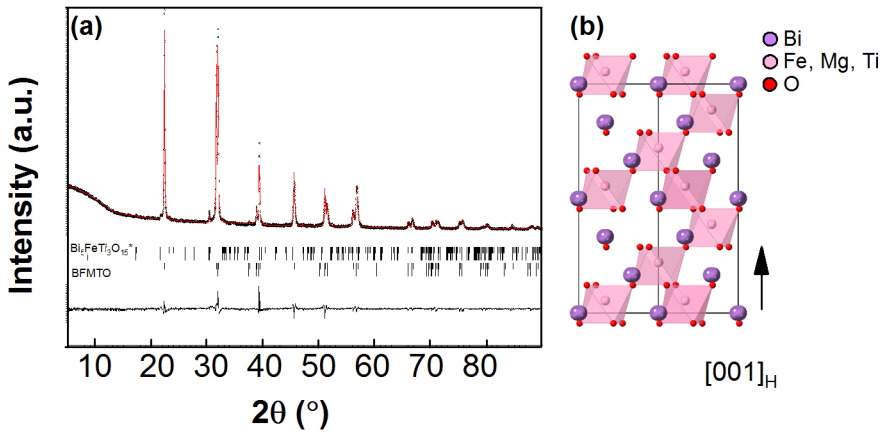

Figure 4.9. *In* ***(a)****, a Rietveld refinement of BFMTO with the extra phase $Bi_5FeTi_3O_{15}$ is shown (red). *Chosen for best structural match, though EDS results suggest actual compound contains some Mg. In* ***(b)****, a graphical representation of the refined crystal structure is shown.*

Table 4.6. *Crystallographic refinement details and bond valence assessment for BFMTO.*

	BFMTO				
Lattice	***a*** = 5.6007, ***c*** = 13.9203, *β* = 120° (*R*3*c*)				
	Fractional Coordinates (x y z)			U_{iso} (Å^{-2})	BV (v.u.)
Bi	0	0.0133	0	0.0329	2.7038
Fe	0	0	0.2208	0.0169	2.8984
Ti	″	″	″	″	3.4408
M^{2+}	″	″	″	″	2.1817
O	0.4494	0.01286	0.9548	0.0291	1.8454
GII					0.2771
Fit	R_{wp} = 5.25%				

There is, however, no apparent indication from the XRPD data that there is structural ordering in the *B*-site of either sample. As was outlined in Chapter 3, iron fluorescence and the close structure factors of Fe, Ti and Ni, mean that weak features associated with structural ordering are likely not observable. Attempts were made to observe such features with TEM. The BFNTO sample was investigated using TEM first, due to its novelty as a compound. However similar to in Chapter 3, electron diffraction patterns did not reveal any indication of long range modulation into a *B*-site ordered perovskite (**Figure 4.10 (a)**). In fact, this sample shows clear absences of <½ ½ ½>$_P^*$ type reflections at this zone axes, which is consistent with an intact ***c***-glide operation (leading to *R*3*c* symmetry). No other kinds of diffuse scattering were spotted that would suggest underlying disorder associated with bismuth displacements either. The results are considered to be reminiscent a long range *B*-site disordered sample, similar to the BFCO case in the previous chapter.

The TEM was useful however in gaining some information about the Bi-rich impurity. A grain of this phase was spotted and shows a 3+3 structural modulation (**Figure 4.10 (b)**), appearing similar to substituted δ-Bi_2O_3 oxides[357]. This does not appear to be tetragonal, as was previously supposed from the β-Bi_2O_3 types peaks seen in the XRD, but is more than likely the same phase with a complex structure arising from incorporation of one or more of the *B*-site metals. The phase $Bi_{18}Ni_8O_{36}$ has been reported to have a structure similar to δ-Bi_2O_3 as well[353]. This is interesting in its own right, but further isolation of this phase was not pursued for further study. The BFMTO sample also was not investigated with TEM, but would be a future avenue for research.

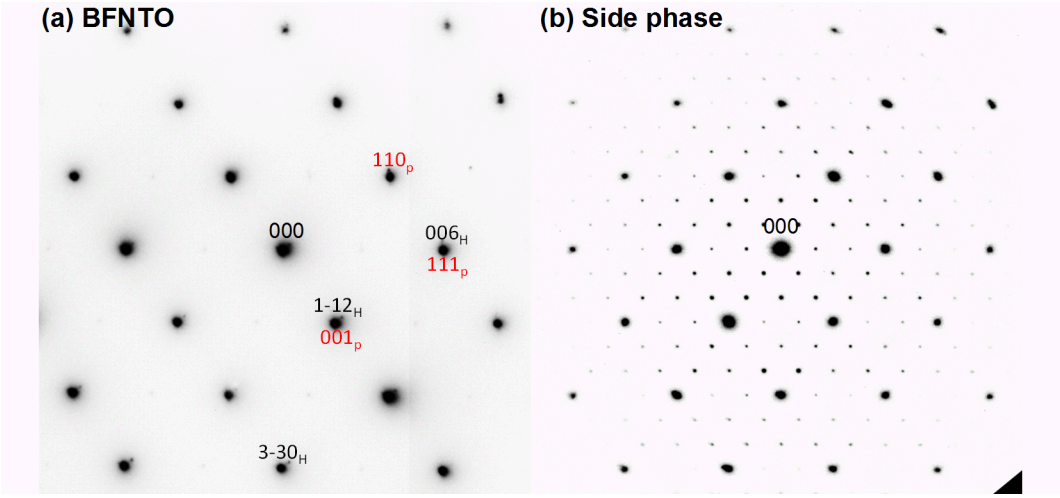

Figure 4.10. *In* ***(a)*** *an EDP of BFNTO down a [-110]$_P$ zone axis is shown, with an absence of the '<½ ½ ½>$_P^*$' peaks (e.g. [003]$_H^*$ expected between the origin and [006]$_H^*$) which indicates a* **c***-glide likely exists. This implies* B*-site disorder consistent with R3c space group assignment. In* ***(b)*** *an EDP of a minor phase is shown which resembles a modulated δ-Bi_2O_3 structure.*

4.2.2 Chemical and Local Structure Analysis from Spectra

Evidently, the structural depictions from diffraction do not capture the complexity of the local environments of the elements in this system. While the structural results do appear to suggest *average* chemical disorder in the *B*-site, mirroring what was seen in BFCO in Chapter 3, the potential for *local* environmental effects remains high due to the large degree of *B*-site substitution. For these reasons, information is sought about specific elements and their environments by spectral means.

4.2.2.1 Mössbauer Spectral Analysis

Mössbauer spectroscopy (^{57}Fe) can reveal information about iron atoms such as their crystal field, the nature of their magnetic ordering and their valence state. By fitting the Isomer Shift (IS), Quadrupole Splitting (QS) and Half-Width Half-Maximum (HWHM) of the spectra obtained

from the BFMTO and BFNTO samples, it is possible to determine whether chemical ordering of the iron atoms is likely. Another benefit of this method is that the weak probe is more likely to interact with the dominant perovskite phase rather than the impurities.

Generally, the fitted values for the QS in these samples are larger than those reported for $BiFeO_3$ and doped analogues with paramagnetic doublets[358-362], though some experiments are conducted above RT (between magnetic T_N and ferroelectric T_C). As the QS reflects the surrounding electric field gradient, this will be influenced by strong polar electrical properties. The IS of the signals reflect the valence state and coordination of the iron. All the signals are consistent with 6-coordinate Fe^{3+} (and not lower coordinations or valences[363]). Both show broad peaks which suggest disordered sites for the iron[309]. However, there are differences in the fitted parameters in each of BFNTO and BFMTO, which suggest some differences in local crystal chemistry (**Table 4.7**).

Interestingly, in BFNTO an asymmetric Mössbauer signal is observed which appears to be a superposition of two paramagnetic Fe^{3+} environments in the sample (**Figure 4.11 (a)**) with different QS and IS. Multiple doublets have been attributed to crystallographic and magnetic anisotropy in magnetically ordered $BiFeO_3$[358, 361, 364, 365] before. However, it appears more likely in this case, that the two doublets arise from different chemical environments. Considering the probability of arranging 6 nearest neighbour *B*-site ions around a single Fe^{3+}, it is found that for BFNTO, situations in which an Fe^{3+} ion is directly neighbouring majority Ni^{2+} ions (3 or more) would occur approximately 40% of the time. This ratio might suggest a possible origin of the two signals seen in this measurement – isolated Fe^{3+} (component 2) and Fe^{3+} with a close neighbouring interaction with a paramagnetic ion (component 1) (**Figure 4.11 (a)**). Component 1 also shows a slightly lower value of the IS, further implying a more electron rich local environment. Proximity to paramagnetic centres that cause asymmetry in BFNTO, would also imply that short range magnetic interactions are present in this sample, but not strong enough to form a magnetically ordered structure at room temperature (which would lead to a sextet signal instead of a doublet). In the BFMTO sample, only Fe^{3+} is strictly paramagnetic. The single, broad doublet observed (**Figure 4.11 (b)**) likely reflects the chemically disordered, magnetically dilute environments possible for the Fe^{3+}, presenting close IS and QS parameters to component 2 in BFNTO.

In addition, the high value of the QS observed in both samples likely reflects the strong EFG established by the bismuth related ferroelectric properties in each sample. It has been suggested from Monte Carlo simulations that the Bi environment in BFMTO is in fact monoclinic, and displacements occur along (at least) 2 axes[102] with a new space group

proposed. The larger apparent distortion in BFMTO compared with BFNTO[74] explains the marginally higher QS value for this material.

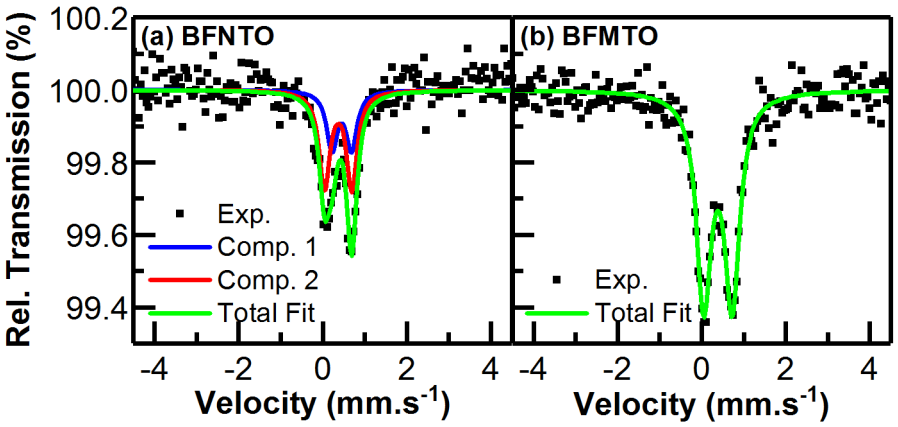

Figure 4.11. *^{57}Fe Mössbauer spectra at room temperature for* ***(a)*** *BFNTO and* ***(b)*** *BFMTO. Fitting of paramagnetic doublets to the raw data is shown. Note: the transmission difference between samples is due to sample volume, not relative iron content.*

Table 4.7. *Mössbauer fitting details for BFNTO and BFMTO. Fitted values are referenced to a room temperature α-Fe spectrum.*

	Component	*IS (mm.s^{-1})*	*HWHM (mm.s^{-1})*	*QS (mm.s^{-1})*	*Area*	*χ^2*
BFNTO	1	0.4535	0.15*	0.4733	0.3731	680.5402
	2	0.3686	0.15*	0.6572	0.6269	
BFMTO	1	0.3857	0.2125	0.6686	1.0000	506.8808

**The linewidth was fixed for each component.*

4.2.2.2 X-ray Photoelectron Spectral Analysis

While Mössbauer spectroscopy gives accurate information about the local environment and valence of iron, in order to learn more about the other elements, other techniques can be used. X-ray photoelectron spectroscopy allows probing of valence states of other elements and gives some more information about charge balance in this system. The measurements in general indicate that between samples, BFNTO exhibits peaks at lower binding energy in comparison to BFMTO, which is attributable to different numbers of electrons in each system. Both also exhibit the anticipated valence states for the transition metals in the *B*-site, though it is noted that both spectra have fitted binding energies offset 0.2 eV from the literature reports referenced (indicating an experimental variance).

The Bi4f$_{7/2}$ signals (**Figure 4.12 (a)**) show a difference in breadth between the two samples. It is possible that the Bi bonding environment is more variable in BFMTO than BFNTO, which has been noted earlier in structural analyses. Both samples exhibit binding energies within

reported ranges for Bi^{3+} in perovskites[78, 83, 89], though a secondary component can also be fitted. This second signal might be attributable to surface bismuth reduction when irradiated. In addition, when quantifying the bismuth content, it is over represented compared to the nominal stoichiometry (**Table 4.8**), again suggesting a surface gathering as a consequence of the technique.

The *B*-site ions are of particular interest. The $Fe2p_{3/2}$ peaks (**Figure 4.12 (b)**) can be fitted with a value consistent with an average of Fe^{3+} reported values[366]. Other authors suggest a possibility for two Fe valence states in BFO based compounds, but the Mössbauer results suggest exclusive Fe^{3+} population. The $Ti2p_{3/2}$ signals (**Figure 4.12 (c)**) show an obvious shift when comparing BFNTO to BFMTO, though both fitting values sit around the expected values for Ti^{4+} in Bi containing oxides[78, 367]. The shift to lower binding energy in BFNTO appears to reflect the change in surrounding potential of the more electron rich nickel in comparison to the magnesium containing BFMTO (this can also be seen when comparing Ti^{4+} binding energies for the related compounds $MgTiO_3$ to $NiTiO_3$[368, 369]). It can be difficult to discern the presence of Ti^{3+} in the samples based on this XPS method alone, and is explored later in **Section 4.3.1** using ESR. The $Ni2p_{3/2}$ signal (**Figure 4.12 (e)**) is complex due to spin orbit coupling. The major peak falls within a range of values reported for Ni^{2+} in Ni-doped BFO[83] and other nickel ferrites[366], titanates[368] and oxides[370, 371]. The presence of Ni^{3+} is not obvious, but is also searched for with ESR in the **Section 4.3.1**. Magnesium binding energies appear to be rarely reported, but the value (**Figure 4.12 (f)**, **Table 4.8**) is consistent Mg^{2+} [372].

Oxygen XPS signals (**Figure 4.12 (d)**) can be difficult to interpret. In this system, at least two main oxygen environments are seen (and can be further fitted to four components). The main signal is consistent bulk oxygen in BFO type samples[78, 83]. The secondary signals are attributed to surface species in several nickel oxide compounds, such as hydroxyl groups, or to oxygen deficient areas with different bonding character[78, 83, 133, 369, 373]. If oxygen vacancies were ubiquitous in these samples, they would likely be apparent in the iron Mössbauer results though.

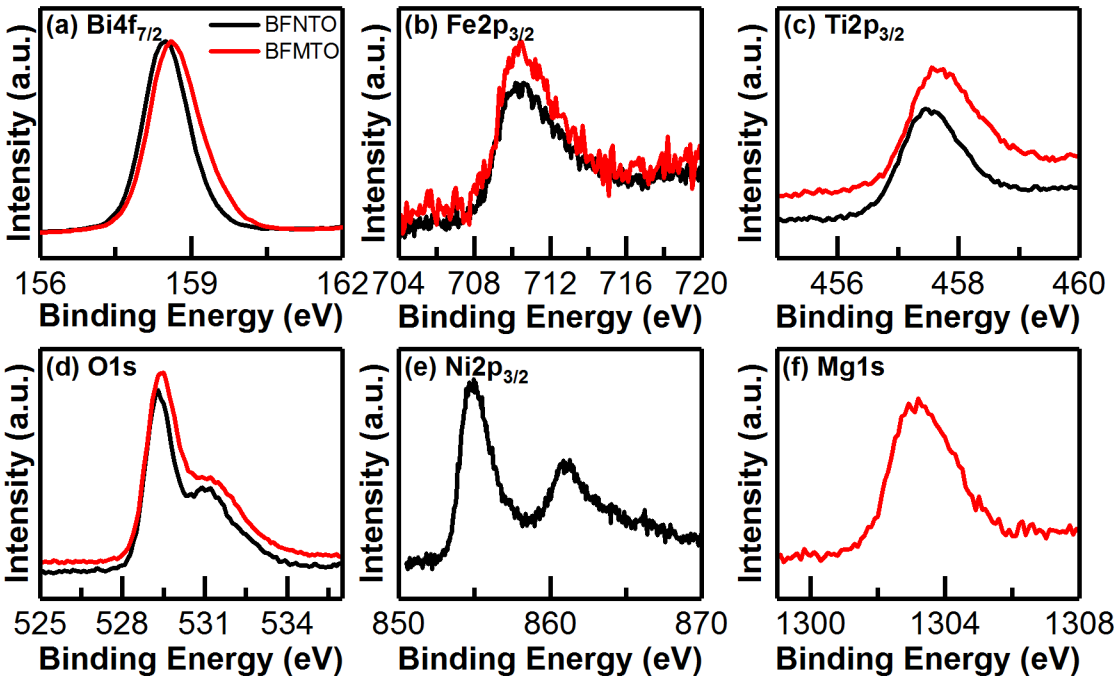

Figure 4.12. *XPS spectra for BFMTO (red) and BFNTO (black). Comparison of signals from (a) bismuth, (b) iron, (c), titanium, (d) oxygen and (e) nickel (BFNTO only) and (f) magnesium (BFMTO only) are shown.*

Table 4.8. *Binding energies of each fitted XPS signal in BFNTO and BFMTO, and the determined quantitative ratio of elements.*

	Bi4f$_{7/2}$	*Fe2p$_{3/2}$*	*Ni2p$_{3/2}$*	*Mg1s*	*Ti2p$_{3/2}$*	*O1s*	*Bi:Fe:M:Ti Ratio*
BFNTO	158.47 159.14	710.27	854.89	-	457.38 457.92	529.3 530.7 531.5 532.7	1.28: 0.21:0.33: 0.42
BFMTO	158.58 159.31	710.36	-	1303.14	457.57 458.28	529.4 530.8 531.8 533.03	1.29:0.19:0.33:0.48

Piecing the results of these spectroscopic analyses together, it appears that both samples are globally chemically disordered, but present some hints of interesting local structure phenomena. The sample BFNTO apparently has a more electron rich environment as evidenced by the XPS binding energies, and a strong possibility for a large population of short range magnetic interactions between Fe^{3+} and Ni^{2+} in the *B*-site from the Mössbauer. By contrast, the BFMTO appears more likely to have variable bismuth bonding, a more positive potential, and less magnetic interactions at the *B*-site. The contrasting choices of M^{2+} in the two samples have the potential to lead to different long range magnetic effects, electrical properties and semiconducting character (as a consequence of number of d-electrons and the

different crystal potentials). The next sections explore these physical properties starting with the magnetism, which has never been characterised in BFNTO, and just once for BFMTO[88].

4.3 Physical Properties of BFMTO and BFNTO

Due to the presence of Fe in these samples, and the underlying perovskite arrangement, these samples are candidate multiferroics and it is important to understand any magnetic phenomena that they might exhibit. While it is apparent from the Mössbauer measurements presented in the previous section that the bulk samples are paramagnetic at room temperature, tracking the behaviour at low temperature is of interest.

4.3.1 Magnetic Properties

4.3.1.1 Magnetization and Electron Spin Resonance Measurements of BFNTO

Both Ni^{2+} (S = 1) and Fe^{3+} (S = 5/2) are present in BFNTO and have the potential to become involved in magnetic ordering within this material. Considering the Goodenough-Kanamori-Anderson rules, strong antiferromagnetic superexchange between Fe^{3+}-O-Fe^{3+}, Ni^{2+}-O-Ni^{2+} and Fe^{3+}-O-Ni^{2+} pairs are expected and interesting magnetic behaviour may be exhibited. Tracking the magnetization of the material with respect to temperature and field, non-typical trends are observed (**Figure 4.13**). A very strong non-linear ***M-H*** response is seen at all temperatures (**Figure 4.13 (a)**), but is far from saturating at the lower temperatures. The curves are also noted to have some inner hysteresis (**Figure 4.13 (a) inset**). It is suggested that this might be a composite of two effects – a ferrimagnetic component (arising from an impurity, giving the characteristic 'S' shape and hysteresis) and an antiferromagnetic component below 200 K (giving the non-saturating response and additional curvature at low field). This is because the Mössbauer measurements showed the main phase to be paramagnetic at room temperature, not ferrimagnetic. This impurity signal could be arising the micron range Ni/Fe spinel particles that were spotted in the SEM, which are likely related to $NiFe_2O_4$, and known to exhibit ferrimagnetism with a T_C above room temperature[374].

The temperature dependent magnetisation in **Figure 4.13 (b)** is also complex, and exhibits a number of points of apparent transitioning behaviour over the temperature range. Firstly, from low temperature to room temperature, the magnetization does not drop close to zero like might be expected for a typical paramagnet, supporting a 'background' contribution from the ferrimagnetic spinel phase that is yet to pass through its T_C. Secondly, some anomalous features are observed which might be ascribed to transitions in the underlying bulk phase BFNTO. Between 2 K and 40 K there is significant inflection reminiscent of a spin reorientation transition. Then, there is another inflection near 200 K, after which the behaviour becomes

more linear, and may be related to a loss of magnetic ordering in the bulk phase (~T_N). Neither transition is expected for a ferrimagnetic spinel phase, and so are suggestive of main phase magnetic phenomenon.

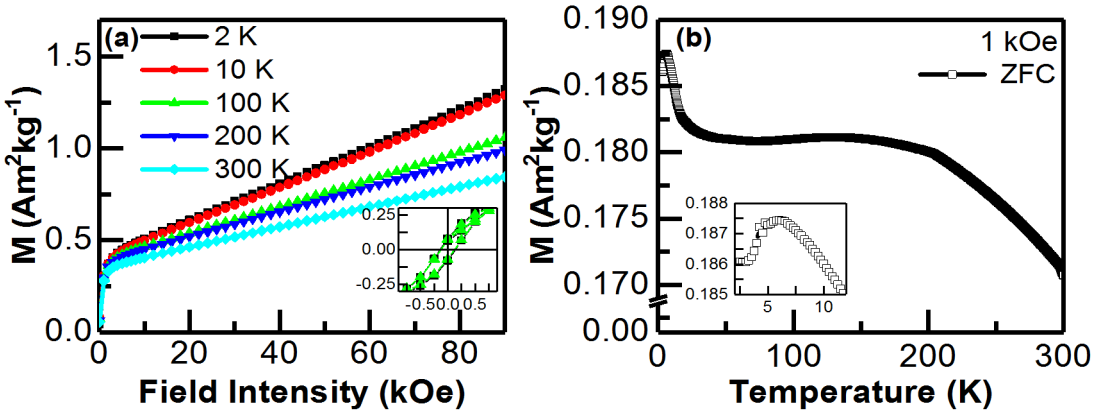

Figure 4.13. *In* ***(a)*** **M-H** *measurements for BFNTO are shown, with evident non-linear low field behaviour common to the ferrimagnetic impurity $NiFe_2O_4$ and additional hysteresis (inset). In* ***(b)*** **M**-*T ZFC data for BFNTO is shown, exhibiting two notable transition-like features at ~ 6 K (peak of feature,* ***inset****) and 200 K.*

By measuring the heat capacity, the presence of magnetic transitions in the sample can be further investigated. A clear transition at ~ 200 K is seen (**Figure 4.14**), consistent with the magnetization measurements, which is strong enough to reflect a phenomenon in the main phase of the sample. A second weaker transition is seen near 35 K which is also consistent with the downward curve of the 'spin reorientation' seen in the ***M***-T data and is also strong enough to be associated with the main phase rather than an impurity. Both transitions appear shifted in comparison with their ***M***-T counterparts by a similar margin.

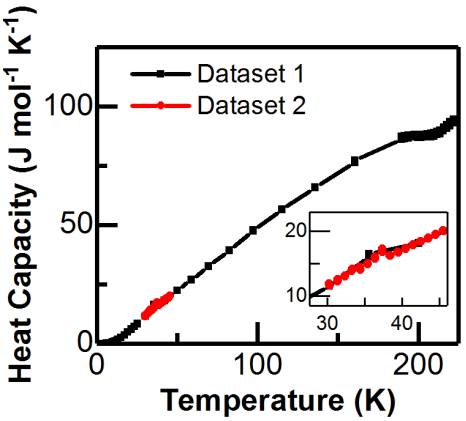

Figure 4.14. *Heat capacity measurements on a BFNTO pellet sample are presented, showing a strong indication of a bulk transition at ~ 200 K, and a weaker, likely impurity related feature at ~ 35 K (a second run was conducted to gather more resolution here, red* ***inset****).*

In order to try and explore these transitions further, the sample was probed using Electron Spin Resonance (ESR) spectroscopy. A transition from a magnetically ordered phase (with a ferro/ferrimagnetic component, full antiferromagnetic ordering may be absent or very weak) to a paramagnetic phase should be easily observable. In this system, Fe^{3+} ions and any isolated Ti^{3+} should be detectable. From these measurements, presented in **Figure 4.15**, a very broad, asymmetric Fe^{3+} signal is observed with *g*-factor ~ 2.9 at 20 K, with its shift from the free-electron value (*g* = 2) presumably due to the zero-field interaction. This strongly implies the signal arises from a magnetically ordered phase with closely associated ions and a strong internal magnetic field. This could be attributed to the canted antiferromagnetic BFNTO phase, appearing similar to other references[375-377], but may all or in part be attributable to the $NiFe_2O_4$ type minor impurity in a ferrimagnetic state also. No clearly separate paramagnetic signal is seen.

On warming to 50 K, the *g*-value of the signal does not shift, indicating the same magnetic environment on temperature increase. This indicates the weak anomaly seen in the heat capacity and magnetization is either not associated with the signal dominating the ESR or the transition temperature is shifted due to the faster probe speed of ESR in comparison with magnetometry.

At room temperature however, the *g*-value shift is noticeable, indicating a loss of magnetic ordering in the main phase of the sample. The signal is still broad though, and somewhat asymmetric. Unfortunately, again it is difficult to ascertain what is influencing these measurements. There is a possibility that the dominant response is from a ferrimagnetic spinel Fe/Ni phase and an AFM BFNTO signal is weak/silent, or a canted AFM main phase signal is apparent, and the ferrimagnetic signal is weak.

It is suspected that the spinel behaviour at low temperatures is what is being seen, as it is observed to be ferrimagnetic until above room temperature[378], and as such should exhibit little temperature dependence in their magnetization until their T_C. Ferrimagnetic species are known to show stronger resonances than AFM species and so would be strong at low temperature. In some studies that probe moderately low temperature, they also observe a consistent *g* ~ 2.6[379] for a superparamagnetic $NiFe_2O_4$ spinel, which somewhat supports the notion that the low temperature signal in part comes from the impurity phase. There is however a significant change in the *g* for this signal from 50 K to RT which may imply an emergence of signal from the main phase, having passed through a transition to a more paramagnetic state, in which it can be seen with ESR. This is reflected also in the decrease in breadth and asymmetry of the signal and is relatively consistent with other studies which monitor signals before and after passing through a critical temperature[375, 380]. The high temperature signal

however is still not as narrow as one might expect for a material with a dominant paramagnetic state. It is suggested that the influence of a ferrimagnetic spinel phase persists to room temperature, creating a broad background, and within BFNTO, a high concentration of aggregated paramagnetic sites (also implied from the Mössbauer fitting) result in a corresponding broad room temperature paramagnetic component as well.

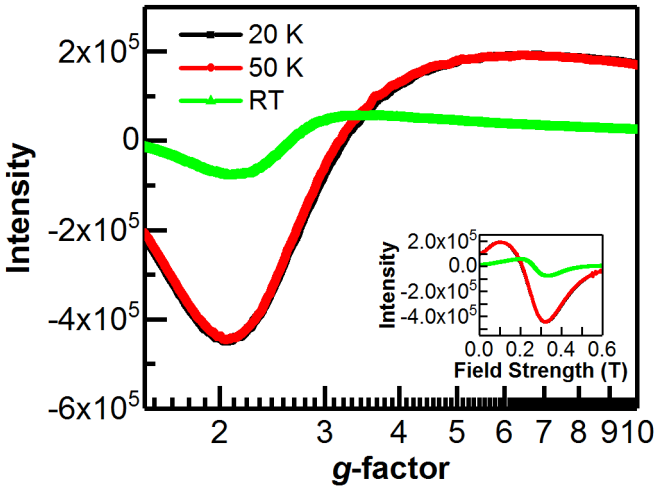

Figure 4.15. *ESR spectra of BFNTO at different temperatures. A clear shift in* g *and adoption of more symmetric, narrow line shapes indicate a significant change in the local magnetic environment of the probed* Fe^{3+} *signals. Note: the sample holders are different for low (20 and 50 K) and high temperature (RT) measurements, as such the change in intensity cannot be ascribed to specific phenomena.* ***Inset****: field dependent spectrum, uncorrected for frequency.*

It is recognized that each of these measurements are consistent with multiple explanations for magnetism within this material, and more measurements are needed to better understand this as part of future study. Recourse to neutron diffraction to probe for the appearance of magnetic peaks associated with the perovskite main phase at low temperature would be of particular value. Nonetheless, this is the first time the magnetic nature of BFNTO has been probed, and it has been shown that there is some suggestion of a possible magnetic response below room temperature. As such, it may be a candidate multiferroic material below room temperature, further evidenced by electrical measurements in the later this section.

4.3.1.2 Magnetization and Electron Spin Resonance Measurements of BFMTO

The magnetic properties of the BFMTO sample are much more typical and less affected by the presence of minor impurities, though the Aurivillius type impurity does have paramagnetic-like behaviour (see Chapter 5). The non-linear field dependent behaviour of the BFMTO sample at low temperature suggests the potential for some persisting magnetic interactions (**Figure 4.16 (a)**). The Langevin function (**Figure 4.16 (b)**) was applied to the 3 K data set, but did not result in a good fit. This indicates the material is likely not truly paramagnetic in this

temperature range and may exist in a semi-ordered state. The average cluster moment *m* obtained from this fit is also less than expected for single Fe ions, and so appears to eliminate superparamagnetism as an ordering type in BFMTO.

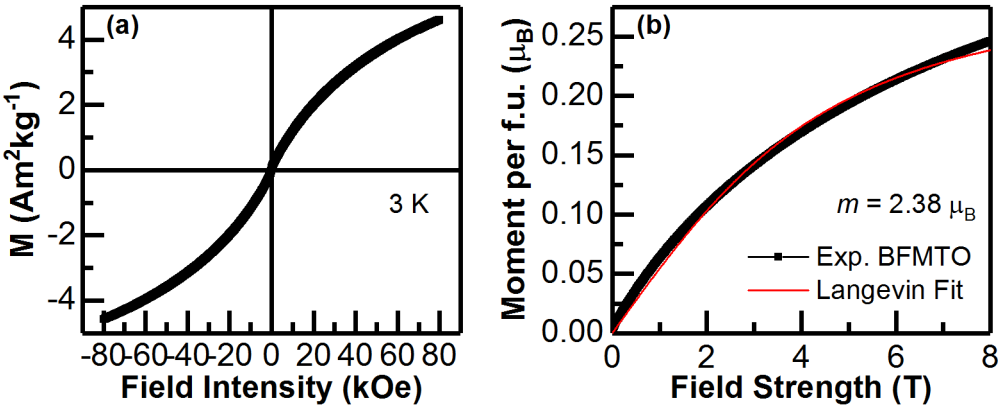

Figure 4.16. *In* ***(a)*** **H** *magnetic field dependent* **M** *data for BFMTO at 3 K is shown, suggesting some low temperature non-paramagnetic behaviour and* ***(b)*** *shows the magnetic moment per* ABO_3 *formula unit vs. the* **B** *magnetic field, fitted with the Langevin function to obtain cluster moment,* m. *This fit is not necessarily consistent with paramagnetism at this temperature.*

The temperature dependent magnetisation (**Figure 4.17 (a)**) mimics that of a paramagnetic material at high temperature. Fitting 1/χ (**Figure 4.17 (b)**) gives a Weiss temperature (θ_w) of -9.6 K, indicating some antiferromagnetic nature to persisting short range interactions and the curve deviates slightly from linear. The fit of the 1/χ plot gives an effective moment of 4.53 μ_B, which is somewhat lower than a typical spin-only value of 5.9 μ_B expected for Fe^{3+} contribution, but could reasonably reflect deviations in stoichiometry/sample purity.

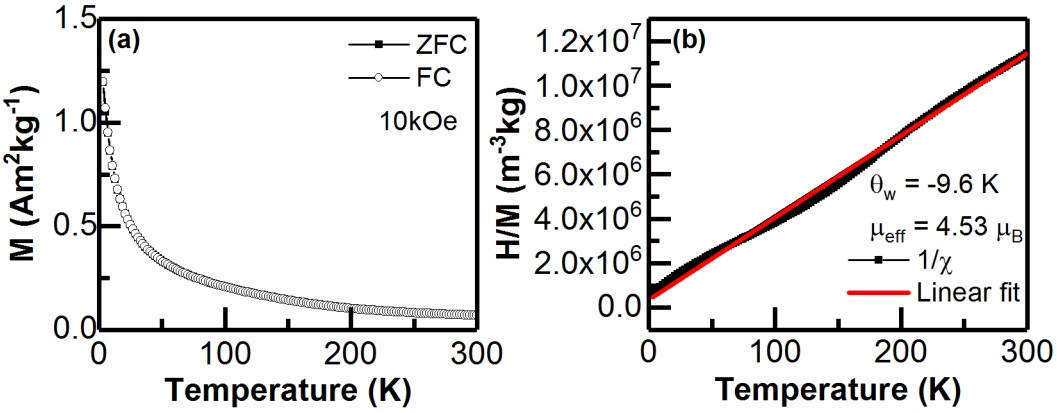

Figure 4.17. *In* ***(a)*** *temperature dependent* **M** *data is shown, indicating mostly paramagnetic behaviour in BFMTO and* ***(b)*** *shows associated Curie-Weiss fitted 1/χ plot, implying some local antiferromagnetic interactions may exist in the dominant paramagnetic state.*

The contrasting behaviour to BFNTO can also be noted in the ESR spectra of BFMTO (**Figure 4.18**). At 20 K, there less of a *g*-shift, consistent with lacking a strong internal magnetic field. The signal is broad and can be fit to two components, indicating a population of iron with short range magnetic interactions and a more isolated paramagnetic component. The increasing temperature does however show appreciable change in the *g*-value from 20 K to 50 K, and an intensity increase is consistent with paramagnetic species becoming increasingly more magnetically isolated (increase in the sharper signal in the fitting). At room temperature, the signal is sharper again, with a *g*-value close to 2, which reflects a more isolated environment. A lower intensity is also detected, but cannot be clearly analysed due to a change in sample holder setup. This gradual change in *g*-value and line width is consistent with expectations from the magnetization measurements, indicating bulk paramagnetism. This behaviour, in conjunction with the magnetization measurements, is very reminiscent of dilute magnetic semiconductors with weak antiferromagnetic interactions[381-383] and can be understood based on the low concentration of iron amongst other non-magnetic elements in the *B*-site. The Ti^{3+} ion was also searched for in this sample but not observed – at room temperature the *g*-value is closer to that expected for an isolated paramagnetic electron however the linewidth and line shape is not typical for Ti^{3+}, implying it arises from Fe^{3+} that still retains some local interactions with other centres.

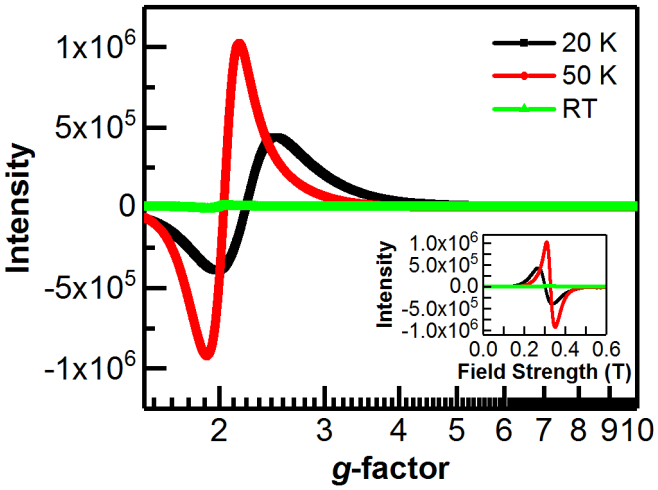

Figure 4.18. *ESR spectra of BFMTO at different temperatures showing a g-factor shift and linewidth narrowing common to samples exhibiting paramagnetic type behaviour. Note: the sample holder is changed for the RT measurement, and so intensity trends cannot be quantified.* ***Inset****: field dependent spectrum, uncorrected for frequency.*

These magnetic observations in combination with the Mössbauer do contrast somewhat with those presented in the literature for BFMTO, in which it was claimed the material was 'ferromagnetic' at room temperature[88] based on a non-linear ***M-H*** measurement. This is not

considered likely based on the measurements presented here, nor from a theoretical perspective given the dilute Fe content in the *B*-site of the sample. As a dilute magnetic semiconductor however, it remains interesting. This magnetic behaviour is reminiscent of the known magnetoelectric perovskite-related phase $Bi_5FeTi_3O_{15}$ shown in the next chapter, presenting further possibilities. The perovskite phases BFNTO, BFMTO and BFCO investigated in this thesis so far, all present quite different magnetic behaviours, a consequence of their *B*-site contents. Their divergent behaviour has been compared for the first time in this thesis. The next section of this chapter goes on to characterise further properties of these materials, highlighting their multifunctionality.

4.3.2 Electrical Properties

Given both samples possess an average rhombohedral non-centrosymmetric perovskite structure, there is the potential for these materials to possess some useful electrical properties. So far the behaviour of BFNTO is unknown but the sample is said to be somewhat conductive, and the presence of ferroelectricity in BFMTO has been suggested by a few authors, but also noted to be experimentally weak and leaky[74]. The low response of BFMTO has in part been attributed to competing local displacements of a bismuth in the sample[102]. In order to further understand the behaviour of these two compounds, Piezoresponse Force Microscopy (PFM) was used to look for ferroelectric domain structures and domain switching ability. This method was chosen primarily due to the aforementioned issue with the BFNTO samples possessing macroscopic cracks and being unsuitable for conventional bulk ferroelectric measurements.

As shown in **Figure 4.19** interesting phenomena are apparent in both materials. In BFNTO **Figure 4.19 (a) – (c)** there are clear polar regions in the amplitude and phase maps within the small sample grains, apparently unrelated to morphology. The phase image shows a 180° contrast between these polar regions, and though not well defined in shape, mirror what was seen for BFCO in Chapter 3. Irregular shapes may reflect compositional disorder in the *B*-site in all three samples. The BFMTO sample **Figure 4.19 (d) – (f)** shows a similar result, though within larger grains. It too demonstrates 180°, irregular shaped polar regions. Regions of the sample were sometimes difficult to image due to the presence of pores, but these features were seen in different locations in each sample.

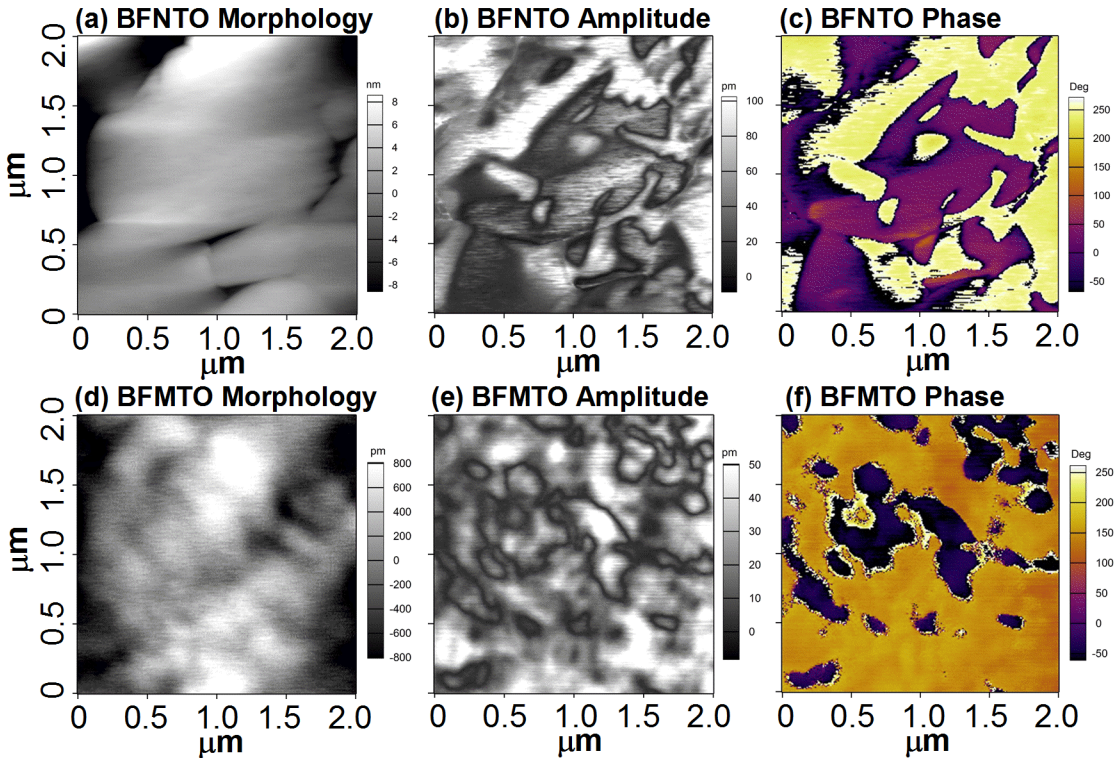

Figure 4.19. *PFM images of BFNTO are shown mapping the* ***(a)*** *morphology,* ***(b)*** *amplitude, and* ***(c)*** *phase. PFM images of BFMTO are also shown with respect to the* ***(d)*** *morphology* ***(e)*** *amplitude, and* ***(f)*** *phase signals. Domain-like 180° polar regions are evident in the phase map.*

The manual domain patterning ability of these samples was then tested (**Figure 4.20**). Such a phenomenon would be useful for domain-engineered bulk photovoltaic devices. It is notable that in both samples, domains could be written using an applied bias of 30 V. Below this value, the patterning was not stable and was quickly released. At 30 V, BFNTO (**Figure 4.20 (a) – (c)**) shows greater stability than BFMTO (**Figure 4.20 (d) – (f)**), which shows a drift in the written boundary. It is unclear if this is related to the weak apparent properties of BFMTO in the literature, but the result remains that both samples show a polar and mechanical response to applied voltage. For the first time, evidence for room temperature polar domains in BFNTO and BFMTO is demonstrated and ferroelectric-like behaviour is suggested.

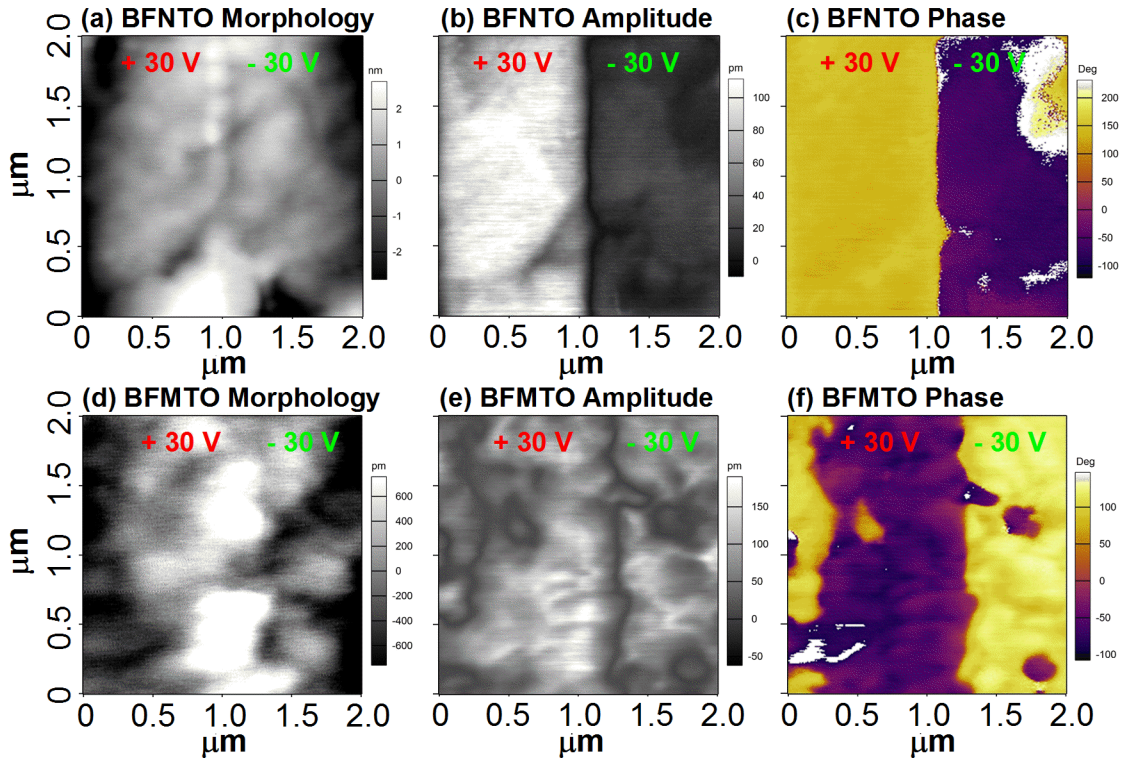

Figure 4.20. *Manually written domains in BFNTO showing (a) morphology, (b) amplitude, and (c) phase mapping. Manually written domains in BFMTO are also shown in the (d) morphology, (e) amplitude, and (f) phase maps. An applied voltage of 30 V was used on both samples.*

4.3.3 Optical and Photofunctional Properties

In addition to ferroelectricity, both samples are noted to have colouration that would indicate some visible light absorption. Confirming this property will help assess the utility of this material for bulk photovoltaic usage, and multiferroic applications. Attention has been drawn to the potential of BFMTO previously [88, 89] , but not BFNTO and so further investigation of both would prove useful.

An indication of what the band gap of these samples might be can be obtained by taking UV-Vis diffuse reflectance measurements. The absorbance profile of the two samples in the visible light window shows an inflection at around 1.7 eV for both samples which is stronger for BFMTO (**Figure 4.21 (a)**). The flatter profile of BFNTO suggests a broader absorption range, but less pronounced low wavelength utilization. In addition, the valence band edge of each sample determined by XPS suggests the valence band of BFMTO is more positive than BFNTO relative to vacuum (**Figure 4.21 (b)**), linking back again to the individual peak fitting earlier. Given BFNTO has a higher concentration of d electrons at the *B*-site, it is not unreasonable to consider this the more electron rich system and perhaps exhibits broader visible light absorbance due to the addition of nickel d-electrons that narrow the band gap from

native $BiFeO_3$. By adding a pairing of M^{2+} and Ti^{4+} into the $BiFeO_3$ system, it is apparent that visible light absorption can be retained.

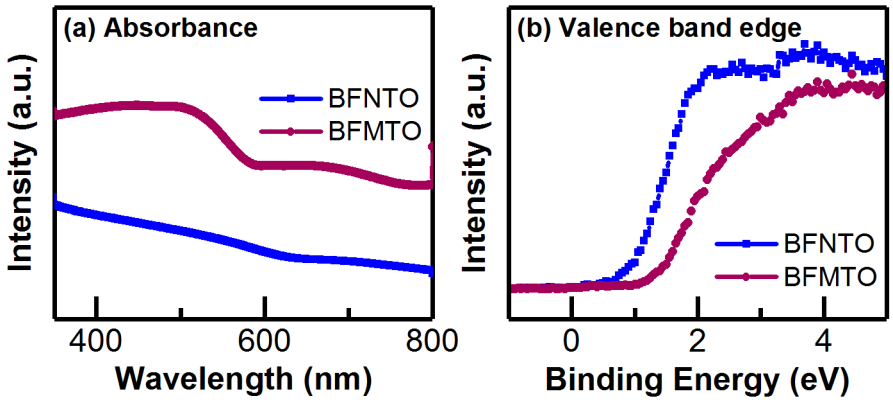

Figure 4.21. *In* ***(a)****, UV-Vis reflectance spectra for BFMTO and BFNTO are shown, indicating the apparent visible light absorbance in both samples and* ***(b)*** *shows the valence band edges from XPS which suggest a closer alignment of BFNTO to the fermi level than BFMTO.*

Knowing these samples absorbed visible light, the PFM study was continued to monitor the variation in the surface potential with respect to visible light irradiation. The idea of the technique is that photoexcited charges that migrate to the sample surface will cause a temporary change in the surface potential. In **Figure 4.22** the results of a slow scan across a region of each sample is shown with a 458 nm laser source intermittently turned on and off. When the light is on and off, both samples are noted to exhibit a significant response with similar magnitude, indicating a photoresponse in both samples. While the surface potential goes down in BFNTO (**Figure 4.22 (a)**, **(b)**) and up in BFMTO **(Figure 4.22 (c)**, **(d)**) when the laser is on, this opposite behaviour is not necessarily indicative of a difference in charge carriers between the samples, given the many possible orientations of grains in a sample. This result would suggest the materials are semiconductive with a bandgap less than the 2.71 eV of the laser, consistent with the UV-Vis absorption results.

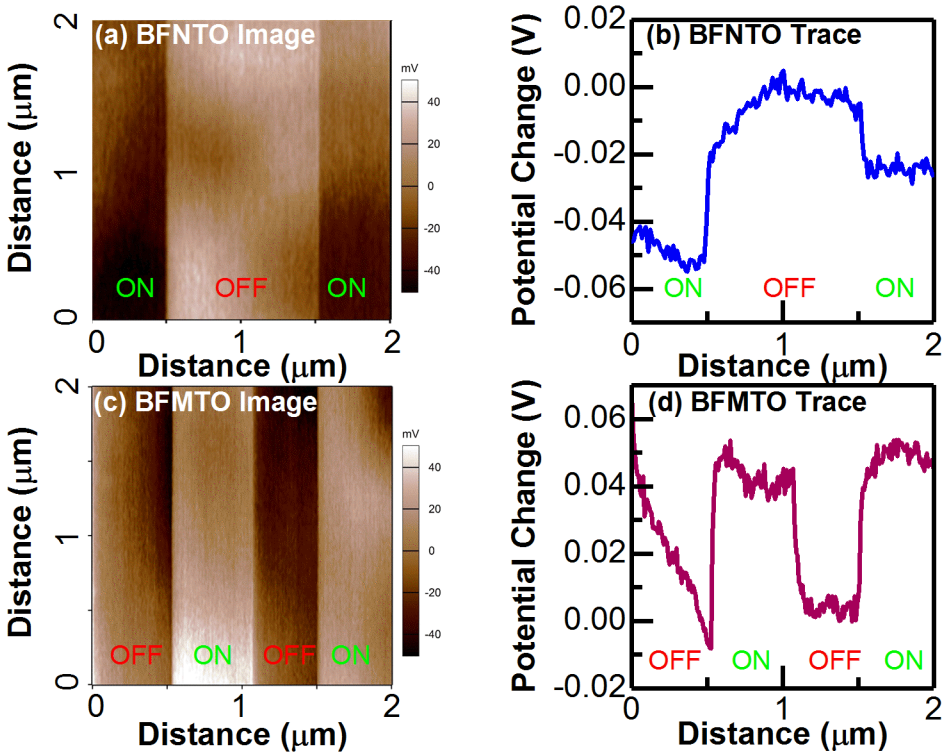

Figure 4.22. *Surface potential measurements made with KPFM and a 458 nm laser turned ON or OFF as indicated. Images are shown for* ***(a)*** *BFNTO and* ***(c)*** *BFMTO and associated line traces are show in* ***(b)*** *for BFNTO and* ***(d)*** *BFMTO.*

As these samples possess local domain structures and are visible light responsive, some basic tests were conducted to understand the macroscopic current-voltage response during illumination (with an Hg lamp) between two electrodes on the sample surface (**Figure 4.23**). Unfortunately, due to the maximum output voltage of the FE head, only 10 V could be applied over 0.5 mm to the sample. The current measured from both samples across the surface is extremely low (leading to noisy traces), but there is a photocurrent observed when the visible light source is applied which is proportionally large for the sample area illuminated. BFNTO shows a higher current, not unexpected based on previous discussion of the electron rich nature. No diode-like response is observed here, and is not expected due to the lack of well-defined native or manually engineered ferroelectric domains, but further supports the other measurements in assessing these materials as visible light photoresponsive.

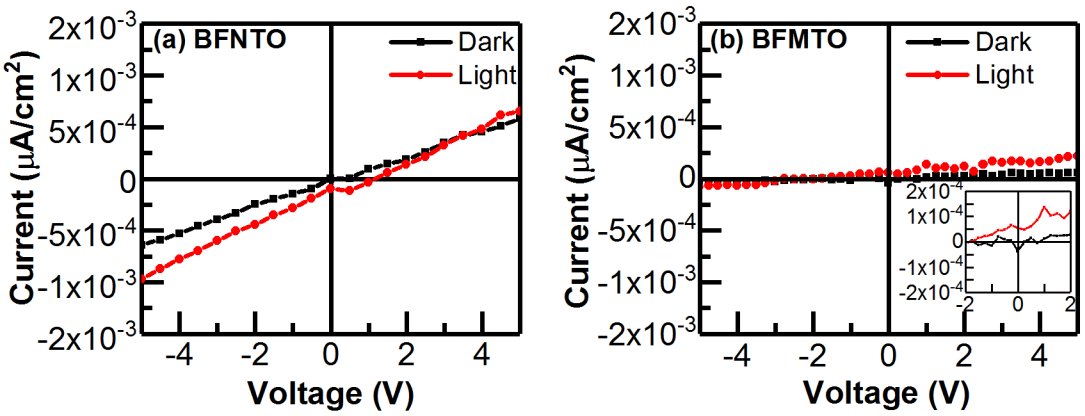

Figure 4.23. *Current-voltage curves for* ***(a)*** *BFNTO and* ***(b)*** *BFMTO are shown, measured across the sample surface between gold electrodes of size 0.8mm^2 and 0.9 mm^2 respectively and spacing 0.5 mm.*

For the first time the local polar responses of these materials were investigated with PFM, and associated with their absorbance characteristics and photoexcited behaviour. From these measurements, it has been shown that in both samples, domains can be written and switched and a photocurrent can be induced with visible light.

4.4 Summary of Chapter 4

In this chapter, it was shown that the materials $BiFe^{3+}_{0.25}Fe^{2+}_{0.375}Ti_{0.375}O_3$, $BiFe_{0.25}Zn_{0.375}Ti_{0.375}O_3$ and $BiFe_{0.25}Cu_{0.375}Ti_{0.375}O_3$ did not form perovskite phases under the tested lab conditions. It was however possible to make $BiFe_{0.25}Mg_{0.375}Ti_{0.375}O_3$ (BFMTO) and $BiFe_{0.25}Ni_{0.375}Ti_{0.375}O_3$ (BFNTO) under ambient pressure. A novel metal organic decomposition method, and an improved solid state method were optimized for the production of BFMTO and BFNTO respectively. Structure analysis showed both exhibited an average rhombohedral crystal structure with *R*3*c* symmetry.

BFNTO was shown to be potentially magnetically ordered below 200 K evidenced by magnetization and heat capacity measurements. Some indication of non-random distribution of elements in the *B*-site is suggested from Mössbauer spectroscopy, measured for the first time. One should be careful when interpreting this magnetic response however due to the influence of a minor spinel impurity. The potential coexistence of magnetism and a polar response in BFNTO below room temperatures makes it a potential candidate type I multiferroic. The BFMTO sample shows more paramagnetic reminiscent behaviour owing to the magnetically dilute *B*-site, also suggested with Mössbauer. These interactions appear to be antiferromagnetic in nature.

Both materials show the ability to be domain-written under applied field, which might be further optimized for production of designer PV devices. Both samples also exhibit visible light absorption, with BFMTO appearing to absorb more short wavelength visible light than BFNTO. An ability to generate photocurrent is demonstrated for both samples, and BFNTO is suggested to be slightly more conductive due to an electron rich composition.

This work adds clarity to the limited reports of these materials investigated in the literature. It was shown that by incorporating Ti^{4+} and a suitable M^{2+} partner ion, the materials can be synthesized without applying pressure and are photofunctional and possess magnetic properties, though weaker than the related perovskites BFCO and BFO. The next chapter addresses how bismuth, titanium and iron in a new structure type develop functionality.

Chapter 5 Aurivillius-type Bismuth Ferrite Titanate Materials

In the previous two chapters specific combinations of elements were introduced into the host oxide material BFO to alter its physical properties and retain the average perovskite structure. While both materials showed photofunctionality and ancillary properties such as ferroelectricity and local antiferromagnetism, it is expected that other related structure types might permit an even more robust complement of properties.

This chapter begins by exploring a new structure type for this thesis: the layered Aurivillius phases. The Aurivillius oxide $Bi_4Ti_3O_{12}$, is modified with iron with the intention of narrowing the band gap. Such mixtures can lead to compounds with the general formula $Bi_{m+1}Fe_{m-3}Ti_3O_{3m+3}$ which can be made under ambient conditions. These new stable layered structures may possess local chemical ordering within their perovskite-like blocks, and as a consequence have the potential for better long range, highly directional, properties.

As outlined in the introduction, there is much that is unclear throughout the literature about how these layered materials can be made and how they function. In particular, the higher Fe content structures are often inhibited by impurity formation and so synthesizing these materials is an important first hurdle to clear. After doing so, persistent questions such as the nature of the chemical ordering, structural distortion, magnetic ordering, ferroelectric domains and visible light responsiveness, and how they vary with respect to m, might be addressed. Answering these questions would also serve to expand the known set of photofunctional materials and give insight into how properties arise in different structure types by contrasting with the similar combination of elements in Chapter 4.

In this chapter, focus is placed on investigating the evolution of magnetic, electrical, optical and photofunctional properties of $Bi_{m+1}Fe_{m-3}Ti_3O_{3m+3}$ (m = 4, 5 and 6). A new method is introduced to synthesize these high-Fe Aurivillius phases to high-purity, allowing the systematic exploration of their structural motifs through X-ray diffraction and Mössbauer to generate crystal structures. This is followed by an evaluation of physical properties.

5.1 Synthesis

In order to systematically study the structure and physical properties of the Aurivillius phases, a synthesis method needs to be developed that can be applied to several members of the series and produce high purity products. This section explores the development of an appropriate method and optimization of the experimental parameters for the best samples.

Three members of the $Bi_{m+1}Fe_{m-3}Ti_3O_{3m+3}$ Aurivillius series were targeted: $Bi_5FeTi_3O_{15}$ (m = 4, 'BFTO-513'), $Bi_6Fe_2Ti_3O_{18}$ (m = 5, 'BFTO-623') and $Bi_7Fe_3Ti_3O_{21}$ (m = 6, 'BFTO-733'). The naming convention, 'BFTO-(m+1)(m-3)3', allows quick reference to the relative numbers of bismuth (m+1), iron (m-3) and titanium ions (3) in each material and the number of perovskite layers (m).

5.1.1 Method Development

5.1.1.1 Solid State Method

The first synthetic method tested was the basic solid state method. This method is known to have low success for BFTO-623 and BFTO-733 resulting in multiphase products[171, 177], and so was not expected to produce high quality samples, but was used to help identify sintering parameters for subsequent methods. Purity of sintered products was monitored using XRPD. In this chapter, the angular range 20–40° 2θ was the most diagnostic for confirming the presence of additional phases in BFTO-type samples and is presented in subsequent figures. A broader angular range XRPD that indicates successful synthesis can be found in **Figure 5.6**.

Indeed, the experimental results show that the nominal BFTO-623 sample ended up contaminated with BFTO-513, and the nominal BFTO-733 run also resulted in additional non-Aurivillius phases (**Figure 5.1**, as matched with software[291]) despite a wide range of tested sintering conditions (**Table 5.1**).

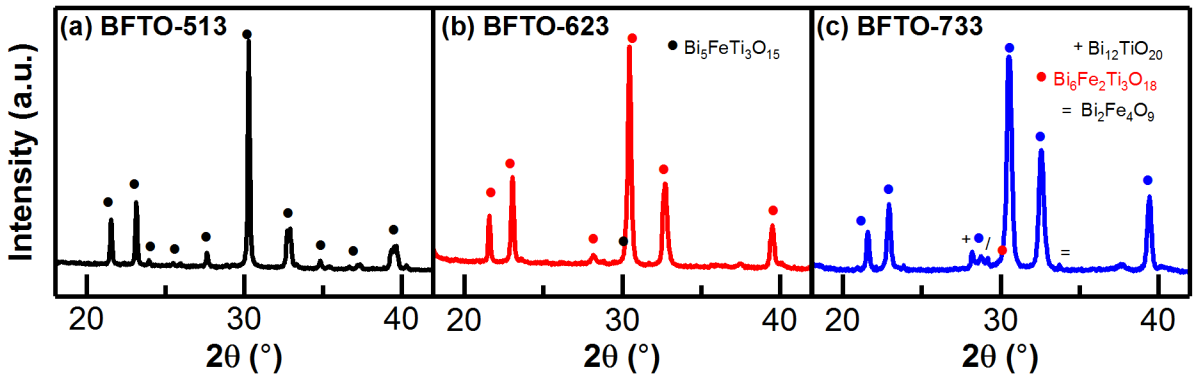

Figure 5.1. *XRPD patterns of samples produced via the solid state method, desired phases BFTO-513 (•), BFTO-623 (•) and BFTO-733 (•) are indicated. No extra phases were detected in* ***(a)****, in* ***(b)*** *broadening indicates the formation of a second Aurivillius phase and in* ***(c)*** *an extra Aurivillius phase, $Bi_2Fe_4O_9$ and a Bi-rich phase were detected. Another unidentified peak is seen, indicated as a '/'. (BFTO-513 was sintered at 820 °C/2 h + 1040 °C/2 h, BFTO-623 at 820 °C/2 h + 920 °C/4 h, and BFTO-733 at 820 °C/2 h + 890 °C/2 h).*

Table 5.1. *Summary of solid state synthesis conditions tested for BFTO samples (no optimums).*

Conditions	*BFTO-513 variations tested*	*BFTO-623 variations tested*	*BFTO-733 variations tested*
Reactant mixture	Hand milled oxides.	Hand milled oxides.	Hand milled oxides, ball milled oxides.
Pre-sintering Steps	Pre-sinter 820 °C for 2 hours.	Pre-sinter 820, and 860 °C for 2 hours.	Pre-sinter 770, and 820 °C for 2 hours.
Main Sintering Temperature	990, 1040, and 1090 °C.	860, 870, 920, 940, 1000 and 1040 °C.	860, 870, 880, 885, 890, 915, 940 and 990 °C.
Main Sintering Time*	2 and 4 hours	90 min, 2, 4, 5 and 6 hours.	2, 4, and 12 hours.

*natural cooling and quench to air cooling were trialled, but produced similar results.

There are apparently some issues with BFTO-623 splitting into other Aurivillius phases (as illustrated and also observed through many other trials). This was flagged as a possible issue with synthesized odd-layered Aurivillius structures as opposed to even ones. In addition, this method clearly does not permit an appropriate degree of mixing to grow homogeneous samples (especially for high Fe compositions) so the study was expanded to other methods.

5.1.1.2 Metal Organic Decomposition – Water

It was thought that in order to produce well-defined, regular repeating layered structures, diffusion of reactant ions should be optimal, best mediated through a metal organic solution based initial reaction (i.e. an MOD method). The MOD based approach was modelled on thin film syntheses[129] and involved first dissolving solid nitrates of bismuth and iron in water ('MOD-H_2O' method) and mixing them with liquid titanium butoxide.

Unfortunately, this method resulted in instantaneous precipitation of solid titanium oxide based species, instead of a homogenous solution. Nevertheless, the suspension was calcined at 600 °C to decompose. Several additional phases were noted to form at this point (**Figure 5.2 (a) – (c)**). The decomposed material was then ground, pressed and sintered at high temperature. After this final step, a dominant bismuth rich side phase was often seen (**Figure 5.2 (d) – (f)**). It was suspected that inhomogeneity developed as a consequence of the precipitation seen during the mixing of raw materials. For these reasons, ethylene glycol was tested as a replacement solvent, taking inspiration from another thin film synthesis[153].

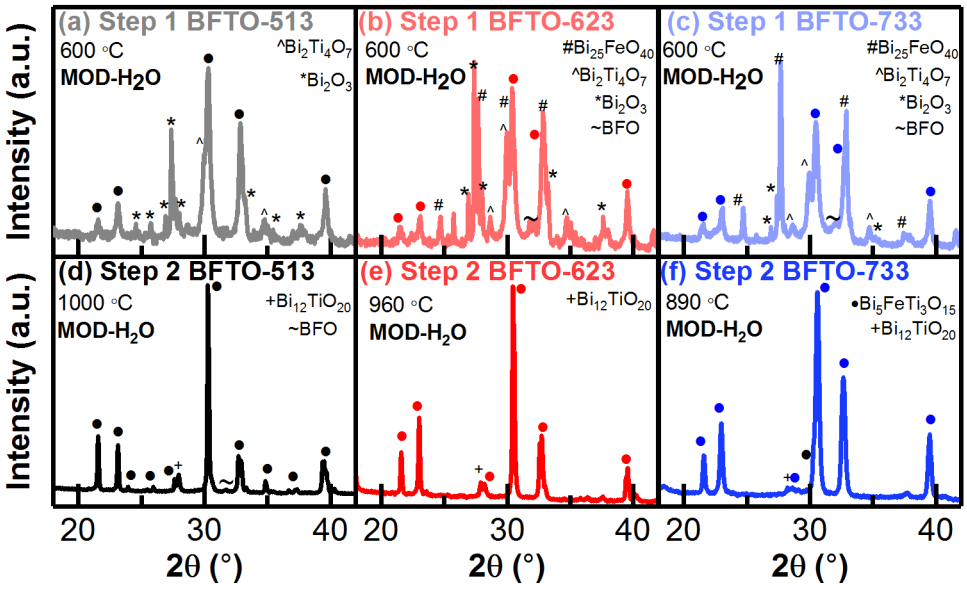

Figure 5.2. *XRPD patterns of samples produced by the MOD-H_2O method, desired phases BFTO-513 (•), BFTO-623 (•) and BFTO-733 (•) are indicated. Patterns* ***(a) – (c)*** *were obtained after calcining at 600 °C while* ***(d) – (f)*** *are from sintering at high temperature. In* ***(a)*** *two dominant side phases are formed, which become two different side phases in the sintered product* ***(d)****. In* ***(b)*** *four side phases are detected which became one in the sintered product* ***(e)****. In* ***(c)*** *four phases are detected, becoming two in the sintered product* ***(f)****.*

5.1.1.3 Metal Organic Decomposition – Ethylene Glycol

By substituting the water solvent for ethylene glycol, all nitrates and the butoxide dissolved to form a clear, homogenous solution with no precipitates ('MOD-EG' method). This new solution was also decomposed carefully at 600 °C, and in contrast to the MOD-H_2O, the MOD-EG method results in majority Aurivillius phase formation directly after the first heat treatment (**Figure 5.3 (a) – (c)**). In this study, only the BFTO-513 mixture showed an additional bismuth rich phase, which was a persistent issue, and likely owes to this composition having the highest bismuth-to-iron/titanium stoichiometry. After regrinding and sintering at elevated temperature followed by a natural cooling to room temperature (**Figure 5.3 (d) – (f)**), the purity improved in comparison to the MOD-H_2O and solid states methods for the higher-iron samples. No additional phases are detected by XRPD for BFTO-623 or BFTO-733 which is a rare and promising result among bulk syntheses in the literature, as highlighted in Chapter 1.

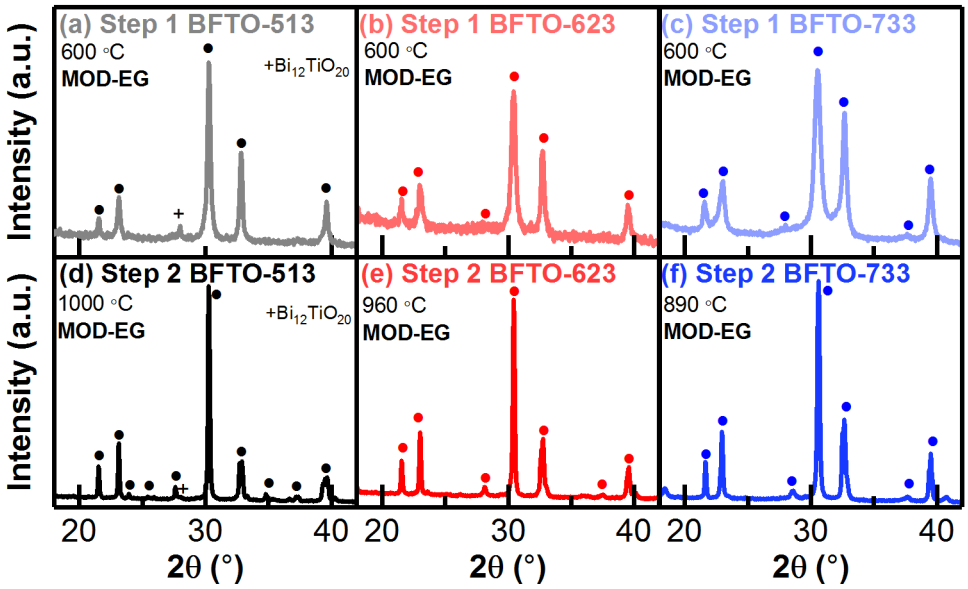

Figure 5.3. *XRPD patterns of samples produced by the MOD-EG method, desired phases BFTO-513 (•), BFTO-623 (•) and BFTO-733 (•) are indicated. Patterns* ***(a) – (c)*** *were obtained after calcining at 600 °C and* ***(d) – (f)*** *are from sintering at high temperature. Note in* ***(a)****, formation of a Bi-rich phase during calcining carried on to the sintered product* ***(d)*** *and repeat trials were unable to avoid this. No detectable extra phases were seen in* ***(e) or (f)****, likely owing to more cleanly calcined precursors* ***(b)*** *and* ***(c)*** *respectively.*

5.1.1.4 Sintering Optimization

Of the three methods tested, MOD-EG was deemed the most suitable for production of high purity samples for systematic study. In order to obtain the best samples, a range of temperature conditions were tested to optimize the final sintering step. It was noted that a balance between selecting a temperature high enough to activate the reaction and low enough to avoid decomposition of the phase back to layered products with smaller perovskite blocks was necessary (consistent with literature observations[384]). Trials showed that sintering for two hours at 1000 °C, 960 °C and 890 °C following a natural cooling to room temperature were identified as optimal for the production of BFTO-513, BFTO-623 and BFTO-733 respectively (**Figure 5.4**).

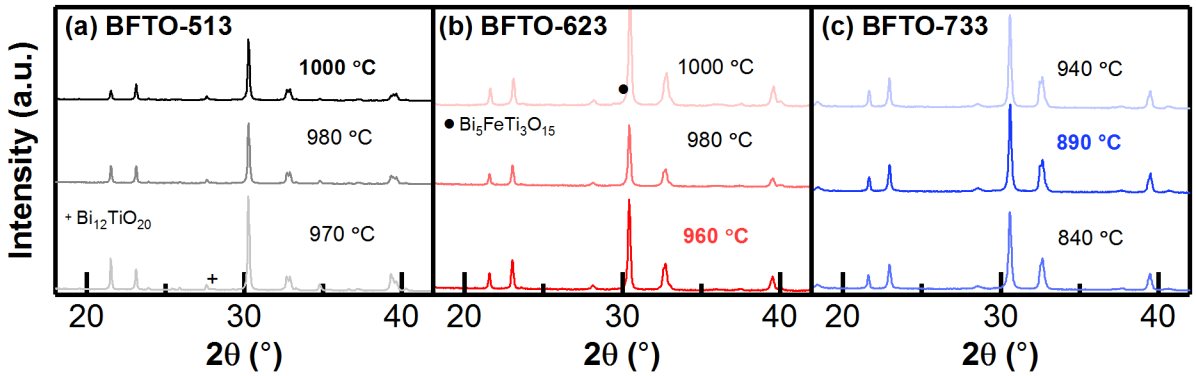

Figure 5.4. *XRPD patterns of samples produced by the MOD-EG method at different temperatures. The determined optimal temperatures are the darkest curves. In* ***(a)****, a minimization of Bi-rich phase prioritized, in* ***(b)*** *a narrowing of central peak was prioritized and in* ***(c)*** *little change was observed above ~ 890 °C so the lower temperature was used for convenience. Unmarked peaks correspond to the desired Aurivillius phases.*

5.1.2 Phase Analysis of Optimized Samples

Having optimized the MOD-EG method to produce seemingly high purity samples, microscopy was utilised to confirm the identity of presenting phases and the grain morphology. Evidence for a plate-like grain morphology can be seen in SE micrographs even in the polished surface of BFTO-513 (**Figure 5.5 (a)**, typical for this phase[174]). It was also noted that the BFTO-513 sample contains a Bi-rich phase between the grains (**Figure 5.5 (d)**, BSE image, example circled) which is consistent with the extra peak noted in the XRPD pattern. The morphology of BFTO-623 is extremely porous (**Figure 5.5 (b)**) as a consequence of the synthetic method which is time optimized for purity, not density. The BFTO-623 sample shows homogenous colouration, though plate like grains of a BFTO-513 side phase are infrequently spotted (**Figure 5.5 (e)**, circled). The BFTO-733 sample also shows morphology consistent with growth from solution (**Figure 5.5 (c)**). The backscattered image (**Figure 5.5 (f)**) shows no evidence for additional phases.

The EDXS composition analyses demonstrates some deviation in the measured quantities of *B*-site elements in comparison to expectations (**Table 5.2**). These compositions are calculated considering full occupation of the Aurivillius Bi sites. Given these samples are porous and have a rough morphology, the signal analysed is reduced by 1 – 2% which may account for an over estimation of bismuth and underestimation of iron/titanium. However, it should be considered that this deficiency may indicate mislayering in the material and deviation from nominal composition. Nonetheless, these proportions are not consistent with any other likely phases and the iron and titanium as calculated are used in magnetic analysis below.

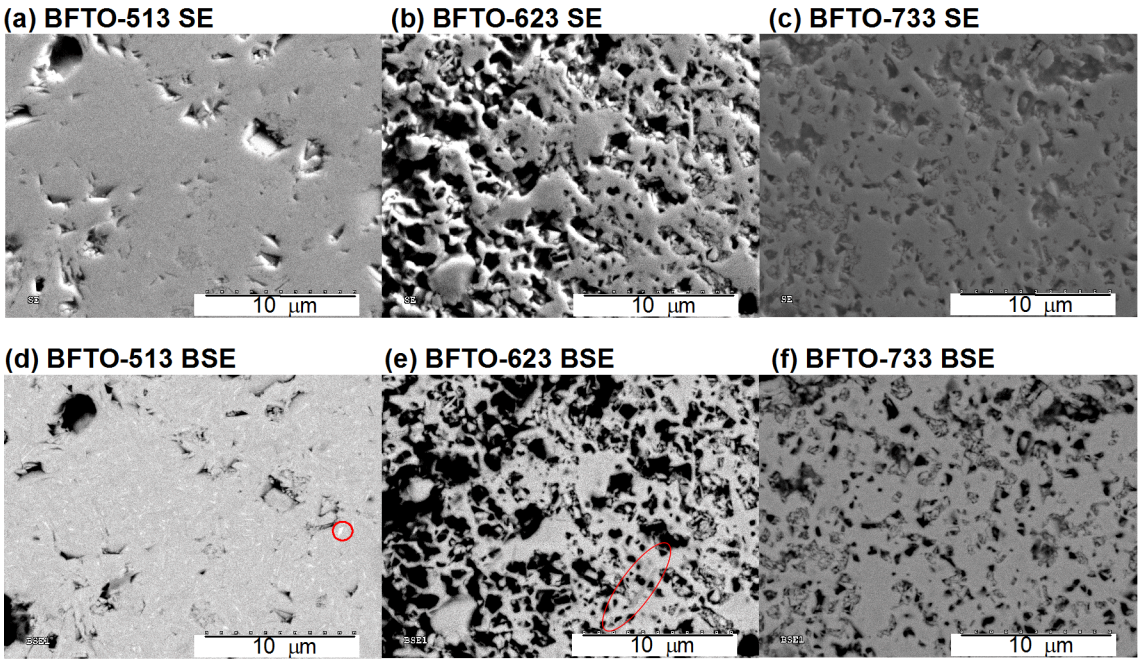

Figure 5.5. *SEM micrographs of high purity MOD-EG synthesized samples. Samples were hand-polished for EDXS analysis. Images* ***(a) – (c)*** *show SE and* ***(d) – (f)*** *show BSE images. In* ***(d)*** *Bi rich areas can be seen between plate-like grains (red circle). In* ***(e)*** *some plate like structures can also be seen, indicating a small population of BFTO-513 exists in the BFTO-623 sample (red oval). In* ***(f)*** *no extra phases are detected. These samples are highly pure but also highly porous.*

Table 5.2. *EDXS elemental data from micron-scale areas of MOD-EG BFTO samples.*

Sample	*Cation fraction*		
	*Bi**	*Fe*	*Ti*
BFTO-513	5	0.99	2.84
BFTO-623	6	1.87	2.98
BFTO-733	7	2.62	3.05

*calculated assuming Aurivillius *A*-site is fully occupied with Bi

The materials discussed in the remainder of this chapter refer to these optimized, high purity samples produced by the MOD-EG method outlined above. References to the materials as BFTO-513, BFTO-623 and BFTO-723 in the remainder of this chapter relate to this sample set, and the structure and property evolution of each composition is systematically compared.

5.2 Structural Evolution

Among the literature on the Aurivillius compounds, there is a lack of reported crystal structures (as outlined in the introduction). A few different orthorhombic space groups are reported with different degrees of octahedral titling. It also unclear if there is any chemical ordering of iron

and titanium in the perovskite layers. Having made three phases to a high degree of purity, attempts were made to add clarity to these structural problems.

5.2.1 Average Structure Evolution – Basic Model

A simple comparison of XRPD data from the high purity samples of BFTO-513, BFTO-623 and BFTO-733 reveals a systematic shifting of peaks as additional layers are added to the structure (**Figure 5.6**). The peaks can be fitted to an orthorhombic unit cell. The most commonly reported space group for the Aurivillius phases, *F*2*mm*[159, 167, 169, 174], was used for this initial basic modelling. A comparison of fitted orthorhombic lattice parameters shows an extension of the long axis by ~ 8 Å (**Figure 5.7**) between the materials, consistent with the addition of extra perovskite layers in each case.

The lattice parameters of the BFTO-623 sample are on the higher side of the literature reports, suggesting the possibility of some 'disorder' in the layering of this sample. This is also suggested by appreciably broad peaks associated with planes perpendicular to the long axis (see **Figure 5.6, inset**, red curve ~ 17° 2θ). The grain size of the BFTO-623 and BFTO-733 samples is smaller than BFTO-513 which explains some systematic broadening, but not some of the localized broad peaks which are most severe in BFTO-623. This sample is also unique as the only compound with a nominally odd number of perovskite layers in the crystal structure, and thus can exhibit different symmetry features and strain distributions, which is likely what makes it more difficult to synthesize and may affect the resulting properties. In addition, as the number of layers is increased, the more likely it becomes for stacking faults and intergrowths to develop[385, 386], which can make structure refinement challenging.

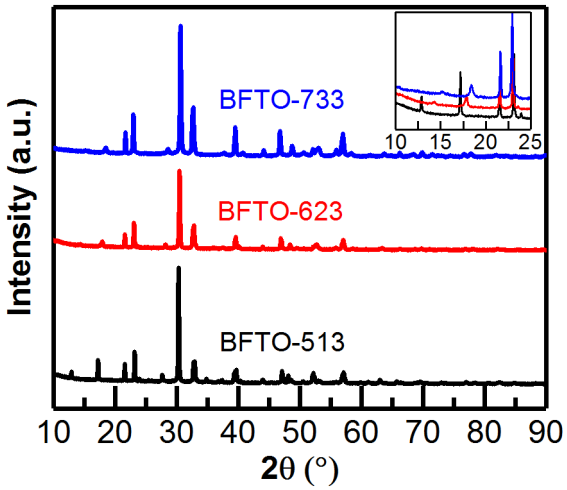

Figure 5.6. *Comparative plot of XRPD patterns for high purity BFTO samples produced with the MOD-EG method. Inset shows shifting peaks on increasing number of layers, and peak broadening. Asymmetric broadening for BFTO-623 at ~ 17° is most notable (**inset**).*

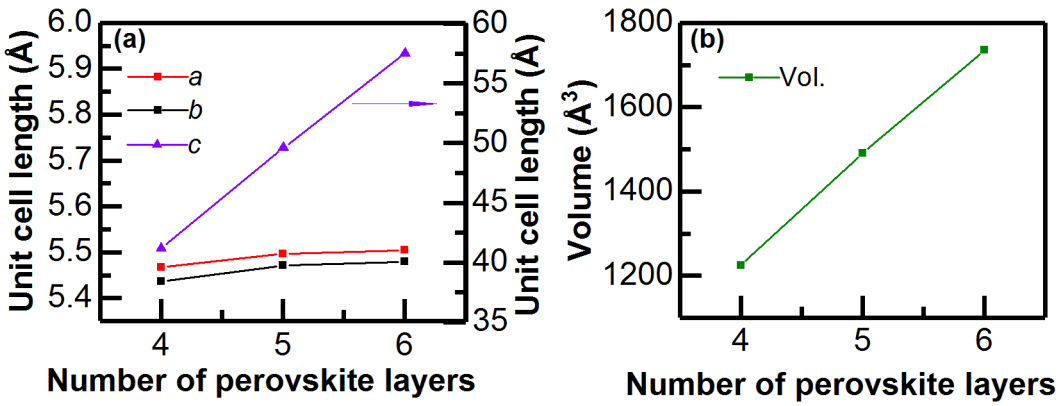

Figure 5.7. *Plot of refined orthorhombic unit cell parameters* ***(a)*** *and volume* ***(b)*** *for the BFTO materials. There is a significant increase in the long axis* **c** *as the number of layers are increased.*

In order to understand the average structure of these compounds, Rietveld refinement was performed in the space group *F*2*mm*. This space group captures some information about off centre displacements of Bi and Ti/Fe with respect to the polar axis of the unit cell (defined as the crystallographic '***a***' axis in the refinements presented in this thesis) which are the main contributors to the ferroelectric character in these materials. It should be noted that this space group does not capture octahedral tilting modes which impact ferroelectric properties, and are known to exist in the host $Bi_4Ti_3O_{12}$ material[387]. However, an idea of the relative metal ion coordinates and potential chemical ordering phenomena might be obtained from refinement in *F*2*mm* as a starting point for improved future refinements.

This first set of refinements were conducted on the collected lab XRPD data. Several models were developed to test different fixed site occupancies in the perovskite *B*-sites to probe for preferential chemical ordering (**Figure 5.8**). These were based on *F*2*mm* reported structures for each compound[159, 167, 169, 174]. The oxygen positions were fixed at those quoted in the literature reports, as the lab XRPD data could not provide good resolution for such light elements. The cation positions and their thermal parameters were refined. The March-Dollase[388] function was used to account for preferred orientation in the prepared samples.

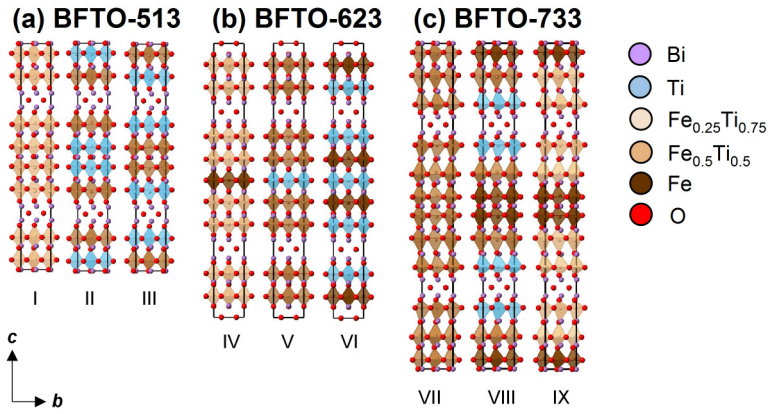

Figure 5.8. *Graphical representation of* ***(a)*** *BFTO-513,* ***(b)*** *BFTO-623 and* ***(c)*** *BFTO-733 structures in the* F2mm *space group as reported by others, which do not allow for octahedral rotations. Models I-IX represent different chemical occupancy models which were used in the subsequent refinement.*

Refinements tended to converge with both the transition metal cations in the *B*-site (Fe and Ti) shifted with respect to the bismuth *A*-site cations along the polar axis, suggesting exhibition of ferroelectricity in each case, though the error bars on the positions were high (**Table 5.3**). The refinement of the thermal parameters (U_{iso}) for each cation was somewhat informative in identifying sites in the structure that may be subject to more complex local structural and/or chemical order. In all three materials, the bismuth ions in the $[Bi_2O_2]^{2+}$ layers have the highest and most variable thermal parameters between models, suggesting some structural disorder between layers. The thermal parameters of the transition metal ions in the *B*-sites all suggest some instability. In BFTO-513 the thermal parameters for the outer layers are consistently high but moderately alleviated by placing more titanium at this site. However, there are still indications of a possible need for an extra degree of freedom in the modelling of this position. In BFTO-623, the inner site shows a large thermal parameter, somewhat alleviated by placing more titanium in the centre, but again indicates an issue with the structural model. The low thermal parameters of the outer sites indicate a need for more intensity in these areas in the refinement, which may reflect a need for more iron in the outer sites in the model. In BFTO-733 the thermal parameters of each site are reasonable, but again higher in the inner sites and lower in the outer site, suggesting a moderate preference for iron either spread across all sites, or in the outer sites.

Table 5.3. *Rietveld refined thermal parameters U_{iso} for the transition metal ions in* F2mm *BFTO materials.*

Sample	*Model*	*Outer site U_{iso} ($Å^{-2}$)*	*Middle site U_{iso} ($Å^{-2}$)*	*Inner site U_{iso} ($Å^{-2}$)*	*R_{wp} (%)*
BFTO-513	I	0.17(4)	N/A	0.06(2)	5.98
	II	0.12(4)	N/A	0.10(3)	6.02
	III	0.18(4)	N/A	0.03(2)	6.04
BFTO-623	IV	-0.003(20)*	-0.01(2)*	0.2(1)	6.33
	V	0.003(21)	-0.006(25)*	0.1(1)	6.29
	VI	-0.0004(212)*	0.002(27)	0.1(1)	6.31
BFTO-733	VII	0.003(39)	0.02(5)	0.06(5)	6.29
	VIII	0.003(41)	0.02(5)	0.08(6)	6.33
	IX	-0.005(36)*	0.02(5)	0.09(6)	6.14

**Unfeasible negative values suggest sites that require more in-depth structural and chemical descriptions.*

In each refinement, the standard error associated with the refinement is quite high, and so a definitive choice of best model could not be made. A cautious interpretation of these results is also necessary as the EDXS analyses revealed potential stoichiometric deviation in BFTO-623 and BFTO-733, and the XRPD data has limitations to elemental resolution (as outlined in Chapter 3). In order to get a better idea about the elemental distribution, Mössbauer spectroscopy was utilized instead.

5.2.2 Mössbauer Study of Iron Location

As presented in the previous chapter, Mössbauer spectroscopy can be a very useful method of extracting information about the local environments of iron atoms in solid materials. Spectra obtained from all three sample compositions at room temperature show symmetric, but broad, paramagnetic doublets. The isomer shifts for each signal are consistent with the Fe^{3+} valence state, in line with expectations. The symmetric nature of the doublets do not suggest strong preferences for chemical ordering, or occupation of sites with distinctly different local electric field gradients.

Spectra shown in **Figure 5.9** can be modelled well using a broad doublet with the fitting parameters outlined in **Table 5.4**. The IS and QS are similar, but the slightly smaller QS in BFTO-733 may suggest a weaker electric field gradient (perhaps resulting in lower spontaneous ferroelectric polarisation). The marginally larger IS would also reflect a more iron rich environment in BFTO-733 in comparison with the other materials. The broader signal in BFTO-623, reflected in the Half Width Half Maximum (HWHM) refinement, may imply a degree of structural disorder leading to a distribution of local environments[309].

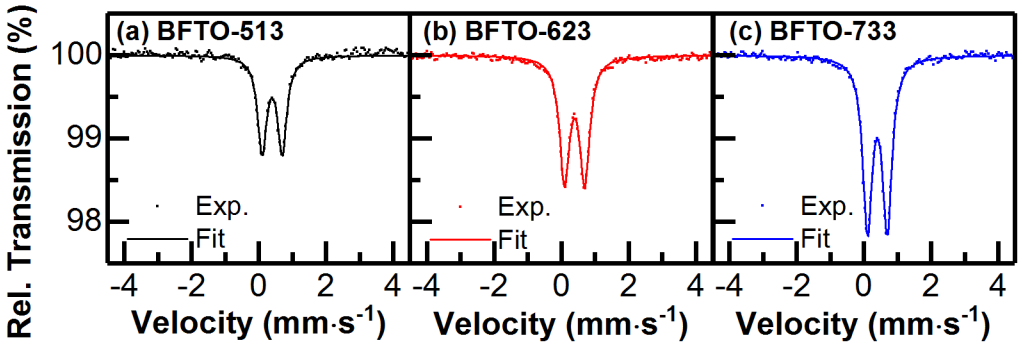

Figure 5.9. *Room temperature ^{57}Fe Mössbauer spectra from BFTO samples showing the relative transmission as a function of source velocity. Symmetric, paramagnetic signals are observed and fitted to a single broad doublet.*

Table 5.4. *Single paramagnetic doublet fit parameters for each BFTO Mössbauer spectrum.*

Material	*IS (mm.s^{-1})*	*HWHM (mm.s^{-1})*	*QS (mm.s^{-1})*	*χ^2*
BFTO-513	0.3999	0.1613	0.5958	338.7151
BFTO-623	0.3978	0.1764	0.6007	290.7053
BFTO-733	0.4032	0.1681	0.5862	265.5781

Interestingly, throughout the literature Mössbauer studies present a wide range of fitted parameters from IS 0.16 – 0.44 and QS from 0.3 – 0.75 mm.s^{-1} [124, 140, 165, 173, 175, 389-391]. The interpretations for the nature of iron's local environment in these compounds is diverse. It has been suggested that at least two crystallographic sites are distinguishable in Mössbauer in all of the three nominal compositions under investigation, with some suggestion of the outer site possessing a larger electric field gradient and hence corresponding to signals with a large QS value from fitting[391]. In BFTO-513 which is the most often investigated, it has been suggested that Fe is distributed equally over two unique sites[165], though others suggest that there is more Ti^{4+} in the site that borders the $[Bi_2O_2]^{2+}$ layer[126]. Systematic studies suggest that as the number of layers increase, the Fe^{3+} randomizes over two sites[389] and there is also suggestion that one of these sites may be tetrahedral[173].

To make sense of this, the crystal structure is considered. In BFTO-513 there are two crystallographically distinct sites iron can occupy – the octahedral site that borders the $[Bi_2O_2]^{2+}$ layer (2 ions) and the octahedral site inside the centre of the perovskite block (2 ions). In BFTO-623 there is a third unique octahedral site inside the true middle of the perovskite block (1 ion) and in BFTO-733 this inner site is a pair of ions. The initial results would indicate either occupation of a single site in each of the three cases, or occupation of sites that have very close crystal field parameters in equal quantities, contrary to the other Mössbauer studies.

A refitting of this data was attempted with multiple paramagnetic components. The fitting results shown in **Figure 5.10** and **Table 5.5**, show a fit with more than one paramagnetic component for BFTO-513 and BFTO-733, but the overall fit improvement is not significant in comparison with the single doublet fit in **Table 5.4**. Interestingly, BFTO-623 could not be refined with an extra component. This implies there is no quantitative evidence for a distribution of iron in distinctly different crystal field environments. It is proposed that the broad experimental signals actually represent a spread occupation of crystallographically similar sites in the perovskite block which produce close QS and IS values, rather than any true long range chemical ordering.

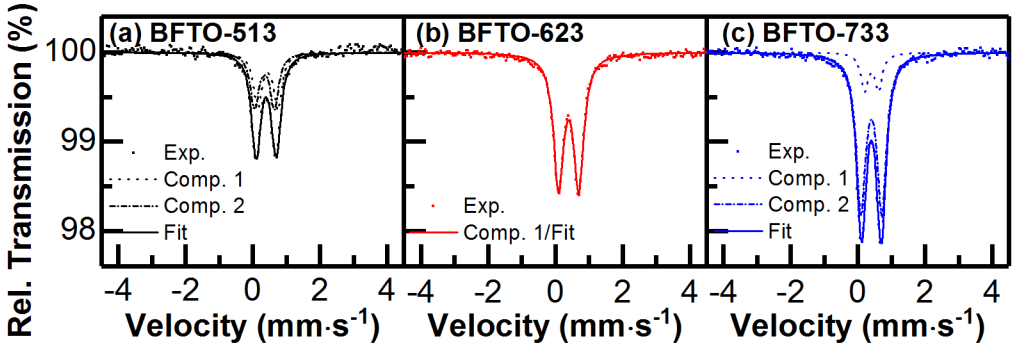

Figure 5.10. *Room temperature ^{57}Fe Mössbauer spectra of the three BFTO materials shown* ***Figure 5.9****, but showing results from two component fits (only possible in* ***(a)*** *and* ***(c)****).*

Table 5.5. *Multiple paramagnetic components fit parameters for each BFTO Mössbauer spectrum.*

Material	*Component*	*IS (mm.s^{-1})*	*HWHM (mm.s^{-1})*	*QS (mm.s^{-1})*	*Proportion*	*χ^2*
BFTO-513	1	0.4478	0.143	0.6025	0.4931	332.7589
	2	0.3503	0.1482	0.5891	0.5069	
BFTO-623	1	0.3978	0.1764	0.6007	1.0000	290.7053
BFTO-733	1	0.4094	0.1307	0.4194	0.1596	258.4884
	2	0.4024	0.1634	0.6231	0.8404	

5.2.3 Average Structure Evolution – Refined Model

Having seen in the Mössbauer measurements that disordered chemical occupation of the layered sites is most likely, a new set of structure refinements were conducted employing random elemental occupancies. This study began by developing new models for BFTO-513 and BFTO-733 which included octahedral tilting modes. These two odd-numbered Aurivillius structures have been quoted to have the space group $A2_1am$ in some studies (with only BFTO-513 having structural parameters reported[164, 165]). Models were built by combining the literature $A2_1am$ BFTO-513 structure and the refined coordinates from the previous $F2mm$ refinement

in **Section 5.2.1**. The titanium and iron distribution in these models was set to be random, reflecting the Mössbauer results. A visual representation of the occupancies used are shown in **Figure 5.11**, and the imposed octahedral rotations about ***a*** are also clearly shown.

The refinement of the metal positions and U_{iso} only were conducted, and given the occupancies were random for the Fe and Ti, the U_{iso} values for each site were set to be equal. The oxygen positions were again fixed to values from the literature. The results of the refinements of BFTO-513 and BFTO-733 are presented in **Tables 5.6** and **5.7** respectively. The extra degree of freedom this space group affords in the ***b***-axis displacement improves the overall fit of both materials, though in general the Fe and Ti ions share high thermal parameters. Again, the standard uncertainties on the positions and thermal parameters are high making direct comparison difficult, but the trend remains that the shifts of Bi and Ti/Fe with respect to one another along the polar axis is higher in BFTO-513. It should be noted that in both structures, the ***c***-axis displacement of the outer perovskite layer ion is relatively larger than the inner ions (visually obvious in **Figure 5.11**), suggesting this site is naturally distorted by the neighbouring $[Bi_2O_2]^{2+}$ layer.

Table 5.6. *Refined fractional coordinates and thermal parameters for bismuth and Ti/Fe ions in BFTO-513.*

BFTO-513	*$A2_1am$, **a** = 5.4676(4) **b** = 5.4364(4) **c** = 41.190(2) Å*				
	Occupancy	*x (polar)*	*y*	*z*	*U_{iso} (Å^{-2})*
Bi1 (centre)	$Bi_{1.0}$	0.24(1)	0.75(1)	0	0.045(5)
Bi2 (mid layer)	$Bi_{1.0}$	0.24(1)	0.75(1)	0.1049(2)	0.047(4)
Bi3 ($[Bi_2O_2]^{2+}$)	$Bi_{1.0}$	0.25(1)	0.733(6)	0.2193(2)	0.055(4)
Fe/Ti1 (outer)	$Fe_{0.25}Ti_{0.75}$	0.29(2)	0.26(3)	0.1514(7)	0.071(6)*
Fe/Ti2 (inner)	$Fe_{0.25}Ti_{0.75}$	0.27(4)	0.25(6)	0.0503(9)	0.071(6)*
R_{wp}	4.50				

*fixed to be equal

Table 5.7. *Refined fractional coordinates and thermal parameters for bismuth and Ti/Fe ions in BFTO-733.*

BFTO-733	*$A2_1am$, **a** = 5.4792(6) **b** = 5.5051(6) **c** = 57.536(7) Å*				
	Occupancy	*x (polar)*	*y*	*z*	*U_{iso} (Å^{-2})*
Bi1 (centre)	$Bi_{1.0}$	0.25(3)	0.75(2)	0	0.02(2)
Bi2 (mid mid)	$Bi_{1.0}$	0.25(2)	0.76(1)	0.0729(5)	0.01(1)
Bi3 (mid outer)	$Bi_{1.0}$	0.25(4)	0.74(2)	0.1479(5)	0.04(1)
Bi4 ($[Bi_2O_2]^{2+}$)	$Bi_{1.0}$	0.25(3)	0.76(2)	0.2256(4)	0.07(1)
Fe/Ti1 (outer)	$Fe_{0.5}Ti_{0.5}$	0.25(5)	0.25(7)	0.188(1)	0.07(6)*
Fe/Ti2 (middle)	$Fe_{0.5}Ti_{0.5}$	0.22(5)	0.21(3)	0.105(1)	0.07(6)*
Fe/Ti3 (inner)	$Fe_{0.5}Ti_{0.5}$	0.22(5)	0.25(6)	0.037(2)	0.07(6)*
R_{wp}	5.78				

*fixed to be equal

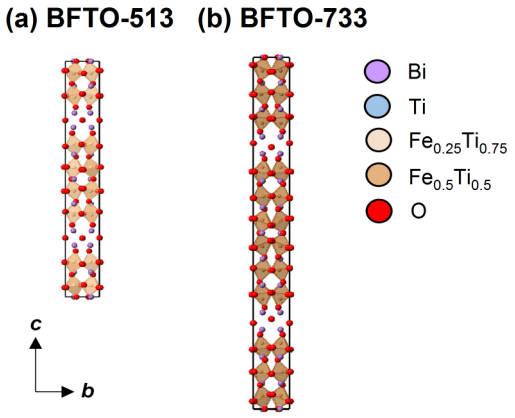

Figure 5.11. *Graphical representation of Rietveld refinements for* ***(a)*** *BFTO-513 in* $A2_1am$*, and* ***(b)*** *BFTO-733 in* $A2_1am$*, projected along the polar* **a***-axis, showing the octahedral rotations and relative site occupancies.*

BFTO-623 having an odd number of layers, should have a different space group compared with the other two materials when tilting is considered. It is sometimes reported to have the space group *B2cb*[146, 166, 392] which permits rotation (though no structure information has been reported). A model was built based on the structure of $Bi_4Ti_3O_{12}$ (BTO)[109] but a meaningful fit could not be obtained for this sample. It is suspected that a likelihood of structural faulting in the sample in combination with an ill-defined model have played a role here and thus to be reconsidered in future works.

From this average structure analysis, it is apparent that BFTO-513 with 4 layers and BFTO-733 with 6 layers have been synthesized, with the best fit obtained when octahedral tilting is taken into account. However, there are clear limitations to this refinement, and it would be desirable to repeat using more advanced diffraction methods such as neutron diffraction. The reason for a lack of published structures and certainty around the location of Fe and Ti in the layers is believed to be a consequence of difficultly growing phases with uniformly layered structures, especially in high iron samples. Insight into the tilted structure of BFTO-733 from this perspective is a unique and valuable contribution and unusual observations in the chemical nature of the material are flagged.

In general, it appears that there is little evidence for chemical ordering in these samples when the Mössbauer data are considered. Such a random distribution of iron has implications for the physical properties, particularly the magnetism which would require close proximity for long range ordering. It also seems likely that both BFTO-513 and BFTO-733 would be ferroelectric, while the behaviour of BFTO-623 remains uncertain and so the magnitude of the ferroelectric properties should also be evaluated.

5.3 Physical Properties

5.3.1 Magnetic Properties

If the outer perovskite sites in these layered structures were consistently and highly occupied by iron, it may have been possible to establish long range magnetic ordering. However, the detection of likely random occupancy, and lack of magnetic splitting in the Mössbauer, suggests any magnetic interactions would be mostly local. This does give interesting opportunities for 2D or clustered magnetic effects within the perovskite layers though. Temperature and field dependent magnetization of the three materials BFTO-513, BFTO-623 and BFTO-733 were measured. The magnetic responses change subtly, but clearly as the iron content and structure changes.

At 3 K in the field dependent testing, BFTO-513 shows non-linearity, though no clear hysteretic behaviour (**Figure 5.12 (a)** and **inset**). This may indicate a proportion of local magnetically interacting ions such as in dilute magnetic semiconductors, or superparamagnetism with underlying antiferromagnetic interactions[131, 141]. With respect to temperature, this material shows paramagnetic type behaviour over most of the range (**Figure 5.12 (b)**).

The BFTO-623 sample shows clear hysteresis in the ***M-H*** plots (**Figure 5.12 (a)** and **inset**). This implies proximity to a transition in the magnetic behaviour in which a net moment arises. There is decreased magnetization at low temperature (**Figure 5.12 (b)**) (and a different inflection, seen more clearly in $1/\chi$ in **Figure 5.13**) in comparison to BFTO-513 and an inflection and ZFC/FC divergence below 15 K. This has also been seen by others[122], and a higher coercivity in the ***M-H*** below such transitions is noted[122, 138].

In the BFTO-733 sample the ***M-H*** curves are more linear and unsaturating (**Figure 12 (a)**). The low temperature magnetization is lower than the previous samples, briefly increasing into an apparent transition near 100 K (**Figure 12(b)**). This behaviour is more reminiscent of antiferromagnetism below 100 K. Some ZFC/FC divergence is also noted at low region of the ***M***-T, and in conjunction with some minor hysteresis in the ***M-H***, indicates the region below 100 K is in some kind of ordered state, though may not be part of a fully 3D, long range structure due to the broadness of the transition feature. This is likely the same type of transition seen in BFTO-623 but at a higher temperature. This transition has been suggested to be a spin glass transition[122] due to the ZFC/FC divergence and also a transition from canted antiferromagnetism to paramagnetism (after which the remanence is lost) and the increasing broadness of the transition is associated with structural inhomogeneity[138]. In this case, the transition appears at lower temperatures than is typically reported. Low temperature Mössbauer experiments in the literature suggest the emergence of sextet signals below the

aforementioned transitions[122] (which was not seen in this study) and inconclusive evolution of magnetic peaks for BFTO-733 at low temperature[151].

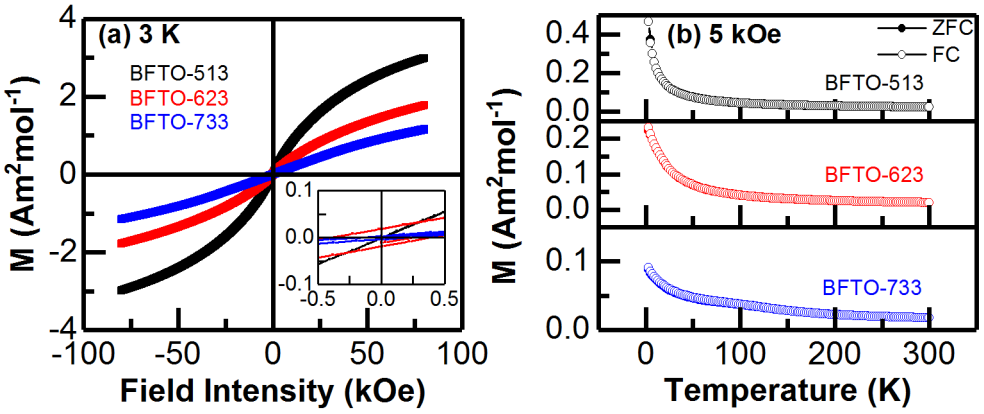

Figure 5.12. *In* ***(a)****, field dependent magnetization curves of the samples at 3 K show emergence of more typical antiferromagnetic like responses as layers/Fe content is increased. Inset shows appreciable hysteresis in BFTO-623 which is likely due to proximity to a transition at this temperature. In* ***(b)*** *the temperature dependent magnetization of samples under a field of 5 kOe is presented, exhibiting some ZFC/FC divergence in BFTO-733.*

To extract further information about the nature of magnetic interactions in this system, the ***M***-T data are fitted to the Curie-Weiss law (**Figure 5.13**). Fitting the paramagnetic portion of the ***M***-T data gives negative intercepts with the x-axis for all three materials, suggesting dominant antiferromagnetic interactions. This is expected from the GKA rules for magnetic superexchange between Fe^{3+}-O-Fe^{3+} pairs. The effective moments calculated for BFTO-623 and BFTO-733 (based on proportion of ion in the Aurivillius phase determined by EDXS) are shy of those expected for an S = 5/2 Fe^{3+} species which would nominally be near 5.9 μ_B, but are reasonable. Lower values of μ_{eff} for BFTO-513 has been reported by others[122, 131, 138] and may be suggestive of clustered centres, though the values of higher layer compounds are not given.

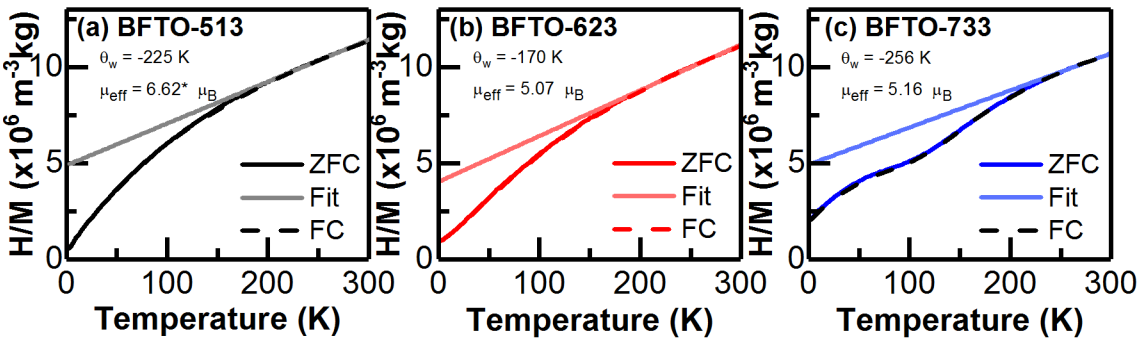

Figure 5.13. *1/χ plots for* ***(a)*** *BFTO-513,* ***(b)*** *BFTO-623 and* ***(c)*** *BFTO-733, linearly fitted in the paramagnetic region to extract the Curie-Weiss temperature (θ_w) and effective moment (μ_{eff}) as noted on each graph. Contrasting low temperature behaviour is clearly noted. *Sample has impurity Bi_2O_3 which affects mass-based calculation.*

In order to explore the possibility of superparamagnetism in these samples, fitting of the field dependent magnetic data was also attempted. Neither BFTO-623 nor BFTO-733 could be fitted to a Langevin function, which implies at 3 K, they are not actually paramagnetic. The Langevin function could be applied to BFTO-513 in order to determine the average cluster moment, but the function does not produce a good fit (**Figure 5.14**). The calculated Langevin cluster moment is low, and in conjunction with a lack of evidence for a superparamagnetic blocking temperature transition in the ***M***-T data and microscopy studies indicating this sample had micron sized particles, this is not likely a superparamagnetic compound. Rather BFTO-513 seems more reminiscent of BFMTO in the previous chapter, where it is not quite in a paramagnetic state and retains some kind of magnetic interaction. This may be related to their similar Fe^{3+} contents and chemical disorder. Another reference also notes how BFTO-513 does not fit to alternate models such as the Brillouin function either[123].

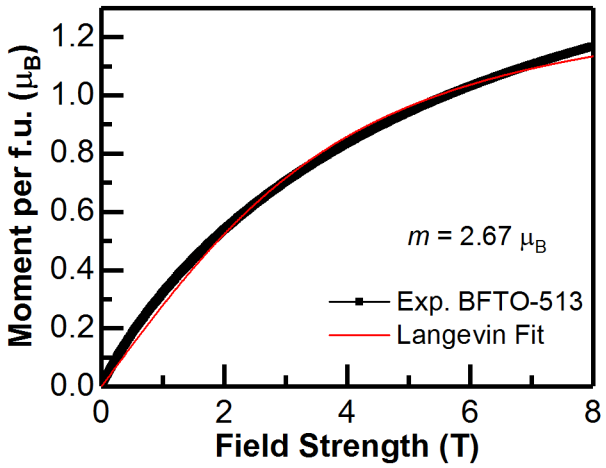

Figure 5.14. *Langevin fitting of* ***M-H*** *for BFTO-513 to produce a cluster moment of 2.67 μ_B. The fitting suggests a state near paramagnetism, but does not involve large clusters.*

These results suggest that, in conjunction with the Mössbauer spectra, the iron in these systems is appreciably disordered and dilute, precluding it from forming long range magnetically ordered structures at high temperatures. However non-typical low temperature interactions appear to exist and the nature of the transition (most obvious in the BFTO-733 sample) is quite interesting and it is desirable to further study the dynamics of this transition with inelastic neutron spectroscopy.

Interestingly, magnetoelectric effects are reported in BFTO-513 in the literature[393]. In order for this effect to be exhibited via the inverse Dzyaloshinkskii-Moriya interaction, an asymmetric non-collinear spin configuration is required[145]. This would imply that despite appearing paramagnetic in magnetization studies, there are some kind of short range magnetic interactions that foster this effect and persist to room temperature, which supports the findings of this study. This may also hold promise for BFMTO in the previous chapter. However, to further investigate this, the materials would also need to be suitably ferroelectric.

5.3.2 Electrical Properties

In addition to the magnetism, it has been suggested in a few reports that the ferroelectric properties are robust in these Aurivillius phases and persist to high levels of iron in films[139, 152, 155]. While it is not thought that iron influences the ferroelectric properties extensively[126], the ferroelectric Curie temperature (still >RT) reportedly decreases with increasing iron[138]. The ferroelectric trends were investigated using Piezoresponse Force Microscopy at room temperature as reliable bulk piezoresponse measurements were not possible on all samples due to low density. Very clear, striped 180° domains were imaged in the BFTO-513 sample consistent with an orthorhombic polar crystal structure (**Figure 5.15 (a) – (c)**). In BFTO-733, there is some suggestion of other, non-180° domains, resembling BTO[114] (**Figure 5.15 (d) – (f)**). Both the grain size and the domain size is observed to decrease from low layers to high layers. The small grain size may be attributed to the lower sintering temperature, however the smaller domain size is more likely to be attributable to variation in the chemical composition restricting domain size. This may be the first time that such clear striped domains have been imaged in this sample, appearing less defined and with different shapes in the only other available studies[139, 145, 148, 150, 172, 393].

It was not possible to image domains in BFTO-623 and this is suspected to be due to sample quality. Interestingly ferroelectric domains have not been imaged in literature on this material either[172]. This poses the question as to whether a lack of well-defined domains is connected to a general difference in the odd numbered phases in comparison to the even numbered ones.

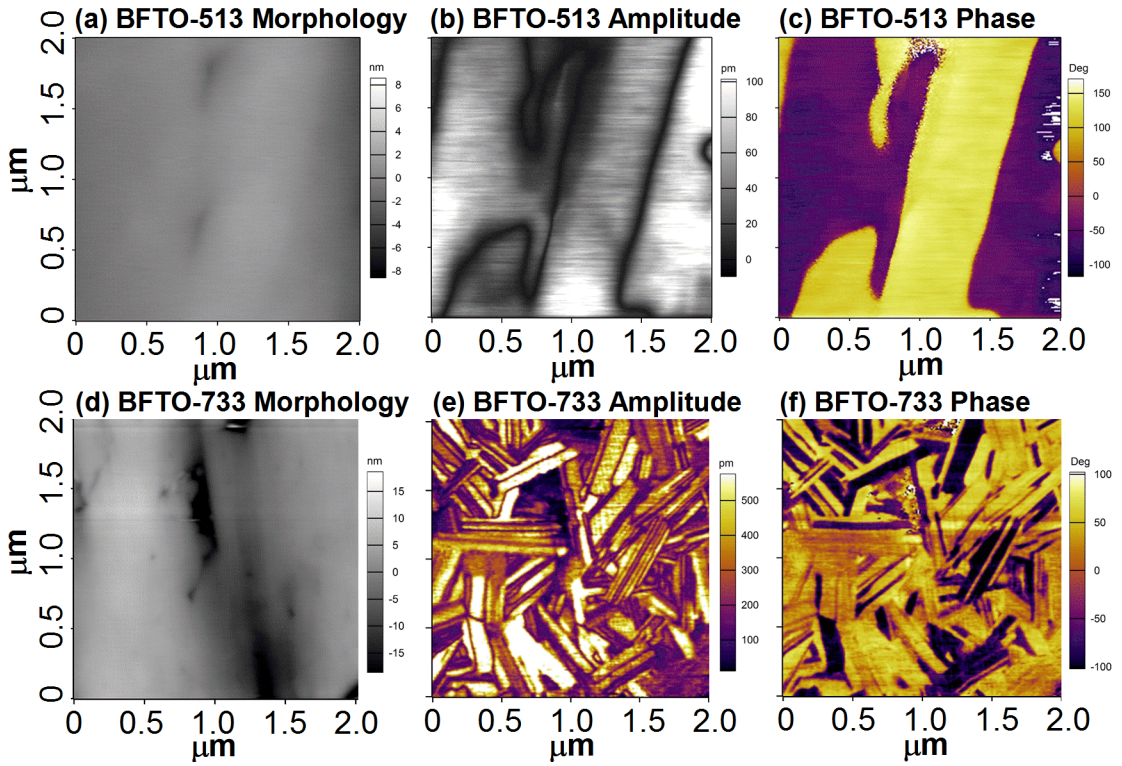

Figure 5.15. *In* ***(a)*** *and* ***(d)*** *the morphology of samples BFTO-513 and BFTO-733 are respectively shown. The* ***(b)*** *and* ***(e)*** *plots show the corresponding PFM amplitude maps and* ***(c)*** *and* ***(f)*** *show the phase contrast. Stripe-like 180° domains are observed in both samples, with evidence for some addition non-180° domains in* ***(f)****.*

Hysteresis measurements were made on all samples using the PFM technique, including BFTO-623, which requires only a small area. The comparison of the phase, amplitude and piezoresponse of the three materials shows a decreasing trend on increasing iron content/number of layers, but is still apparent in all samples (**Figure 5.16**). The iron may be having the effect of reducing domain size and overall polar response.

The increase in coercivity in BFTO-623 may suggest a defect induced domain wall pinning phenomenon as a consequence of structural disorder (commonly noted in $BiFeO_3$ systems[57]). Though it should also be noted that in odd number Aurivillius compounds like BFTO-623, there is the possibility of small ***c***-axis polarisation in addition to the polar ***a***-axis[387] which changes the possible domain configurations, and as the strain distribution in odd numbered structures is also different[394], it is not unreasonable for the piezoresponse to appear different in comparison with the other two materials. The possibility of stacking faults in this sample can also lead to an inconsistent repeating of layers can add symmetry restrictions to the observation of polar domains[154]. Indeed, BFTO-623 and BFTO-733 show non-180° switching in this measurement (**Figure 5.16 (a)**) and strongly asymmetric amplitude responses (**Figure 5.16 (b)**).

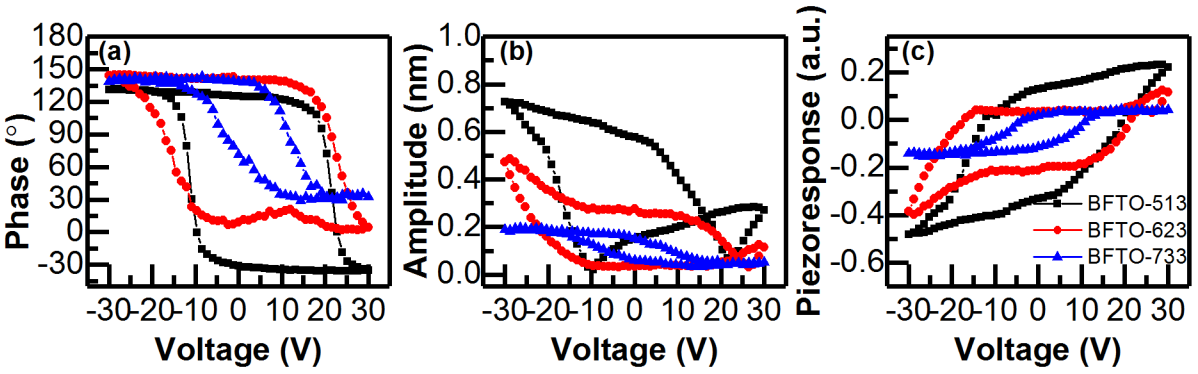

Figure 5.16. *PFM switching spectra for BFTO samples. Phase* ***(a)****, amplitude* ***(b)*** *and piezoresponse* ***(c)*** *are shown. Increasing iron content leads to decreasing piezoresponse.*

In these samples, such domain structures and piezoresponses are very promising for engineering functional devices. This is especially useful for the high iron content samples which show possible magnetic ordering at low temperatures. Both effects coexistent and an ability to manually write ferroelectric domains might lead to next generation memory storage devices. Should they also show visible light utility, photovoltaic application might also be a possibility.

5.3.3 Optical and Photofunctional Properties

The photofunctional responses of the three different materials in the bulk form are rarely compared in the same study. Given all three samples showed evidence for a ferroelectric response, they are candidates for exhibiting the bulk photovoltaic effect. In order to measure this visible light utility in this thesis, UV-Vis diffuse reflectance measurements were undertaken. The spectra obtained (**Figure 5.17**) suggest that all three samples utilize the visible light range quite effectively. The sample BFTO-733 in particular shows a sharp and clear absorption edge near ~ 2 eV. These results are mostly within the range reported for other bulk studies[127, 130, 133, 135, 136], however the BFTO-513 sample, which from its physical colour (yellow in comparison to the orange of other sample) might be expected to have a wider band gap[128, 135], shows quite a flat absorbance profile. Influence from particle morphology (and associated reflectance) in this sample might be a contributing factor to the flat profile[135, 395]. The origin of visible light absorbance is attributed theoretically to expansion of the conduction band by introduction of iron, eventually dominating transitions from the valence band to the higher energy Ti3d bands[126-128, 133]. A visible light absorbance has previously been connected to photocatalytic and/or photovoltaic ability in individual members of the Aurivillius series[127, 128, 132, 136] and so it is suggested that each will show similar performance in visible light photofunctional applications.

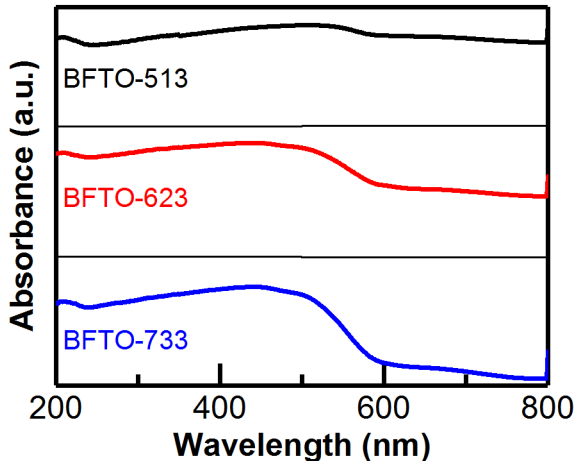

Figure 5.17. *Visible light absorbance profiles of BFTO materials show apparent edges in the ~ 2 eV range.*

The electronic response of the material to light irradiation was then tested by locally mapping the surface potential variation of the samples (with PFM) on exposure to laser light. The results showed a very strong response of similar magnitude in both the BFTO-513 and BFTO-733 samples, and a lower but still significant response in the BFTO-623 sample (**Figure 5.18**). All samples showed a stronger response than BFMTO and BFNTO shown in the previous chapter, suggesting not only strong visible light absorption but also strong directional transport. The lower performance of the BFTO-623 of the three is suspected to arise from structural disorder and macroscopic sample quality, as is reflected in the other polar measurements. The similar response in all samples indicates their fundamental band gaps are narrower than the irradiation source.

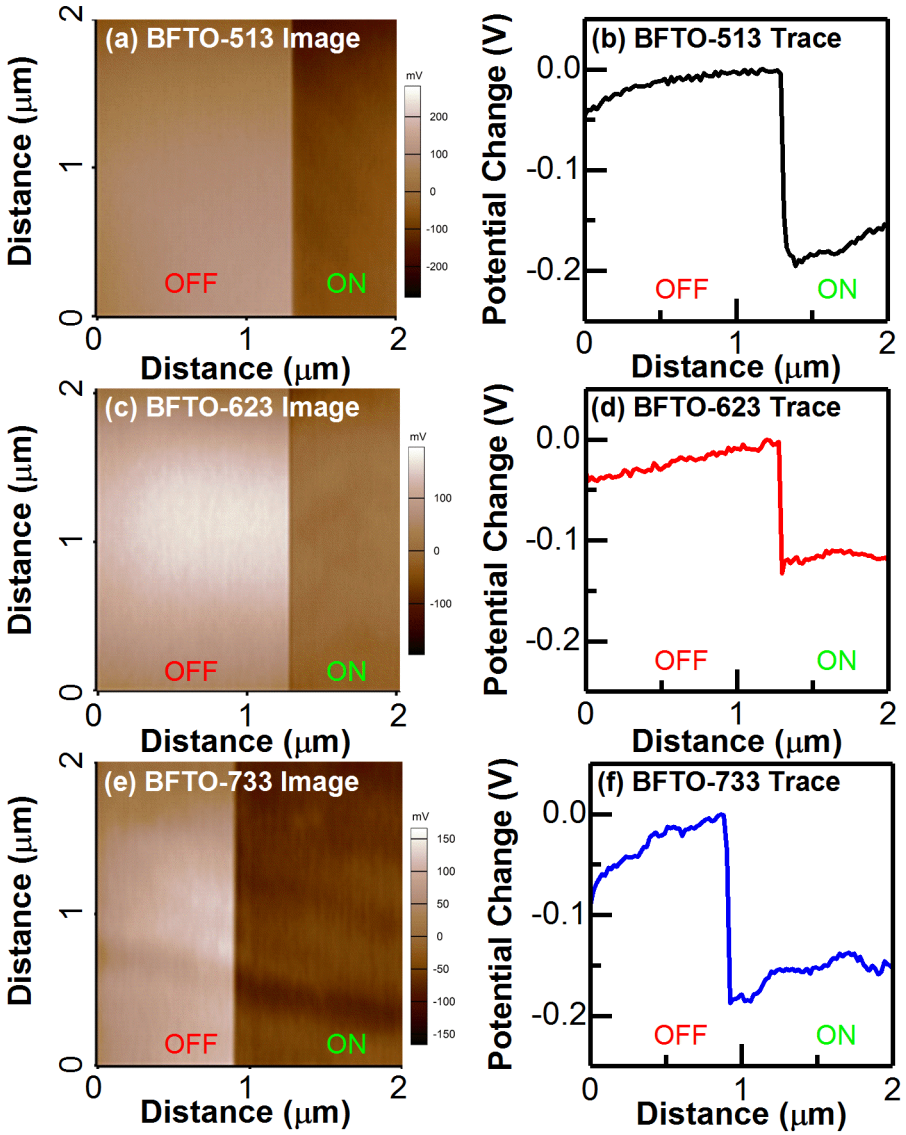

Figure 5.18. *Surface potential of each BFTO sample in ambient (OFF) and 458 nm laser (ON) lighting conditions. Decreasing potential on irradiation suggests migration of photoexcited charges to the surface in all three samples.*

This result is further extended to monitoring the current-voltage relationship of the sample over a large distance, using visible light irradiation from a mercury lamp to incite a response. It is notable that the dark current increases proportional to the amount of Fe in the sample (**Figure 5.19**, closed symbols), suggesting a strong influence on the energetic barriers to conduction. On irradiation, a photocurrent is observed in each sample and a diversion to more linear current-voltage behaviour (**Figure 5.19**, open symbols). Since these samples could not be poled using this equipment (limited to an application of 10 V), this may explain the lack of strong diodic-shaped current-voltage curve otherwise expected from the observation of domains in the sample.

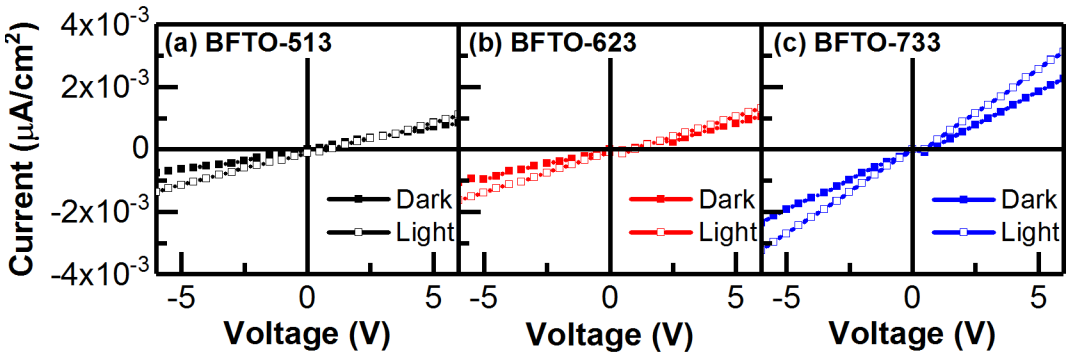

Figure 5.19. *Current-voltage curves on the surface of all three BFTO materials between ~ 0.4 mm separated gold electrodes in the dark (closed symbols) and light (open symbols). More linear responses can be detected in light conditions, and all three samples show obvious photocurrent.*

It has been systematically shown that a photocurrent can be induced in all three samples. The existence this photoresponse in these materials, in addition to a robust polar response, and local magnetic response, further expands the utility of these multifunctional materials and by selecting an appropriate Ti:Fe ratio, the properties may be tuneable for a desired application.

5.4 Summary of Chapter 5

In this study high purity syntheses of Aurivillius compounds with four, five and six-layer perovskite blocks were achieved via a metal organic decomposition. This bulk synthesis method is a notable improvement on methods used in the literature, particularly for the synthesis of BFTO-733. This work allowed systematic study of the materials in relation to the evolution of structure and properties.

The possibility of octahedral tilting was explored in Rietveld refinement of the average structures of these compounds which has not often been reported before. A good refinement of the even layered compounds in the polar orthorhombic space group $A2_1am$ was obtained, though refinement of the odd numbered BFTO-623 was inconclusive and suggested a possible propensity for this target composition to result in disordered structures instead. Locally, it was demonstrated that the materials had a disordered distribution of iron in the perovskite layers using Mössbauer spectroscopy, which is in contrast to other reports.

It is suggested that this occupation trend inhibits long range magnetic ordering, which is reflected in the magnetization measurements. Only some suggestion of antiferromagnetic type longer-range order at low temperature is seen (below 100 K in BFTO-733 and 15 K in BFTO-

623) and the modelling of ***M-H*** data at 3 K indicates none of the three samples are typically paramagnetic, supporting some kind of other interacting state.

It is also shown that all samples exhibit ferroelectric properties, and iron seems to have only a marginal decreasing effect on the magnitude of the polar response. All three materials are also able to generate a photocurrent under visible light radiation due to a ~ 2 eV band gap, which is a stronger result than the other titanium containing samples in Chapter 4. The BFTO-623 material is consistently noted to show slightly anomalous properties like polar coercivity, and decreased relative photocurrent, which is linked back to the suggested structural disorder. Irrespective of that disorder, the material is still multifunctional and promising in many ways.

In this chapter the Aurivillius bismuth iron titanates are shown to be another group of photofunctional oxides which can be made under ambient pressure conditions. While titanium again seems to preclude strong magnetic properties as in Chapter 4, this structure type supports greatly improved photofunctionality, likely as a consequence of its clearly defined ferroelectric domains. Similar combinations of elements with different structure types evidently have an impact on functionality, as is further addressed with a new host oxide in the next two chapters.

Chapter 6 Vanadium and Nitrogen Modified Anatase-type Titanium Dioxide Materials

In the previous chapters, modification of oxide materials through elemental substitution was addressed. In each of these cases, elemental complexity resulted in random occupation of octahedral sites in the structure, which impacted predominately on ancillary properties like magnetism. In this chapter, a new oxide is chemically modified with both cations and anions (albeit in much smaller amounts), to target alteration of the specific photofunctional property of photocatalysis.

The anatase polymorph of TiO_2 can be synthesized with a very small particle size, making it a great host oxide for modification to target photocatalysis. However, with an indirect band gap of ~ 3.2 eV, doping is required to increase its visible light utility. As outlined in the introduction, it has been proposed in the literature that pairing V^{5+} with N^{3-} is a way to effectively extend the valance and conduction bands and effectively narrow the band gap. Strong and stable V^{5+}-N^{3-} pairings are computationally predicted to be the only type of defect that forms.

Among the experimental literature however, while (V,N)-TiO_2 anatase has been made, its ability to act as a photocatalyst appears variable. One of the key issues appears to be a mix of vanadium (V^{5+}, V^{4+}) and titanium (Ti^{3+}, Ti^{4+}) valence states and locations for nitrogen (interstitial, substitutional) within the host TiO_2 anatase structure, deviating from computational prediction. This raises questions about how the dopants are actually incorporated into anatase, what impact the synthesis conditions have on the product, how the resultant defects actually impact photofunctionality and what needs to be considered in rational design of catalysts.

This chapter works to resolve these questions and build on the thesis theme of how chemical control and structure impact functionality. Vanadium modified anatase TiO_2 is produced by utilizing a known method for making the sister compound (Nb^{5+},N^{3-})-TiO_2. The structure and valence states are studied with diffraction, microscopy, and spectroscopy to determine if and how this co-doped product can be formed, and how this relates to any presented photocatalytic ability.

6.1 Synthesis

In order to try and control the vanadium valence state on introduction into anatase TiO_2, a method was required that could facilitate simultaneous incorporation of nitrogen, and also result in a small particle size appropriate for photocatalytic testing.

6.1.1 Solvothermal Method

Reports of (V,N) co-doped anatase in the literature use a mix of different methods and reactants[214-219], making it difficult to isolate which steps are important to valence control and functionality. For this reason, a synthesis was designed around a solvothermal method which has been shown to be extremely successful in producing the analogous (Nb,N) co-doped TiO_2 anatase[206]. The solvothermal method is different to the synthesis methods presented so far in this thesis, in that it is a fundamentally wet chemical method, and does not use high temperature sintering to promote a reaction. Instead, the reactants are dissolved in a solvent and subject to high pressure and temperatures above the solvents usual boiling point. In this supercritical state, small oxide crystals can be nucleated as the reactants polymerize and organic species decompose. This is a useful method for producing nanomaterials.

In this solvothermal study, the raw materials were dissolved in ethanol and reacted in autoclaves at 200 °C for 17 hours. The source of titanium was $TiCl_4$ and for nitrogen HNO_3 was chosen. As part of this investigation was a desire to study how the vanadium source and nitrogen co-dopant levels influenced the valence control and functionality in the product, two vanadium sources were used: $VOCl_3$ (V^{5+}) and $VO(C_5H_7O_2)_2$ (V^{4+}). Amounts of both were chosen to give a nominal vanadium doping level of ~ 5 at. % (cations). The choice of 5 at. % nominal doping is to reflect the various simulation studies on the generation of the V^{5+}-N^{3-} defect pair. The nitrogen (HNO_3) was added in various levels of excess with the goal of obtaining a product with V^{5+} and N^{3-} in a close to 1:1 ratio doped into the TiO_2 anatase matrix. A summary of the syntheses is presented in **Table 6.1**.

Table 6.1. *Summary of doping schemes in synthesized VTON samples.*

Material Name	*Nominal Dopant Ratio V:Ti:N*	*Vanadium source*
VTON-A	0.05:1:9	$VO(C_5H_7O_2)_2$
VTON-B1	0.05:1:5	$VOCl_3$
VTON-B2	0.05:1:10	$VOCl_3$
VTON-B3	0.05:1:20	$VOCl_3$
VTON-B4	0.05:1:40	$VOCl_3$

6.1.2 Microstructure

The products of the solvothermal reaction were fine powders. The colour of the particles ranged from light grey to a light brown. The morphology also seemed highly dependent on the relative amount of nitric acid used in the synthesis as observed in SE micrographs (**Figure 6.1, 6.2**). This change in morphology might reflect formation of more than one polymorph, an effect which is noted to be pH sensitive in other studies[396]. In **Figure 6.1 (a)** the individual particle size of VTON-B1 is ~ 20 nm, and forms agglomerates of mixed size from 100 – 300 nm. VTON-B2 (**Figure 6.1 (b)**) shows larger and more regular agglomerates of size ~ 500 nm. By VTON-

B3 (**Figure 6.1 (c)**) the individual particle shape changes and reduces in size and with the largest amount of nitric acid in VTON-B4 (**Figure 6.1 (d)**), the individual particles are now clearly needle-like and forming large agglomerates. In **Figure 6.2**, the VTON-A sample shows very similar morphology to VTON-B2, suggesting the similar nitric acid content has a strong impact on the morphology, and the vanadium source may have less of an effect. All samples have nanosized individual particles suggesting the method was useful in engineering a material with an appropriate morphology for catalytic testing.

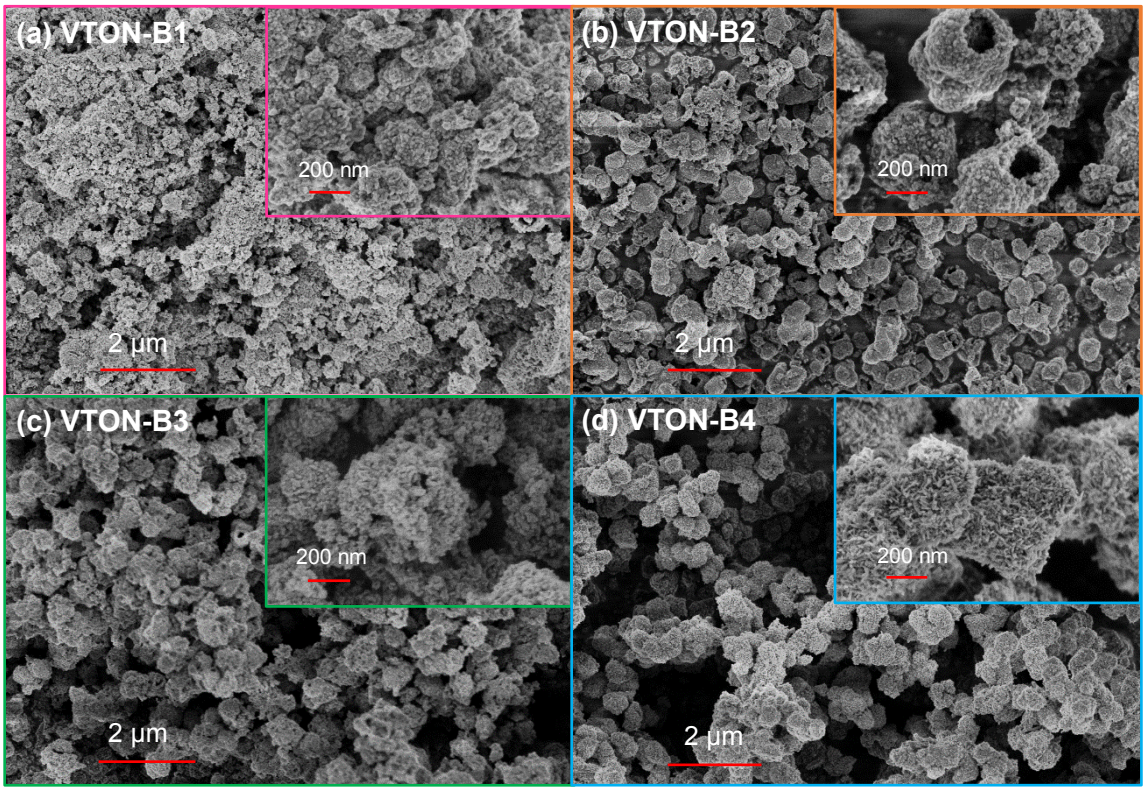

Figure 6.1. *Secondary electron micrographs of VTON-B series samples produced with a* $VOCl_3$ *source and increasing levels of nitric acid from B1 – B4. Morphology of individual particles becomes more needle-like and agglomerate clusters also change from images* ***(a) – (d)****, suggesting a link to the nitric acid volume used in reaction.*

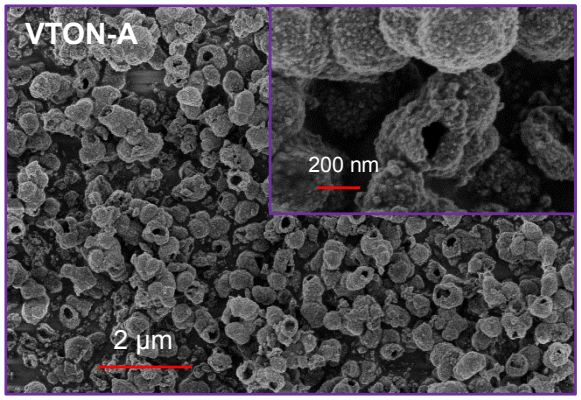

Figure 6.2. *Secondary electron image of VTON-A material show agglomerated structure and individual particles size of ~ 20 nm similar to VTON-B2.*

A confirmation of the phase purity of these samples was required given that TiO_2 has three common polymorphs, each with different band gaps and properties. Then, chemical analyses were require to evaluate the success of the doping procedure.

6.2 Chemical and Structural Analysis

6.2.1 X-ray Diffraction Trends

The structure of the synthesized materials was monitored using X-ray powder diffraction (**Figure 6.3**). Given the particles were so small in size, the resulting peaks were very broad. However, basic information could be obtained. Materials that were prepared with a nominal Ti:N ratio of 1:10 or less (samples VTON-A, B1 and B2) contained particles that could be indexed to an anatase average structure (space group $I4_1/amd$, lattice parameters given in **Table 6.2**), whereas higher volumes of nitric acid resulted in the formation of an additional phase which was indexed to brookite TiO_2 (samples B3 and B4, **Figure 6.3** green and blue plots). This extra phase might reflect the texture effects seen in morphology.

An indication of the particle size trend was obtained by applying Scherrer's equation (see Chapter 2) to the collected XRPD data. It is generally noted in **Table 6.2** that as nitric acid is increased, the particle size of the anatase phase is observed to decrease, which also matches the microscopy data. The particle size appears to be within a range where the stabilities of brookite and anatase become comparable[180], and the lowering pH on increasing addition of HNO_3[397] may be contributing to the overall phase composition. Comparing these results with the literature synthesis of V,N-TiO_2, the particles synthesized in this study are of a similar size[214-216]. Of the samples without brookite peaks, B1 seems to be exhibiting the smallest particle size.

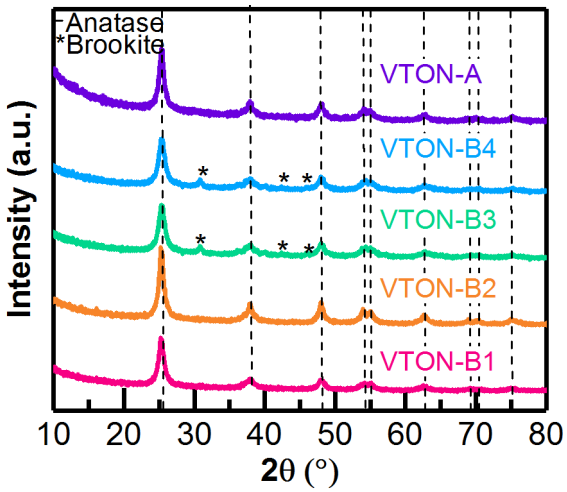

Figure 6.3. *XRPD patterns of VTON materials showing a dominant anatase phase in each with a broad peak shape. Samples B3 and B4 show clear extra peaks corresponding to a brookite TiO_2 phase.*

Table 6.2. *Refined lattice parameters of the anatase phase in each synthesized VTON material and parameters used for application to the Scherrer equation.*

Sample	***a*** *(Å)*	***c*** *(Å)*	*(101) 2θ (°)*	*B (°)*	*D (nm)*
VTON-A	3.7917	9.5005	25.2678	0.8285	9.8
VTON-B1	3.7861	9.4983	25.3016	0.9707	8.4
VTON-B2	3.7891	9.4959	25.2846	0.7771	10.5
VTON-B3	3.7846	9.4662	25.3185	1.0764	7.6*
VTON-B4	3.7818	9.4304	25.3555	1.6604	4.9*

*size of anatase phase, in these samples. A brookite phase is also present.

In these samples, a clear decrease in the lattice parameters is noted in the anatase phase of the impure B3 and B4 samples, while the A, B1 and B2 sample have parameters similar to those reported for un-doped anatase TiO_2[398]. Previous V,N-TiO_2 studies report smaller[217, 219], larger[216] or unchanged[215] lattice parameters for their products in comparison to the un-doped anatase have been reported in the literature, all still taken to indicate successful doping. Given singly doped vanadium systems sometimes note an initial increase in lattice parameters from 0 to ~ 3 at.% V[221, 223, 399] and smaller parameters from after[227, 400-402], and singly N-doped systems report increases[403] or no change[204], the co-doping reports likely hinge on the total doping level of vanadium in particular. In order to investigate these trends further, it was necessary to confirm successful doping and investigate valence states by further experiment. This could be done using XPS.

6.2.2 Chemical Analysis

6.2.2.1 X-ray Photoelectron Spectroscopy Valence Analysis

Determining the valance state of the cations and presence of dopant anions in these materials is of key importance to understanding their functionality. Increased catalytic ability is often said to be associated with V^{5+} located at the surface of the particles, in comparison to buried V^{4+} states[215, 219, 226, 404]. A good technique to investigate this is XPS. While the average penetration depth of this technique is only 10 nm, this matches well with the experimental particle sizes of these samples. This means that representative dopant types, levels and their valence states can be detected.

Figure 6.4 shows characteristics peaks for V **(a)**, Ti **(b)** and N **(c)** in the XPS spectra from each material. An absence of Ti^{3+} in these samples is noted which contrasts to some references[214, 215, 218-220]. Two signals for nitrogen were detected which are consistent with other reports which claim bulk N doping[214-216, 218, 219]. However, the biggest deviation between these materials and other studies, is observed in the $V2p_{3/2}$ peak.

The $V2p_{3/2}$ peak of each sample is very broad (**Figure 6.4 (a)**) suggesting two or more valence states are present in each. This peak was fitted for each sample and the resulted are presented in **Table 6.3**. The binding energies determined for each peak were assigned to V^{3+} and V^{4+} based on previous reports[216, 405-407]. Generally, as the amount of nitric acid was increased the total amount of vanadium increased, and the proportion of lower valence states also appeared linked to an increase in nitrogen. A numeric summary of each vanadium valence state/signal as a proportion of the cations in the sample, and the nitrogen signals as a proportion of the bulk anion signals is given in **Table 6.3**. The calculated formulae for the meantime assume both dopants are substitutional and is used simply illustrate relative concentration of elements in the product.

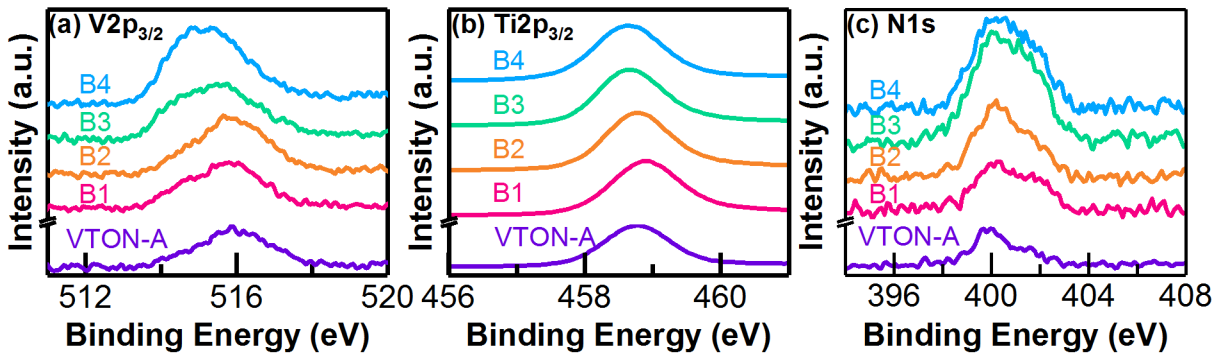

Figure 6.4. *XPS spectra of the* ***(a)*** *$V2p_{3/2}$,* ***(b)*** *$Ti2p_{3/2}$ and* ***(c)*** *N1s peaks for each VTON sample. A broad, multivalent V peak is seen in each. There appears to be a correlation between the V valence spread and shape of the N1s peak.*

Table 6.3. *Proportion of vanadium valence states from V2p$_{3/2}$ peak fitting of VTON materials and the determined composition in comparison to nominal dopant ratios. Fitted binding energies are given in brackets (eV).*

Sample	*Nominal Dopant Ratio V:Ti:N*	*% V3+*	*% V4+*	*Composition from XPS*
VTON-A*	0.05:1:9	29 (514.95)	71 (516.15)	$V_{0.035}Ti_{0.965}O_{1.9460}N_{0.0536}$
VTON-B1	0.05:1:5	35 (514.74)	65 (516.02)	$V_{0.030}Ti_{0.970}O_{1.9740}N_{0.0258}$
VTON-B2*	0.05:1:10	28 (514.94)	72 (516.07)	$V_{0.034}Ti_{0.966}O_{1.9620}N_{0.0380}$
VTON-B3	0.05:1:20	56 (514.84)	44 (516.13)	$V_{0.042}Ti_{0.958}O_{1.9262}N_{0.0738}$
VTON-B4	0.05:1:40	61 (514.75)	39 (515.93)	$V_{0.048}Ti_{0.952}O_{1.9450}N_{0.0550}$

*Two peak fit

It should be noted that the A and B2 materials have a very similar amount vanadium, and can be fitted with similar proportions of V^{3+} and V^{4+}. However, these materials do show a higher binding energy shoulder, allowing them to be fit similarly well with three components (**Figure 6.5. (a), (c)**). In such a fit, only 19% of the total vanadium would be in this higher valence state, which is still lower than anticipated from the (V,N) co-doping simulation studies[207-213]. This high energy peak would be centred at 516.7 eV in both cases, which is below the typical value quoted for V^{5+} [399-401], and so it is not clear that this is a true result. The two-component fit is considered the better depiction for this study (**Figure 6.5 (b), (d)**).

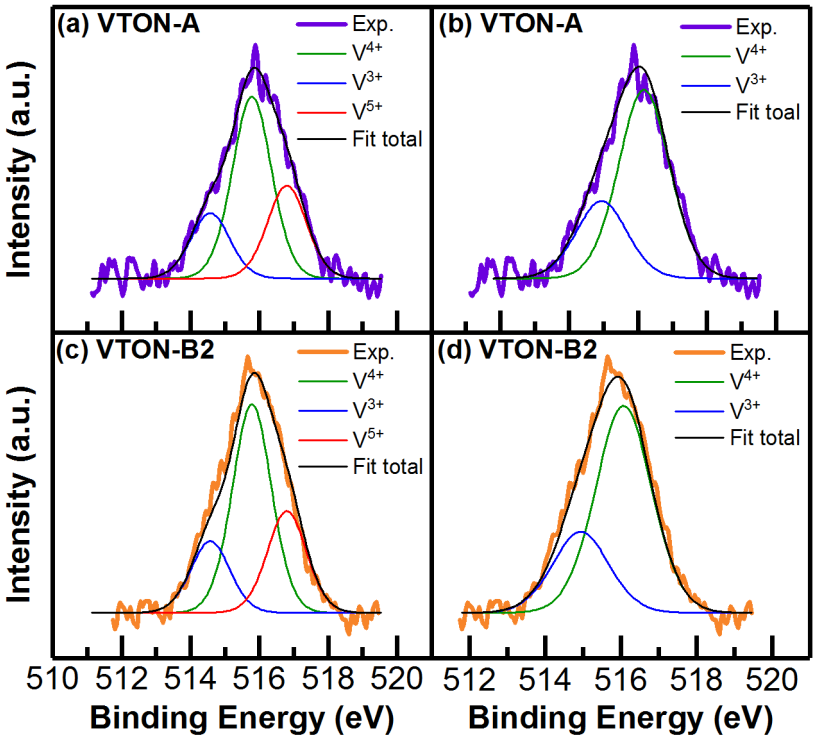

Figure 6.5. *Alternate fitting of V2p$_{3/2}$ peak for sample VTON-A and B2 suggesting a three-component fit might also be valid **(a)** and **(c)**, but the two-component fit **(b)** and **(d)** has more consistent peaks centrings with the literature and is deemed a better model.*

A prevalence of the V^{3+} and V^{4+} valence states is apparent in these samples, even when V^{5+} starting materials are used. Every literature report studied in preparation for this work did report or show evidence for more than one valence state in their product, irrespective of the starting valence of the raw material (3 [217], 4 [216, 218] and 5+ [214, 215, 219]) which is attributed to the low energy associated with the reduction of vanadium ions in solution reactions[226]. However, only one report reviewed for this thesis noted a 3+/4+ vanadium valence prevalence[226]. They attribute this to bulk doping as opposed to surface doping of vanadium ions which are readily oxidized to V^{5+}.

Other studies have also shown from spectroscopy that V^{5+} is likely to be at the surface, whereas V^{4+} is in the bulk[24], suggesting vanadium may be doping well into the bulk of the particles. Octahedra in the anatase structure can share four edges with their neighbours instead of the maximum of two in rutile, so V^{5+} may have less of a preference for substitutional coordination in the bulk of anatase than V^{4+} ions according to Pauling's rules[300]. The anatase structure also has voids in which lower valence ions can fit comfortably, such as V^{3+} which might go a way to explaining this observation.

The influence of the nitric acid seems particularly apparent in the correlation between the shape of the nitrogen XPS signal (increase in 402 eV edge), and the presence of a large proportion of V^{3+} (**Figure 6.4 (a)** and **(c)** above, samples B1, B3 and B4 in particular). Interestingly, despite this link, there is no clear evidence for vanadium nitride (V^{3+}-N^{3-}) type direct bonding (N1s peak at ~ 398 eV[408]). A recent publication does suggest that the lower binding energy edge to the $V2p_{3/2}$ peak (that has been ascribed to V^{3+} in this work) might be evidence for direct V-N bonding[220]. However from a consideration of charge compensation within the anatase structure, and absence of corresponding nitride peak, there is not clear evidence for such a defect in this study. The nitrogen signal that is measured in this study reflects other reports[206, 214-216, 218, 219] , indicating it has been successfully incorporated, but may not be strictly substitutional, a concept that remains contentious in the literature. From these observations, it seems V^{3+} and N form correlated defects, but at least one would likely be in non-substitutional geometry.

Overall, there is a tandem doping effect whereby the ratio of V:N in the reaction mixture has a linear relationship with the proportion of vanadium detected in the product. This effect has been noted in other reports of (V,N) co-doping[215] and in similar systems[205] and has been thought to be related to direct bonding between V^{5+}-N^{3-}, predicted computationally, but the results from this work suggest it is not that straightforward. A prevalence of V^{4+} is noted all samples. This matches well to the general decrease seen in the structural parameters as V^{4+} has a smaller radius than Ti^{4+} in an octahedral environment[75]. Clusters of V^{4+} would also result in the

decreasing effect. However the larger V^{3+} and N^{3-} ions, while present, do not seem to cause a lattice expansion and may suggest they possess more complicated coordination geometries.

To summarize, the XPS points to successful doping of vanadium and nitrogen, however the vanadium exists in two reduced states. This suggests the vanadium exists deeply doped in the samples rather than at the surface. The nitrogen appears to help more vanadium be introduced, but there is no clear evidence for the formation of V^{5+}-N^{3-} clusters, rather some substitutional V^{4+} and some correlated V^{3+} and N^{3-} with complex geometries. In order to further confirm which species do exist in these samples and isolate their role in functionality, ESR spectroscopy was used.

6.2.2.2 Electron Spin Resonance Spectroscopy Location Analysis

The XPS results showed that all materials possessed a large population of V^{4+} species which are paramagnetic. More could be learned about the location of vanadium dopants in these samples by using ESR spectroscopy. In addition, any isolated Ti^{3+} which can be difficult to see in XPS should be detectable. The three phase-pure compositions A, B1 and B2 were all investigated with this technique. Each contain different mixtures of vanadium valence states and V:N ratios.

Spectra collected at room temperature showed a main signal centred ~ 350 mT in each sample with a hyperfine splitting arising from the unpaired electron and the nuclear spin of the naturally abundant 7/2 vanadium (**Figure 6.6 (a) – (c)**). The total signals could be decomposed into three separate V^{4+} signals through fitting (**Figure 6.6 (d) – (f)**) suggesting the samples contain three structurally distinct V^{4+} environments. No signals corresponding to Ti^{3+} or N-containing radical species were observed.

The largest component is a broad, structure-less background signal which is typically attributed in the literature to a proportionally large population of aggregated vanadium centres[222, 223]. An additional structure-less low field signal is also observed centred at ~ 160 mT (**Figure 6.7 (a)**), which is consistent with a 'half-field' 'forbidden' +/- 2 spin state transition from the same aggregate vanadium population[409]. The structured part of the signal can be attributed to (at least) two 'isolated' V^{4+} environments with axial crystal field symmetry. This is most likely to be associated with different octahedral bonding environments for these vanadium species. This is most obvious in the 'split' peaks on the high field side of the main signal (> 375 mT, **Figure 6.7 (b)**).

There are also qualitative differences in each of the three measured spectra which may arise from small changes in the ***g*** tensors for each octahedral environment and/or the presence of yet another unique 'isolated' V^{4+} environment. This is particularly evident in the sample B1

which shows shoulders on the peaks observed on the low field portion of the main signal (250 – 350 mT, **Figure 6.6 (b)**), but has not been successfully captured in the simulation. Sample B1 also shows a larger comparative population of aggregate V^{4+} centres.

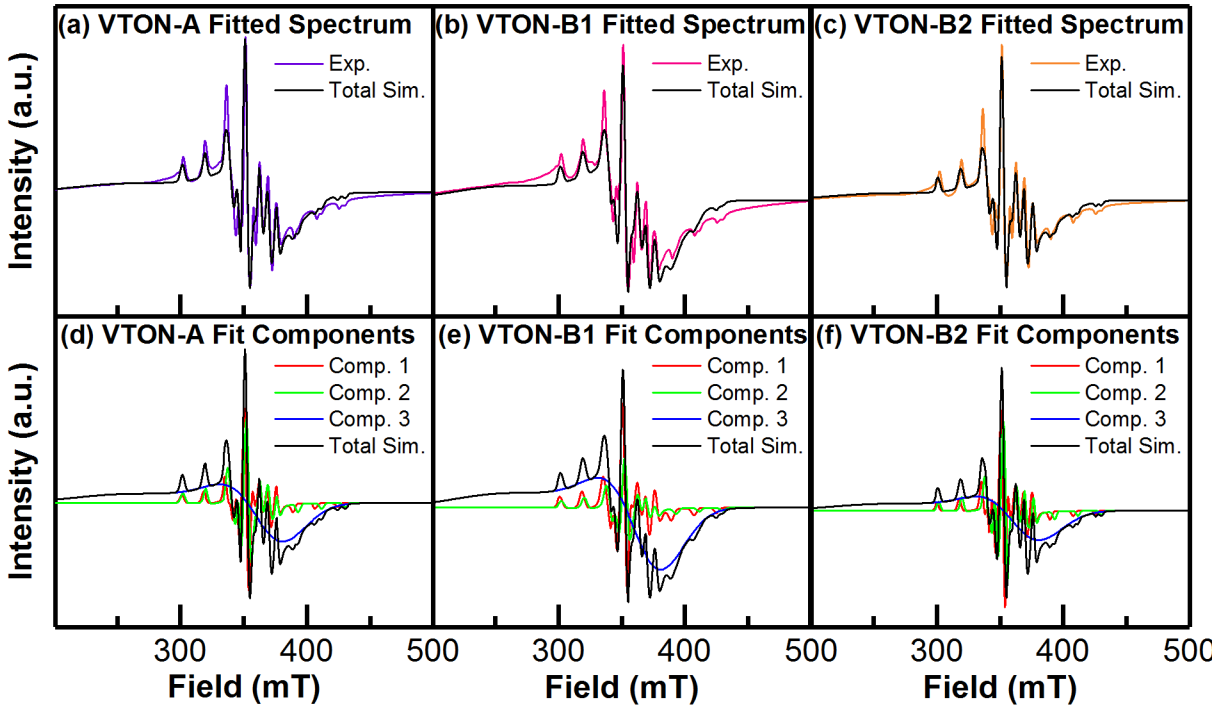

Figure 6.6. *Experimental ESR powder spectra obtained from* ***(a)*** *VTON-A,* ***(b)*** *VTON-B1 and* ***(c)*** *VTON-B2 are shown, fitted with a simulated spectrum (black). In* ***(d)****,* ***(e)*** *and* ***(f)****, the components of the corresponding simulated spectra are shown, including two isolated axial octahedral signals (comp. 1 and 2) and a broad aggregate signal (comp. 3). The intensity is normalized for fitting and comparison.*

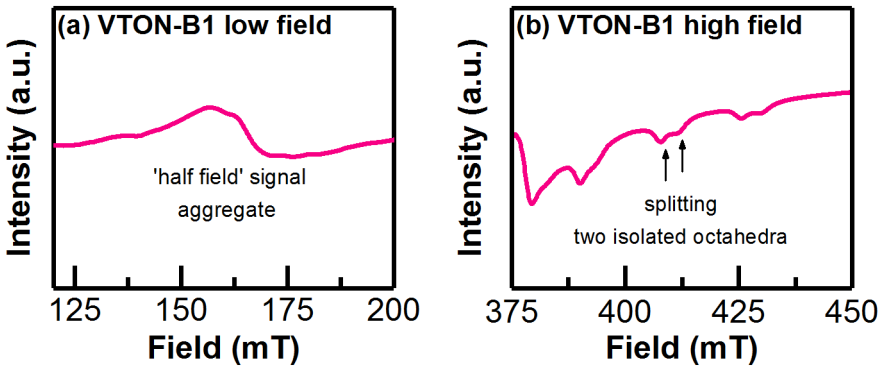

Figure 6.7. *In* ***(a)****, a selected low-field region of the VTON-B1 spectrum is shown, where a 'half-field' signal appears arising from the aggregate* V^{4+} *population. In* ***(b)*** *a selected high-field region of VTON-B1 is shown which has two clear 'isolated' octahedral environments for vanadium.*

The fitting results are presented in **Table 6.4**. The ***g*** and ***A*** tensors of the 'isolated' signals (component 1 and component 2) are similar to those reported in other studies of V-doped anatase samples (***g*** perpendicular 1.957 – 1.97, ***g*** parallel 1.917 – 1.938, ***A*** perpendicular 110 – 156 MHz ***A*** parallel 427 – 483 MHz [222-224, 226, 227, 402, 410]). There is not a clear consensus among these reports as to whether these signals arise from interstitial or substitutional V^{4+}, but lower ***g*** values are more often attributed to substitutional doping. Considering these earlier reports, samples A and B2 have proportionally larger amounts of this type of environment. Sample B1 on the other hand, has a possible 3rd axial environment, and a proportionally larger 'aggregate' population (component 3). Given the comparatively large proportion of the 'aggregate' signal in all samples though, the differences between the smaller isolated signals are not as significant.

Table 6.4. *Fitted* **g** *and hyperfine* **A** *parameters for the signals observed in VTON-A, B1 and B2 ESR spectra and their relative proportions.*

		A		*B1*		*B2*	
		g	***A*** *(MHz)*	***g***	***A*** *(MHz)*	***g***	***A*** *(MHz)*
Component 1 (isolated, substitutional)	Perpendicular	1.968	154.4	1.968	153.5	1.969	153.3
	Parallel	1.939	479.5	1.936	488.3	1.937	487.8
	Fraction of fit	0.062		0.064		0.07	
Component 2 (isolated, substitutional)	Perpendicular	1.962	146.1	1.962	146.9	1.96	145.9
	Parallel	1.922	493.7	1.92	487.5	1.922	494.4
	Fraction of fit	0.074		0.039		0.076	
Component 3 (clustered, substitutional)	Perpendicular	1.92	1	1.92	1	1.92	1
	Parallel	2.85		2.85		2.85	
	Fraction of fit	0.864		0.897		0.854	

From these ESR spectra, it is clear that the local environments of V^{4+} in all samples are varied including isolated substitutional species and clustered aggregates. Through this technique characterised just one valance state of vanadium (V^{3+} is S = 1, and V^{5+} is diamagnetic), while two were previously detected with XPS, so it stands to reason that the vanadium local environments are even more varied than anticipated. While the literature computational studies suggest a single structural environment for vanadium, directly bonded to nitrogen, for the compositional range tested, it appears experimentally this is not the case.

6.2.3 Defect Discussion

From these spectroscopic studies, there is evidence for a large population of V^{4+} in each material which exists both in aggregated and distinct, isolated octahedral coordination environments. A population of V^{3+} is also detected, which is correlated with introduced N, but are not clearly bonded to one another. There is a lack of V^{5+} and titanium only exists as Ti^{4+}. In order to obtain a charge balanced product from this combination of defects, it seems likely that V^{4+} is introduced directly into the TiO_2 framework as an isovalent substitution. In order for V^{3+} and N^{3-} to simultaneously exist, it seems likely that either V^{3+} is in an interstitial site, thereby increasing the cation charge to counteract N^{3-} in a substitutional position or N has a lower valence, perhaps in an 'NO' type interstitial configuration as reported by others, in order to balance reduced V^{3+} in a substitutional site. It is interesting to note, that both in this study, and in the literature, no synthesized material appears to be exhibiting the isolated directly bonded V^{5+}-N^{3-} pairs from the theoretical simulations[207-213]. Possible reasons for this deviation are the reactivity of vanadium, and the nature of the anatase structure.

Irrespective of the valence state of the vanadium source material in the initial reaction, both result in a valance change in the final product. Under standard conditions, the reduction potentials for VO_2^+/V^{4+}, VO^{2+}/V^{3+}, and TiO^{2+}/Ti^{3+} [411] ions in solution are +1.0, +0.35 and +0.1 V respectively. This means, reduction of V^{5+} to V^{4+} and V^{4+} to V^{3+} are more likely than Ti^{4+} to Ti^{3+}, mirroring observations made in this study. Lowering the solution pH, which is a consequence of adding more of the nitrogen source, can further promote this process, explaining the higher proportion of V^{3+} in samples with the most HNO_3 (i.e. B3 and B4). In addition, the reduction potential of $NbO_{0.5}/Nb^{4+}$ is -0.25 V[411], which explains why multiple valence states are not seen in the comparative niobium solvothermal study[206], as the reduction process is strongly disfavoured.

Given all vanadium source materials and methods explored in the literature also lead to a second valence state in the product, it seems the anatase structure itself is a determining factor for the likely valences in these products. It is often reported that as doping levels are increased, the proportion of reduced valence vanadium increases[221, 222, 227, 412]. Looking at bond valence calculations (calculated using the soft BV method[301]) on the anatase crystal structure[179] with vanadium placed in the structure with different starting valences (**Table 6.5**, sites shown in **Figure 6.8**), it seems that for a substitutional incorporation of V^{4+} in an octahedral site, the lowest GII for the structure (likely correlating with a lower total energy) is achieved. It is possible that when doping levels are increased, incorporation of vanadium needs to occur more deeply in the sample, favouring low valence states, instead of staying on the surface as V^{5+} [221, 226].

Table 6.5. *Global instability index from bond valence sum calculations on the anatase structure with vanadium incorporated in different valence states.* ***Figure 6.8*** *(right) depicts dopant sites.*

Vanadium species	*GII (v.u.)*
V^{5+} Substitutional	0.1464
V^{4+} Substitutional	0.0540
V^{3+} Substitutional	0.1332
V^{5+} Interstitial	0.7130
V^{4+} Interstitial	0.6006
V^{3+} Interstitial	0.4751

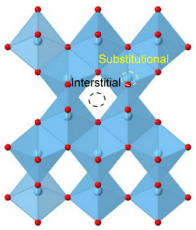

From these results, it seems possible that the V^{3+} species observed in these samples may occupy interstitial sites and the extra positive charge could offset the presence of N^{3-} in the sample to achieve charge balance. This in conjunction with the V^{4+} in multiple sites has implications for the exhibition of optical and photocatalytic properties. It also remains to be seen if this combination of defects will extend the valence and conduction band of TiO_2 or form mid gap states. If the prevalence of electron rich vanadium in this material causes it to act as an n-type semiconductor, its junction with solution may cause a space charge region to develop. This could lead to a greater prevalence of holes at the surface and affect the attainable redox potential for reaction. To gain further information, optical and photofunctional experiments were carried out.

6.3 Optical and Photofunctional Properties

6.3.1 Visible Light Absorption

To get an idea of the impacts of these defects on the band structure, absorbance curves were first obtained with spectrophotometry (**Figure 6.9 (a)**). An absorption edge around 400 nm is apparent in all samples which is consistent with the main O2p – Ti3d valance band to conduction band transition for TiO_2 anatase (indirect, ~ 387 nm[200]). Tailing is observed in all samples, which is noted in the literature to be associated with both vanadium[400] doping and nitrogen doping[204]. Evidence for an extra peak is seen in the region 450 – 550 nm and has been ascribed to d-d transitions of V^{4+} [221], pointing towards the presence of 'gap states' within the formal band gap. This is more obvious in samples with a larger proportion of V^{4+} such as sample B3 (**Figure 6.9 (a)**, green).

A Tauc plot (**Figure 6.9 (b)**) was produced considering an indirect band gap model (as is typical for anatase structures) to investigate the effect of V doping on the main VB – CB transition. The energy of the band gap estimated from this main transition shows a trend to decrease on increased total vanadium content in the samples. The band gaps range from 3.06 eV (B1) to

2.46 eV (B4) which are all below that of un-doped anatase and in theory could facilitate visible light photocatalysis. In addition, the valence band edge of the samples as determined from XPS (**Figure 6.9 (c)**), is around 2.0 eV from the Fermi level in all samples. Considering the band gaps, this would place the conduction band in each sample closer to the fermi level, possibly limiting the redox potential attainable from these samples. Degradation of dyes such as RhB in water have been shown to proceed by catalyst mediated radical formation[413]. This means the redox potential at the VB and the CB need to drive oxidization processes like ·OH generation from H_2O (+2.27 eV. at pH 7 [213]) and reduction processes like O_2 to $O_2^{\cdot-}$ (-0.28 eV at pH 7 [213]) respectively. These catalysts may be better for the oxidation reactions, and limited for reduction reactions, limiting the overall rate.

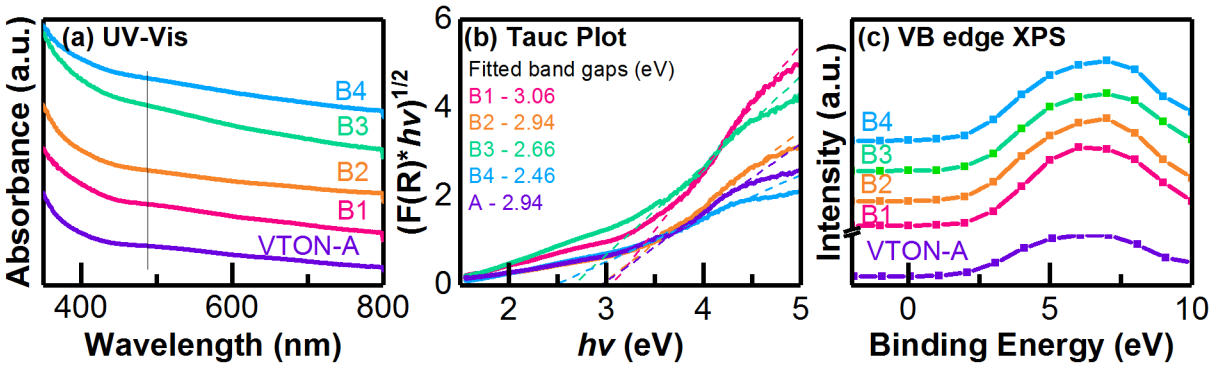

Figure 6.9. *In **(a)**, absorbance curves for each of the VTON samples are shown, with an edge near 400 nm and a peak near 500 nm (black line) corresponding to V^{4+} gap states in some samples. In **(b)** a Tauc plot is shown, produced from reflectivity data which was fitted to obtain a band gap for the main transition. This decreases on increasing total amount of vanadium in the sample. The valence band edge from XPS is shown in **(c)**. The edge is ~ 2 eV back from the fermi level.*

6.3.2 Photocatalysis

Having characterised the variation of composition, valence, structure and visible light absorbance of these samples, their practical ability to photocatalytically degrade Rhodamine B (RhB) is tested to help understand how these factors influence the evolution of catalytic functionality. Monitoring changes in the RhB concentration over time exposed to visible light and the catalysts (**Figure 6.10**), the catalyst sample which shows the most obvious dye decomposition is VTON-B1. The overall performance of all three samples is low in comparison with another (V,N)-TiO_2 study conducted against RhB[214]. It is also noted that samples containing brookite (B3, B4) have even lower behaviour (not shown), in line with expectations around the photofunctionality of the brookite polymorph[12].

It is noted that B1 has the smallest particle size of the phase-pure materials which might be a contributing factor to its better functionality, but overall the low performance for all three materials might be attributable to low valence vanadium. The presence of gap-states induced by V^{4+} could be acting as a recombination centre for photoexcited electrons, negating any effect from the narrowing fundamental gap. It has also been shown that not only are there a number of different defects present, but they can have mixed geometries, implying a lack of homogeneity that could be impeding charge transport. It is likely no coincidence that literature reports indicate high catalytic activity for lower doping levels (V:N is 2:4 [214], 2:1 [215], 1.1 : 4.1 [219]) in which a large population of V^{5+} is also present. Greater levels of doping apparently generate deeper, variable and low valence states in this system, which act as detrimental defects.

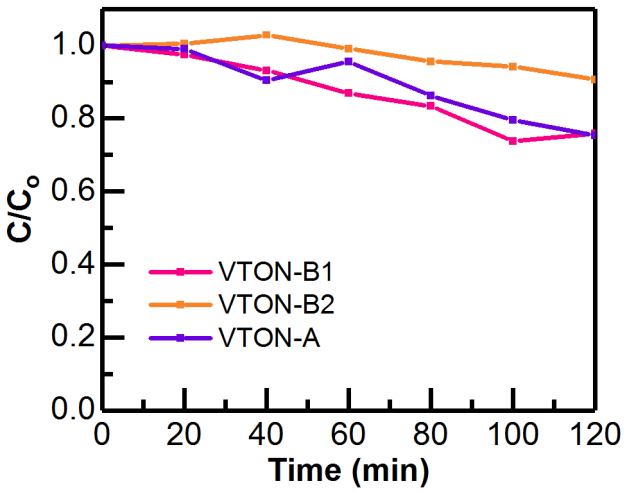

Figure 6.10. *Relative concentration of RhB dye over time exposed to catalysts VTON-A, B1 and B2 and visible light. None were able to degrade the dye over a period of 2 hours, but B1 has the most consistent decreasing effect.*

It is theorized that in order to prevent the formation of low valence vanadium, the pH of the solution needs to be carefully controlled and an alternative source of nitrogen used, as well as lowering the total vanadium content to avoid structural effects on the valence state and aggregation. It is not clear however, whether a truly homogenous product can be formed with V^{5+}-N^{3-} defect pairs throughout as the simulations suggests. It has been shown that rational defect design for photocatalysis may not always be attainable in practice if the dopant scheme is highly sensitive to the chemical environment.

6.4 Summary of Chapter 6

In this work nanoparticles of (V,N)-TiO_2 are produced which are anatase up to doping levels of 3.5 at. % V using a solvothermal method with different sources of vanadium. The use of nitric acid as a nitrogen source results in a tandem doping effect and near 1:1 V:N incorporation, but does also induce brookite formation and vanadium valence reduction at higher levels.

An analysis of the valence states using XPS shows that all samples possess V^{4+} and V^{3+} rather than the expected V^{5+}, regardless of the valence of the starting material. Probing the local structural environment of the major vanadium component (V^{4+}) with ESR reveals paramagnetic vanadium in at least three different structurally distinct sites, of which an aggregate population is the most significant, suggesting doping is both deep in the samples, and not homogenously distributed. Together, this suggests vanadium is incorporated as V^{4+} substitutionally and V^{3+} and N are incorporated in more complex, likely non-substitutional ways, to achieve charge balance in the system.

UV-Vis spectrophotometry, while showing a narrowed band-gap in comparison with un-doped TiO_2, also shows the presence of electronic gaps states, likely arising from the prevalent V^{4+}. These gap states are likely acting as recombination traps, as evidenced by poor photocatalytic ability against the dye RhB. The best performance is seen from samples that contain the lowest total doping levels where detrimental vanadium states have not yet developed, which reflects literature that reports optimal performance from doping levels much lower than in the computational simulations.

Overall, it is apparent that when designing co-dopant schemes to optimize properties like visible light absorption, it is important to also consider the propensity for the dopant ions to adopt appropriate valence states and occupy intended target crystallographic sites. This chapter demonstrates how chemical modifications, even in small amounts can lead to a broad possibility of outcomes, and influence the emerging properties. The effects of multiple valence states of vanadium coexisting in a new structure type are investigated in the next chapter.

Chapter 7 Vanadium Modified Rutile-type Titanium Dioxide Materials

In the previous chapter it was apparent that vanadium adopted lower valences states when introduced into the anatase host structure, and this was detrimental to the overall functionality, despite having an effect on narrowing the band gap. Continuing on from the previous chapter, this final content chapter explores how multiple vanadium valence states can be sustained in the rutile polymorph of TiO_2, and investigates other semiconducting phenomena rather than photocatalytic functions.

Rutile TiO_2 has a band gap of ~ 3 eV and while narrower than anatase, it still uses UV light more effectively than visible light. Modification of rutile TiO_2 with other elements may serve to narrow its band gap while also changing its charge transport characteristics. Modification of rutile TiO_2 with pentavalent ions like Ta^{5+} and Nb^{5+} can enhance the n-type semiconductive nature of rutile. However, introducing V^{5+} can potentially lead to a different effect as a consequence of its ability to change valence.

As noted in the introduction, vanadium has a documented bad gap reducing effect on rutile TiO_2. However, there is mixed information regarding which valence state vanadium is in when incorporated, how much total vanadium can be incorporated, how the properties are affected as a consequence of concentration and valence state, and whether mixed valence products might exhibit metal-insulator or semiconducting character.

This chapter serves to investigate these questions and so gain an understanding of the electronic properties vanadium modified rutile TiO_2 might exhibit and how this is established in terms of chemistry and structure. A solid state synthesis route is presented to create multivalent vanadium modified TiO_2, using V_2O_5 as a raw material (V^{5+}) and moderately reducing conditions. The vanadium solubility, mixed valence states and resulting structure, optical, electrical and electronic properties of the products are determined through diffraction and spectral techniques.

7.1 Synthesis

In this thesis the development of simple, low-cost syntheses for the production of functional oxides have been prioritized. In this section, synthesis attempts and optimized methods for the production of vanadium modified rutile TiO_2 are presented, with vanadium concentrations 1 – 70 at. % of the total cations. Percentages of vanadium quoted henceforth in this chapter refer to the atomic percentage of total cations in the sample unless otherwise stated. The

naming convention of samples presented in the chapter henceforth is VTOX-y where 'X' is the percentage vanadium (e.g. '50' = $V_{0.5}Ti_{0.5}O_2$) and '-y' represents the sintering environment used (either 'LO' for the low oxygen or 'O' for the moderate oxygen method).

7.1.1 Syntheses with Various Vanadium Concentrations

The most straightforward method to substitute maximal vanadium into rutile TiO_2 with mixed valence states was to use commercially available mixed-phase V_2O_5 powders and anatase TiO_2 (which transitions to rutile above ~ 600 °C in the presence of vanadium[227, 252, 414]) as the raw materials. The raw materials were combined in acetone (not ethanol used in other chapters, as V_2O_5 was found to react and forms side products with this solvent) and ball milled in order to obtain a homogenous mixture with a small particle size. While V_2O_5 has a natural yellow/brown colouration, after milling the mixtures appeared blue, then dried to a green colour. There is a possibility that the process of ball milling induced a valence state change in the vanadium, as noted by others in V_2O_5[415] and in V_2O_5 and TiO_2 mixtures under high energy circumstances[416, 417], which was then partially re-oxidized on standing in this experiment. This might imply some useful pre-reactions. The dried powders were then pressed into pellets without binders and prepared for sintering.

The sintering process required some optimizing. In order to obtain a rutile product after sintering, the temperature had to be high enough for the raw TiO_2 phase to transition from anatase to rutile. It also needed to be high enough to react but not so high as to separate out due to the low melting point of V_2O_5 (~ 690 °C). Finally, an atmosphere reducing enough to prevent V_2O_5 remaining a separate oxidized phase was required. Two distinct sintering methods are presented in this chapter, the Low Oxygen method and the Moderate Oxygen method.

7.1.1.1 Low Oxygen Method

The first method (Low Oxygen method, '-LO') involved a sintering event (or events) on a platinum foil boat in a tube furnace under flowing nitrogen gas, which provided a moderately reducing atmosphere. Nitrogen gas is a cheap and safe to handle reducing agent which has not been explored thoroughly in syntheses of these kinds of materials before in the available literature and avoids use of sealed ampules and vacuum furnaces. The tube furnace used in these experiments has a quartz inner tube, limiting the maximum operating temperature for an extended dwell time to 1050 °C.

In **Figure 7.1** XRPD patterns of the best sintering results for each composition synthesized using the 'LO' method are presented. The specific sintering conditions are outlined in **Table 7.1**. At low levels of doping (1% V, VTO1-LO) unreacted materials are seen, which imply

the 1050 °C temperature limit is insufficient for this composition. From 2 – 50% V using the LO method, a rutile structured phase is evident. Despite 1050 °C being hot enough to react and form a single phase, the 2 – 10% samples do not densify well after a single sintering. A regrinding and resintering did help in densification 5 and 10%. For samples with 20% substitution and beyond melting behaviour was seen which did aid in densification, but also distorted the macroscopic shape of the samples. This is particularly relevant for VTO50-LO type samples, the synthesis for which is explored in later sections. The 70% sample (VTO70-LO) showed appreciable melting even at 750 °C and is notably two-phase in the XRPD patterns, with the additional phase matching to V_2O_5.

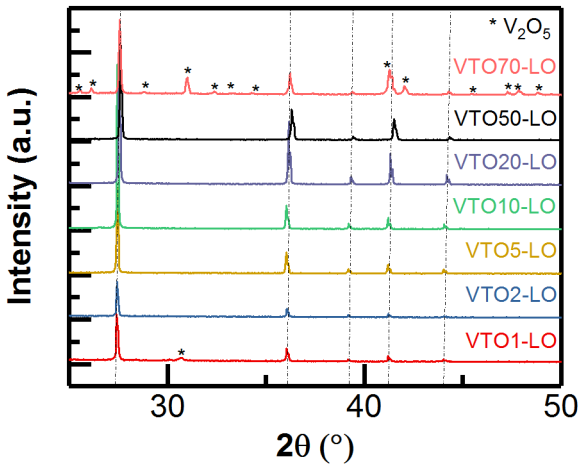

Figure 7.1. *XRPD patterns of vanadium substituted rutile samples produced by the 'LO' method. Replacement levels of 1 – 70% were explored, but show the temperature is insufficient at 1% and a solubility limit has been reached by 70%. Rutile peak locations are indicated by dashed lines.*

Table 7.1. *Summary of 'LO' method sintering temperatures and times for each VTO composition.*

Sample	*Sintering 1 (tube furnace)*	*Sintering 2 (tube furnace)*
VTO1-LO	1050 °C/ 20 hours	-
VTO2-LO	1050 °C/ 20 hours	-
VTO5-LO	1050 °C/ 13 hours	1050 °C/ 15 hours*
VTO10-LO	1050 °C/ 13 hours	1050 °C/ 15 hours*
VTO20-LO	1050 °C/ 20 hours	-
VTO50-LO	900-1050 °C/ 20 hours**	-
VTO70-LO	750 °C/ 12 hours	-

*necessary for densification
**optimization presented later in this section

These results imply that the 'LO' reducing conditions are sufficient for a broad range of vanadium incorporation levels but there is a limit is somewhere between 50 and 70%. This limit is higher than the 10% limit found when synthesized in air[250-253] and lower than the 80-

90% using VO_2 as a raw material[259-261, 286]. However, this method only allowed a narrow range over which sintering temperature could be optimized for good sample quality. This led to an exploration of a second method using a higher temperature furnace.

7.1.1.2 Moderate Oxygen Method

The second method attempted (moderate oxygen method, '-O') utilized a muffle furnace for a second sintering which had a higher attainable temperature. This was connected to a nitrogen supply line, but did not flow, providing only minimal reducing effect beyond the natural effect of high temperature, and as such there is 'moderate' oxygen available. The samples were sintered initially using a tube furnace, reground, then sintered a second time in the muffle furnace to ensure densification and the detailed conditions are presented in **Table 7.2**.

Applying the 'O' method, it was found that denser, phase pure rutile samples with 1 – 10% vanadium could be made (**Figure 7.2**). However, incorporations of 20% and beyond resulted in the appearance of V_2O_5, similar to literature studies using an air atmosphere. This supports the prediction that the muffle furnace conditions were indeed more oxidizing than the tube furnace conditions, and the solubility of vanadium in the samples is evidently decreased. The fact that some vanadium was reoxidized in the two step 'O' method trials implies that a proportion of the vanadium may have been on the surface of crystal grains rather than deeply substituted into the rutile framework, as bulk vanadium is not found to be easily oxidized[237], an important note of discussion in later sections.

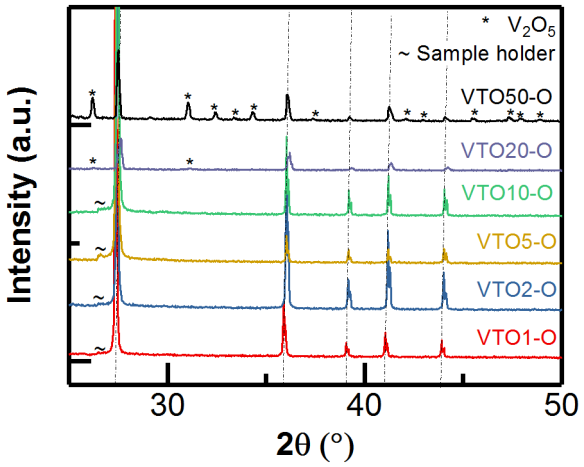

Figure 7.2. *XRPD patterns of samples produced by the 'O' method. Peaks associated with V_2O_5 were seen at 20% incorporation and beyond, suggesting the solubility is dependent on oxygen partial pressure. Rutile peak locations are indicated by dashed lines.*

Table 7.2. *Best sintering temperatures and times for 'O' method VTO samples.*

Sample	*Sintering 1 (tube furnace)*	*Sintering 2 (muffle furnace)*
VTO1-O	1050 °C/ 15 hours	1300 °C/ 10 hours
VTO2-O	1050 °C/ 15 hours	1300 °C/ 10 hours
VTO5-O	1050 °C/ 13 hours	1200 °C/ 10 hours
VTO10-O	1050 °C/ 18 hours	1200 °C/ 5 hours
VTO20-O	1050 °C/ 18 hours	1050 °C/ 10 hours
VTO50-O	1050 °C/ 18 hours	850 °C/ 10 hours

Across these synthesis trials, the maximum amount of vanadium introduced was 50% using the 'LO' method. This composition had the most potential for a large range of vanadium valence states, and so further optimization of the synthesis was conducted for generation of high quality samples suitable for electrical, electronic and magnetic analysis.

7.1.2 Optimization of VTO50 Synthesis

When using the 'LO' method to produce rutile samples with 50% vanadium replacement some melting behaviour was noted during sintering. Several tests were conducted to see if a combination of sintering parameters and preparation methods could be used to ensure phase purity and sample quality. A summary of conditions tested and the related samples are presented in **Table 7.3**.

Table 7.3. *Summary of sintering conditions tested for 'LO' optimization of VTO50. Optimum conditions used to produce samples studied in later sections are indicated.*

Condition	*Variations tested*
Reactant Mixture	Ball milled oxides (optimum) and hand milled oxides.
Pre-sintering Steps	PVA added to oxides before pressing, pellets pressed to 10 tonnes pressure (opt.), furnace heating rate 4 – 6 °C/min (opt.) and furnace heating rate 8 – 10 °C/min.
Main Sintering Temperature	610, 800, 850, 870, 900 (opt.) and 1050 °C (opt.*).
Main Sintering Time	15 minutes, 4, 18, 19, 20 (opt.), 47 and 64 hours.
Post-Sintering Steps	Grind and re-sinter at higher temperature, and grind and re-sinter at lower temperature.

*samples used in the WDXS and XPS measurements

It was found that no combination of double sintering led to an improved product via the solid state method. The most sensitive parameters were the temperature and duration of the sintering step. In **Figure 7.3** a time comparison is shown which suggests 800 °C is too low for the reaction even after 64 hours of sintering. While this temperature did appear to reduce melting, longer times showed little improvement.

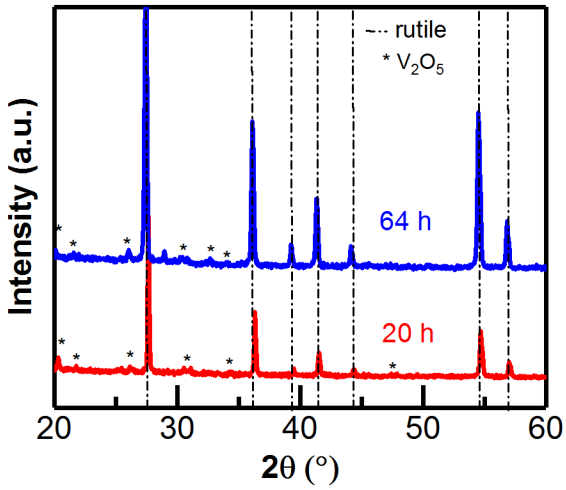

Figure 7.3. *Comparison of VTO50-LO samples sintered at 800 °C for 20 hours (red) and 64 hours (blue). Rutile peaks are indicated by lines, showing additional peaks associated with V_2O_5 do not vanish with extra time, and 800 °C in insufficient for synthesis.*

Increasing the temperatures, it was found 900 °C and above were appropriate for the reaction (**Figure 7.4**) though unavoidably resulted in distortion of the pellets. A sintering time of 20 hours gave good phase purity and density at these temperatures. In samples that exhibited the most distortion from melting, an additional phase was sometimes observed in the XRPD. This could be mechanically removed with polishing of the samples, and is thought to be associated with a pooling of vanadium melt.

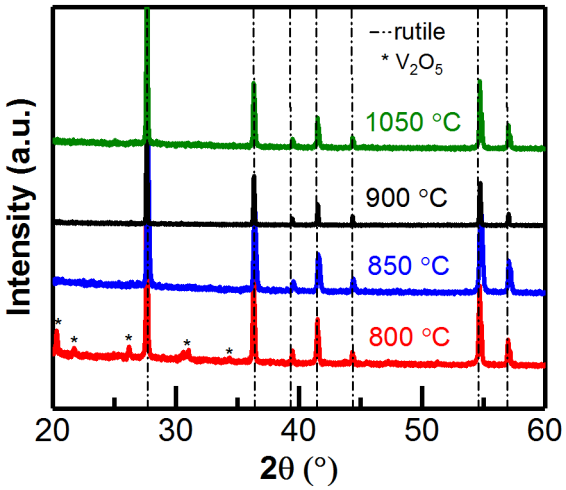

Figure 7.4. *XRPD patterns of VTO50-LO samples sintered for 20 hours at 800 °C (red), 850 °C (blue) , 900 °C (black) and 1050 °C (green), implying sintering at temperatures of ≥ 900 °C for 20 hours is optimal for rutile phase formation.*

From this work, it is notable that 50% vanadium could be incorporated into these samples without phase separation. This has not previously been shown to be possible with just reducing

gases[252] and required VO_2 and/or vacuum sealing[249, 259-261, 286] reducing conditions. This is an unprecedented result using a low complexity single-step synthesis method.

From this overall synthetic study, a solid state method was successfully developed to produce samples with 1 – 50% vanadium in the rutile phase. The results indicate the solubility of vanadium into TiO_2 exists depends on the oxygen partial pressure, and the limits are different to previous reports. This implies a likely change in vanadium valence states on introduction into the rutile framework. The next section explores the chemical nature of vanadium and how it fits into the rutile structure.

7.2 Chemical and Structural Analysis

7.2.1 X-ray Diffraction Trends

Noting samples with the rutile structure had been obtained, the change in the size of the unit cell as vanadium was incorporated was investigated. This gave an idea about the location of the vanadium in the rutile matrix and its valence state. A notable change is observed in the rutile lattice of the samples as determined by XRPD. Each fitted to a $P4_2/mnm$ rutile unit cell and there was a consistent decreasing trend in both the ***a*** and ***c*** lattice parameters as more vanadium was added (**Figure 7.5**). It appears the most change occurs before 5% and the unit cell slowly decreases from then onwards. The overall cell shrinkage implies an average decrease in the octahedral site size in the structure.

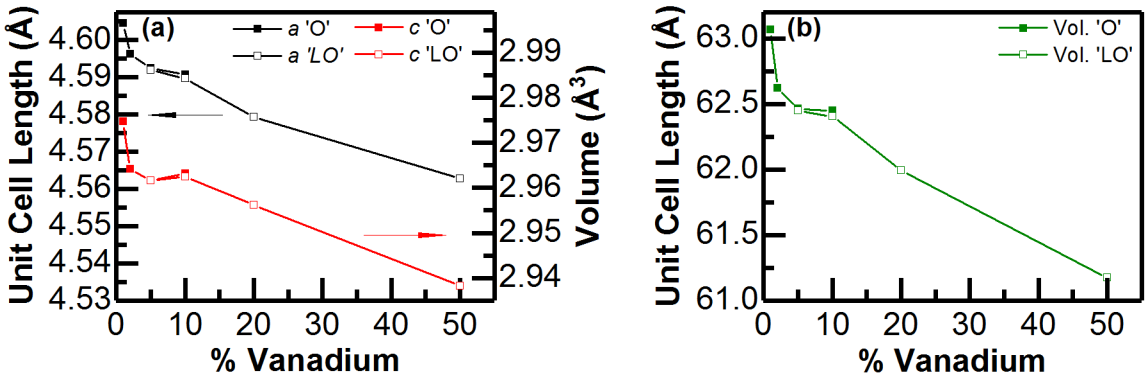

Figure 7.5. *Lattice parameters obtained from fitting of XRPD patterns of VTO samples to a* P4_2/mnm *unit cell. A decreasing cell size is noted on increasing incorporation of vanadium.*

The size of the three common vanadium valences are V^{5+} – 68 pm, V^{4+} – 72 pm and V^{3+} – 78 pm[75]. The size of Ti^{4+} in octahedral coordination is typically 74.5 pm[75], thus the decrease in lattice size observed may correlate with the titanium being substituted with the smaller V^{4+} or V^{5+} ions. Some simulations have shown that vanadium has a tendency to aggregate[267], and

short bonds between vanadium can form[286, 418] related to V^{4+}. At this point it is expected that substitutional V^{4+} is likely the majority vanadium state that arises from this sample preparation.

However, it is also evident from these diffraction results that the trend in lattice parameters is non-linear. This is not solid solution behaviour, and suggests different composition and conditions lead to different combinations of defects and structural manifestations. The surface is another possible destination for vanadium, most probably in the highly oxidized V^{5+} state. This would not necessary result in a decrease in measured bulk lattice parameters. Thus, one way to interpret the lattice trend between the 'LO' and 'O' methods might be that vanadium is being introduced substitutionally up to 10% doping (decreasing the lattice parameters), but the O method is not reducing enough to encourage deeper doping beyond this concentration, leading it more surface V^{5+} doping near the solubility limit (plateau in lattice parameters to 10%). When the method is changed to the more reducing 'LO' method, deep incorporation of V^{4+} is resumed (and a further lattice shrinkage is observed from 10 – 50%). To verify what is happening from this lattice plateau to 50% incorporation in terms of vanadium valence, spectral analyses were conducted.

7.2.2 Wavelength Dispersive X-ray Spectroscopy Composition Analysis

Wavelength Dispersive X-ray Spectroscopy (WDXS) can be used to accurately determine chemical composition in solid samples. By using this method, resolution of spectral peaks arising from neighbouring elements on the periodic table (such as V and Ti) can achieved. The samples VTO5-LO, VTO10-LO, VTO20-LO and VTO50-LO were analysed to confirm vanadium was indeed successfully incorporated and also to get a preliminary idea of the valence state evolution.

The mass of 'V_2O_5' and 'TiO_2' in the sample were initially determined by this method. By averaging the concentration of 'V_2O_5' and 'TiO_2' across 7 – 10 points in each sample (reflecting appropriate grains for analysis within the measurement frame) the relative amounts of V and Ti ions were determined for comparison to the nominal composition (**Table 7.4**). Errors are calculated and propagated from the standard deviations of the initial set of points measured. It was found that the experimental compositions are close to the nominal incorporation amounts. There was some more variability from point to point in the more highly doped samples but phase segregation was not apparent.

The summation of the various oxides in each sample however totalled to greater than 100% (VTO5 – 100.2%, VTO10 – 101.2%, VTO20 – 103.3% and VTO50 – 107.4%), thus suggesting that the valence state of the vanadium oxide is not solely V^{5+}. In all samples a proportion of 'K_2O' was detected, a common surface contaminant which was not included in further analysis and in samples that were reground by ball milling for the purpose of densification (VTO5 and

VTO10) non-negligible concentration of 'ZrO_2' was also detected and so was included in overall assessment of composition and valence. By then subtracting any additional mass from the vanadium oxide signal, the formula of the vanadium oxide was recalculated and the V^{n+} valence value '*n'* was estimated. From this method, it appears that the likely valence state of the vanadium is lower than V^{5+}, and trends to being more highly reduced in samples with a larger total amount of vanadium.

Table 7.4. *Nominal and expected vanadium to titanium ratios and estimated vanadium valence states in VTO samples determined by WDXS.*

Sample	*Nominal* V_xTi_{1-x}	*Experimental* V_xTi_{1-x}	*Estimated Average Valence* n
VTO5-LO	$V_{0.05}Ti_{0.95}$	$V_{0.048\pm0.009}Ti_{0.952\pm0.013}$	4.66
VTO10-LO	$V_{0.10}Ti_{0.90}$	$V_{0.097\pm0.014}Ti_{0.903\pm0.017}$	3.77
VTO20-LO	$V_{0.20}Ti_{0.80}$	$V_{0.210\pm0.021}Ti_{0.790\pm0.016}$	3.44
VTO50-LO	$V_{0.50}Ti_{0.50}$	$V_{0.447\pm0.090}Ti_{0.553\pm0.082}$	3.38

This analysis gave an indication that the proportion of lower valence vanadium in the rutile structure increased as the total vanadium content was increased. This reflects the initial interpretation of the diffraction data. However, this approach is not accurate for determining proportions of each valence state. It also does not necessarily help in understanding what is happening at the immediate sample surface, which is postulated to contain more V^{5+}. For these reasons, another spectroscopic technique was used for complementary analysis.

7.2.3 X-ray Photoelectron Spectroscopy Valence Analysis

The 'LO' method materials VTO5, 10, 20 and 50 were also analysed using XPS to determine information about the valence states at the sample surface. The results show a broad $V2p_{3/2}$ peak for all four levels of incorporation (**Figure 7.6 (a)**). This peak can be fit to multiple valence states[405-407, 419], with the V^{5+} state similarly predominant at levels of incorporation up to 10% and V^{4+} becomes more prevalent as the vanadium is increased to 50% (**Table 7.5**). A small population of V^{3+} does appear in the VTO50 sample. The $Ti2p_{3/2}$ peak does not show a clear shift to lower binding energy that would indicate reduction of this species and is assigned as Ti^{4+} (**Figure 7.6 (b)**).

The general trend of a lowered valence state with increased vanadium introduction reflects that estimated from WDXS, though is on average higher in valence. Compositions determined from XPS also overestimate the vanadium content particularly at low levels of doping, as tabulated in **Table 7.5**. As only nanometres in depth are sampled with this method whereas WDXS samples microns, this may imply a proportion of vanadium, particularly V^{5+}, is surface localized. This may be prevalent in the lower doped samples, whereas on higher levels of

incorporation, vanadium is distributed more deeply throughout the sample due to the development of a lower valence state, and the elemental ratio becomes more accurate.

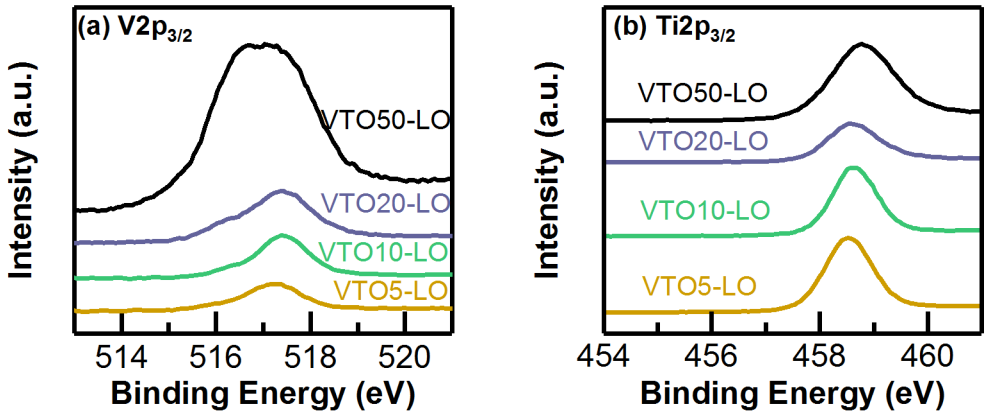

Figure 7.6. *XPS spectra of VTO-LO samples showing* ***(a)*** *the $V2p_{3/2}$ signal which is split into different valence states and* ***(b)*** *the $Ti2p_{3/2}$ signal which is less varied.*

Table 7.5. *Proportion of vanadium valence states from $V2p_{3/2}$ XPS peak fitting of VTO-LO samples. Binding energies for each fitted peak are listed in brackets (eV).*

Sample	*V^{3+} %*	*V^{4+} %*	*V^{5+} %*	*XPS Experimental V_xTi_{1-x}*
VTO5-LO	-	15 (515.98)	85 (517.23)	$V_{0.13}Ti_{0.87}$
VTO10-LO	-	15 (516.25)	85 (517.43)	$V_{0.20}Ti_{0.80}$
VTO20-LO	-	25 (516.22)	75 (517.44)	$V_{0.36}Ti_{0.64}$
VTO50-LO	5 (515.01)	52 (516.43)	43 (517.59)	$V_{0.51}Ti_{0.49}$

From both XPS and WDXS there is evidence of the valance state of vanadium lowing on increasing concentration. The decreasing lattice parameter trend noted earlier can explained by the apparently large population of V^{4+} being incorporated into the rutile structure substitutionally. Additionally, the dropping of valence seen from 5 – 20% in both methods may reflect the vanadium doping limit often observed at 10% in the literature. It is possible that surface sites may become saturated, and beyond this limit, more reducing conditions are required to encourage deep doping of V^{4+} (and V^{3+}), but this requires further testing.

A rapid increase of low valence states for high levels of vanadium incorporation should have a drastic effect on the electronic band structure and associated properties. How vanadium content and valences are related to the experimentally observed optical absorption, AC conductivity, and magnetism are explored next.

7.3 Optical, Electrical and Electronic Properties

7.3.1 Visible Light Absorption

Vanadium modified rutile TiO_2 samples made by both the 'LO' and 'O' methods exhibited a colour change on increasing levels of vanadium. From 1%, the samples begin to develop a light brown colouration, darkening as vanadium increased through dark maroon to black at 10% incorporation and beyond. This is a good indication that the optical properties are much changed, and likely other electronic properties too, as a consequence of the vanadium levels and valence states.

Spectrophotometry was used to measure the visible light absorbance of the samples produced by both methods. **Figure 7.7** shows that an introduction of vanadium using the 'LO' synthesis results in a gradual flattening of the absorbance profile of each sample in the visible light region. This implies vanadium doping induces an ability to absorb visible light, but does also shift any apparent band gap to outside the spectral range (less than 1.55 eV) for vanadium levels above 5%. The extremely flat nature of the 50% profile may suggest an absence of a band gap, and its potential metallic character is explored in later sections. This does not necessarily imply good photofunctionality, but a narrowed band gap may still be useful in other ways.

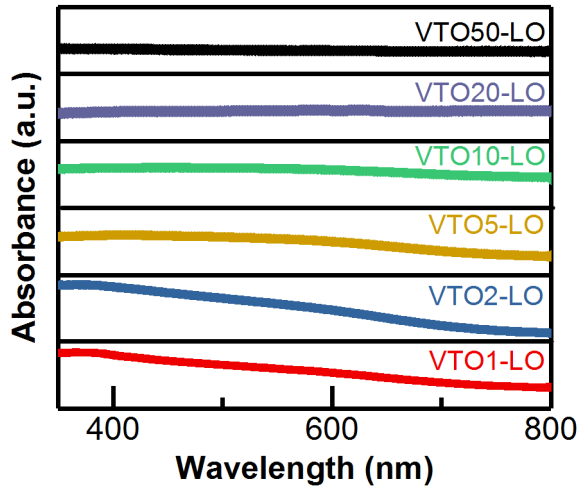

Figure 7.7. *Absorbance measurements for samples produced using the 'LO' method, showing flat profiles beyond 5% vanadium incorporation.*

Similarly, samples made using the 'O' method also showed profile flattening on increased vanadium incorporation (**Figure 7.8**). A vanadium free sample was also synthesizable via this method and is included as a comparison. It is evident that the visible light utility is greatly extended immediately on introduction of small levels of vanadium.

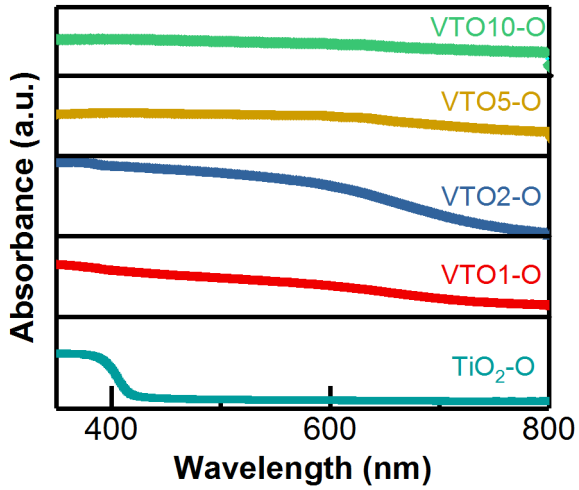

Figure 7.8. *Absorbance measurements for samples produced using the 'O' method, showing significant changes from un-doped rutile, and mostly flat profiles beyond 5% vanadium.*

Comparing this result to the literature, others have reported that a visible light band gap still exists at 5 – 10% doping levels of vanadium[254, 263, 278] while in this work it flattens quickly on increasing vanadium similar to another reflection study[280]. This may reflect the inherently mixed valence nature of the samples in this study, which are expected to produce an abundance of electronic states within the rutile band gap, thus effectively reducing the energy of optical transitions.

A narrow band gap can lead to changes in conductive properties. Differences in the AC impedance with respect to composition and temperature can provide information about charge transport dynamics. This method is used to study whether/how vanadium and its valence states change the semiconductive behaviour of rutile TiO_2.

7.3.2 Impedance Spectroscopy

7.3.2.1 Vanadium Concentration Dependence

Un-doped rutile TiO_2 is well-known for its excellent polar electrical functionality and a wide band gap. Such materials are often characterised using impedance spectroscopy. From complex impedance measurements, inferences can be made about properties of the sample that impede current (such as the materials resistance, capacitance and inductance), if more than one part of the sample contributes to its overall behaviour and if this behaviour is frequency and/or temperature dependent.

In **Figure 7.9** Nyquist plots are shown, in which the real and imaginary components of the AC impedance of both the 'LO' and 'O' method samples over the measurement range 20 Hz – 2 MHz are plotted against each other. These measurements are made under ambient light conditions. The real part of the impedance is the resistance while the imaginary part is

influenced by reactance (comprising of capacitive or inductive elements). Wide, single arced, semi-circular plots are expected for materials with some resistive and capacitive character. At 1% vanadium incorporation, the sample shows such an arc (**Figure 7.9 (a)**). However, on increasing vanadium, there is clearly more than one arc (centred at different frequencies), indicating more than one type of species present that responds to an electrical field, and that they operate with different relative speeds (e.g. VTO20-LO, **Figure 7.9 (e)**). This likely reflects short range and long range conduction within the sample. As vanadium is increased, the speeds increase until only the slow arc is seen (the fast one is outside the measurement frequency range). The width of the curves (real resistance) decrease suggesting the samples are becoming more conductive, and the vertical height of the curves also decrease suggesting a loss of capacitive behaviour. A loss of capacitance might be related to different ionic polarization after structural modification.

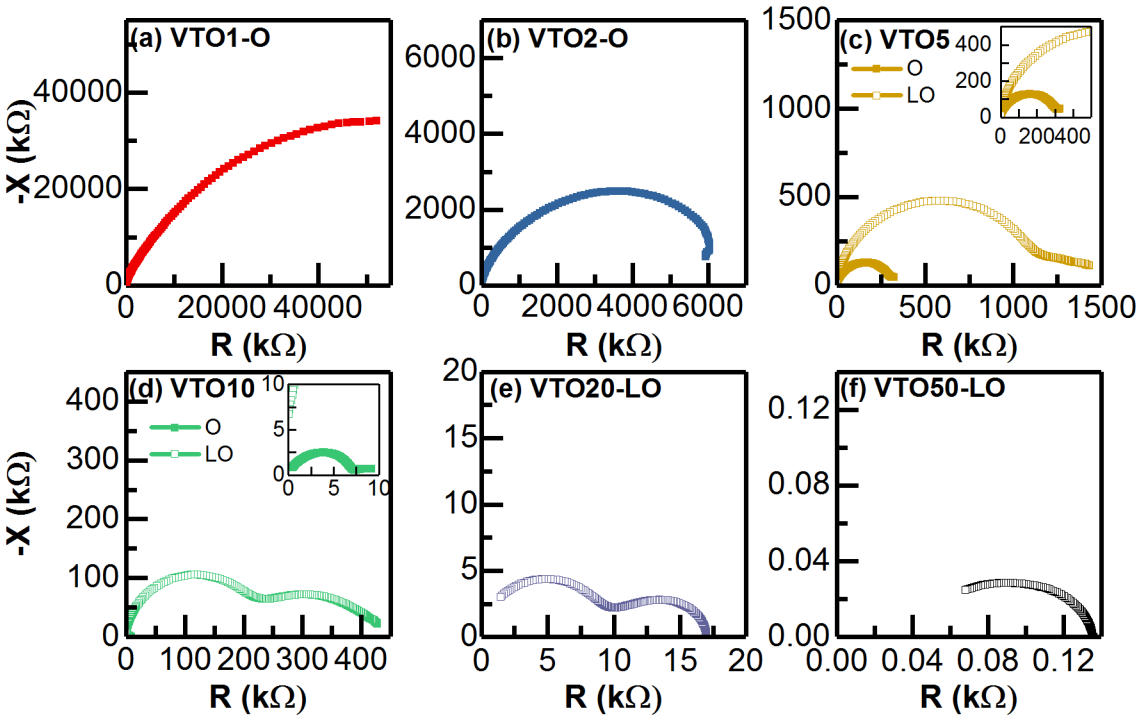

Figure 7.9. *Nyquist plots of samples made by both the 'O' and 'LO' methods. Low frequency data points appear on the right of each plot, with high frequency near the origin. Multiple arcs indicated transport mechanisms with different speeds, which become faster and less impeded as vanadium increased from 1 – 50%.*

A cross section of these arcs at specific frequencies was taken then converted to resistivity, which accounts for the sample dimensions (**Figure 7.10**). The high frequency data increases in resistivity and converges with, and then decreases with, the low frequency data. This reflects the fast mechanism moving outside the frequency range, then both data points capturing the second slower mechanism. This decrease in apparent resistivity as vanadium is increased

may be due to an increased supply of charge carriers, or perhaps a mediation of conduction through closely correlated reduced vanadium centres. The 'O' method samples appear less resistive, likely as a consequence of their higher densities.

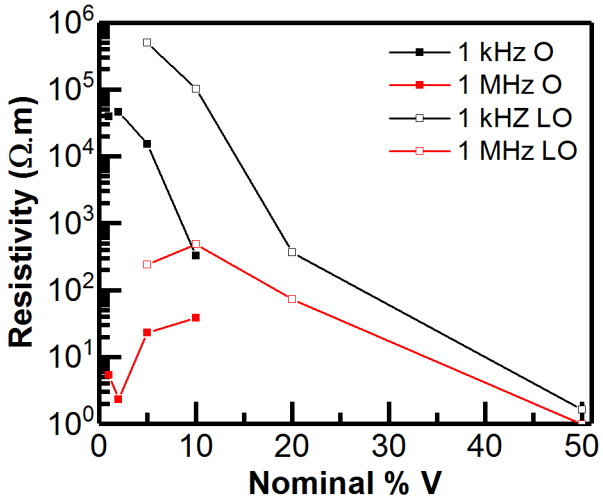

Figure 7.10. *Resistivity values at frequencies 1 kHZ and 1 MHz for each sample at room temperature.*

The extra arc seen in these measurements appears to be closely associated with the vanadium introduction. From the XPS and WDXS data shown previously it is also apparent that the total amount of V^{4+} increases with increasing levels, particularly around 10%, where this second arc is very obvious. This slower mechanism being related to a motion of this paramagnetic electron over a small volume seems a possible explanation. To understand this better, the temperature dependent behaviour of VTO50 with the highest V^{4+} content is studied.

7.3.2.2 Temperature Dependence in VTO50

At room temperature VTO50 shows a single arc in the AC impedance, likely the slower of two mechanisms, which implies low real resistance and some small amount of retained capacitive character. From the early optical studies, this material is expected to have a narrow bandgap which may easily be overcome by thermal excitation. By studying the impedance over a wider range of temperatures (10 K to 450 K), it is possible monitor possible semiconducting behaviour.

Figure 7.11 presents data from selected temperature windows over which impedance was measured. It is notable that below ~ 121 K only a single arc is observed, indicating only the fast conduction mechanism is observed in the frequency window and the second is too slow. From ~ 121 to ~ 241 K two mechanisms are observed, the second slower mechanism now thermally activated to be in the frequency window (**Figure 7.11 (b)**). From ~ 241 K to ~ 304 K only the slower mechanism is visible, with the faster one outside the frequency window. Then

beyond 304 K, the material begins to show inductive behaviour (vertical line) at high frequency (**Figure 7.11 (c)**) and some hysteresis as the sample is cooled. The first take away is that the resistance drops as the temperature is increased which is a classic feature of a semiconducting material. Secondly, the way these arcs appear and disappear in the frequency range as both mechanisms become faster mirrors the effect of introducing extra vanadium in the last subsection. A cross section at high and low frequency presented in **Figure 7.12** also mimics this effect. This seems to suggest the increasing conductivity with respect to doping and temperature comes from increasing the carrier concentration. Lastly, the disappearance of the second mechanism and appearance of the inductive third mechanism might suggest some kind of transition associated with the vanadium valences. If the inductive effect comes from the sample (not the electrode) and is associated with the paramagnetic electrons, it should be possible to detect anomalies in temperature dependent magnetic measurements.

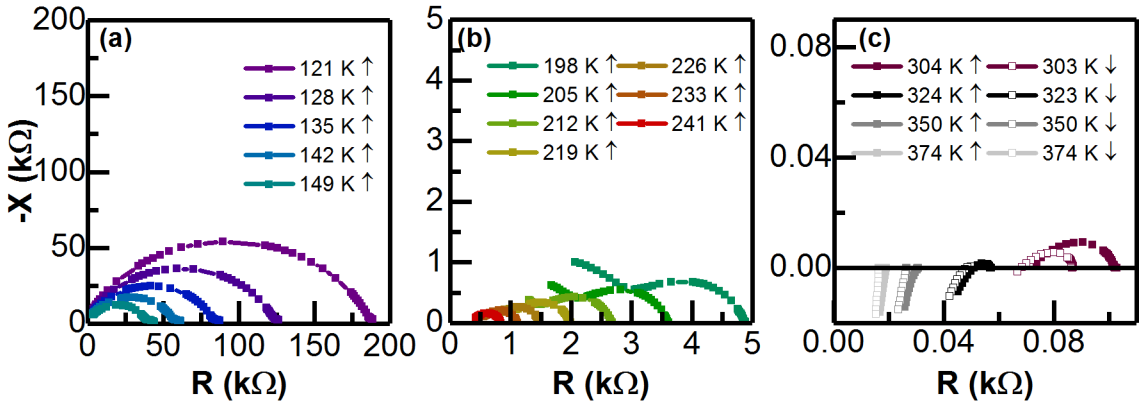

Figure 7.11. *Nyquist plots of temperature dependent impedance data for V50TO-LO showing temperature intervals during which different mechanisms are observable. Measurements made on heating are indicated with ↑, and cooling with ↓.*

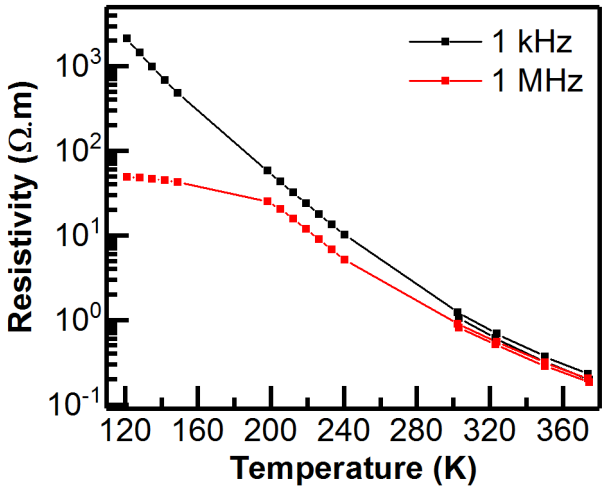

Figure 7.12. *Cross section of resistivity values at 1 kHZ and 1 MHz for VTO50.*

7.3.3 Magnetism in VTO50

In the previous sections it was noted that at 50% vanadium replacement the material showed no apparent band gap in the visible light region and low AC impedance which appeared to become inductive above room temperature. If the second arc and third inductive region are associated with the reduced V^{4+} and V^{3+} detected, then it might be possible to also see a corresponding change in the magnetization.

Magnetization of this material was measured over a broad temperature range and appears quite typically paramagnetic (**Figure 7.13**) until above room temperature between 325 and 350 K (**Figure 7.13, inset**) where there is an inflection. This indicates a change in the magnetic state of this material. This result is largely consistent with simulations of V-modified rutile TiO_2 which suggest there should be ferromagnetic interactions between neighbouring ions but no long range order[265-267]. However, the broad inflection of the magnetization above room temperature is unusual. This seems to suggest an increase in magnetization as if a component previously diamagnetic has become paramagnetic. A possible explanation for this is found in another VTO report[286] which suggests some diamagnetic V^{4+}-V^{4+} bonded pairs exist and persist for all levels of vanadium incorporation. This pairing phenomenon is often suggested to be the origin of metal-insulator (MI) transitions in both VO_2 and the spinodally decomposed VTO[420]. Thus, in the VTO50 sample studied, some V^{4+} might be paired at low temperature, subtracting from the effective magnetic moment, then uncouple at high temperature to increase the magnetization.

In the literature, this pairing effect and associated MI transition typically results in orders of magnitude change in magnetization and conductivity measurements[261]. The measurements made in this study do not show such significant changes. Given in these literature examples all the vanadium is in the V^{4+} state, and in this sample only a proportion of the total vanadium is, perhaps these effects have been weakened. The presence of other valence states of vanadium seem the likely cause of disrupted spinodal decomposition, leading to this intermediate behaviour and is somewhat supported by reports on altervalent doping changing MI character[421]. This might be further tested in future works by extending the sintering times significantly and seeing if any spinodal decomposition is ever observed.

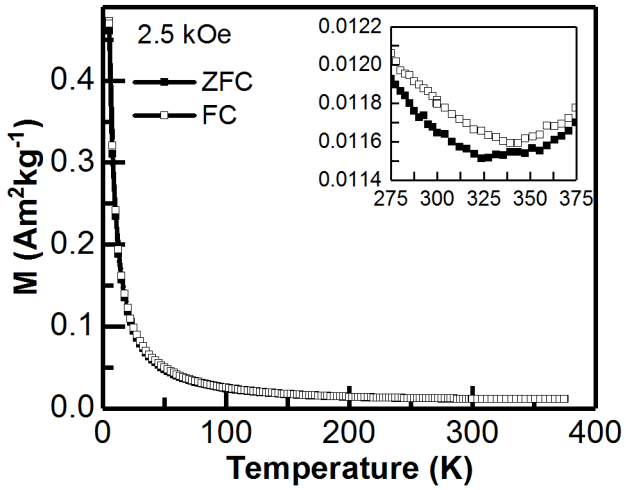

Figure 7.13. *Magnetization with respect to temperature data for VTO50-LO showing paramagnetic dependence until ~ 325 K (**inset**). There is a difference between the inflection points in ZFC and FC measurements.*

This section has shown that the optical, electrical and magnetic properties are perturbed from the behaviour of the related compounds TiO_2 and VO_2 with the same structure type. The origin of the differences seems to be associated with the multivalent nature. In the next section, questions around how vanadium is actually being incorporated into rutile are discussed, to explain these observed physical properties.

7.4 Defect Chemistry Discussion

There are number of possible mechanisms through which vanadium is being incorporated into the TiO_2 rutile framework to lead to the observed valence states and properties. The synthetic processes are conducted under reducing conditions and the V_2O_5 raw material may be converted to VO_2 by this method. Incorporation of vanadium as units of VO_2 into TiO_2 is charge neutral (**Equation 7.1**) and suggested to be a low energy process in theoretical study[268]. This is one explanation for the abundance of V^{4+} detected in XPS and WDXS.

$$VO_2 \xrightarrow{TiO_2} 2V_{Ti} + 2O_o \quad \textbf{(7.1)}$$

This might also be explained by V_2O_5 incorporation inducing free electron formation and evolution of oxygen per the below expression.

$$V_2O_5 \xrightarrow{2TiO_2} 2V_{Ti}^{\cdot} + 4O_o + \frac{1}{2}O_2 \uparrow + 2e^- \quad \textbf{(7.2)}$$

These electrons then have the opportunities to become localised on a number of species as below.

$$V^{5+} + e^- \rightarrow V^{4+} \quad \textbf{(7.3)}$$

$$Ti^{4+} + e^- \rightarrow Ti^{3+} \quad \textbf{(7.4)}$$

$$V^{4+} + e^- \rightarrow V^{3+} \quad \textbf{(7.5)}$$

This study has shown evidence for V^{4+} and V^{3+} in these materials, but not Ti^{3+}. This is supported by theoretical reports which suggest vanadium is the most likely to trap free electrons and result in a reduced state with a single unpaired electron on V^{4+} [265-268]. Experiments also show that even in oxidizing conditions, V^{4+} is found to form and penetrate deeply into the rutile framework[227, 264].

The V^{5+} ions on the other hand seem more likely to be surface localized in the rutile structure. The bulk substitutional octahedral sides share two edges which can be a disfavoured coordination for the high valence V^{5+} ion (Paulings rules[300]). The native coordination of V^{5+} is square pyramidal[422] which can be accommodated on the rutile surface with some adsorbed species[277] but not as easily in the bulk. Experimentally in this study it was shown that a proportion of V^{5+} exists at the sample surface with XPS, whereas WDXS showed evidence for the reduced states V^{4+} and V^{3+} in the bulk. The XPS V^{5+} signal appears to plateau at 10% doping, mirroring changes in XRPD lattice parameters. This may imply the possibility of incorporating V^{5+} at the sample surface up until a doping limit. This limit is also reflected in this work where V_2O_5 exists as a side phase during synthesis in more oxidizing conditions and in higher vanadium samples (see **Section 7.1.1.2**), also noted in the literature[251]. Deeply doped

V^{4+} should not be easily re-oxidized like this[237, 247], so the V^{5+} at the surface should be a unique population.

Further charge balance within this system could be achieved through deeply doped V^{3+} species, which are implied from this experiment, and/or vacancies which been implicated in other M^{5+} studies[421]. Example defect equations are shown below.

$$V_1O_{2.5} \xrightarrow{2TiO_2} V_{Ti}^{\cdot} + Va_{Ti}^{''''} + 2.5O_o + 1.5Va_o^{\cdot\cdot} \quad \textbf{(7.6)}$$

$$V_1O_{1.5} + V_1O_{2.5} \xrightarrow{2TiO_2} V_{Ti}' + V_{Ti}^{\cdot} + 4O_o \quad \textbf{(7.7)}$$

Thus, the rutile structure appears to place limitations on obtainable valence states, explaining the dominant V^{4+} and a mix of other defects. This defect combination explains the experimentally measured properties, such as the strong visible light absorption due to V^{5+}, V^{4+} and V^{3+} gaps states[267, 268, 271, 274, 275] and the decreasing DC resistivity as a consequence of the low-valent vanadium. As per the findings from the previous chapter, these materials would not be optimal photocatalysts due to a high chance of gap state recombination, but the clear semiconductive character induced by increasing vanadium is a useful property and may be applied to other electronic technologies. In addition, the multivalent VTO50 samples appears to have unusual magnetic properties that might be tuneable if valence states can be further altered in synthesis.

7.5 Summary of Chapter 7

A simple solid state method was developed to incorporate up to 50 at. % vanadium into rutile TiO_2 by using a nitrogen atmosphere. Using XPS it was found that the vanadium is in a majority V^{5+} state at the surface in samples containing less than 10% vanadium. Above 10%, the V^{4+} increases and some V^{3+} is detected at 50%. WDXS measurements suggest further reduction may occur to include large levels of V^{3+} in 10% and higher vanadium concentrations. Changes in the structure also suggest a unit cell contraction as more vanadium is added, though it is non-linear and depends strongly on synthesis methods. Together this suggests that V^{4+} is in the bulk substitutional sites, V^{3+} in bulk undetermined sites, and V^{5+} on the surface. A limit appears to exist around 10% after which further incorporation of vanadium can only be obtained by the lowering of the valence state mediated by the synthesis environment, mirroring literature vanadium solubility studies.

The presence of multiple vanadium valences has led to a demonstrated change in the visible light absorption characteristics of the samples. From 0 – 10% incorporation, samples have an absorption edge in the visible light range, where at 10% and above, the whole visible light

range is effectively absorbed. This is most likely due to the reduced vanadium generating low lying gap states and effectively narrowing the band gap.

The influence of vanadium and its multiple valences is also apparent in impedance measurements. On increasing vanadium, the resistive part of the impedance drops, and two clear transport mechanisms within the samples are observed in the frequency window. The second mechanism appears related to the vanadium, and may reflect a charge transport process. The overall decrease in resistance seems to reflect the increasing number of electrons in the system added through vanadium.

A more in-depth examination of the 50% replacement sample shows semiconducting temperature dependence from 10 – 450 K. An onset of inductive behaviour is seen above room temperature which might be evidence for a change in the underlying behaviour of the paramagnetic ions. This is supported by an anomaly in the magnetization which may imply an increase in available V^{4+} above room temperature. This phenomenon seems related to the metal-insulator transition reported for similar materials in the literature, but is reduced in magnitude likely by the coexisting V^{5+}. Nonetheless, the material made in this study is suggested to be a very narrow band gap semiconductor

From these results it was seen that introducing elements with variable valence states can be a way of changing the host oxide's band gap, though it can result in complex effects on the electronic properties. In conjunction with the previous chapter, this study serves to further explore how defects can influence properties and how different structure types can support different functions for similar combinations of elements.

Chapter 8 Conclusions and Future Directions

8.1 Thesis Summary and Contributions

In this thesis, characteristics of five classes of candidate photofunctional oxide materials were investigated to contribute to the development of future energy transformation technologies. These materials were carefully selected for their potential functionality, but the literature contained many gaps surrounding their syntheses, elemental and valence state distributions, physical properties, and apparent photofunctionality. Through investigation it was shown that these specific characteristics are intrinsically linked. We are one step closer to being able to control such factors and implement these materials in photofunctional applications.

In **Chapter 3**, the material BFCO was explored. BFCO was known in the literature to be difficult to synthesize, but also possessed potential for good multiferroic and photovoltaic properties if it could be made in a double perovskite structure. In this chapter, a solid state synthesis method was presented which employed a quartz crucible to generate bulk samples for the first time. This synthesis permitted structural characterisation by X-ray, neutron and electron diffraction. These complementary studies showed the structure of bulk BFCO to have chemical disorder of Fe and Cr in the perovskite *B*-site, in contrast to reports of thin film BFCO. A lower calculated DFT energy for chemical disorder supports the formation of this phase under bulk synthesis conditions. The chemical disorder meant the magnetic properties were affected, and it was shown for the first time that antiferromagnetic ordering with a weak net moment (likely arising instead from spin canting) persists to above room temperature. However, ferroelectric character was observed despite disorder, making it a generally useful candidate multiferroic material. Strong visible light absorption and a photocurrent were also observed, confirming it as a photofunctional oxide.

This investigation exemplified the effect chemical ordering within the perovskite structure can have on physical properties. This formed a firm foundation from which to investigate further chemical modification of the perovskite $BiFeO_3$ in search for more synthesizable multifunctional materials.

In **Chapter 4** the modification of $BiFeO_3$ with titanium and the divalent cations Fe^{2+}, Ni^{2+}, Mg^{2+}, Zn^{2+} and Cu^{2+} was explored. The Mg^{2+} and Ni^{2+} ions were shown to produce the perovskite phases BFMTO and BFNTO under ambient pressure. Very little was known about these phases in the literature. By developing metal organic decomposition and solid state synthesis methods, a suite of novel characterisations could be made. From X-ray diffraction and Mössbauer spectroscopy, these materials also appeared to have chemical disorder in the perovskite *B*-site. The disorder and presence of diluting diamagnetic Ti^{4+} and Mg^{2+} resulted in

bulk paramagnetic behaviour in BFMTO, though some local interactions may exist at temperatures near 3 K. The behaviour of BFNTO is much more unusual, showing a potentially ordered state below room temperature from a heat capacity study, but other magnetic tests were heavily influenced by a ferrimagnetic impurity. Nonetheless, both BFMTO and BFNTO showed evidence for ferroelectric domain formation and an ability to generate photocurrent which were measured for the first time. While these materials appear to be more insulating than BFCO, and possess different magnetic character, they were still shown to be multifunctional.

Again, photofunctionality in the tested oxide materials has been confirmed in Chapter 4. In conjunction with Chapter 3, it is clear that the perovskite structure permits a wide range of properties but does not easily sustain chemical ordering. By shifting to a related structure type in Chapter 5 which could also exhibit multiferroism, the consequences of chemical modification on properties could be further explored.

In **Chapter 5**, the Aurivillius phases BFTO-513, BFTO-623 and BFTO-733 were studied, which retained the perovskite structural motif of edge connected octahedra in blocks, sandwiched between layers of bismuth oxide. The literature on the materials suggested multiferroism and photofunctionality, but as more iron is introduced into the structure, the synthesis becomes notoriously difficult. In Chapter 5 a straightforward metal organic decomposition method to produce high purity samples was introduced, overcoming this apparent difficulty. After successful synthesis, structure refinement was conducted in order to investigate what appeared to be seldom reported crystal structures. From X-ray diffraction data, structural inhomogeneities may exist in these samples, perhaps as a consequence of structural faulting and leading to difficulty in refinement. It was also shown through Mössbauer that little evidence for chemical ordering can be found in these systems. Again, Fe is distributed randomly, and like in Chapter 4, any magnetic ordering is well below room temperature. The BFTO-733 sample does appear to exhibit a clear and unusual magnetic transition near 100 K which may suggest low dimensional antiferromagnetism. Ferroelectric domains were clearly imaged in BFTO-513 and BFTO-733 for the first time, showing that the change in structure type from perovskite to Aurivillius has altered the polar properties. The photofunctional properties also increase with increasing iron. The BFTO-733 sample is considered highly for photofunctional applications.

Work in Chapter 5 involved studying a systematic compositional change from more diamagnetic ions to more paramagnetic ions within a crystal structure, and observing the associated changes in the magnetic properties. This presents a framework in which magnetism could be tuned. The effect of changing the structure type was also apparent on polar

properties. Extending these ideas, a specific photofunctional property was targeted through modification of a new structure type – anatase TiO_2 – in Chapter 6.

In **Chapter 6** an exploration of co-doping vanadium and nitrogen into anatase TiO_2 was undertaken. The combination of V^{5+}-N^{3-} had been flagged many times in the literature as a way to band gap reduction and good photocatalysis. However, curious extra valence states of vanadium and inconsistent catalytic performance suggested there was more to be learned. In Chapter 6, a synthetic method known to work for other M^{5+}-N^{3-} combinations was employed to make samples for study. It was found that while production of anatase nanoparticles was possible, phase formation was sensitive to pH (brought about by the nitrogen source) limiting dopant incorporation. Studying the samples also revealed two vanadium valences (V^{4+} and V^{3+}). The V^{3+} appears correlated with increased overall vanadium and with added nitrogen, but the expected V^{5+}-N^{3-} dopant pair is not evident. There is evidence for substitutional V^{4+} in more than one unique coordination, and V^{3+} and N likely exist in a non-substitutional bonding configuration. This result leads to gap state formation within the optical band gap, and associated poor catalytic performance as a wastewater photocatalyst.

Chapter 6 demonstrated how rationally designing materials to have a particular effect on the band gap hinges on being able to achieve the appropriate valence state and doping location for those elements. This links back into designing materials with long range chemical ordering for other physical properties like magnetism in Chapter 3. The synthetic process has its own requirements. This system raised questions about how vanadium might be supported in other crystal structures and so in Chapter 7, the effects of vanadium valence states on the functionality of TiO_2 rutile is addressed.

Vanadium has a documented effect on the visible light photofunctionality of rutile TiO_2, but its connection with the valence states of vanadium is not known, nor is the synthetic restrictions on what valence states can be achieved. **Chapter 7** shows how using nitrogen gas as a reducing agent, reduction of vanadium can be encouraged to make materials with up to 50 at. % V. Similar to Chapter 6, the valence state of vanadium drops with increased total incorporation. Evidence for V^{5+} existing at the sample surface and V^{4+} and V^{3+} in the sample bulk suggests the vanadium behaviour is structure limited. These mixed valence products show drastic changes in the visible light utility with an apparent narrower-than-visible light gap obtained for doping levels of 5% and above, likely attributable to gap states. As the vanadium is increased, changes are also observed in electrical properties, with multiple conduction mechanisms and clear semiconductive character. High doping samples (50 at. % V) also show a dynamic magnetic phenomenon which possibly relates to changes in V^{4+} availability.

The study outlined in Chapter 7 gave further insights into how targeting band gap reduction with elemental modification can be accomplished through multiple valence states, but this may be more useful for electronics in general rather than specific photofunctional applications. Here the tolerance of the structure to elemental modification is an important consideration.

Through each chapter many oxide materials were confirmed to possess photofunctional character. Overlapping elements and structural motifs allowed translation of synthesis and characterisation methods to new materials. Novel syntheses allowed new properties to be measured including magnetism, ferroelectricity, photocurrent generation and visible light absorption, which appeared connected to the structure and elemental ordering in the materials.

8.2 Limitations, Implications and Future Work

There are ways in which the work presented in this thesis could be extended to obtain an even better understanding of the links between synthesis, structure and properties of photofunctional materials. The syntheses presented could be enhanced by testing some additional conditions for example. Currently, the sample syntheses are optimized for phase purity instead of density and electrical measurements are made on a local scale as a consequence. To get a better idea of bulk behaviour, synthetic methods need to be further optimized. Some of the syntheses which did not produce functional materials might also be studied further. It is desirable to try more forcing synthesis conditions for Fe^{2+}, Cu^{2+} and Zn^{2+} modified $BiFe_{0.25}M_{0.375}Ti_{0.375}O_3$ to see if any new phases can be formed, to try different nitrogen sources in production of VTON samples to expand understanding of its role in catalysis, and also to try extended sintering times for VTO50 to see if spinodal decomposition can ever be induced when multiple vanadium valences coexist.

The structural and elemental characterisations presented in this thesis are also limited in places. The Chapter 5 samples in particular suffered from a high background in XRPD measurements which made structure refinement challenging. Chemical ordering in BFMTO and BFNTO could also not be definitively determined with the presented diffraction methods. All might be resolved with neutron diffraction experiments to produce better data for refinement and perhaps conduct a titling mode decomposition analysis. Neutrons also present an opportunity to study the apparent magnetic transitions in BFTO-733 and BFNTO. High resolution TEM imaging might also be a good complement to such studies for detecting chemically ordered domains. In terms of valence analysis, the combination of XPS, WDXS and ESR could not capture all valence states at all depths in the VTO and VTON samples, so further techniques could be pursued for depth profiling.

The photofunctional characterisations in this thesis are also fairly preliminary. To truly assess solar potential, measurements under standard sun conditions would be highly desirable. Modifying the experimental setup to allow poling of samples before measurements of photocurrent may also help assess photovoltaic utility. In addition, while evidence for chemical disorder and band gap reduction has been observed in each material, its direct link remains less clear than others. This could be further investigated through *ab initio* calculation of band structures. This is however a challenging prospect to capture the properties of a disordered system.

Despite such limitations, this thesis resulted in a number of interesting findings. These findings not only expand the literature on the investigated materials, but highlight key materials that could be adapted into practical devices, and also provide new perspectives through which to study entirely new sets of materials. There a several avenues that could be explored beyond what is addressed in this thesis.

Materials from this thesis might now be adapted into practical solar devices. The materials BFCO and BFTO-733 look particularly promising for photovoltaics and new insights into low complexity synthesis methods for these might be scalable for prototype device fabrication. Growth of multilayer epitaxial thin films with several absorption characteristics might also be an avenue to explore for enhanced photofunctionality. For photocatalytic applications, cleavage of Aurivillius structures into 2D sheets of perovskite blocks would also be an exciting prospect, as might combining the VTON samples with a co-catalyst to drive oxidation and reduction reactions with the correct potentials. It is acknowledged however that some of the materials contain environmentally harmful (V, Ni) and expensive (Bi) elements. Experimenting with elemental substitution to reduce their quantities in the final product would assist in making these materials more environmentally practical.

Many other types of physical properties were identified in each of the investigated materials. This opens avenues for mixed function devices. For example, the combination of magnetic and ferroelectric character in several samples have applications in spintronics and data storage, while semiconductors like VTO might be useful in sensor technology.

This work has revealed how difficult it is to realise theoretically predicted chemical ordering and/or valence state trends in oxides. This knowledge could be used to look at other materials from a new perspective. Bismuth vanadates for example, are a natural intersection of the materials covered in this thesis. The material $BiVO_4$ shows exciting photocatalytic water splitting behaviour, and $Bi_4V_2O_{11}$ (with an Aurivillius-like structure) is also known for visible light responsiveness. Using knowledge gained in this thesis, it would be interesting to study how vanadium valence states and ordering of dopants (such as W or Ti) would affect their

photofunctionality. In addition, general insights from this thesis can also help with the prediction and design of new photofunctional materials.

8.3 Closing

The set of materials investigated in this thesis are photofunctional and there are clear links between the synthesis, structure, chemical distribution and the exhibition of physical properties. A holistic understanding of these factors is crucial to implementation in practical devices, thus building foundations for the use of oxide materials in energy transformation. This is a step towards the cheap, tuneable, renewable energy technologies that are needed in supporting changing world energy demands.

References

1. E. Kabir, P. Kumar, S. Kumar, A. A. Adelodun and K.-H. Kim, Renewable and Sustainable Energy Reviews **82**, 894-900 (2018).
2. F. E. Osterloh, Chemistry of Materials **20** (1), 35-54 (2007).
3. G. Zhang, G. Liu, L. Wang and J. T. Irvine, Chemical Society Reviews **45** (21), 5951-5984 (2016).
4. Y. Yuan, Z. Xiao, B. Yang and J. Huang, Journal of Materials Chemistry A **2** (17), 6027-6041 (2014).
5. U. I. Gaya and A. H. Abdullah, Journal of Photochemistry and Photobiology C: Photochemistry Reviews **9** (1), 1-12 (2008).
6. A. Hagfeldt, G. Boschloo, L. Sun, L. Kloo and H. Pettersson, Chemical Reviews **110** (11), 6595-6663 (2010).
7. O. Carp, C. L. Huisman and A. Reller, Progress in Solid State Chemistry **32** (1-2), 33-177 (2004).
8. T. Ishihara, *Inorganic Perovskite Oxides,* (Springer International Publishing, 2017), 1-1.
9. R. Hoffmann, Angewandte Chemie International Edition **26** (9), 846-878 (1987).
10. A. McEvoy, A. McEvoy, T. Markvart and L. Castaner, *Practical Handbook of Photovoltaics : Fundamentals and Applications,* (Elsevier Science & Technology, 2011), Chapter IA.
11. L. Li, P. A. Salvador and G. S. Rohrer, Nanoscale **6** (1), 24-42 (2014).
12. J. Zhang, P. Zhou, J. Liu and J. Yu, Physical Chemistry Chemical Physics **16** (38), 20382-20386 (2014).
13. A. K. Bain and P. Chand, *Ferroelectrics : Principles and Applications,* (John Wiley & Sons, Incorporated, 2017), Chapter 4.
14. A. R. West, *Solid State Chemistry and Its Applications,* (John Wiley & Sons, Incorporated, 2014), Chapter 8.
15. M. Lorenz, M. R. Rao, T. Venkatesan, E. Fortunato, P. Barquinha, R. Branquinho, D. Salgueiro, R. Martins, E. Carlos and A. Liu, Journal of Physics D: Applied Physics **49** (43), 433001 (2016).
16. J. M. Frost, K. T. Butler, F. Brivio, C. H. Hendon, M. Van Schilfgaarde and A. Walsh, Nano Letters **14** (5), 2584-2590 (2014).
17. V. Fridkin, Crystallography Reports **46** (4), 654-658 (2001).
18. K. H. J. Buschow and F. R. Boer, *Physics of Magnetism and Magnetic Materials,* (Kluwer Academic Publishers, 2004), Chapter 2.
19. J. B. Goodenough, Physical Review **100** (2), 564 (1955).
20. J. Kanamori, Journal of Physics and Chemistry of Solids **10** (2-3), 87-98 (1959).
21. P. W. Anderson, Physical Review **115** (1), 2 (1959).
22. V. A. Sadykov, *Perovskite: Crystallography, Chemistry and Catalytic Performance,* (Nova Science Publishers, Inc., 2013), Chapter 2.
23. M. Opel, Journal of Physics D: Applied Physics **45** (3), 033001 (2011).
24. A. R. West, *Solid State Chemistry and Its Applications,* (John Wiley & Sons, Incorporated, 2014), Chapter 9.
25. J. Dulińska-Litewka, A. Łazarczyk, P. Hałubiec, O. Szafrański, K. Karnas and A. Karewicz, Materials **12** (4), 617 (2019).
26. D. Khomskii, Physics **2**, 20 (2009).
27. N. Spaldin and R. Ramesh, Nature Materials **18** (3), 203 (2019).
28. M. Gajek, M. Bibes, S. Fusil, K. Bouzehouane, J. Fontcuberta, A. Barthélémy and A. Fert, Nature Materials **6** (4), 296-302 (2007).
29. N. A. Hill, Journal of Physical Chemistry B **104** (29), 6694-6709 (2000).
30. M. Pena and J. Fierro, Chemical Reviews **101** (7), 1981-2018 (2001).
31. J.-M. Moreau, C. Michel, R. Gerson and W. J. James, Journal of Physics and Chemistry of Solids **32** (6), 1315-1320 (1971).

32. A. Glazer, Acta Crystallographica Section B: Structural Crystallography and Crystal Chemistry **28** (11), 3384-3392 (1972).
33. G. Meyer, R. Nelmes and J. Hutton, Ferroelectrics **21**, 461-462 (1978).
34. M. M. Kumar, V. R. Palkar, K. Srinivas and S. V. Suryanarayana, Applied Physics Letters **76** (19), 2764-2766 (2000).
35. S. M. Selbach, T. Tybell, M. A. Einarsrud and T. Grande, Advanced Materials **20** (19), 3692-3696 (2008).
36. G. Catalan and J. F. Scott, Advanced Materials **21** (24), 2463-2485 (2009).
37. A. K. Pradhan, K. Zhang, D. Hunter, J. Dadson, G. Loiutts, P. Bhattacharya, R. Katiyar, J. Zhang, D. J. Sellmyer and U. Roy, Journal of Applied Physics **97** (9), 093903 (2005).
38. J. Yu and J. Chu, Chinese Science Bulletin **53** (14), 2097-2112 (2008).
39. I. Sosnowska, T. P. Neumaier and E. Steichele, Journal of Physics C: Solid State Physics **15** (23), 4835 (1982).
40. I. Gross, W. Akhtar, V. Garcia, L. J. Martinez, S. Chouaieb, K. Garcia, C. Carretero, A. Barthelemy, P. Appel, P. Maletinsky, J. V. Kim, J. Y. Chauleau, N. Jaouen, M. Viret, M. Bibes, S. Fusil and V. Jacques, Nature **549** (7671), 252-256 (2017).
41. A. M. Kadomtseva, A. K. Zvezdin, Y. F. Popov, A. P. Pyatakov and G. P. Vorob'ev, Journal of Experimental and Theoretical Physics Letters **79** (11), 571-581 (2004).
42. A. Popkov, M. Davydova, K. Zvezdin, S. Solov'Yov and A. Zvezdin, Physical Review B **93** (9), 094435 (2016).
43. P. Baettig and N. A. Spaldin, Applied Physics Letters **86** (1), 012505/012501-012505/012503 (2005).
44. K. Liu, H. Fan, P. Ren and C. Yang, Journal of Alloys and Compounds **509** (5), 1901-1905 (2011).
45. P. Ravindran, R. Vidya, A. Kjekshus, H. Fjellvag and O. Eriksson, Physical Review B: Condensed Matter and Materials Physics **74** (22), 224412/224411-224412/224418 (2006).
46. J. B. Neaton, C. Ederer, U. V. Waghmare, N. A. Spaldin and K. M. Rabe, Physical Review B: Condensed Matter and Materials Physics **71** (1), 014113/014111-014113/014118 (2005).
47. S. M. Young, F. Zheng and A. M. Rappe, Physical Review Letters **109** (23), 236601 (2012).
48. W. Ji, K. Yao and Y. C. Liang, Advanced Materials **22** (15), 1763-1766 (2010).
49. T. Choi, S. Lee, Y. Choi, V. Kiryukhin and S.-W. Cheong, Science **324** (5923), 63-66 (2009).
50. T. Gao, Z. Chen, F. Niu, D. Zhou, Q. Huang, Y. Zhu, L. Qin, X. Sun and Y. Huang, Journal of Alloys and Compounds **648**, 564-570 (2015).
51. C. M. Cho, J. H. Noh, I. S. Cho, J. S. An, K. S. Hong and J. Y. Kim, Journal of the American Ceramic Society **91** (11), 3753-3755 (2008).
52. K. A. McDonnell, N. Wadnerkar, N. J. English, M. Rahman and D. Dowling, Chemical Physics Letters **572**, 78-84 (2013).
53. S. M. Selbach, M.-A. Einarsrud and T. Grande, Chemistry of Materials **21** (1), 169-173 (2008).
54. M. Bernardo, T. Jardiel, M. Peiteado, A. Caballero and M. Villegas, Journal of the European Ceramic Society **31** (16), 3047-3053 (2011).
55. M. Valant, A.-K. Axelsson and N. Alford, Chemistry of Materials **19** (22), 5431-5436 (2007).
56. J. Silva, A. Reyes, H. Esparza, H. Camacho and L. Fuentes, Integrated Ferroelectrics **126** (1), 47-59 (2011).
57. T. Rojac, A. Bencan, B. Malic, G. Tutuncu, J. L. Jones, J. E. Daniels and D. Damjanovic, Journal of the American Ceramic Society **97** (7), 1993-2011 (2014).
58. P. Baettig, C. Ederer and N. A. Spaldin, Physical Review B: Condensed Matter and Materials Physics **72** (21), 214105/214101-214105/214108 (2005).
59. R. Nechache, C. Harnagea, S. Li, L. Cardenas, W. Huang, J. Chakrabartty and F. Rosei, Nature Photonics **9** (1), 61-67 (2015).

60. R. Nechache, C. Harnagea, S. Licoccia, E. Traversa, A. Ruediger, A. Pignolet and F. Rosei, Applied Physics Letters **98** (20), 202902/202901-202902/202903 (2011).
61. A. Quattropani, A. Makhort, M. V. Rastei, G. Versini, G. Schmerber, A. Dinia, S. Barre, A. Slaoui, J.-L. Rehspringer and T. Fix, Nanoscale (2018).
62. R. Nechache, C. Nauenheim, U. Lanke, A. Pignolet, F. Rosei and A. Ruediger, Journal of Physics: Condensed Matter **24** (14), 142202/142201-142202/142205 (2012).
63. J. L. Zhu, H. X. Yang, S. M. Feng, L. J. Wang, Q. Q. Liu, C. Q. Jin, X. H. Wang, L. T. Li and J. Yu, International Journal of Modern Physics B **27** (15), 1362023/1362021-1362023/1362028 (2013).
64. V. Shabadi, M. Major, P. Komissinskiy, M. Vafaee, A. Radetinac, M. Baghaie Yazdi, W. Donner and L. Alff, Journal of Applied Physics **116** (11), 114901/114901-114901/114908 (2014).
65. M. R. Suchomel, C. I. Thomas, M. Allix, M. J. Rosseinsky, A. M. Fogg and M. F. Thomas, Applied Physics Letters **90** (20), 209901/209901 (2007).
66. Y. Shimakawa, M. Azuma and N. Ichikawa, Materials **4** (1), 153-168 (2011).
67. C. T. Chantler, Journal of Physical and Chemical Reference Data **29** (4), 597-1056 (2000).
68. V. F. Sears, Neutron News **3** (3), 26-37 (1992).
69. R. Nechache, C. Harnagea, A. Pignolet, F. Normandin, T. Veres, L.-P. Carignan and D. Menard, Applied Physics Letters **89** (10), 102902/102901-102902/102903 (2006).
70. G. Vinai, A. Khare, D. S. Rana, E. Di Gennaro, B. Gobaut, R. Moroni, A. Y. Petrov, U. Scotti di Uccio, G. Rossi, F. Miletto Granozio, G. Panaccione and P. Torelli, APL Materials **3** (11), 116107/116101-116107/116107 (2015).
71. L. Sha, J. Miao, S. Z. Wu, X. G. Xu, Y. Jiang and L. J. Qiao, Journal of Alloys and Compounds **554**, 299-303 (2013).
72. F. Chang, N. Zhang, F. Yang, S. Wang and G. Song, Journal of Physics D: Applied Physics **40** (24), 7799-7803 (2007).
73. I. V. Lisnevskaya, T. G. Lupeiko and E. A. Bikyashev, Russian Journal of Inorganic Chemistry **60** (2), 140-146 (2015).
74. C. A. Bridges, M. Allix, M. R. Suchomel, X. Kuang, I. Sterianou, D. C. Sinclair and M. J. Rosseinsky, Angewandte Chemie International Edition **46** (46), 8785-8789 (2007).
75. *WebElements,(*
76. X. Qi, J. Dho, R. Tomov, M. G. Blamire and J. L. MacManus-Driscoll, Applied Physics Letters **86** (6), 062903 (2005).
77. W. Cai, C. Fu, R. Gao, W. Jiang, X. Deng and G. Chen, Journal of Alloys and Compounds **617**, 240-246 (2014).
78. N. Rong, M. Chu, Y. Tang, C. Zhang, X. Cui, H. He, Y. Zhang and P. Xiao, Journal of Materials Science **51** (12), 5712-5723 (2016).
79. V. Khomchenko, I. Troyanchuk, V. Sikolenko and J. Paixão, Journal of Materials Science **48** (10), 3852-3856 (2013).
80. P. Kharel, S. Talebi, B. Ramachandran, A. Dixit, V. Naik, M. Sahana, C. Sudakar, R. Naik, M. Rao and G. Lawes, Journal of Physics: Condensed Matter **21** (3), 036001 (2008).
81. Y. Wang and C.-W. Nan, Applied Physics Letters **89** (5), 052903 (2006).
82. Y.-H. Wang and X. Qi, Procedia Engineering **36**, 455-461 (2012).
83. X. Wang, G. Hu, L. Cheng, C. Yang and W. Wu, Applied Physics Letters **99** (26), 262901 (2011).
84. D. K. Mishra and X. Qi, Journal of Alloys and Compounds **504** (1), 27-31 (2010).
85. C. Madhu, M. B. Bellakki and V. Manivannan, Indian Journal of Engineering & Materials Sciences **7**, 131-139 (2010).
86. R. Yang, S. Lin, X. Fang, X. Gao, M. Zeng and J. Liu, Journal of Applied Physics **114** (23), 233912 (2013).
87. Y. Han, Y. Ma, C. Quan, N. Gao, Q. Zhang, W. Mao, J. Zhang, J. Yang and W. Huang, Ceramics International **41** (2), 2476-2483 (2015).
88. T. Wang, H. Deng, W. Zhou, P. Yang and J. Chu, Journal of Materials Science: Materials in Electronics **28** (1), 934-938 (2017).

89. W. Zhang, J. Chen, X. An, Q. Wang, L. Fan, F. Wang, J. Deng, R. Yu and X. Xing, Dalton Transactions **43** (24), 9255-9259 (2014).
90. H.-J. Feng and F.-M. Liu, Physics Letters A **372** (11), 1904-1909 (2008).
91. A. Kumar and K. Yadav, Journal of Physics and Chemistry of Solids **72** (11), 1189-1194 (2011).
92. K. Kitada, M. Kobune, W. Adachi, T. Yazawa, H. Saitoh, K. Aoki, J. i. Mizuki, K. Ishikawa, Y. Hiranaga and Y. Cho, Chemistry Letters **37** (5), 560-561 (2008).
93. J. Zhu, S. Feng, Q. Liu, J. Zhang, H. Xu, Y. Li, X. Li, J. Liu, Q. Huang and Y. Zhao, Journal of Applied Physics **113** (14), 143514 (2013).
94. Y. Inaguma and T. Katsumata, Ferroelectrics **286** (1), 111-117 (2003).
95. Y. Li, Y. Fan, H. Zhang, X. Teng, X. Dong, H. Liu, X. Ge, Q. Li, W. Chen and Z. Ge, Journal of Superconductivity and Novel Magnetism **27** (5), 1239-1243 (2014).
96. Y. Q. Tan, J. L. Zhang, W. T. Hao, G. Chen, W. B. Su and C. L. Wang, Materials Chemistry and Physics **124** (2-3), 1100-1104 (2010).
97. H. Wu, Y. Lin, J. Gong, F. Zhang, M. Zeng, M. Qin, Z. Zhang, Q. Ru, Z. Liu and X. Gao, Journal of Physics D: Applied Physics **46** (14), 145001 (2013).
98. G. Hu, S. Fan, C. Yang and W. Wu, Applied Physics Letters **92** (19), 192905 (2008).
99. J. Cho, T. Song, L. Wang, H.-G. Yeo, Y.-S. Sung, M.-H. Kim and D.-S. Park, Journal of Applied Physics **105** (6), 061640 (2009).
100. K. Yazawa, S. Yasui, H. Morioka, T. Yamada, H. Uchida, A. Gruverman and H. Funakubo, Journal of the Ceramic Society of Japan **118** (1380), 659-663 (2010).
101. M. R. Dolgos, U. Adem, A. Manjon-Sanz, X. Wan, T. P. Comyn, T. Stevenson, J. Bennett, A. J. Bell, T. T. Tran and P. S. Halasyamani, Angewandte Chemie **124** (43), 10928-10933 (2012).
102. S. Y. Chong, R. J. Szczecinski, C. A. Bridges, M. G. Tucker, J. B. Claridge and M. J. Rosseinsky, Journal of the American Chemical Society **134** (13), 5836-5849 (2012).
103. M. Dolgos, U. Adem, X. Wan, Z. Xu, A. Bell, T. Comyn, T. Stevenson, J. Bennett, J. Claridge and M. Rosseinsky, Chemical Science **3** (5), 1426-1435 (2012).
104. B. Aurivillius, Arkiv för Kemi **1**, 463-480 (1949).
105. B. Aurivillius, Arkiv för Kemi **1**, 499-512 (1949).
106. B. Aurivillius, Arkiv för Kemi **2**, 519-527 (1950).
107. A. Rae, J. Thompson and R. Withers, Acta Crystallographica Section B **47** (6), 870-881 (1991).
108. Y. Shimakawa, Y. Kubo, Y. Nakagawa, T. Kamiyama, H. Asano and F. Izumi, Applied Physics Letters **74** (13), 1904-1906 (1999).
109. A. D. Rae, J. G. Thompson, R. Withers and A. C. Willis, Acta Crystallographica Section B **46** (4), 474-487 (1990).
110. B. Frit and J. Mercurio, Journal of Alloys and Compounds **188**, 27-35 (1992).
111. T. Jardiel, A. Caballero and M. Villegas, Journal of the Ceramic Society of Japan **116** (1352), 511-518 (2008).
112. A. Missyul, I. Zvereva, T. T. Palstra and A. Kurbakov, Materials Research Bulletin **45** (5), 546-550 (2010).
113. K. R. Kendall, C. Navas, J. K. Thomas and H.-C. zur Loye, Chemistry of Materials **8** (3), 642-649 (1996).
114. W. Ye, C. Lu, Y. Zhang and Y. Zhou, Journal of Applied Crystallography **48** (4), 1080-1088 (2015).
115. M. G. Navarro-Rojero, J. J. Romero, F. Rubio-Marcos and J. F. Fernandez, Ceramics International **36** (4), 1319-1325 (2010).
116. F. Gao, Q. Zhang, G. Ding, N. Qin and D. Bao, Journal of the American Ceramic Society **94** (11), 3867-3870 (2011).
117. B. Park, B. Kang, S. Bu, T. Noh, J. Lee and W. Jo, Nature **401** (6754), 682 (1999).
118. D. J. Singh, S. S. A. Seo and H. N. Lee, Physical Review B **82** (18), 180103 (2010).
119. L. Pintilie, M. Alexe, A. Pignolet and D. Hesse, Applied Physics Letters **73** (3), 342-344 (1998).

120. H. He, Z. He, Z. Jiang, J. Wang, T. Liu and N. Wang, Journal of Alloys and Compounds **694**, 998-1003 (2017).
121. W. Wei, Y. Dai and B. Huang, The Journal of Physical Chemistry C **113** (14), 5658-5663 (2009).
122. E. Jartych, T. Pikula, M. Mazurek, A. Lisinska-Czekaj, D. Czekaj, K. Gaska, J. Przewoznik, C. Kapusta and Z. Surowiec, Journal of Magnetism and Magnetic Materials **342**, 27-34 (2013).
123. N. Lomanova, I. Pleshakov, M. Volkov and V. Gusarov, Materials Science and Engineering: B **214**, 51-56 (2016).
124. N. A. Lomanova, V. G. Semenov, V. V. Panchuk and V. V. Gusarov, Journal of Alloys and Compounds **528**, 103-108 (2012).
125. N. A. Lomanova, I. V. Pleshakov, M. P. Volkov and V. V. Gusarov, Journal of Thermal Analysis and Calorimetry **131** (1), 473-478 (2018).
126. A. Y. Birenbaum and C. Ederer, Physical Review B **90** (21), 214109 (2014).
127. S. Sun, W. Wang, H. Xu, L. Zhou, M. Shang and L. Zhang, The Journal of Physical Chemistry C **112** (46), 17835-17843 (2008).
128. J. S. Jang, S. S. Yoon, P. H. Borse, K. T. Lim, T. E. Hong, E. D. Jeong, O.-S. Jung, Y. B. Shim and H. G. Kim, Journal of the Ceramic Society of Japan **117** (1371), 1268-1272 (2009).
129. W. Bai, Y. Gao, J. Zhu, X. Meng, T. Lin, J. Yang, Z. Zhu and J. Chu, Journal of Applied Physics **109** (6), 064901 (2011).
130. M. Wu, Z. Tian, S. Yuan and Z. Huang, Materials Letters **68**, 190-192 (2012).
131. G. Chen, W. Bai, L. Sun, J. Wu, Q. Ren, W. Xu, J. Yang, X. Meng, X. Tang and C.-G. Duan, Journal of Applied Physics **113** (3), 034901 (2013).
132. S. Kooriyattil, R. K. Katiyar, S. P. Pavunny, G. Morell and R. S. Katiyar, Applied Physics Letters **105** (7), 072908 (2014).
133. X. Liu, L. Xu, Y. Huang, C. Qin, L. Qin and H. J. Seo, Ceramics International **43** (15), 12372-12380 (2017).
134. W. Bai, W. Xu, J. Wu, J. Zhu, G. Chen, J. Yang, T. Lin, X. Meng, X. Tang and J. Chu, Thin Solid Films **525**, 195-199 (2012).
135. M. B. Sreedhara, B. E. Prasad, M. Moirangthem, R. Murugavel and C. N. R. Rao, Journal of Solid State Chemistry **224**, 21-27 (2015).
136. X. Li, Z. Ju, F. Li, Y. Huang, Y. Xie, Z. Fu, R. Knize and Y. Lu, Journal of Materials Chemistry A **2** (33), 13366-13372 (2014).
137. A. Srinivas, S. V. Suryanarayana, G. S. Kumar and M. M. Kumar, Journal of Physics: Condensed Matter **11** (16), 3335-3340 (1999).
138. J.-B. Li, Y.-P. Huang, H.-B. Jin, G.-H. Rao and J.-K. Liang, Journal of the American Ceramic Society **96** (12), 3920-3925 (2013).
139. T. Jia, H. Kimura, Z. Cheng and H. Zhao, Journal of Vacuum Science & Technology A **33** (6), 060605/060601-060605/060606 (2015).
140. T. Pikula, P. Guzdek, J. Dzik, A. Lisińska-Czekaj and E. Jartych, Acta Physica Polonica A **127**, 296 (2015).
141. X. W. Dong, K. F. Wang, J. G. Wan, J. S. Zhu and J. M. Liu, Journal of Applied Physics **103** (9), 094101/094101-094101/094104 (2008).
142. J.-j. Ji, H. Sun, X.-y. Mao, W. Wang and X.-b. Chen, Journal of Sol-gel Science and Technology **61** (2), 328-331 (2012).
143. X. Mao, W. Wang and X. Chen, Solid State Communications **147** (5-6), 186-189 (2008).
144. S. Yan, Z. Feng, Z. Ma, Y. Zhang and W. Ye, Materials Letters **227**, 247-249 (2018).
145. H. Zhao, H. Kimura, Z. Cheng, M. Osada, J. Wang, X. Wang, S. Dou, Y. Liu, J. Yu and T. Matsumoto, Scientific Reports **4**, 5255 (2014).
146. J. Yang, W. Tong, Z. Liu, X. Zhu, J. Dai, W. Song, Z. Yang and Y. Sun, Physical Review B **86** (10), 104410 (2012).
147. J. Lu, L. Qiao, X. Ma and W. Chu, Journal of Physics: Condensed Matter **18** (20), 4801 (2006).
148. H. Sun, B. Zou, X. Ni, X. Mao, X. Chen and J. Zhu, Journal of Materials Science **50** (16), 5475-5481 (2015).

149. A. Srinivas, M. M. Kumar, S. Suryanarayana and T. Bhimasankaram, Materials Research Bulletin **34** (6), 989-996 (1999).
150. L. Keeney, T. Maity, M. Schmidt, A. Amann, N. Deepak, N. Petkov, S. Roy, M. E. Pemble and R. W. Whatmore, Journal of the American Ceramic Society **96** (8), 2339-2357 (2013).
151. S. Patwe, S. Achary, J. Manjanna, A. Tyagi, S. Deshpande, S. Mishra, P. Krishna and A. Shinde, Applied Physics Letters **103** (12), 122901 (2013).
152. D. Song, J. Yang, Y. Wang and X. Zhu, Ceramics International **43** (18), 17148-17152 (2017).
153. C. M. Raghavan, J. W. Kim and S. S. Kim, Sae Mulli **65** (6), 542-549 (2015).
154. S. Sun, C. Liu, G. Wang, Z. Chen, T. Chen, R. Peng and Y. Lu, Journal of the American Ceramic Society **99** (9), 3033-3038 (2016).
155. D. Song, J. Yang, B. Yang, L. Chen, F. Wang and X. Zhu, Journal of Materials Chemistry C **6**, 8618-8627 (2018).
156. N. A. Lomanova, M. I. Morozov, V. L. Ugolkov and V. V. Gusarov, Inorganic Materials **42** (2), 189-195 (2006).
157. M. Wu, Z. Tian, S. Yuan, H. Duan and Y. Qiu, Physics Letters A **376** (28-29), 2062-2066 (2012).
158. P. Jiang, Z. Duan, L. Xu, X. Zhang, Y. Li, Z. Hu and J. Chu, Journal of Applied Physics **115** (8), 083101 (2014).
159. F. Kubel and H. Schmid, Ferroelectrics **129** (1), 101-112 (1992).
160. A. Snedden, C. H. Hervoches and P. Lightfoot, Physical Review B **67** (9), 092102 (2003).
161. U. Salazar-Kuri, M. Mendoza, J. Siqueiros, J. Gervacio-Arciniega and R. Silva, Materials Research Express **1** (4), 045702 (2014).
162. R. Singh, T. Bhimasankaram, G. Kumar and S. Suryanarayana, Solid State Communications **91** (7), 567-569 (1994).
163. J. Dercz, J. Bartkowska, G. Dercz, P. Stoch and M. Łukasik, International Journal of Thermophysics **34** (4), 567-574 (2013).
164. T. Ko, C. Jun and J. Lee, The Korean Journal of Ceramics **5** (4), 341-347 (1999).
165. C. H. Hervoches, A. Snedden, R. Riggs, S. H. Kilcoyne, P. Manuel and P. Lightfoot, Journal of Solid State Chemistry **164** (2), 280-291 (2002).
166. D. Song, X. Zuo, B. Yuan, X. Tang, W. Song, J. Yang, X. Zhu and Y. Sun, CrystEngComm **17** (7), 1609-1614 (2015).
167. M. Garcia-Guaderrama, L. Fuentes-Montero, A. Rodriguez and L. Fuentes, Integrated Ferroelectrics **83** (1), 41-47 (2006).
168. M. Montero-Cabrera, M. García-Guaderrama, A. Mehta, S. Webb, L. Fuentes-Montero, J. Duarte Moller and L. Fuentes-Cobas, Revista Mexicana de Física **54**, 42-45 (2008).
169. M. Krzhizhanovskaya, S. Filatov, V. Gusarov, P. Paufler, R. Bubnova, M. Morozov and D. C. Meyer, Zeitschrift für Anorganische und Allgemeine Chemie **631** (9), 1603-1608 (2005).
170. G. N. Subbanna, L. Ganapathi, C. N. R. Rao and D. A. Jefferson, Materials Research Bulletin **22** (2), 205-209 (1987).
171. M. I. Morozov and V. V. Gusarov, Inorganic Materials **38** (7), 723-729 (2002).
172. L. Keeney, P. F. Zhang, C. Groh, M. E. Pemble and R. W. Whatmore, Journal of Applied Physics **108** (4), 042004/042001-042004/042009 (2010).
173. E. Jartych, M. Mazurek, A. Lisinska-Czekaj and D. Czekaj, Journal of Magnetism and Magnetic Materials **322** (1), 51-55 (2009).
174. M. Garcia-Guaderrama, L. Fuentes, M. Montero-Cabrera, A. Marquez-Lucero and M. Villafuerte-Castrejon, Integrated Ferroelectrics **71** (1), 233-239 (2005).
175. J. Rymarczyk, A. Hanc, G. Dercz and J. Ilczuk, Acta Physica Polonica A **114** (6), 1579-1584 (2008).
176. A. Lisińska-Czekaj, M. Lubina, D. Czekaj, M. Rerak, B. Garbarz-Glos and W. Bąk, Archives of Metallurgy and Materials **61** (2), 881-886 (2016).
177. N. Lomanova and V. Gusarov, Russian Journal of Inorganic Chemistry **55** (10), 1541-1545 (2010).

178. W. H. Baur and A. A. Khan, Acta Crystallographica Section B: Structural Crystallography and Crystal Chemistry **27** (11), 2133-2139 (1971).
179. M. Horn, C. Schwebdtfeger and E. Meagher, Zeitschrift für Kristallographie-Crystalline Materials **136** (1-6), 273-281 (1972).
180. T. A Kandiel, R. Dillert and D. Bahnemann, Current Inorganic Chemistry **2** (2), 94-114 (2012).
181. H. Zhang and J. F. Banfield, The Journal of Physical Chemistry B **104** (15), 3481-3487 (2000).
182. D. Reyes-Coronado, G. Rodríguez-Gattorno, M. Espinosa-Pesqueira, C. Cab, R. d. de Coss and G. Oskam, Nanotechnology **19** (14), 145605 (2008).
183. S.-D. Mo and W. Ching, Physical Review B **51** (19), 13023 (1995).
184. M. Landmann, E. Rauls and W. Schmidt, Journal of Physics: Condensed Matter **24** (19), 195503 (2012).
185. M. Ni, M. K. Leung, D. Y. Leung and K. Sumathy, Renewable and Sustainable Energy Reviews **11** (3), 401-425 (2007).
186. N. S. Allen, M. Edge, J. Verran, J. Stratton, J. Maltby and C. Bygott, Polymer Degradation and Stability **93** (9), 1632-1646 (2008).
187. M. Nowotny, T. Bak and J. Nowotny, The Journal of Physical Chemistry B **110** (33), 16270-16282 (2006).
188. A. Weibel, R. Bouchet and P. Knauth, Solid State Ionics **177** (3-4), 229-236 (2006).
189. B. J. Morgan and G. W. Watson, The Journal of Physical Chemistry C **114** (5), 2321-2328 (2010).
190. V. Pfeifer, P. Erhart, S. Li, K. Rachut, J. Morasch, J. Brötz, P. Reckers, T. Mayer, S. Rühle and A. Zaban, The Journal of Physical Chemistry Letters **4** (23), 4182-4187 (2013).
191. J. J. Yang, J. P. Strachan, F. Miao, M.-X. Zhang, M. D. Pickett, W. Yi, D. A. Ohlberg, G. Medeiros-Ribeiro and R. S. Williams, Applied Physics A **102** (4), 785-789 (2011).
192. R. A. Parker, Physical Review **124** (6), 1719 (1961).
193. W. Hu, Y. Liu, R. L. Withers, T. J. Frankcombe, L. Norén, A. Snashall, M. Kitchin, P. Smith, B. Gong and H. Chen, Nature Materials **12** (9), 821 (2013).
194. D. McWhan, A. Menth, J. Remeika, W. Brinkman and T. Rice, Physical Review B **7** (5), 1920 (1973).
195. M. Imada, A. Fujimori and Y. Tokura, Reviews of Modern Physics **70** (4), 1039 (1998).
196. D. McWhan, M. Marezio, J. Remeika and P. Dernier, Physical Review B **10** (2), 490 (1974).
197. B. Li, Y. Xu, G. Rong, M. Jing and Y. Xie, Nanotechnology **17** (10), 2560 (2006).
198. D. Bullett, Journal of Physics C: Solid State Physics **13** (23), L595 (1980).
199. M. Rauf and S. S. Ashraf, Chemical Engineering Journal **151** (1-3), 10-18 (2009).
200. F. De Angelis, C. Di Valentin, S. Fantacci, A. Vittadini and A. Selloni, Chemical Reviews **114** (19), 9708-9753 (2014).
201. A. Zaleska, Recent Patents on Engineering **2** (3), 157-164 (2008).
202. S. G. Kumar and L. G. Devi, The Journal of Physical Chemistry A **115** (46), 13211-13241 (2011).
203. R. Asahi, T. Morikawa, H. Irie and T. Ohwaki, Chemical Reviews **114** (19), 9824-9852 (2014).
204. R. Asahi, T. Morikawa, T. Ohwaki, K. Aoki and Y. Taga, Science **293** (5528), 269-271 (2001).
205. Q. Sun, B. R. McBride and Y. Liu, Research and Reviews in Electrochemistry **8** (1) (2017).
206. Q. Sun, D. Cortie, S. Zhang, T. J. Frankcombe, G. She, J. Gao, L. R. Sheppard, W. Hu, H. Chen and S. Zhuo, Advanced Materials **29** (11) (2017).
207. Z. Zhao and Q. Liu, Catalysis Letters **124** (1-2), 111-117 (2008).
208. X. Ma, L. Miao, S. Bie and J. Jiang, Solid State Communications **150** (13), 689-692 (2010).
209. X. Wenhui, M. Xinguo, W. Tong, H. Zhiqi, W. Huihu and H. Chuyun, Journal of Semiconductors **35** (10), 102002 (2014).

210. Q. Meng, T. Wang, E. Liu, X. Ma, Q. Ge and J. Gong, Physical Chemistry Chemical Physics **15** (24), 9549-9561 (2013).
211. Y. Gai, J. Li, S.-S. Li, J.-B. Xia and S.-H. Wei, Physical Review Letters **102** (3), 036402 (2009).
212. Y. Gu, C. Cai, Q. Feng and Y. Li, Chinese Optics Letters **12** (9), 091602 (2014).
213. S. N. Phattalung, S. Limpijumnong and J. Yu, Applied Catalysis B: Environmental **200**, 1-9 (2017).
214. R. Jaiswal, N. Patel, D. Kothari and A. Miotello, Applied Catalysis B: Environmental **126**, 47-54 (2012).
215. N. K. Eswar, P. C. Ramamurthy and G. Madras, New Journal of Chemistry **40** (4), 3464-3475 (2016).
216. D.-E. Gu, B.-C. Yang and Y.-D. Hu, Catalysis Communications **9** (6), 1472-1476 (2008).
217. H. N. T. Phung, P. A. Duong, H. V. T. Le and N. D. Truong, Journal of the Korean Physical Society **70** (11), 995-1000 (2017).
218. H. Khatibnezhad and M. A. F. Sani, Research on Chemical Intermediates **41** (10), 7349-7361 (2015).
219. M. Zhang, D. Lu, Z. Zhang, Y. Guo and J. Yang, Journal of The Electrochemical Society **162** (8), H557-H563 (2015).
220. R. Varma, M. Yadav, K. Tiwari, N. Makani, S. Gupta, D. C. Kothari, A. Miotello and N. Patel, Photochemistry and Photobiology **94** (5), 955-964 (2018).
221. A. Kubacka, M. Fernández-García and G. Colón, Journal of Catalysis **254** (2), 272-284 (2008).
222. V. Luca, S. Thomson and R. F. Howe, Journal of the Chemical Society, Faraday Transactions **93** (12), 2195-2202 (1997).
223. G. Busca and E. Giamello, Materials Chemistry and Physics **25** (5), 475-485 (1990).
224. R. Gallay, J. Van der Klink and J. Moser, Physical Review B **34** (5), 3060 (1986).
225. S. T. Martin, C. L. Morrison and M. R. Hoffmann, The Journal of Physical Chemistry **98** (51), 13695-13704 (1994).
226. S.-m. Chang and W.-s. Liu, Applied Catalysis B: Environmental **101** (3-4), 333-342 (2011).
227. J. Balikdjian, A. Davidson, S. Launay, H. Eckert and M. Che, The Journal of Physical Chemistry B **104** (38), 8931-8939 (2000).
228. S. Navale, A. V. Murugan and V. Ravi, Ceramics International **33** (2), 301-303 (2007).
229. M. Altomare, K. Lee, M. S. Killian, E. Selli and P. Schmuki, Chemistry–A European Journal **19** (19), 5841-5844 (2013).
230. K. E. Karakitsou and X. E. Verykios, The Journal of Physical Chemistry **97** (6), 1184-1189 (1993).
231. A. V. Emeline, Y. Furubayashi, X. Zhang, M. Jin, T. Murakami and A. Fujishima, The Journal of Physical Chemistry B **109** (51), 24441-24444 (2005).
232. J. F. Baumard and E. Tani, The Journal of Chemical Physics **67** (3), 857-860 (1977).
233. L. R. Sheppard, J. Holik, R. Liu, S. Macartney and R. Wuhrer, Journal of the American Ceramic Society **97** (12), 3793-3799 (2014).
234. A. J. Atanacio, T. Bak and J. Nowotny, The Journal of Physical Chemistry C **118** (21), 11174-11185 (2014).
235. M. Inomata, K. Mori, A. Miyamoto, T. Ui and Y. Murakami, Journal of Physical Chemistry **87** (5), 754-761 (1983).
236. A. Davidson, B. Morin and M. Che, Colloids and Surfaces A: Physicochemical and Engineering Aspects **72**, 245-255 (1993).
237. J. Haber and P. Nowak, Langmuir **11** (3), 1024-1032 (1995).
238. C. B. Rodella and V. R. Mastelaro, Journal of Physics and Chemistry of Solids **64** (5), 833-839 (2003).
239. A. Altynnikov, G. Zenkovets and V. Anufrienko, Reaction Kinetics and Catalysis Letters **52** (1), 59-63 (1994).

240. G. Centi, D. Pinelli, F. Trifiro, D. Ghoussoub, M. Guelton and L. Gengembre, Journal of Catalysis **130** (1), 238-256 (1991).
241. W. E. Slinkard and P. B. DeGroot, Journal of Catalysis **68** (2), 423-432 (1981).
242. R. Kozlowski, R. Pettifer and J. Thomas, The Journal of Physical Chemistry **87** (25), 5176-5181 (1983).
243. G. Oliveri, G. Ramis, G. Busca and V. Sanchezá Escribano, Journal of Materials Chemistry **3** (12), 1239-1249 (1993).
244. E. Cazzanelli, L. Papalino, S. Capoleoni, R. Ceccato and G. Carturan, Ionics **8** (3-4), 244-251 (2002).
245. Y.-l. Gao, Q.-y. Chen, H.-x. Tong, H.-p. Hu, D. Qian, Y.-h. Yang and J.-l. Zhou, Journal of Central South University of Technology **16** (6), 919 (2009).
246. H. Guo, D. Li, D. Jiang, H. Xiao, W. Li and Y. Sun, Catalysis Today **158** (3-4), 439-445 (2010).
247. G. Centi, E. Giamello, D. Pinelli and F. Trifiro, Journal of Catalysis **130** (1), 220-237 (1991).
248. B. Golovkin, Russian Journal of General Chemistry **75** (12), 1857-1863 (2005).
249. M.-W. Park, H.-J. Kwon, J.-S. Lee, J.-C. Park, J.-H. Kim and C.-G. Kim, Electronic Materials Letters **7** (4), 327-331 (2011).
250. M. Tena, A. Mestre, A. García, S. Sorlí and G. Monrós, Journal of Sol-gel Science and Technology **26** (1-3), 813-816 (2003).
251. D. Habel, J. B. Stelzer, E. Feike, C. Schröder, A. Hösch, C. Hess, A. Knop-Gericke, J. Caro and H. Schubert, Journal of the European Ceramic Society **26** (15), 3287-3294 (2006).
252. D. Habel, O. Goerke, M. Tovar, E. Kondratenko and H. Schubert, Journal of Phase Equilibria and Diffusion **29** (6), 482 (2008).
253. P. J. Pomonis and J. C. Vickerman, Faraday Discussions of the Chemical Society **72**, 247-262 (1981).
254. G. Zhao, G. Han, M. Takahashi and T. Yoko, Thin Solid Films **410** (1-2), 14-20 (2002).
255. Z. Tian, S. Yuan, S. Yuan, H. Xie, J. He, Y. Wang, K. Liu and S. Yin, Solid State Communications **146** (11-12), 522-525 (2008).
256. R. Loehman, C. R. Rao and J. M. Honig, The Journal of Physical Chemistry **73** (6), 1781-1784 (1969).
257. B.-O. Marinder and A. Magnéli, Acta Chemica Scandinavica **12** (6), 1345-1347 (1958).
258. T. Horlin, T. Niklewski and M. Nygren, Acta Chemica Scandinavica Ser. A **A30** (8), 619-624 (1976).
259. T. Phillips, K. Moorjani, J. Murphy and T. Poehler, Journal of the Electrochemical Society **129** (6), 1210-1215 (1982).
260. B. Poumellec, J. Marucco and B. Touzelin, Physical Review B **35** (5), 2284 (1987).
261. Z. Hiroi, H. Hayamizu, T. Yoshida, Y. Muraoka, Y. Okamoto, J.-i. Yamaura and Y. Ueda, Chemistry of Materials **25** (11), 2202-2210 (2013).
262. D. A. Duncan, D. Kreikemeyer-Lorenzo, E. Primorac, O. Karslioğlu, M. Naschitzki, W. Unterberger, H. Kuhlenbeck and D. Woodruff, Surface Science **630**, 64-70 (2014).
263. N. Khatun, P. Rajput, D. Bhattacharya, S. Jha, S. Biring and S. Sen, Ceramics International **43** (16), 14128-14134 (2017).
264. A. Kokorin, A. Sukhanov, O. Gromov, V. Arakelyan, V. Aroutiounian and V. Voronkova, Applied Magnetic Resonance **47** (5), 479-485 (2016).
265. G. Gao, K. Yao and Z. Liu, Physics Letters A **359** (5), 523-527 (2006).
266. K. He, G. Zheng, G. Chen, T. Lü, M. Wan and G. Ji, Solid State Communications **144** (1-2), 54-57 (2007).
267. R. Grau-Crespo and U. Schwingenschlögl, Journal of Physics: Condensed Matter **23** (33), 334216 (2011).
268. M. M. Islam, T. Bredow and A. Gerson, ChemPhysChem **12** (17), 3467-3473 (2011).
269. D. Y. Lee, W. J. Lee, J. S. Song, J. H. Koh and Y. S. Kim, Computational Materials Science **30** (3-4), 383-388 (2004).
270. A. Stashans and J. Escobar, International Journal of Modern Physics B **29** (15), 1550094 (2015).

271. S.-D. Mo, L. Lin and D. Lin, Journal of Physics and Chemistry of Solids **55** (11), 1309-1313 (1994).
272. M. Saini, M. Kumar and T. Som, Applied Surface Science **418**, 302-307 (2017).
273. H. Sutrisno, ALCHEMY: Jurnal Penelitian Kimia **14** (1), 60-71 (2018).
274. D. Sayle, C. Catlow, M. Perrin and P. Nortier, Journal of Physics and Chemistry of Solids **56** (6), 799-805 (1995).
275. T. Nishikawa, T. Nakajima and Y. Shinohara, Journal of Molecular Structure: THEOCHEM **545** (1-3), 67-74 (2001).
276. S. Karvinen, P. Hirva and T. A. Pakkanen, Journal of Molecular Structure: THEOCHEM **626** (1-3), 271-277 (2003).
277. L. Depero, Journal of Solid State Chemistry **103** (2), 528-532 (1993).
278. M. Park, Y. Lim, Y. Sung, D. Kwak and J. Lee, Acta Physica Polonica A **129** (4), 875-877 (2016).
279. W. Zhou, Q. Liu, Z. Zhu and J. Zhang, Journal of Physics D: Applied Physics **43** (3), 035301 (2010).
280. D. Wu, H. Tong, Q. Chen and C. Xia, Integrated Ferroelectrics **127** (1), 55-62 (2011).
281. A. I. Kokorin, V. M. Arakelyan and V. M. Arutyunian, Russian Chemical Bulletin **52** (1), 93-97 (2003).
282. K. Sakata, Physica Status Solidi B **116** (1), 145-153 (1983).
283. G. C. Vásquez, M. A. Peche-Herrero, D. Maestre, A. Cremades, J. Ramírez-Castellanos, J. M. González-Calbet and J. Piqueras, The Journal of Physical Chemistry C **117** (4), 1941-1947 (2013).
284. J. Choi, H. Park and M. R. Hoffmann, The Journal of Physical Chemistry C **114** (2), 783-792 (2009).
285. K. Sakata and T. Sakata, Japanese Journal of Applied Physics **6** (1), 112 (1967).
286. T. Horlin, T. Niklewski and M. Nygren, Journal de Physique Colloques (4), 69-73 (1976).
287. I. Kristensen, Journal of Applied Physics **39** (11), 5341-5342 (1968).
288. H. Rietveld, Journal of Applied Crystallography **2** (2), 65-71 (1969).
289. R. B. Von Dreele, *Reitveld Refinement with GSAS, Lecture Slides*, (2016).
290. B. H. Toby, Powder Diffraction **21** (1), 67-70 (2006).
291. T. Degen, M. Sadki, E. Bron, U. König and G. Nénert, Powder Diffraction **29** (S2), S13-S18 (2014).
292. V. Petříček, M. Dušek and L. Palatinus, Zeitschrift für Kristallographie-Crystalline Materials **229** (5), 345-352 (2014).
293. F. Karlsruhe, *International Crystal Structure Database*, https://icsd.fiz-karlsruhe.de/index.xhtml, (2019).
294. P. Scherrer, Göttinger Nachrichten Math, 98-100 (1918).
295. K.-D. Liss, B. Hunter, M. Hagen, T. Noakes and S. Kennedy, Physica B: Condensed Matter **385**, 1010-1012 (2006).
296. S. Hull, R. Smith, W. David, A. Hannon, J. Mayers and R. Cywinski, Physica B: Condensed Matter **180**, 1000-1002 (1992).
297. O. Arnold, J.-C. Bilheux, J. Borreguero, A. Buts, S. I. Campbell, L. Chapon, M. Doucet, N. Draper, R. F. Leal and M. Gigg, Nuclear Instruments and Methods in Physics Research Section A: Accelerators, Spectrometers, Detectors and Associated Equipment **764**, 156-166 (2014).
298. A. C. Larson and R. B. Von Dreele, *General Structure Analysis System (GSAS)*, Los Alamos National Laboratory Report LAUR **86-748**, (2000).
299. B. H. Toby, Journal of Applied Crystallography **34** (2), 210-213 (2001).
300. L. Pauling, Journal of the American Chemical Society **51** (4), 1010-1026 (1929).
301. S. Adams, *softBV*, http://www.softbv.net/, (2019).
302. A. Takamatsu and H. Ikeno, Science and Technology of Advanced Materials **19** (1), 101-107 (2018).
303. S. Adams, Acta Crystallographica Section B: Structural Science **57** (3), 278-287 (2001).

304. F. Jensen, *Introduction to Computational Chemistry,* (John Wiley & Sons, Incorporated, 2016), Chapter 6.
305. P. Blaha, K. Schwarz, G. Madsen, D. Kvasnicka and J. Luitz, *WIEN2k: An Augmented Plane Wave+ Local Orbitals Program for Calculating Crystal Properties*, (2001).
306. J. P. Perdew, K. Burke and M. Ernzerhof, Physics Review Letters **77** (18), 3865 (1996).
307. A. R. West, *Solid State Chemistry and Its Applications,* (John Wiley & Sons, Incorporated, 2014), Chapter 6.
308. P. van der Heide, *X-ray Photoelectron Spectroscopy : An Introduction to Principles and Practices,* (Wiley, 2011), Chapters 1-2.
309. V. V. Ovchinnikov and V. Riecansky, *Mossbauer Analysis of the Atomic and Magnetic Structure of Alloys,* (Cambridge International Science Publishing, 2006), Chapter 1.
310. A. P. Douvalis, A. Polymeros and T. Bakas, Journal of Physics: Conference Series **217**, 012014 (2010).
311. J. Coey, M. Venkatesan and H. Xu, *Functional Metal Oxides: New Science and Novel Applications,* (Wiley-VCH Verlag GmbH & Co. KGaA, 2013), Chapter 1.
312. K. H. J. Buschow and F. R. Boer, *Physics of Magnetism and Magnetic Materials,* (Kluwer Academic Publishers, 2004), Chapter 4.
313. E. Du Trémolet de Lacheisserie, U. J. Fourier, D. Gignoux and M. Schlenker, *Magnetism,* (Springer, 2005), Chapter 4.
314. R. L. Carlin and A. J. van Duyneveldt, *Magnetic Properties of Transition Metal Compounds,* (Springer, 1977), Chapter 1.
315. J. Davenas and P. M. Rabette, *Contribution of Clusters Physics to Materials Science and Technology: From Isolated Clusters to Aggregated Materials,* (Springer Netherlands, 2012).
316. K. H. J. Buschow and F. R. Boer, *Physics of Magnetism and Magnetic Materials,* (Kluwer Academic Publishers, 2004), Chapter 10.
317. J. A. Weil and J. R. Bolton, *Electron Paramagnetic Resonance: Elementary Theory and Practical Applications,* (Wiley, 2007), Chapter 1.
318. S. Stoll and A. Schweiger, Journal of Magnetic Resonance **178** (1), 42-55 (2006).
319. L. Nuccio, L. Schulz and A. Drew, Journal of Physics D: Applied Physics **47** (47), 473001 (2014).
320. R. Proksch and S. Kalinin, *Piezoresponse Force Microscopy with Asylum Research AFMs, PFM Application Note*, (2014).
321. S. Jesse, H. N. Lee and S. V. Kalinin, Review of Scientific Instruments **77** (7), 073702 (2006).
322. G. Haugstad, *Atomic Force Microscopy : Understanding Basic Modes and Advanced Applications,* (John Wiley & Sons, Incorporated, 2012), Chapter 9.
323. Y. Barsukov and J. R. Macdonald, Characterization of Materials **2**, 898-913 (2012).
324. B. Hapke, *Theory of Reflectance and Emittance Spectroscopy,* (Cambridge University Press, 2012), Chapter 14.
325. J. Tauc, R. Grigorovici and A. Vancu, Physical Status Solidi B **15** (2), 627-637 (1966).
326. S. Warda, W. Pietzuch, W. Massa, U. Kesper and D. Reinen, Journal of Solid State Chemistry **149** (2), 209-217 (2000).
327. M. Valant and D. Suvorov, Chemistry of Materials **14** (8), 3471-3476 (2002).
328. B. R. McBride, J. Lieschke, A. Berlie, D. L. Cortie, H. Y. Playford, T. Lu, N. Narayanan, R. L. Withers, D. Yu and Y. Liu, Journal of Applied Physics **123** (15), 154104 (2018).
329. P. Haas, F. Tran and P. Blaha, Physical Review B **79** (8), 085104 (2009).
330. J. Bertinshaw, D. Cortie, Z. Cheng, M. Avdeev, A. Studer, F. Klose, C. Ulrich and X. Wang, Physical Review B **89** (14), 144422 (2014).
331. R. Nechache, C. Harnagea and A. Pignolet, Journal of Physics: Condensed Matter **24** (9), 096001/096001-096001/096013 (2012).
332. P. C. Rout, A. Putatunda and V. Srinivasan, Physical Review B **93** (10), 104415 (2016).
333. N. Ichikawa, M. Arai, Y. Imai, K. Hagiwara, H. Sakama, M. Azuma, Y. Shimakawa, M. Takano, Y. Kotaka and M. Yonetani, Applied Physics Express **1** (10), 101302 (2008).
334. F. Morin, Physical Review **78** (6), 819 (1950).

335. D. L. Cortie, T. Buck, M. Dehn, V. Karner, R. Kiefl, C. Levy, R. McFadden, G. Morris, I. McKenzie and M. Pearson, Physical Review Letters **116** (10), 106103 (2016).
336. D. L. Cortie, A. Stampfl, F. Klose, Y. Du, X. Wang, H. Zhao, H. Kimura and Z. Cheng, Applied Physics Letters **101** (17), 172404 (2012).
337. S. S. K. Reddy, N. Raju, C. G. Reddy, P. Y. Reddy, K. R. Reddy and V. R. Reddy, Journal of Magnetism and Magnetic Materials **396**, 214-218 (2015).
338. Y. Fang, Y. Yang, X. Liu, J. Kang, L. Hao, X. Chen, L. Xie, G. Sun, V. Chandragiri and C.-W. Wang, Scientific Reports **6**, 33448 (2016).
339. J. Androulakis, N. Katsarakis and J. Giapintzakis, Physical Review B **64** (17), 174401 (2001).
340. M. R. Suchomel, A. M. Fogg, M. Allix, H. Niu, J. B. Claridge and M. J. Rosseinsky, Chemistry of Materials **18** (21), 4987-4989 (2006).
341. K. Miura, M. Kubota, M. Azuma and H. Funakubo, Japanese Journal of Applied Physics **48** (9S1), 09KF05 (2009).
342. M. H. Lee, D. J. Kim, J. S. Park, S. W. Kim, T. K. Song, M.-H. Kim, W.-J. Kim, D. Do and I.-K. Jeong, Advanced Materials **27** (43), 6976-6982 (2015).
343. B. Hallstedt, D. Risold and L. J. Gauckler, Journal of the American Ceramic Society **79** (2), 353-358 (1996).
344. J. Guha, Š. Kunej and D. Suvorov, Journal of Materials Science **39** (3), 911-918 (2004).
345. N. Kumada, N. Takahashi, N. Kinomura and A. Sleight, Materials Research Bulletin **32** (8), 1003-1008 (1997).
346. H. Mizoguchi, N. S. Bhuvanesh and P. M. Woodward, Chemical Communications (9), 1084-1085 (2003).
347. M. I. Pownceby and M. J. Fisher-White, Contributions to Mineralogy and Petrology **135** (2-3), 198-211 (1999).
348. E. Woermann, B. Brezney and A. Muan, American Journal of Science **267**, 463-479 (1969).
349. A.-T. Qiu, L.-J. Liu, P. Wei, X.-G. Lu and C.-H. Li, Transactions of Nonferrous Metals Society of China **21** (8), 1808-1816 (2011).
350. R. Palai, R. Katiyar, H. Schmid, P. Tissot, S. Clark, J. Robertson, S. Redfern, G. Catalan and J. Scott, Physical Review B **77** (1), 014110 (2008).
351. R. Taylor, Journal of the American Ceramic Society **46** (6), 276-279 (1963).
352. J. Lopez-Martinez, A. Romero-Serrano, A. Hernandez-Ramirez, B. Zeifert, C. Gomez-Yañez and M. Hallen-Lopez, Journal of the European Ceramic Society **34** (15), 3729-3734 (2014).
353. A. Ramanan, J. Gopalakrishnan and C. Rao, Materials Research Bulletin **16** (2), 169-174 (1981).
354. V. Raghavan, Journal of Phase Equilibria and Diffusion **31** (4), 369-371 (2010).
355. J. Ducke, M. Trömel, D. Hohlwein and P. Kizler, Acta Crystallographica Section C: Crystal Structure Communications **52** (6), 1329-1331 (1996).
356. E. W. Gorter, Philips Research Reports **9**, 295-320,321-365 (1954).
357. C. D. Ling, S. Schmid, P. E. Blanchard, V. Petricek, G. J. McIntyre, N. Sharma, A. Maljuk, A. A. Yaremchenko, V. V. Kharton and M. Gutmann, Journal of the American Chemical Society **135** (17), 6477-6484 (2013).
358. J. Landers, S. Salamon, M. Escobar Castillo, D. Lupascu and H. Wende, Nano Letters **14** (11), 6061-6065 (2014).
359. C. Blaauw and F. Van der Woude, Journal of Physics C: Solid State Physics **6** (8), 1422 (1973).
360. A. Biran, P. Montano and U. Shimony, Journal of Physics and Chemistry of Solids **32** (2), 327-334 (1971).
361. D. Kothari, V. R. Reddy, A. Gupta, C. Meneghini and G. Aquilanti, Journal of Physics: Condensed Matter **22** (35), 356001 (2010).
362. V. Bhide and M. Multani, Solid State Communications **3** (9), 271-274 (1965).

363. F. Craciun, F. Cordero, B. S. Vasile, V. Fruth, M. Zaharescu, I. Atkinson, R. Trusca, L. Diamandescu, L. C. Tanase and P. Galizia, Physical Chemistry Chemical Physics **20** (21), 14652-14663 (2018).
364. A. Palewicz, T. Szumiata, R. Przeniosło, I. Sosnowska and I. Margiolaki, Solid State Communications **140** (7-8), 359-363 (2006).
365. J. Prado-Gonjal, D. Ávila, M. Villafuerte-Castrejón, F. González-García, L. Fuentes, R. Gómez, J. Pérez-Mazariego, V. Marquina and E. Morán, Solid State Sciences **13** (11), 2030-2036 (2011).
366. M. C. Biesinger, B. P. Payne, A. P. Grosvenor, L. W. Lau, A. R. Gerson and R. S. C. Smart, Applied Surface Science **257** (7), 2717-2730 (2011).
367. Č. Jovalekić, M. Pavlović, P. Osmokrović and L. Atanasoska, Applied Physics Letters **72** (9), 1051-1053 (1998).
368. S. H. Chuang, M. L. Hsieh, S. C. Wu, H. C. Lin, T. S. Chao and T. H. Hou, Journal of the American Ceramic Society **94** (1), 250-254 (2011).
369. N. Zhang, Y. Qu, K. Pan, G. Wang and Y. Li, Nano Research **9** (3), 726-734 (2016).
370. A. Davidson, J. Tempere, M. Che, H. Roulet and G. Dufour, The Journal of Physical Chemistry **100** (12), 4919-4929 (1996).
371. A. P. Grosvenor, M. C. Biesinger, R. S. C. Smart and N. S. McIntyre, Surface Science **600** (9), 1771-1779 (2006).
372. Y. Shen, Y. Wu, X. Li, Q. Zhao and Y. Hou, Materials Letters **96**, 85-88 (2013).
373. S. Feng, W. Yang and Z. Wang, Materials Science and Engineering: B **176** (18), 1509-1512 (2011).
374. K. Ugendar, S. Samanta, S. Rayaprol, V. Siruguri, G. Markandeyulu and B. Nanda, Physical Review B **96** (3), 035138 (2017).
375. G. Singh and S. Bhat, Applied Magnetic Resonance **46** (8), 921-929 (2015).
376. S. Chauhan, M. Kumar and P. Pal, RSC Advances **6** (72), 68028-68040 (2016).
377. F. Yan, G. Xing, R. Wang and L. Li, Scientific Reports **5**, 9128 (2015).
378. M. Ouaissa, A. Benyoussef, G. S. Abo, S. Ouaissa, M. Hafid and M. Belaiche, Journal of Superconductivity and Novel Magnetism **28** (4), 1371-1377 (2015).
379. G. Dixit, J. P. Singh, R. Srivastava and H. Agrawal, Journal of Magnetism and Magnetic Materials **324** (4), 479-483 (2012).
380. R. Upadhyay, K. Parekh and R. Mehta, Physical Review B **68** (22), 224434 (2003).
381. I. Djerdj, G. Garnweitner, D. Arčon, M. Pregelj, Z. Jagličić and M. Niederberger, Journal of Materials Chemistry **18** (43), 5208-5217 (2008).
382. E. Chikoidze, Y. Dumont, H. von Bardeleben, W. Pacuski and O. Gorochov, Superlattices and Microstructures **42** (1-6), 176-184 (2007).
383. A. Zorko, M. Pregelj, M. Gomilšek, Z. Jagličić, D. Pajić, M. Telling, I. Arčon, I. Mikulska and M. Valant, Scientific Reports **5**, 7703 (2015).
384. N. A. Lomanova and V. V. Gusarov, Russian Journal of Inorganic Chemistry **56** (4), 616-620 (2011).
385. G. N. Subbanna and L. Ganapathi, Bulletin of Materials Science **9** (1), 29-35 (1987).
386. J. B. Li, Y. P. Huang, G. H. Rao, G. Y. Liu, J. Luo, J. R. Chen and J. K. Liang, Applied Physics Letters **96** (22), 222903/222901-222903/222903 (2010).
387. R. Withers, J. Thompson and A. Rae, Journal of Solid State Chemistry **94** (2), 404-417 (1991).
388. W. Dollase, Journal of Applied Crystallography **19** (4), 267-272 (1986).
389. N. A. Lomanova, V. G. Semenov, V. V. Panchuk and V. V. Gusarov, Doklady Chemistry **447** (2), 293-295 (2012).
390. M. Mazurek, E. Jartych and D. Oleszak, Nukleonika **58** (1), 143-147 (2013).
391. M. Mazurek and E. Jartych, Nukleonika **62** (2), 153-157 (2017).
392. W. Bai, G. Chen, J. Zhu, J. Yang, T. Lin, X. Meng, X. Tang, C. Duan and J. Chu, Applied Physics Letters **100** (8), 082902 (2012).
393. T. Jia, H. Kimura, Z. Cheng, H. Zhao, Y.-H. Kim, M. Osada, T. Matsumoto, N. Shibata and Y. Ikuhara, NPG Asia Materials **9** (2), e349 (2017).

394. R. Newnham, R. Wolfe and J. Dorrian, Materials Research Bulletin **6** (10), 1029-1039 (1971).
395. D. G. Porob and P. A. Maggard, Materials Research Bulletin **41** (8), 1513-1519 (2006).
396. S. Cassaignon, M. Koelsch and J.-P. Jolivet, Journal of Materials Science **42** (16), 6689-6695 (2007).
397. Y. Hu, H.-L. Tsai and C.-L. Huang, Journal of the European Ceramic Society **23** (5), 691-696 (2003).
398. I. Djerdj and A. Tonejc, Journal of Alloys and Compounds **413** (1), 159-174 (2006).
399. M. Khan, Y. Song, N. Chen and W. Cao, Materials Chemistry and Physics **142** (1), 148-153 (2013).
400. J. C.-S. Wu and C.-H. Chen, Journal of Photochemistry and Photobiology A: Chemistry **163** (3), 509-515 (2004).
401. B. Tian, C. Li, F. Gu, H. Jiang, Y. Hu and J. Zhang, Chemical Engineering Journal **151** (1), 220-227 (2009).
402. A. Kubacka, A. Fuerte, A. Martinez-Arias and M. Fernandez-Garcia, Applied Catalysis B: Environmental **74** (1), 26-33 (2007).
403. M.-C. Yang, T.-S. Yang and M.-S. Wong, Thin Solid Films **469**, 1-5 (2004).
404. G. Rossi, M. Calizzi, V. Di Cintio, S. Magkos, L. Amidani, L. Pasquini and F. Boscherini, The Journal of Physical Chemistry C **120** (14), 7457-7466 (2016).
405. G. Silversmit, D. Depla, H. Poelman, G. B. Marin and R. De Gryse, Journal of Electron Spectroscopy and Related Phenomena **135** (2), 167-175 (2004).
406. M. C. Biesinger, L. W. Lau, A. R. Gerson and R. S. C. Smart, Applied Surface Science **257** (3), 887-898 (2010).
407. E. Hryha, E. Rutqvist and L. Nyborg, Surface and Interface Analysis **44** (8), 1022-1025 (2012).
408. A. Glaser, S. Surnev, F. Netzer, N. Fateh, G. Fontalvo and C. Mitterer, Surface Science **601** (4), 1153-1159 (2007).
409. G. Zolnierkiewicz, J. Typek, N. Guskos and M. Bosacka, Journal of Non-Crystalline Solids **354** (35-39), 4506-4509 (2008).
410. S. Klosek and D. Raftery, The Journal of Physical Chemistry B **105** (14), 2815-2819 (2001).
411. S. G. Bratsch, Journal of Physical and Chemical Reference Data **18** (1), 1-21 (1989).
412. L. Li, C.-y. Liu and Y. Liu, Materials Chemistry and Physics **113** (2), 551-557 (2009).
413. W.-K. Jo and R. J. Tayade, Chinese Journal of Catalysis **35** (11), 1781-1792 (2014).
414. L. Alemany, F. Delgado and J. Blasco, Reaction Kinetics and Catalysis Letters **53** (1), 177-182 (1994).
415. V. Zazhigalov, A. Kharlamov, I. Bacherikova, G. Komashko, S. Khalameida, L. Bogutskaya, J. Stoch and A. Koval, Theoretical and Experimental Chemistry **34** (3), 162-164 (1998).
416. S. Begin-Colin, G. Le Caër, A. Mocellin, C. Jurenka and M. Zandona, Journal of Solid State Chemistry **127** (1), 98-108 (1996).
417. L. Dall'Acqua, M. Baricco, F. Berti, L. Lietti and E. Giamello, Journal of Materials Chemistry **8** (6), 1441-1446 (1998).
418. B.-O. Marinder and A. Magneli, Acta Chemica Scandinavica **11** (10), 1635-1640 (1957).
419. J. Mendialdua, R. Casanova and Y. Barbaux, Journal of Electron Spectroscopy and Related Phenomena **71** (3), 249-261 (1995).
420. Z. Hiroi, Progress in Solid State Chemistry **43** (1-2), 47-69 (2015).
421. M. Ogata, K. Kadowaki, M. Ijiri, Y. Takemoto, K. Terashima, T. Wakita, T. Yokoya and Y. Muraoka, Journal of the European Ceramic Society **37** (9), 3177-3183 (2017).
422. R. Enjalbert and J. Galy, Acta Crystallographica Section C **42** (11), 1467-1469 (1986).